LEABHARLANN CHOLÁISTE NA TRÍONÓIDE, BAILE ÁTHA CLIATH | TRINITY COLLEGE LIBRARY DUBLIN
Ollscoil Átha Cliath | The University of Dublin

Terms and Conditions of Use of Digitised Theses from Trinity College Library Dublin

Copyright statement

All material supplied by Trinity College Library is protected by copyright (under the Copyright and Related Rights Act, 2000 as amended) and other relevant Intellectual Property Rights. By accessing and using a Digitised Thesis from Trinity College Library you acknowledge that all Intellectual Property Rights in any Works supplied are the sole and exclusive property of the copyright and/or other IPR holder. Specific copyright holders may not be explicitly identified. Use of materials from other sources within a thesis should not be construed as a claim over them.

A non-exclusive, non-transferable licence is hereby granted to those using or reproducing, in whole or in part, the material for valid purposes, providing the copyright owners are acknowledged using the normal conventions. Where specific permission to use material is required, this is identified and such permission must be sought from the copyright holder or agency cited.

Liability statement

By using a Digitised Thesis, I accept that Trinity College Dublin bears no legal responsibility for the accuracy, legality or comprehensiveness of materials contained within the thesis, and that Trinity College Dublin accepts no liability for indirect, consequential, or incidental, damages or losses arising from use of the thesis for whatever reason. Information located in a thesis may be subject to specific use constraints, details of which may not be explicitly described. It is the responsibility of potential and actual users to be aware of such constraints and to abide by them. By making use of material from a digitised thesis, you accept these copyright and disclaimer provisions. Where it is brought to the attention of Trinity College Library that there may be a breach of copyright or other restraint, it is the policy to withdraw or take down access to a thesis while the issue is being resolved.

Access Agreement

By using a Digitised Thesis from Trinity College Library you are bound by the following Terms & Conditions. Please read them carefully.

I have read and I understand the following statement: All material supplied via a Digitised Thesis from Trinity College Library is protected by copyright and other intellectual property rights, and duplication or sale of all or part of any of a thesis is not permitted, except that material may be duplicated by you for your research use or for educational purposes in electronic or print form providing the copyright owners are acknowledged using the normal conventions. You must obtain permission for any other use. Electronic or print copies may not be offered, whether for sale or otherwise to anyone. This copy has been supplied on the understanding that it is copyright material and that no quotation from the thesis may be published without proper acknowledgement.

Geochemical signature of rift relocations at Iceland

Rachel Lucy Walters

A dissertation submitted for the degree of
Doctor of Philosophy
at the University of Dublin, Trinity College

2010

This dissertation has not previously been submitted as an exercise for a degree at this or any other university. It describes my original work, but includes the unpublished and published work of others; duly acknowledged in the text where appropriate. Trinity College Library may lend or copy this dissertation upon request. Permission is given only for single copies made for study purposes subject to normal conditions of acknowledgement.

TRINITY COLLEGE
2 7 AUG 2010
LIBRARY DUBLIN
THES
8939

R.L. Walters

Rachel Lucy Walters

Department of Geology, Trinity College Dublin

April 2010

Summary

Iceland is located at the intersection between the Mid-Atlantic Ridge and a mantle plume. Three active rift segments at Iceland represent the onshore expression of the Mid-Atlantic Ridge. Iceland's tectonic evolution has been dominated by rift relocations, a process where extension across one rift segment is gradually transferred to a new adjacent rift segment. Rift relocations are driven by the northwestward migration of Iceland over the mantle plume conduit, which is currently located underneath Vatnajökull icecap in central Iceland. The complete rift cycle is represented by the currently active Eastern Volcanic Zone (birth), Northern Volcanic Zone (steady-state) and Western Volcanic Zone (decline).

The aim of this dissertation is to characterise the geochemical signature of the different rift stages at Iceland and link differences in the lava chemistry with variations in the mantle melt compositions and melting process. Rift relocations result in significant changes in the spreading rate because two adjacent rifts are simultaneously active for several million years. In the first part of the dissertation, the geochemical signatures of all the active volcanic zones at Iceland, lavas from near the most recently extinct spreading axis, lavas from off-axis volcanic centres and Tertiary lavas are charaterised and compared to each other. In the second part, a new time-dependent model of upwelling and melting beneath a mid-ocean ridge is developed to understand the effects of spreading rate variations on the depth and degree of melting, and the resultant melt composition.

A new geochemical dataset was obtained for a series of young lava flows from the Skagi peninsular in northern Iceland. These young flows may be the last eruptions from a dying rift or the result of a transient episode of melting. The young lavas exhibit a relatively enriched geochemical signature compared to the established volcanic zones. New insight into the likely tectonic origin of young Skagi lavas is gained by identifying strong similarities between the chemistries of the young Skagi lavas, Eastern Volcanic Zone lavas and lavas from off-axis volcanoes.

A geochemical investigation into the different stages of the rift cycle is used to determine the change in geochemical signatures which can be associated with rift relocations as opposed to other factors such as glaciation and temporal plume variation. The most incompatible element enrichment is associated with the propagating tip of the Eastern Volcanic Zone and is produced by very small degrees of deep mantle melting, with a strong influence of garnet field melting. The established steady-state Northern Volcanic

Zone, away from the geochemical influence of the plume, has a significantly depleted signature compared to the Eastern Volcanic Zone. In central Iceland the Northern Volcanic Zone has a more enriched geochemical signature similar to that of the northern end of the Eastern Volcanic Zone. This enriched signature in central Iceland combined with the thickest crust in Iceland represents the influence of the plume on the melting regime. The Western Volcanic Zone has a similar geochemical signature to the steady-state Northern Volcanic Zone and shows no evidence of geochemical change during its decline.

Further geochemical comparison between Tertiary lava flows and present day rift activity is carried out to gain a better understanding of which types of lava flows are preserved in the exposed Tertiary crust in Iceland. A strong similarity is observed between the Tertiary geochemical signature and the Northern Volcanic Zone in central Iceland signature. This similarity suggests that a large proportion of the exposed Tertiary crust is formed by lava flows which have resulted from a similar melting regime to central Iceland, which is strongly influenced by active upwelling from the plume.

The spreading rate varies between different rift stages at Iceland from as little as 2 mm yr^{-1} at the declining end of the Western Volcanic Zone to the full Iceland spreading rate of 18 mm yr^{-1} across the Northern Volcanic Zone. The new model is constructed by adapting a published parameterisation of steady-state hydrous mantle melting to time-dependent melting. The model predicts the change in the melting regime associated with a rift relocation, showing that melting in a growing rift axis starts at small degrees, deep in the mantle, increasing in degree rapidly as the spreading rate increases. The crustal thickness and degree of melting is constant throughout the steady-state rift stage and remains relatively constant throughout the majority of decline. The final extinction of the rift is observed as a very rapid, but minor, decrease in the crustal thickness and degree of melting in the last Ma of activity. The model geochemical signature of enrichment during the birth of a rift axis, decreasing to a relatively depleted signature at steady-state and remaining relatively depleted throughout the decline of a rift axis correlates well with the geochemical signature of the Eastern Volcanic Zone, Northern Volcanic Zone and Western Volcanic Zone. Therefore, the enrichment observed in young Skagi lavas is more likely linked to a transient melting episode caused by temporal variations in plume activity, rather than the simple decline of a rift axis.

To my friends

Do not stand at my grave and weep,
I am not there. I do not sleep.
I am a thousand winds that blow.
I am the diamond glints on snow.
I am the sunlight on ripened grain.
I am the gentle Autumn rain.
When you awaken in the morning's hush
I am the swift uplifting rush
Of quiet birds in circled flight.
I am the soft stars that shine at night.
Do not stand at my grave and cry;
I am not there. I did not die.

Mary Elizabeth Frye (1905–2004)

Acknowledgements

I would like to say a huge thank you to my two supervisors Stephen Jones and John Maclennan who gave up so much of their time to help me over the last 4 years. They have provided continuous enthusiasm for the project, including carrying out fieldwork for me before the project even started, providing useful ideas, constructive criticism and good company on field trips and conferences. Steve's unrivalled knowledge of GMT, AWK and FORTRAN77, combined with his knowledge of the North Atlantic, has been invaluable, as has John's excellent knowledge of the geology of Iceland and geochemistry. I would not be writing this dissertation without the encouragement of John Dixon; I would like to thank him for his care throughout my undergraduate degree. Godfrey Fitton has provided great support throughout this project, not least in providing a vehicle for field work, sharing his immense volume of geochemical data and excellent knowledge of Icelandic geology. I must thank Emma Passmore for giving up a week to potter round the northern coast of Iceland with me and drive me anywhere on request.

For their contribution to lab work there are so many people I want to thank. Firstly, for patient instruction in XRF preparation and for analysing my samples for majors and traces I would like to thank Godfrey Fitton and Nic Odling. Rob Ellam and Jason Day provided REE analysis. Many thanks to Hazel Chapman and Jason Day for their patience and thoroughness when teaching me the methods for REE and isotope sample preparation. I am grateful to Sébastian Garcia and Arní Hjartarson for donating samples to the project for geochemical analysis. Financial support for this project was gratefully received from Science Foundation Ireland.

I would like to thank my office mates Eleanor Donoghue and Paul Byrne for keeping me in good company and providing advice, support and mountains of chocolate. I owe so much more than thanks to Sarah Heal who was given me invaluable friendship, a running partner and generally put up with me for the last 4 years — I hope there will be many more. I am also very grateful for the care and friendship of Viv Williams over the last 2 years. I would like to thank her for providing me with a home from home, whenever I needed.

A big thank you to Mags Duncan for being there to chat to whenever I needed. I am very grateful to Hilary and David Spurgeon for their generosity in letting me occupy their spare room. Finally, I would like to thank Sue Rose for being my family and supporting me so much throughout this project. I am forever in her debt.

Contents

1 Introduction **1**

1.1 Project Aim 1

1.2 Dissertation Organisation 2

2 Background **5**

2.1 Geology of Iceland: An Introduction 5

2.1.1 Regional Tectonic Setting 5

2.1.2 Volcanic Activity and Lava Stratigraphy 7

2.1.3 Tectonic Evolution: Rift Relocations 10

2.2 Geochemistry 18

2.2.1 Iceland Geochemical Anomaly 18

2.2.2 Mantle Source 20

2.2.3 Crustal Assimilation 20

2.2.4 Magma Mixing 21

2.2.5 Fractional Crystallisation 21

2.2.6 Hydrothermal Alteration 22

2.3 Mantle Melting 23

2.3.1 Introduction 23

2.3.2 Mantle Flow and the Melting Region 25

2.3.3 Mode of Melting: Batch versus Fractional 26
2.3.4 Melt Transport 27
2.3.5 Geochemical Behaviour During Melting 28
2.3.6 Temporal Variations: Rift Jumps and Glaciation 30

3 The Skagafjördur Region, Northern Iceland **33**
3.1 Introduction 33
3.2 Geological Background 36
3.3 Field Observations 37
3.4 Sample Descriptions 42
3.5 Geochemical Observations 44
3.6 Discussion and Conclusions 53

4 Temporal Variations in Geochemical Signature at Iceland **57**
4.1 Introduction 57
4.2 Background 58
4.2.1 Temporal Processes 58
4.2.2 Rift Cycle at Iceland 59
4.2.3 Existing Geochemical Data 62
4.3 Geochemical Observations 67
4.3.1 Skagi versus Western Volcanic Zone 68
4.3.2 Skagi versus Northern Volcanic Zone 79
4.3.3 Skagi versus Eastern Volcanic Zone 86
4.3.4 Skagi versus Off-axis Volcanism 95
4.4 REE Inversion Modelling 100
4.4.1 Background 100

4.4.2 Application to Skagi 101
4.5 Discussion and Conclusions 102

5 Geochemical Insights into Crustal Accretion at Iceland 107

5.1 Introduction 107
5.2 Background 108
5.3 Geochemical Observations of Tertiary Lavas 112
5.4 Geochemical Comparisons 126
5.4.1 Tertiary versus Neovolcanic Zones 128
5.4.2 Tertiary versus Off-axis Volcanism 139
5.4.3 Tertiary versus Stóravíti 147
5.4.4 Tertiary versus Extinct Skagi Rift 150
5.4.5 Dyke Chemistry 153
5.4.6 Statistical Analysis 159
5.5 Discussion 160
5.6 Conclusions 167

6 Model Theory and Development 169

6.1 Introduction 169
6.2 Background 170
6.2.1 Existing Numerical Models 170
6.2.2 Limitations 174
6.3 Model Outline 177
6.4 Mantle Flow Field 182
6.5 Thermal Structure 183
6.5.1 Boundary Conditions 183

6.5.2 Starting Thermal Structure 184
6.5.3 Thermal Advection and Diffusion 184
6.6 Mantle Residue 185
6.6.1 Definition 185
6.6.2 Boundary Conditions 185
6.6.3 Initial Conditions 185
6.6.4 Residue Evolution 186
6.7 Melting 186
6.7.1 Anhydrous Melting 187
6.7.2 Latent Heat of Melting 188
6.7.3 Anhydrous Melting Derivatives 189
6.7.4 Hydrous Melting 192
6.7.5 Hydrous Melting Derivatives 194
6.7.6 Change in Melt Fraction 196
6.8 Crustal Thickness 196
6.9 Composition 198
6.10 Summary 200

7 Model Application **203**

7.1 Introduction 203
7.2 Background 203
7.2.1 Wedge Angle Variations 204
7.2.2 Modelling Rift Jumps 207
7.2.3 Calculating Mean F 207
7.2.4 Composition 207
7.3 Model Testing 209

7.4 Model Experiments 213
7.4.1 Spreading Rate 213
7.4.2 Wedge Angle 214
7.4.3 Mantle Potential Temperature 219
7.4.4 Water Content 222
7.5 Application to Iceland 225
7.5.1 Constraints 225
7.5.2 Comparative Observations 226
7.5.3 Results 227
7.6 Discussion and Further Application 243
7.6.1 Iceland 243
7.6.2 Phoenix Ridge 244
7.6.3 Non-volcanic Margins 245
7.7 Conclusions 246

8 Discussion and Conclusions **249**

8.1 Origin of Skagi Quaternary Melts 249
8.2 Kinematics and Dynamics of Rift Relocations 255
8.3 Conclusions 256
8.4 Further Work 258
8.4.1 Skagi 258
8.4.2 Tertiary crust 258
8.4.3 Numerical Modelling 259

References **263**

A Geological Map of Skagi **277**

B Analytical Methods **279**

B.1 Whole-rock Powder Preparation 279

B.2 X-ray Fluorescence Analysis 279

B.3 Inductively Coupled Plasma Mass Spectrometry 283

B.4 Solid Source Mass Spectrometry: Sr and Nd Isotope Analysis 285

C Data Tables **287**

D Additional Model Theory **297**

D.1 Half-Space Cooling Model 297

D.2 Control Volume Formulation Method 297

D.2.1 General Features of the Control Volume Method 300

D.2.2 Application to Temperature 302

D.2.3 Application to Residue 303

D.3 Lagrangian Derivative 304

List of Figures

2.1 Bathymetry of the North Atlantic 7

2.2 Short-wavelength gravity for the North Atlantic: V-shaped ridges . . . 8

2.3 Models for propagation of temperature anomalies beneath Iceland . . . 12

2.4 Compositional map of Iceland's main volcanic zones 13

2.5 Simplified geological map of Iceland 14

2.6 Tectonic map of Iceland 15

2.7 Schematic diagram of a rift relocation 16

2.8 Garcia et al. (2003) sample map 17

2.9 Garcia et al. (2003) $^{40}Ar/^{39}Ar$ dating results 17

2.10 $^{87}Sr/^{86}Sr$ and La/Sm variations for the Mid-Atlantic Ridge 19

2.11 Adiabatic decompression melting paths 24

2.12 Schematic representation of the melting region 26

2.13 Herdubreid glacial table mountain 32

2.14 Theistareykjabunga postglacial lava shield 32

3.1 Geological map of Iceland 34

3.2 Sketch geological cross-section of Skagi 34

3.3 Geological map of the Skagafjördur region 38

3.4 Photograph and sketch of Selnes Bay 40

3.5 Photograph of Tertiary lava flow weathering 41

3.6 Photograph of fluvio-glacial sediments 42
3.7 Photograph of columnar jointing 42
3.8 Photograph of Ketubjörg volcanic vent 43
3.9 Photograph of Quaternary dyke at Selvík 44
3.10 Locations and TAS diagram for Skagi samples 46
3.11 TAS diagrams for Skagi: lavas and dykes 47
3.12 Major and trace element variation in across Skagafjördur region 48
3.13 Major element variation in Skagi: Quaternary versus Tertiary 50
3.14 Trace element variation in Skagi: Quaternary versus Tertiary 51
3.15 REE concentrations in Skagi lava flows: Quaternary versus Tertiary . . 52
3.16 REE concentrations in Skagi dykes: Quaternary versus Tertiary 52
3.17 Isotope ratio variation with latitude in Skagi 54
3.18 Isotope ratio variation in Skagi 55

4.1 Tectonic map of Iceland 61
4.2 Crustal thickness map of Iceland 66
4.3 TiO_2 and trace element variations: Skagi versus Langjökull 72
4.4 REE: Skagi versus Langjökull 73
4.5 TiO_2 and trace element variations: Skagi versus Western Volcanic Zone 75
4.6 REE: Skagi versus Western Volcanic Zone 76
4.7 TiO_2 and trace element variations with latitude: west Iceland 77
4.8 Isotope ratio variation with latitude: west Iceland 78
4.9 TiO_2 and trace element variations: Skagi versus Northern Volcanic Zone 81
4.10 REE: Skagi versus Northern Volcanic Zone 82
4.11 TiO_2 and trace element variations: Skagi versus central Iceland 84
4.12 REE: Skagi versus central Iceland 85

4.13 TiO_2 and trace element variations: Skagi versus Eastern Volcanic Zone 89

4.14 REE: Skagi versus Eastern Volcanic Zone 90

4.15 TiO_2 and trace element variations with latitude: east Iceland 93

4.16 Isotope ratio variation with latitude: east Iceland 94

4.17 TiO_2 and trace element variations: Skagi versus Grímsnes 96

4.18 REE: Skagi versus Grímsnes 97

4.19 TiO_2 and trace element variations: Skagi versus Snaefell 98

4.20 TiO_2 and trace element variations: Skagi versus Snaefellsnes 99

4.21 Skagi REE inversion results: model fit 102

4.22 Skagi REE inversion results: melt fraction versus depth 103

5.1 Photograph of Tertiary lava pile, northwest Iceland 109

5.2 Photograph of Tertiary central volcano, western Iceland 110

5.3 Pálmason model of crustal accretion 111

5.4 Variation of Zr/Nb with age in Icelandic basalts 111

5.5 Variation of Zr/Nb with volume in Icelandic basalts 112

5.6 Sample locations and TAS diagram for Tertiary 114

5.7 TAS diagrams for Tertiary 115

5.8 Major element variation in North Tertiary lavas 117

5.9 Major element variation in Northwest Tertiary lavas 118

5.10 Major element variation in East Tertiary lavas 119

5.11 Trace element variation in North Tertiary lavas 121

5.12 Trace element variation in Northwest Tertiary lavas 122

5.13 Trace element variation in East Tertiary lavas 123

5.14 REE concentrations in East Tertiary lavas 124

5.15 Cumulative % frequency comparison: all Tertiary data 125

5.16 Isotope ratio variation in Tertiary crust 127
5.17 TiO_2 and Zr/Y variations: Tertiary versus Western Volcanic Zone . . . 131
5.18 REE: Tertiary versus Western Volcanic Zone 132
5.19 TiO_2 and Zr/Y variations: Tertiary versus Northern Volcanic Zone . . 133
5.20 REE: Tertiary versus Northern Volcanic Zone 134
5.21 TiO_2 and Zr/Y variations: Tertiary versus central Iceland 135
5.22 Sm/Yb and Nb/Y variations: Tertiary versus central Iceland 136
5.23 REE: Tertiary versus central Iceland 136
5.24 TiO_2 and Zr/Y variations: Tertiary versus Eastern Volcanic Zone . . . 137
5.25 REE: Tertiary versus Eastern Volcanic Zone 138
5.26 TiO_2 and Zr/Y variations: Tertiary versus Grímsnes 141
5.27 REE: Tertiary versus Grímsnes 142
5.28 TiO_2 and Zr/Y variations: Tertiary versus Snaefellsnes 143
5.29 REE: Tertiary versus Snaefellsnes 144
5.30 TiO_2 and Zr/Y variations: Tertiary versus Snaefell 145
5.31 REE: Tertiary versus Snaefell 146
5.32 TiO_2 and Zr/Y variations: Tertiary versus Stóravíti 148
5.33 REE: Tertiary versus Stóravíti 149
5.34 TiO_2 and Zr/Y variations: Tertiary versus Skagi 151
5.35 REE: Tertiary versus Skagi 152
5.36 Major and trace element variation in dykes 155
5.37 TiO_2 and Zr/Y variations: Tertiary versus dykes 156
5.38 REE: Tertiary versus dykes 157
5.39 TiO_2 and Zr/Y distributions: Northern Volcanic Zone versus dykes . . 158
5.40 Tectonic map of Iceland with plume track 164

6.1 Model flowchart 179

6.2 Simple 2D corner flow geometry 183

6.3 Anhydrous melting curves 189

6.4 Hydrous melting curves from Katz et al. (2003) 192

6.5 Variation in composition (C_L/C_0) with melt fraction 199

7.1 Bathymetric cross section of V-shaped ridges 206

7.2 Variation in wedge angle with upwelling rate 206

7.3 Melt fraction-depth profiles for different spreading rates 210

7.4 Melt fraction-depth profiles, Bown and White (1994) 210

7.5 Melt fraction-depth profiles for different T_p and H_2O 211

7.6 Melt fraction-depth profiles, Katz et al. (2003) 212

7.7 Variation in crustal thickness for different spreading rates 214

7.8 Variation in composition with spreading rate 215

7.9 Variation in crustal thickness for different wedge angles at 50 mm yr^{-1} 217

7.10 Variation in crustal thickness for different wedge angles at 20 mm yr^{-1} 218

7.11 Variation in composition with wedge angle 218

7.12 Variation in crustal thickness for different potential temperature 221

7.13 Variation in composition with mantle potential temperature 221

7.14 Variation in crustal thickness for different water contents 223

7.15 Melt fraction-depth profiles for varying water contents 224

7.16 Variation in composition with water content 224

7.17 Velocity model for a rift relocation at Iceland 226

7.18 Iceland model: variation in crustal thickness for varying T_p 230

7.19 Iceland model: variation in crustal thickness for varying H_2O 230

7.20 Iceland model: melt fraction-depth profiles for anhydrous melting . . . 231

7.21 Iceland model: melt fraction-depth profiles for hydrous melting 231

7.22 Iceland model: melt fraction-depth profiles for rift initiation 232

7.23 Iceland model: variation in composition for fictive elements, anhydrous melting 236

7.24 Iceland model: variation in composition for fictive elements, hydrous melting 236

7.25 Iceland model: variation in composition for real elements, anhydrous melting 237

7.26 Iceland model: variation in composition for real elements, hydrous melting 237

7.27 Iceland model: Nb/Y variation through time 240

7.28 Iceland model: Zr/Y variation through time 241

7.29 Iceland model: Sm/Yb variation through time 242

7.30 Iberian continental margin 246

8.1 Schematic diagram of a radiating mantle pulse beneath the Skagi rift . 254

D.1 Control volume 299

List of Tables

4.1 Compilation of published geochemical data: references 63

4.2 Partition coefficients 68

5.1 K-S statistic results 159

6.1 Model parameters 180

6.2 Melting parameters 181

7.1 Bulk partition coefficients 208

B.1 Major element XRF precision and accuracy estimates 281

B.2 Trace element XRF precision and accuracy estimates 282

B.3 REE ICP-MS precision and accuracy estimates 284

C.1 Sample locations and descriptions 288

C.2 Sample locations and descriptions 289

C.3 Major element data 290

C.4 Major element data 291

C.5 Trace element data 292

C.6 Trace element data 293

C.7 REE data 294

C.8 REE data continued 295

C.9 Sr and Nd isotope data 296

C.10 Iceland geochemical database 296

Chapter 1

Introduction

1.1 Project Aim

Mid-ocean ridges have been studied extensively using various geophysical and geochemical methods to gain new insights into the formation of new oceanic crust. The composition of Mid-Ocean Ridge Basalt (MORB) lavas has been found to vary between different locations and, more recently established, through time. The temporal variations in geochemistry can be linked to tectonic events such as the growth and death of rift segments (Choe et al., 2007), as well as variations in mantle processes. There have been several time-dependent models of melting beneath mid-ocean ridges (e.g. Bown and White, 1995; Mittelstaedt et al., 2008), but these models have not considered the effects of variable spreading rate on the volume and composition of ridge products.

Iceland's tectonic evolution has been dominated by rift relocations. Rift relocations at Iceland occur as discrete eastward jumps of the active spreading axes and are thought to be driven by the relative eastward migration of mantle plume centre. The rift jumps are characterised by the death of one rift axis to facilitate the growth of another, with two adjacent rifts active together for several million years before the old rift becomes completely extinct. Rift relocations are a common feature associated with plume-ridge interaction and have been observed at the Galapagos, Louisville, Shona and Kerguelen hotspots (Small, 1995). The processes controlling rift relocations are poorly understood. This study aims to provide quantitative constraints on the changes in melting and chemistry associated with these tectonic events from both geochemical observations and numerical models. These constraints provide new insights into which

processes at Iceland result in the observed geochemical variations and which factors may influence the initiation of new rift segments in a mid-ocean ridge setting.

Iceland is chosen as the main study area because it is the largest subaerial exposure of an active mid-ocean ridge. This exposure allows new lava samples to be placed in a stratigraphy, which is not possible for samples retrieved from sea floor dredging for example. There is also a wealth of geochemical data already available for many of the active volcanic regions at Iceland. All three stages in the evolution of a rift axis are preserved at Iceland; growth, steady-state and death. Geochemical comparison of different rift stages is based on the collation of over 2000 existing geochemical analyses for the active rifts and Tertiary crust. However, very little geochemical data exists for dying rifts, therefore a suite of over 50 new samples were collected over two field seasons (2005, 2006) for the extinct Skagi rift to produce a detailed geochemical study of a dying rift. It must be taken into consideration that Iceland exhibits anomalous rates of melting which produce up to 40 km thick crust compared to typical oceanic crustal thicknesses of 6–8 km. Therefore, inferences made about melt generation from the geochemical signature at Iceland may not be wholly applicable to typical mid-ocean ridge settings. However, it can be shown that some of the temporal geochemical variations associated with rift relocations observed at Iceland are similar to those observed in normal mid-ocean ridge settings.

The main aims of this dissertation are to characterise the geochemistry of different rift stages at Iceland and infer how the melting regime may vary through time. An important part of this aim is to determine the tectonic origin of the Quaternary lavas at Skagi. A new time-dependent model of upwelling and melting beneath a mid-ocean ridge is developed to allow a quantitative assessment of the effect of spreading rate variations, such as during a rift relocation, on melting processes and the volume and composition of melt. The results of the model are compared with the geochemical variations observed at Iceland.

1.2 Dissertation Organisation

Chapter 2 provides an introduction to the geology of Iceland and to studies on rift relocations. The basic concepts of mantle melting are described along with the most recent studies regarding the main controls on lava chemistry, including source variation, melt transport and mixing, crustal assimilation, fractional crystallisation and hydrothermal

alteration. An introduction to the behaviour of elements during melting is also given.

Chapter 3 describes the main lava stratigraphy observed in the Skagafjördur region in northern Iceland and characterises the geochemical signature of the lava flows and dykes from the extinct Skagi Rift. Field observations and new geochemical data are presented. Comparisons are made between the composition of lavas and dykes, Tertiary and Quaternary age lavas and lavas from different parts of the region.

Chapter 4 describes the geochemical signature of each of the active rift zones on Iceland from existing observations. These active rift zones are compared with each other and with the extinct Skagi rift. The geochemical observations are shown in relation to existing geophysical observations such as crustal thickness. It is clear that the different stages of the rift cycle exhibit different geochemical signatures which could be related to crustal thickness variations. The results from Rare Earth Element (REE) inversion modelling carried out on the extinct Skagi Rift data are also presented in this chapter and compared with existing results from the Northern Volcanic Zone.

Chapter 5 presents a geochemical investigation into crustal accretion processes that operated to form the Tertiary crust at Iceland. Comparisons are made between existing Tertiary data, neovolcanic zones and the extinct Skagi Rift. The results provide new insights into the preservation bias introduced following the emplacement of lava flows.

Chapter 6 gives an account of published numerical modelling of melting at mid-ocean ridges, including assumptions and limitations. A new model of time-dependent melting at mid-ocean ridges is described including a detailed description of both the governing equations and the computational methods.

Chapter 7 contains the model results and its application to Iceland. The model is tested for consistency against existing models of steady-state mid-ocean ridge melting.

Chapter 8 presents a final discussion of how the new observations from geochemical and numerical investigations relate to the overall tectonic setting at Iceland. The main conclusions and suggested further research provide the final section of this dissertation.

Chapter 2

Background

The first part of this chapter will provide a brief introduction to the geology of Iceland including a description of the regional tectonic setting, current volcanic activity and kinematics of rift relocations. It will also include a description of the main controls on the geochemical signatures of Icelandic lavas. The second part of the chapter will summarise the basic concepts of mantle melting. In order to estimate the volume and composition of melt produced by mid-ocean ridges, the melting regime and geometry of the melting region must be established. Factors which control the dynamics of mantle melting are qualitatively discussed in section 2.3 to provide background for the more detailed explanation of the numerical model theory and development (chapter 6).

2.1 Geology of Iceland: An Introduction

2.1.1 Regional Tectonic Setting

Iceland is situated in the middle of the North Atlantic where the Mid-Atlantic Ridge crosses a mantle plume. The mantle underneath Iceland is hotter than normal and produces excess melting and thicker than normal crust. The thick crust combined with dynamic support from the hot mantle results in the subaerial exposure of a large section of active mid-ocean ridge (Jones et al., 2002). The off-shore segments of the Mid-Atlantic Ridge connect to Iceland on the south-west coast (Reykjanes Ridge) and the central north coast (Kolbeinsey Ridge). The Reykjanes Ridge is linked to the Western Volcanic Zone and the Kolbeinsey Ridge is linked to the presently active

Northern Volcanic Zone via the Tjörnes Fracture Zone. The full spreading rate of the Mid-Atlantic Ridge at Iceland is approximately 18 mm yr^{-1} (DeMets et al., 1994) and it is therefore classed as slow spreading ridge. The local spreading direction is N100°E (DeMets et al., 1990) which is slightly oblique to the rest of the North Atlantic.

Figure 2.1 of North Atlantic bathymetry shows Iceland surrounded by a large flat-topped shelf reflecting the thick oceanic crust, which has a distinct edge. This steep slope is attributed to crustal flow beneath Iceland resulting in a steep flow front in the Moho which is reflected in the bathymetry (Jones and Maclennan, 2005). The Iceland shelf forms the central part of the Greenland-Iceland-Faroes Ridge, a hotspot track resulting from the the interaction between the Iceland Plume and the Mid-Atlantic Ridge. The Iceland plume track has an unusual geometry which is much broader compared to normal plume tracks. This could be attributed to the excessive crustal production resulting in mass re-distribution of the crust, producing a broad zone of thick crust rather than a narrow track. Crustal flow outwards from the plume centre is one mechanism of re-distributing of the crust. Other process which may contribute to crustal re-distribution include weathering, off-axis intrusions and magma flow within the crust.

Temporal variations in the melt production rate at Iceland form lineations in the bathymetry and free-air gravity field in the North Atlantic region, known as V-shaped ridges (figure 2.2). The presence of prominent ridges in the bathymetry south of Iceland was first noted by Vogt (1971). Jones et al. (2002) observed these ridges in detail using the short wavelength component of the free-air gravity field, identifying V-shaped ridges to the north of Iceland as well. These diachronous ridges propagate at least 1000 km from Iceland, indicating that the influence of the Iceland plume on melting at the Mid-Atlantic Ridge is much more extensive than just the Iceland shelf area. White et al. (1995) showed that the crustal thickness variations represented by V-shaped ridges could be accounted for by variations of about 100°C in the mantle potential temperature. Together with Hardarson et al. (1997) they also suggested that the V-shaped ridges are triggered by changes in plume flow caused by rift jumps. However, Jones et al. (2002) argued that the rheology of the lithosphere, with a 100 km thick rheological lid (Ito et al., 1999; Maclennan et al., 2001b), would not allow rift jumps to significantly affect lateral flow in the mantle. Jones et al. (2002) concluded that the variations in melt production results from time-dependent flow in the plume head beneath Iceland and probably relate to temporal variations in the input of material from the plume stalk. The periodicity of V-shaped ridges is similar to that of the rift relocations recorded on Iceland (section 2.1.3) and Jones et al. (2002) suggested

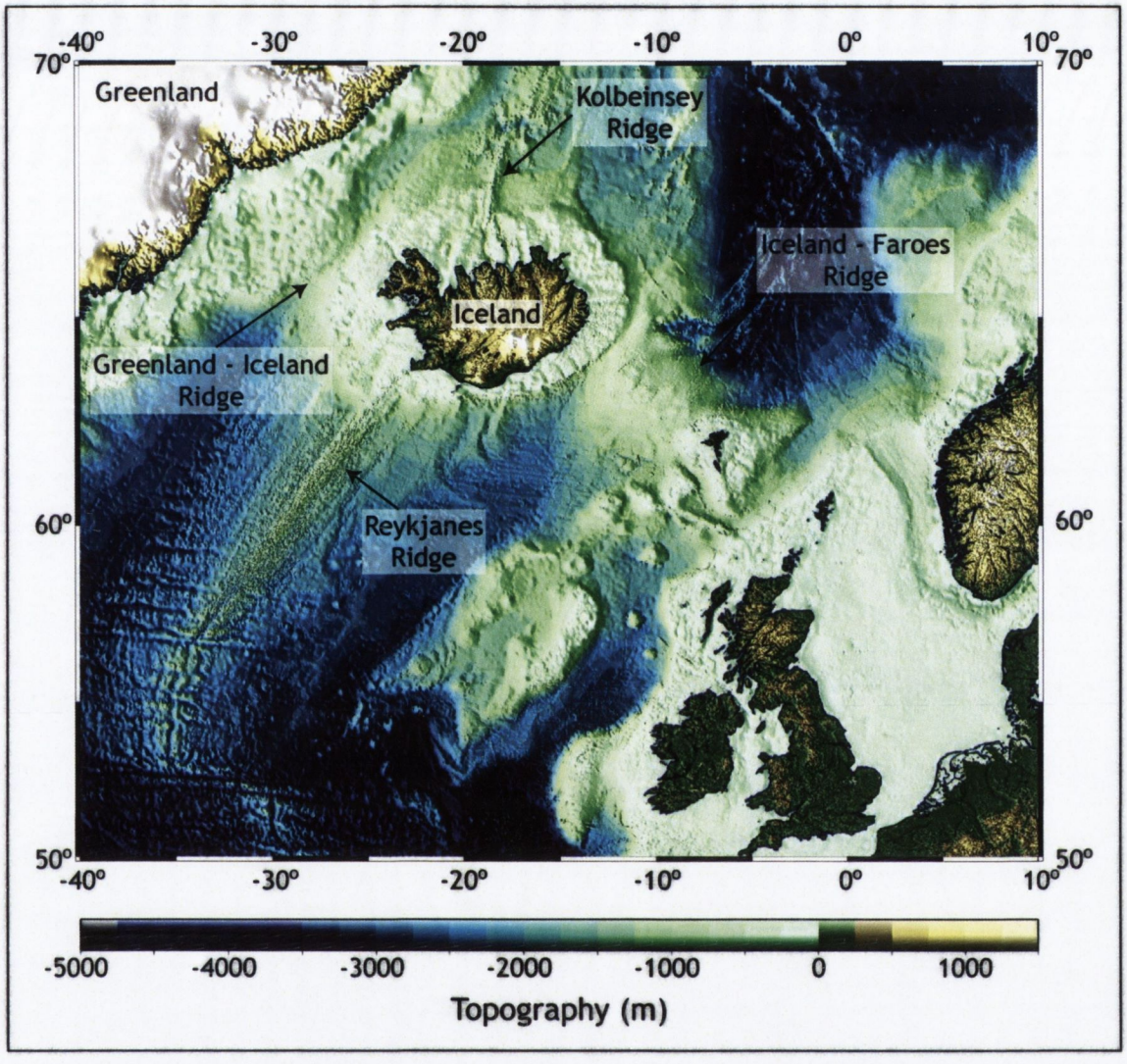

Figure 2.1: Iceland topography (30 m SRTM) and bathymetry of North Atlantic region. Notice the Iceland shelf of over-thickened oceanic crust with a distinct edge (data from Becker and Sandwell, 2005).

that pulses in the mantle plume may have triggered rift jumps and V-shaped ridges. A schematic example of a thermal anomaly propagating through the upper mantle is shown in figure 2.3 (Jones et al., 2002).

2.1.2 Volcanic Activity and Lava Stratigraphy

The onshore expression of the Mid-Atlantic Ridge at Iceland forms three main active volcanic zones, known collectively as the neovolcanic zones: Northern Volcanic Zone, Western Volcanic Zone and Eastern Volcanic Zone (figure 2.5). The Northern Volcanic Zone has been active for about 8 Ma (Garcia et al., 2003). The Western Volcanic Zone



Figure 2.2: Short-wavelength component of satellite gravity field for the North Atlantic, related to variations in the thickness and structure of oceanic crust. Individual V-shaped ridges are identified in sequence 1–7. Coloured lines indicate sediment thickness covering the V-shaped ridge record after Srivastava et al. (1988); yellow, 500 m; green, 1 km; blue, 1.5 km, 2 km and 2.5 km. Figure from Jones et al. (2002).

has been active for 6–7 Ma (Macdougall et al., 1977; Saemundsson, 1979; Jóhanesson, 1980). The Eastern Volcanic Zone has only been active for around 1.5–3 Ma (Saemundsson and Jóhanesson, 1994) and is overlapping with the Western Volcanic Zone. The Eastern Volcanic Zone is currently propagating southwards. Each zone is comprised of a series of volcanic systems defined by fissure swarms, central volcanoes or both (figure 2.6). Fissure swarms can be up to 20 km wide and over 100 km in length, and often have developed central volcanoes. The volcanic systems in general are oriented orthogonal to the regional spreading direction. Extension is focused in the three main volcanic zones; in south Iceland the full spreading rate is currently partitioned between the two overlapping rift zones as extension gradually transfers from the Western Volcanic Zone to the Eastern Volcanic Zone. Geodetic GPS data shows that the Western Volcanic Zone is subject to very little extension at present with the least amount of extension in the northeast at 2.6 ± 0.9 mm yr^{-1} (LaFemina et al., 2005). This arrangement is known as a rift relocation, or rift jump, and these are described in more detail in section 2.1.3. The bulk of volcanic activity is associated with the main rift zones. There are two smaller active flank zones; the Snaefellsnes and Öraefajökull Volcanic Belts, which contribute around 15% of the total eruptive volume at Iceland (Jakobsson, 1972). There is little evidence for extension associated with flank zones (Saemundsson, 1978) and the origin of the Snaefellsnes Volcanic Belt in terms of plate spreading and plume upwelling is very poorly understood.

Approximately 85% of recent basaltic volcanism on Iceland is tholeiitic (Jakobsson, 1972), with transitional and alkaline compositions restricted to the Eastern Volcanic Zone and the off-axis volcanic belts. The most alkaline compositions are associated with the propagating tip of the Eastern Volcanic Zone (Vestmannaeyjar) and the western end of the Snaefellsnes Volcanic Belt (figure 2.4). In addition to basaltic volcanism, small volumes of rhyolites are produced, generally in association with central volcanoes. Icelandic rhyolites are thought to result from re-melting of the crust and extreme fractional crystallisation.

Icelandic Tertiary rocks range in age from approximately 17 Ma (Hardarson et al., 1997) to 3.3 Ma, the start of major glaciation in the northern hemisphere. The Tertiary is exposed in continuous coastal sections in the Northwest, North and Eastern Fjörds and by steep U-shaped glaciated valleys inland. These cliff sections expose regular layering of trap-like basaltic lava flows. Numerous central volcanoes are also preserved in the Tertiary crust. The main features of the Tertiary and the mechanical processes governing its preservation, including Pálmason's model of crustal accretion, are described in chapter 5. The Icelandic Quaternary is defined by the start of major

glaciation at 3.3 Ma and Quaternary lava flows are largely associated with the neovolcanic zones. However, there are a few small outcrops of early Quaternary age lavas in north Iceland which are thought to be associated with an extinct volcanic zone, known as the Skagi rift (figure 2.5). The boundary between the Tertiary and Quaternary can be defined by an unconformity between Tertiary lavas and fluvio-glacial sediments, as observed at Skagi, northern Iceland (section 3.3). Recent volcanic activity (late Quaternary) is defined by a magnetic anomaly at 0.7 Ma and is solely associated with the neovolcanic zones and flank zones as described above.

2.1.3 Tectonic Evolution: Rift Relocations

Iceland's tectonic evolution has been dominated by rift relocations, a common feature of plume-ridge interaction. Rift relocations have been observed in association with the following hotspots: Galápagos, Louisville, Shona, Kerguelen and several other localities (Small, 1995; Mittelstaedt et al., 2008). These tectonic events occur on Iceland as discrete eastward jumps of the active on-shore spreading axes relative to the off-shore Mid-Atlantic Ridge (figure 2.7). They are thought to be ultimately driven by the westward migration of Iceland and the Mid-Atlantic Ridge over the Iceland mantle plume. Since 24 Ma when the Mid-Atlantic Ridge first coincided with the plume as the result of a westward rift relocation, the plume has repeatedly re-focused plate spreading and volcanic activity via rift jumps. Two extinct rifts can be observed in northwest Iceland (figure 2.5): the NW Iceland rift and the Skagi rift. The location of the extinct Skagi rift axis is identified by a regional syncline in the lava flow dip directions. Regional synclines are a characteristic feature of the active volcanic zones on Iceland. An inward dipping lava pile forms when continuous accumulation of lava flows close to the rift axis causes subsidence. This subsidence process is a key part of Pálmason's model of crustal accretion (Pálmason and Saemundsson, 1974) and is described in more detail in section 5.2.

The NW Iceland rift axis is likely to be located offshore from the Northwest Fjörds however it has not yet been mapped. The NW Iceland rift was active until 14.9 Ma when extension transferred to the Skagi rift; this transfer is marked by a major unconformity in northwest Iceland (Hardarson et al., 1997). The Skagi rift is the name given to the palaeorift located west of the Skagi peninsula and it is regarded as the northern extension to the Snaefellsnes Rift Zone. The main phase of activity on the Skagi rift initiated at 14.9 Ma however, it is not clear when activity ceased on this rift. An early

estimate by Saemundsson (1979) indicated that activity ceased on the Skagi rift around 6–7 Ma as extension transferred to the newly active Northern Volcanic Zone. A more recent study by Garcia et al. (2003) suggests that the Skagi rift remained active until approximately 3 Ma. However, a suite of Quaternary lavas exists on the Skagi peninsula of northern Iceland, adjacent to the Skagi palaeorift. These Skagi Quaternary lavas could be younger still than Garcia et al. (2003) predicted because K-Ar dates from several Skagi Quaternary lavas obtained by Everts et al. (1972) ranged from 0.5 to 1.5 Ma. Skagi Quaternary lavas are the main focus of the field work for this project. Their significance in terms of the regional tectonics is discussed in section 4.5.

Garcia et al. (2003) dated 37 dykes across northern Iceland (figure 2.8). Using the age and the distances from the relevant rift axes, they produced a plate spreading velocity model for the rift relocation from the extinct Skagi rift to the presently active Northern Volcanic Zone (figure 2.9). The model suggests that Skagi rift was active between 15 Ma and about 8–8.5 Ma, when the Northern Volcanic Zone was initiated. The two rifts were then simultaneously active for approximately 5–5.5 Ma until the transfer of extension to the Northern Volcanic Zone was completed and the Skagi rift became extinct around 3 Ma. While the two rifts were active together, the extension was partitioned between the two rifts so that the full spreading rate for one rift is reduced to around 9 mm yr^{-1}, half the full spreading rate for Iceland. There is some discrepancy between the current full spreading rate of 18 mm yr^{-1} (DeMets et al., 1994) and the total of 27.7±4.1 mm yr^{-1} reported by Garcia et al. (2003). Garcia et al. (2003) attribute their extreme total to the propagation of uncertainties in the half spreading rates. However, this discrepancy between actual and predicted spreading rates may be the result of using zero width for the zone of accretion whereas in reality at Iceland the volcanic zones are up to 50 km wide. The results from Garcia et al. (2003) indicate that this dual activity may result in asymmetrical spreading. LaFemina et al. (2005) show that the transfer of extension is likely to be a more gradual process. For example, as the Eastern Volcanic Zone propagates southwards the spreading rate increases from the southwest end to the northeast. This is mirrored by an adjacent decrease in the spreading rate from southwest to northeast across the Western Volcanic Zone, with the spreading rate decreasing to around 2 mm yr^{-1}. The effects of a variable spreading rate through time on the degree and depth of melting, and consequently ridge chemistry have not yet been investigated. A time-dependent model of upwelling beneath a mid-ocean ridge is required to model temporal variations in spreading rate outlined in chapter 6.

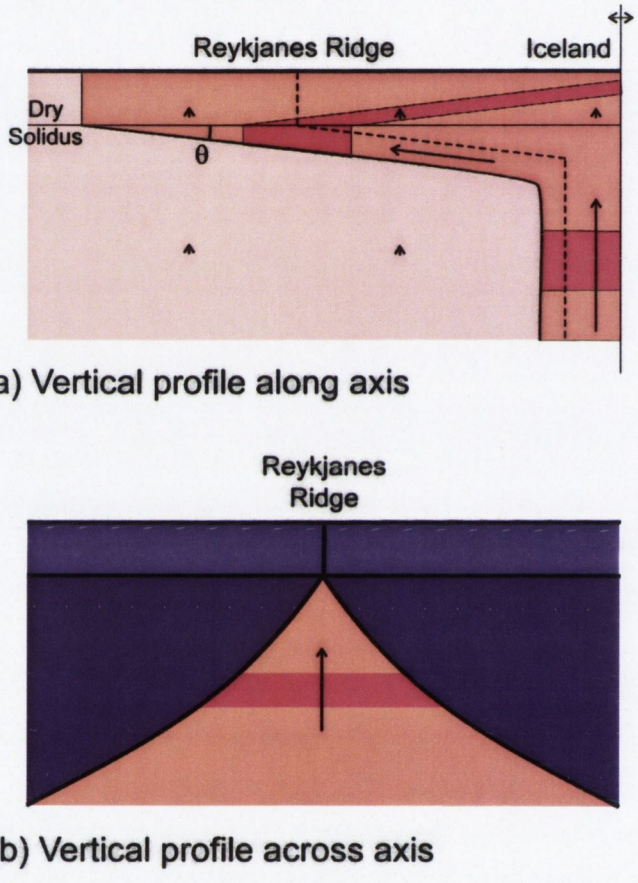

Figure 2.3: Schematic vertical cross-sections though the upper mantle in the plane of the spreading axis, showing the propagation of a temperature anomaly that could kinematically explain the V-shaped ridges. The anomaly is characterised by both horizontal and vertical flow, (a). Mantle viscosity increases significantly above the dry solidus as dehydration occurs (Ito et al., 1999). Below the dry solidus a combination of horizontal flow in the plume head and vertical flow in response to plate separation occurs. Above the dry solidus only vertical flow occurs. (b) shows the anomaly travelling through the melting region at the ridge axis. Figure (a) from Jones et al. (2002).

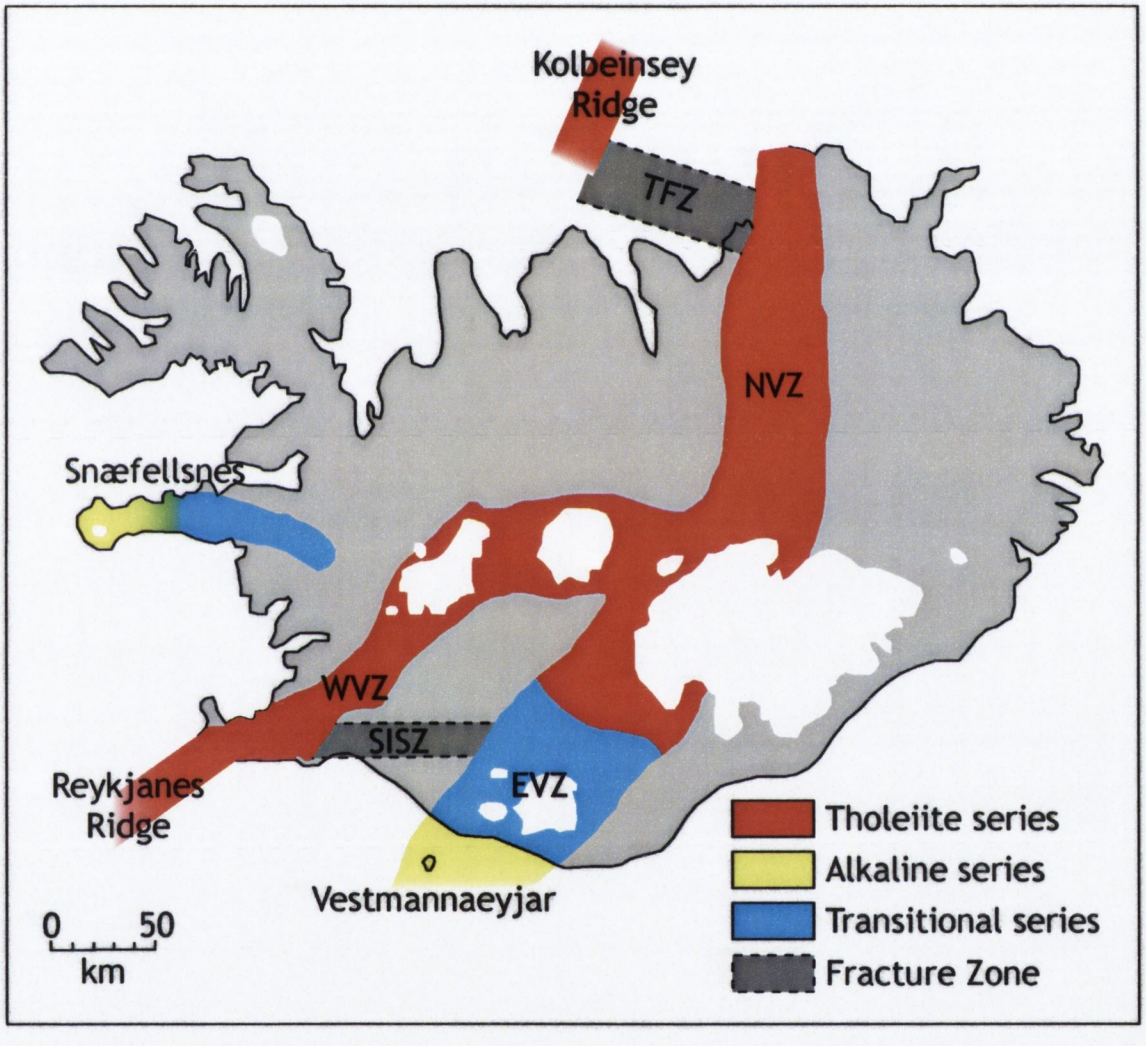

Figure 2.4: Map of Iceland showing the variation in composition from alkaline to tholeiitic volcanism in the main volcanic zones: NVZ. Northern Volcanic Zone; WVZ, Western Volcanic Zone; EVZ, Eastern Volcanic Zone. Also shown are the two fracture zones: SISZ, South Iceland Seismic Zone; TFZ, Tjörnes Fracture Zone. Based on Gudmundsson (2007).

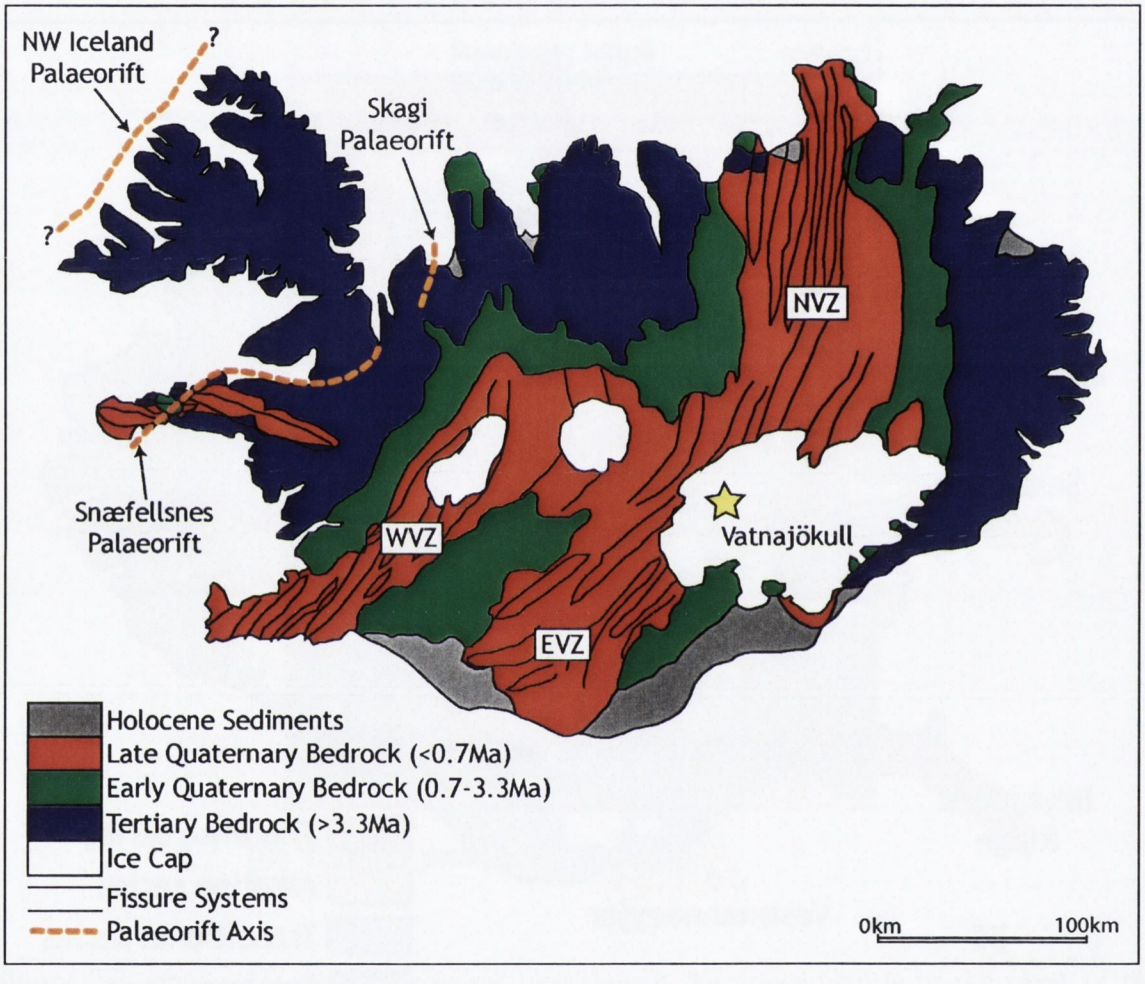

Figure 2.5: A simplified geological map of Iceland. The approximate locations of two extinct rift axes are shown in north-west Iceland. Presently active volcanic zone are shown in red: NVZ, Northern Volcanic Zone; WVZ, Western Volcanic Zone; EVZ, Eastern Volcanic Zone. Approximate plume centre location is shown as a yellow star. Adapted from Jóhanesson and Saemundsson (1998); Palaeorift locations from Hardarson et al. (1997) and Jóhanesson (1980).

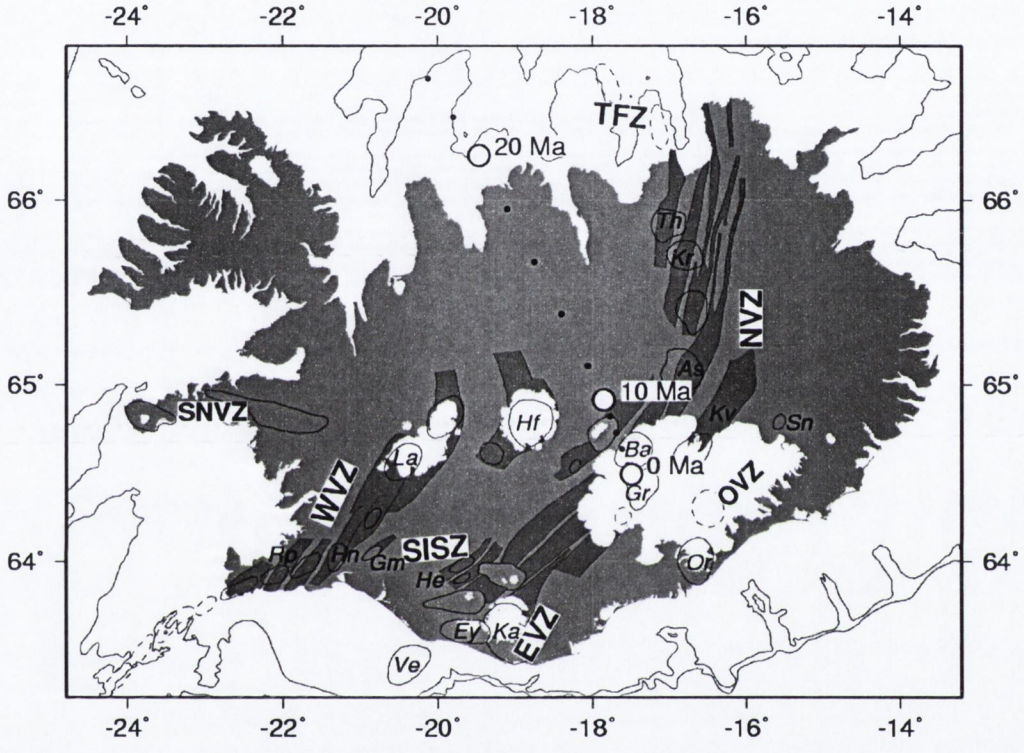

Figure 2.6: Tectonic map of Iceland based on Einarsson & Saemundsson (1987). Fissure swarms associated with volcanic systems forming the three main rift zones are filled dark grey. Central volcanoes are shown as closed circles. The approximate plume track over the last 20 Ma years is shown as black dots every 2 Ma and larger circles at 0, 10 and 20 Ma; no correction is made for plate spreading and rift jumps (Jones, 2003). The present location of the plume centre is beneath Vatnajökull icecap (0 Ma). The neovolcanic zones are labelled: NVZ, Northern Volcanic Zone; WVZ, Western Volcanic Zones; EVZ, Eastern Volcanic Zone. Active seismic zones: SISZ, South Iceland Seismic Zone; TFZ, Tjörnes Fracture Zone. Flank zones: SNVZ, Snaefellsnes Volcanic Zone; OVZ, Oŕaefajökull Volcanic Zone. Main volcanic systems labelled as follows: Th, Theistareykir; Kr, Krafla; As, Askja; Kv, Kverkfjöll; Ba, Bardarbunga; Gr, Grímsvötn; Ka, Katla; Ey, Eyjafjallajökull; He, Hekla; Ve, Vestmannaeyjar; Hf, Höfsjökull, La, Langjökull; Hn, Hengill; Gm, Grímsnes; Rp, Reykjanes Peninsula (includes all 3 systems). Sn, Snaefell and Or, Öraefajökull are volcanic centres.

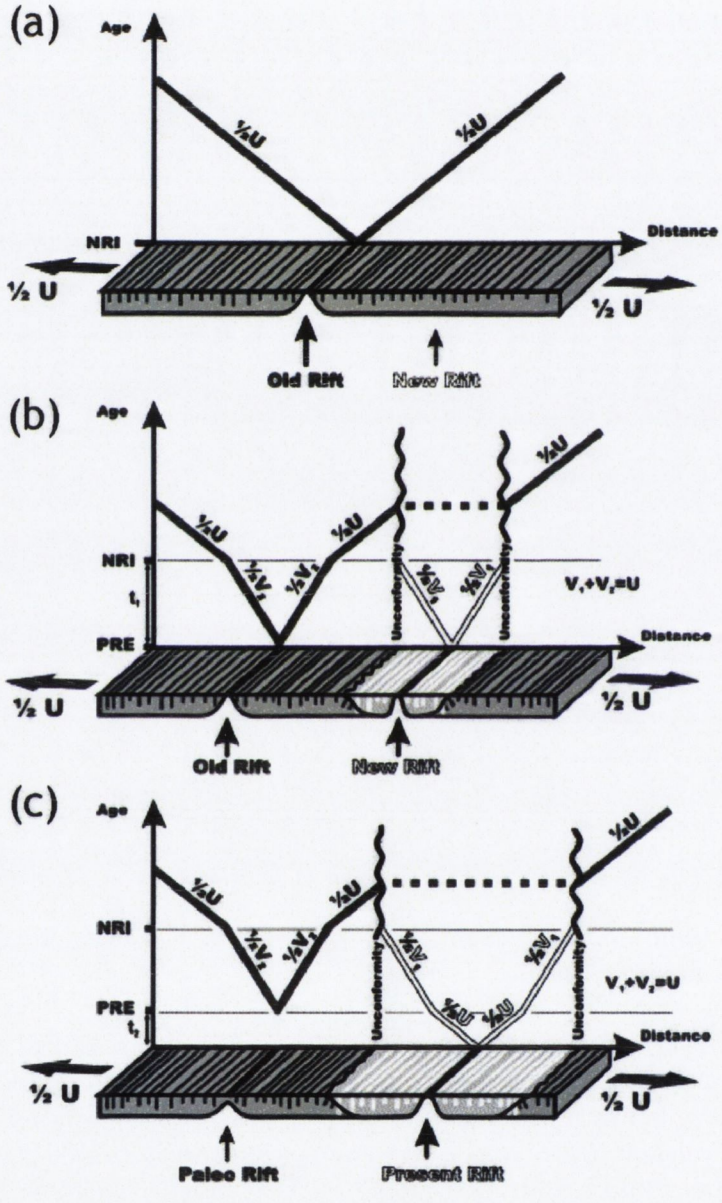

Figure 2.7: A schematic diagram of a rift relocation. (a) shows the old rift active with a full spreading rate, U and the location of the new rift initiation, east of the original rift. (b) shows both rifts active together with the old rift at full spreading rate V_2 and new rift at full spreading rate V_1. The original full spreading rate U is partitioned across the two axes. (c) shows the final stage when the old rift is no longer active and the new rift takes up the full extension U. Unconformities form as new rift lavas are emplaced on top of old lavas from the old rift. Figure taken from Garcia et al. (2003).

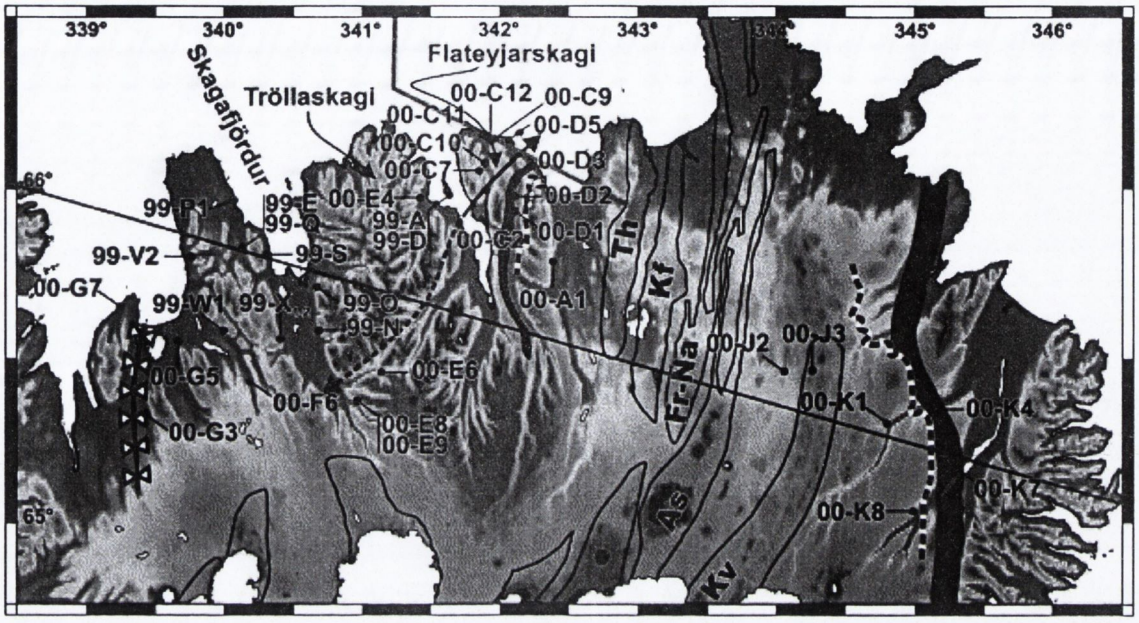

Figure 2.8: Sample locations of dated dykes in northern Iceland. The volcanic systems of the Northern Volcanic Zone are labelled: Th, Theistareykir; Kf, Krafla; Fr-Na, Fremri-Namur; As, Askja; Kv, Kverkfjöll. The synclinal axis marking the location of the extinct Skagi rift is also indicated. The line of cross-section for the plate spreading velocity model (figure 2.9 is shown as a solid thin black line from West to East. Figure from Garcia et al. (2003).

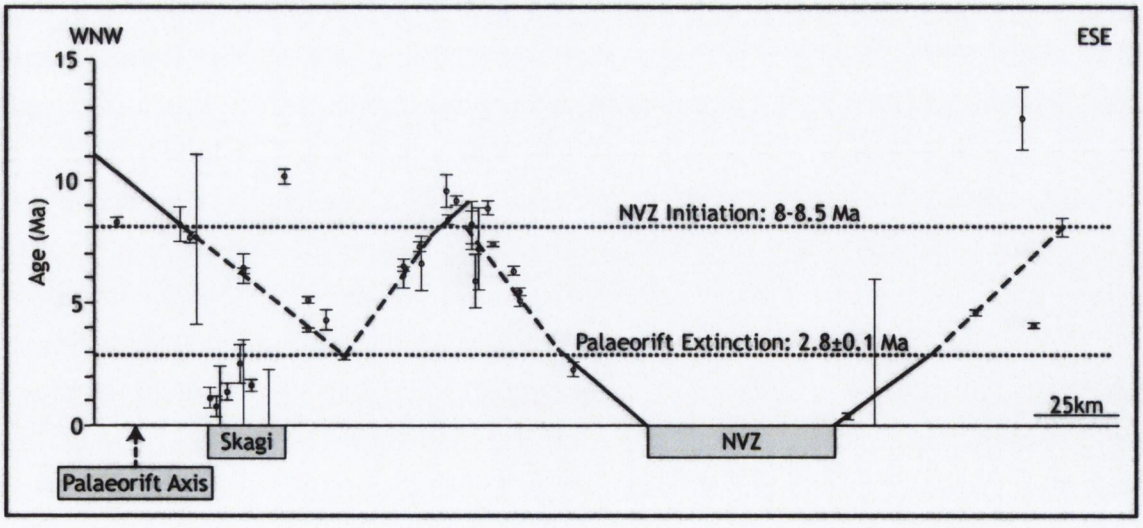

Figure 2.9: Dyke ages inferred from $^{40}Ar/^{39}Ar$ radiochronology plotted on N106°E cross-section across northern Iceland. The Northern Volcanic Zone and the Skagi palaeorift synformal axis are marked. Three poorly defined young ages obtained from the Skagi peninsula are labelled, together with several early K-Ar dates from Everts et al. (1972). Based on Garcia et al. (2003).

2.2 Geochemistry

2.2.1 Iceland Geochemical Anomaly

A broad geochemical anomaly at Iceland is observed as systematic increases in incompatible element enrichment and the Sr-isotope ratio towards Iceland along the Reykjanes Ridge. These variations were first observed by Schilling (1973) and Hart et al. (1973). The compilation of published $^{87}Sr/^{86}Sr$ and La/Sm data for the Mid-Atlantic Ridge from 57°N to 70°N is shown in figure 2.10 (Sigmarsson et al., 2008). The variation in Sr-isotope ratio reveals much higher values for Iceland compared to the Reykjanes and Kolbeinsey Ridges with gradual increases shown from 61°N and 70°N towards Iceland. A similar trend is observed for La/Sm with elevated values at Iceland and gradual increases from 60°N and 70°N towards Iceland. However, a subset of Iceland samples also exhibit very depleted La/Sm values which may reflect melting of an unusually depleted mantle (Sigmarsson et al., 2008). The greater range of incompatible element enrichment at Iceland could be related to several factors; further geochemical investigation is required to ascertain which of the following factors are the most important.

Firstly, the general increase in Sr-isotope ratio towards Iceland along the Mid-Atlantic Ridge, excluding depleted Iceland samples, reflects the greater access to enriched mantle components at Iceland resulting from the influence of the Iceland mantle plume. The geochemical effect of the plume head extends up to 500–600 km south of Iceland, whereas V-shaped ridges propagate at least 1000 km south of Iceland (figure 2.2). This inconsistency has not been explained. Secondly, the effects of rapid decompression melting following recent deglaciation at Iceland has produced extremely depleted incompatible trace element signatures in postglacial lava flows (e.g. Stóravíti, section 5.4; Maclennan et al., 2002). This process would account for the depleted La/Sm values at Iceland as models of decompression by deglaciation can cause melting rates to increase by up to a factor of 30 with the greatest influence in the shallowest parts of the melting region (Jull and McKenzie, 1996). Thirdly, tectonic variations such as rift relocations and off-axis volcanism can result in enriched compositions such as those found in samples from the Eastern Volcanic Zone (South Iceland Volcanic Zone: SIVZ) and the Snaefellsnes Volcanic Zone (SNVZ). The enriched compositions in general reflect smaller degrees of melting and a stronger influence of deep mantle melting than occur in the main established rift zones. Finally, the subaerial exposure of Iceland may cause a sampling bias compared to the 'remote' seafloor dredging to collect samples

from the submerged Mid-Atlantic Ridge. The excellent exposure on Iceland, including the exhumation of crust by glacial erosion, provides access to a range of samples from different units within the lava stratigraphy. Detailed sampling including anything that appears unusual may create a bias to the dredge sampling. Dredging can only retrieve samples from the surface of the ridge and flanks, and the preservation bias this method is subject to must be taken into consideration.

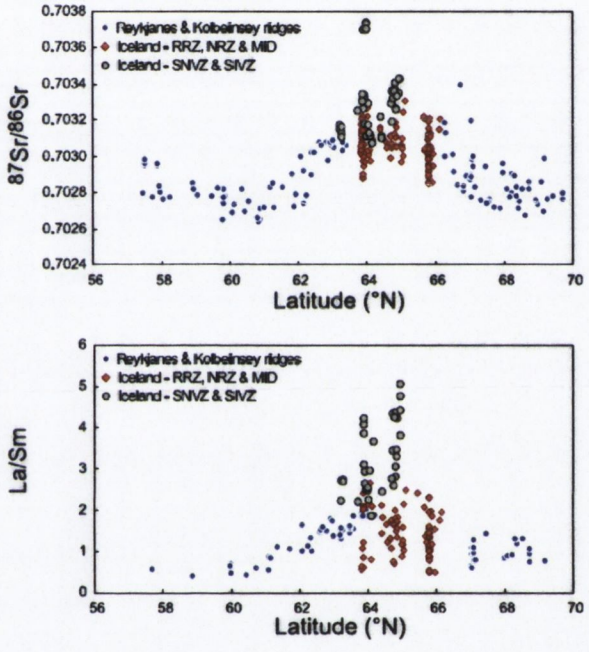

Figure 2.10: $^{87}Sr/^{86}Sr$ and La/Sm variations with latitude along the Mid-Atlantic Ridge adjacent to Iceland. The figure is taken from Sigmarsson et al. (2008). The data used are from 20 different studies, summarised in Sigmarsson et al. (2008).

Six major processes control the geochemistry of rift products at Iceland from source to eruption: partial melting, melt transport, fractional crystallisation, crustal contamination, magma mixing and hydrothermal alteration. These processes along with source variation are discussed below with a view to revealing characteristics of the melting regime. The aim of this project is to understand how geochemical variations can be linked to differences in the melting regime and ultimately tectonic variations. Therefore other factors which affect the geochemistry of rift products apart from melting must be understood and accounted for in the analysis.

2.2.2 Mantle Source

The precise composition of the mantle and in particular, the scale of compositional heterogeneity in the mantle is the subject of great debate. The generally enriched incompatible element signature produced at Iceland is clearly the result of access to a more enriched mantle source than normal MORB, since degrees of melting are much higher at Iceland than for normal MORB, which would normally result in a more depleted geochemistry. There is a consensus that the mantle beneath Iceland is heterogeneous on short length scales as well as over larger distances (Zindler et al., 1979; Hémond et al., 1993; Stracke et al., 2003; Thirwall et al., 2004). Sr-isotope and εNd values in samples from the Northern Volcanic Zone show that there is no systematic variation in isotopic composition with distance from the plume centre as would be expected from simple binary mixing of two end member mantle components. Maclennan et al. (2001b) proposed that the lack of variation is due to little change in the average mantle composition over the scale of a volcanic zone (10's of km). More recent studies suggest a streaky mantle with veins of more enriched, fusible material which melt preferentially to a matrix of a more depleted mantle source (Maclennan, 2008a). Together with extensive mixing during melt transport, a streaky mantle would produce the range of Pb isotope values found in one picrite hand sample from Háleyjabunga, Reykjanes Peninsula, part of the Western Volcanic Zone (Maclennan, 2008a). Because of this wide range in isotope values on relatively small length scales it is necessary only to show that a lava series has isotopic values within the Icelandic range to allow valid comparisons between regions and a useful assessment of melting variations.

2.2.3 Crustal Assimilation

Rhyolitic volcanic centres at Iceland result from extreme fractional crystallisation and major crustal assimilation, therefore, data used throughout this study is filtered to remove any samples with <4 wt% MgO. This filtering removes any acidic samples. This filtering reduces the risk of crustal processes influencing the results of geochemical comparison aimed at identifying differences in the melting regime. A geochemical study by Hémond et al. (1993) concluded that the variation in trace element and isotopic values in basalts cannot be the result of crustal assimilation and instead, reflects the compositional variability created in the mantle either from source heterogeneity or during mantle melting beneath Iceland. Crustal assimilation produces variable oxygen isotope values depending on how much low δ^{18}O crust has contaminated the high δ^{18}O

melt. Maclennan et al. (2001b) confirmed the conclusions of Hémond et al. (1993) by showing that oxygen isotope composition is relatively constant along the Northern Volcanic Zone and therefore there must be a limited variation in the average degree of crustal assimilation throughout the Northern Volcanic Zone.

2.2.4 Magma Mixing

Magma mixing is a general term referring to several different mantle and crustal processes. The mixing of incremental melts during melt extraction and transport is discussed in detail in section 2.3.4. Mixing within the melting region does not affect the comparison of melting regimes across Iceland as it is likely that this process is similar for all volcanic zones and the large number and lateral range of samples gives a more balanced view of the chemistry erupted within a volcanic zone, system or central complex. Further mixing of mantle melts occurs within the lower crust and again this process is likely to be similar across Iceland and the wide range of sampling is used to allow for variations in this mixing process.

Mixing of melts between volcanic zones is extremely unlikely as this would require significant lateral melt transport perpendicular to the predominant tectonic weaknesses which are oriented approximately north-south. Lateral transport along a volcanic zone or system is possible and again this accounted for by a wide range of samples from different areas within a volcanic zone. The final mixing process occurs between basic and acidic melts and the effects can be observed in intermediate composition rocks (Jakobsson et al., 2008). These compositions are not included in this comparative study. Any significant mixing between different magmas can be observed in single element plots versus MgO wt% and taken into consideration.

2.2.5 Fractional Crystallisation

Fractional crystallisation creates significant changes in melt chemistry as crystallising phases may be removed from the cooling melt. For MORB compositions, the phase assemblage evolves from solely olivine to olivine, plagioclase and clinopyroxene as the temperature of the magma decreases (Grove et al., 1992). Removal of crystals from the melt can occur by gravitational settling in a magma chamber (Sparks et al., 1993) or by the extraction of melt from the magma chamber (Sparks et al., 1984; Langmuir, 1989). The behaviour of different elements during crystallisation (and melting) is

described by partition coefficients. These are values assigned to each element and define their potential to be included within different mineral phases. The concentration of a particular element in the melt as fractional crystallisation occurs, assuming a constant partition coefficient, is given by

$$\frac{C_L}{C_0} = F^{(D-1)} \tag{2.1}$$

where C_L is the concentration in the melt, C_0 is the concentration in melt prior to crystallisation, F is the fraction of melt remaining and D is the bulk partition coefficient (Shaw, 1970). As different phases crystallise out of the melt, they preferentially remove elements that are more compatible in them, therefore the bulk partition coefficient is calculated by weighting the various individual partition coefficients for each different phase according to the ratio of phases crystallising. It is necessary for an investigation into the degree and depth of melting to observe elements and element ratios which are essentially immune to fractional crystallisation processes. The behaviour of elements in important phases during melting is discussed in detail in section 2.3.5.

2.2.6 Hydrothermal Alteration

The effects of hydrothermal alteration on incompatible trace element concentrations at Iceland are restricted to Large Ion Lithophile elements such as Sr, Rb and Ba which are fluid-mobile. Sr in particular seems to be particularly susceptible to alteration at Iceland. The possibility of interaction with sea water must be taken in to consideration when analysing Sr isotope values. High field strength elements such as Ti, Nb, Zr, Y and REE are considered immobile in magmatic and hydrothermal systems (Pearce, 1982). Any unexpected mobility would be evident from significant scatter in single element plots and can therefore be taken into consideration if necessary.

2.3 Mantle Melting

2.3.1 Introduction

There are two fundamental factors which cause mantle melting to form oceanic volcanism: adiabatic decompression and increased mantle potential temperature. Extension of the lithosphere at a mid-ocean ridge results in rapid passive upwelling of the underlying asthenospheric mantle. As pressure decreases the rising mantle crosses the solidus P–T conditions, defined by the Clausius-Clapeyron relation, and melting begins. This concept is more formally described using Peclet numbers; the ratio of advection to conduction given by

$$P_e = \frac{V_z l}{\kappa} \tag{2.2}$$

where P_e is the Peclet number, V_z is the upwelling velocity, l is a length scale and κ the thermal diffusivity. If the Peclet number is much greater than 1 then advection dominates heat transport; if the Peclet number is much less than 1 then conduction dominates heat transport. Beneath a mid-ocean ridge such as Iceland, V_z is approximately 10 mm yr^{-1}, l is the thickness of the lithosphere at approximately 100 km and κ is around 10^{-6}. This results in a Peclet number of 30 indicating that advective transport of heat dominates the temperature and the melting beneath Iceland (McKenzie and Bickle, 1988). The potential temperature of the asthenospheric mantle is everywhere hotter than the mantle solidus at atmospheric pressure, so with the exception of very special tectonic situations where thermal re-equilibration is possible, mantle brought close to the surface will always melt (McKenzie and Bickle, 1988). This process is known as adiabatic decompression melting (figure 2.11a).

The mantle potential temperature is the temperature that a piece of mantle would achieve if transported from depth to the surface adiabatically, when no melting is allowed. Areas of higher mantle potential temperatures are associated with upwelling mantle plumes. During adiabatic decompression, a higher mantle potential temperature results in the solidus being crossed at greater depths and therefore, a higher degree of melting is achieved.

Normal mantle potential temperature for the Mid-Atlantic Ridge is approximately 1300°C. This potential temperature increases towards Iceland reaching a maximum of

approximately 1500°C near central Iceland where the centre of the Iceland plume is located (White et al., 1995). The average overall spreading rate at Iceland is around 18 mm yr^{-1} (DeMets et al., 1994) and would normally result in decompression melting to produce a crustal thickness of approximately 6 km (Bown and White, 1994). The average crustal thickness on Reykjanes Ridge approximately 1000 km south of Iceland is 7 km (Sinha et al., 1997). However, the elevated mantle potential temperature at Iceland results in a maximum crustal thickness of approximately 40 km in central Iceland and an average of 20 km away from the plume centre (Darbyshire et al., 1998; Staples et al., 1997), reflecting the much higher degrees of melting in general achieved at Iceland (figure 2.11b). Active upwelling associated with mantle flow from the Iceland plume will also increase melt fraction and crustal thickness by fluxing material through the deepest part of the melting region (Maclennan et al., 2001b). In summary, normal Mid-Atlantic Ridge melting produces 7 km thick crust; passive upwelling of unusually hot mantle produces an extra 13 km of crust resulting in a total crustal thickness of 20 km away from the plume centre at Iceland. In the centre of Iceland a further 20 km of crust is produced by active fluxing of mantle material through the deepest parts of the melting region, resulting in 40 km thick crust (Jones and Maclennan, 2005).

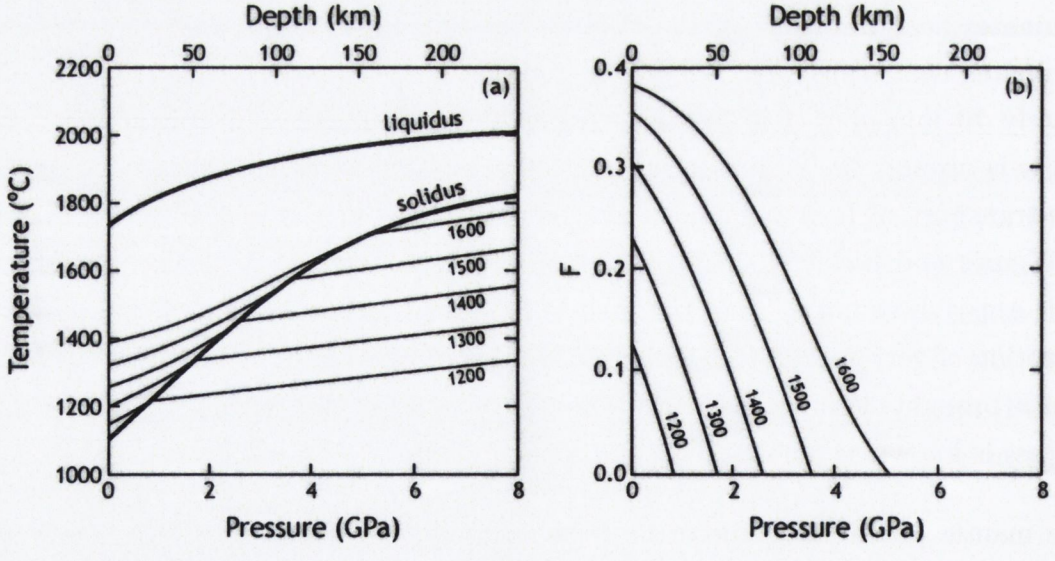

Figure 2.11: An example of adiabatic decompression paths (a) and melt fraction (b) as a function of pressure, for different mantle potential temperatures. The liquidus and solidus curves are for a typical peridotite mantle composition. Curves are calculated from McKenzie and Bickle (1988). Figure from Maclennan (2000).

2.3.2 Mantle Flow and the Melting Region

The melting region is the area over which mantle temperatures are greater than the solidus. The potential temperature and flow of mantle material control the geometry of the melting region. For mantle of a constant potential temperature, the depth at which melting begins will be constant, producing a horizontal base to the melting region. The top of the melting region is defined by the depth at which the temperature and pressure conditions in the mantle return to below the solidus. No further melting will occur when there is no upwelling of mantle material. The P-T conditions of the mantle solidus may vary depending on whether the composition of the mantle has been changed by the extraction of fractional melts. The degree of melting is dependent on temperature difference between the mantle and the solidus at any given pressure, as shown in McKenzie and Bickle (1998).

Passive upwelling of the mantle beneath a spreading ridge results from the separation of the tectonic plates. The resultant flow field is modelled by corner flow of a viscous incompressible fluid (Batchelor, 1967; McKenzie, 1967). This flow field creates a roughly triangular shaped melting region (figure 2.12; Langmuir et al., 1992). At Iceland plume-driven active upwelling can influence the melting regime, fluxing material through the lowest levels of the melting region, creating a higher than normal melting rate for deep melting, greater than 100 km (Maclennan et al., 2001b; Ito et al., 1996). Conductive cooling can also have a significant effect on the depth to the top of the melting region in slow spreading situations (Bown and White, 1994): this is particularly relevant to Iceland.

Bown and White (1994) modelled melting beneath normal mid-ocean ridge settings predicting the base of the melting region at about 50 km. This estimate is based on anhydrous melting for normal mantle potential temperature of 1300°C. Higher mantle potential temperature extends the depth of melting initiation. The presence of water in the mantle reduces the temperature of the solidus and therefore, increases the depth of the base of the melting region. Hirth and Kohlstedt (1996) predicted that melting would begin at 115 km beneath mid-ocean ridges with a mantle potential temperature of 1350°C and an ambient water content of 125±75 wt ppm, estimated from the literature. Katz et al. (2003) presented a new parameterisation of the hydrous solidus to predict depths of 90–105 km for a potential temperature of 1350°C and 135–150 km for 1450°C, for a range of 65–200 wt ppm water. The geochemical evidence for the initiation of melting beneath mid-ocean ridges within the garnet stability field is summarised in Shen and Forsyth (1995). The extreme light REE enrichment and high

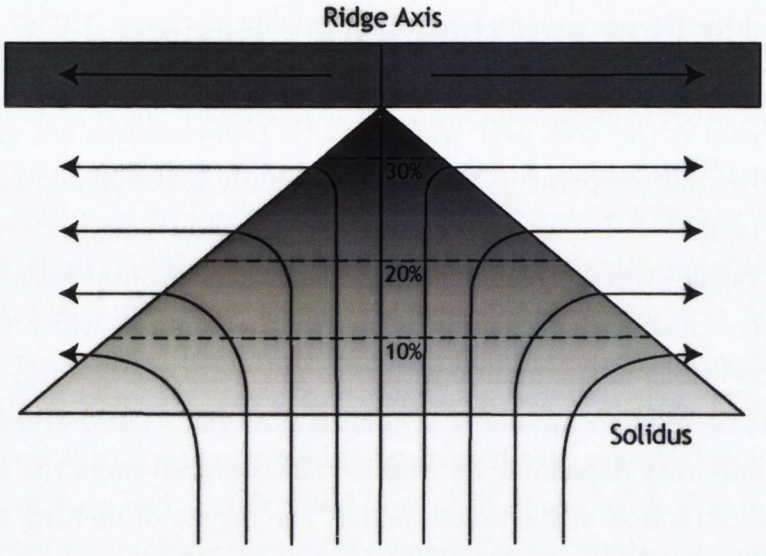

Figure 2.12: Schematic representation of the melting region resulting from passive upwelling beneath a spreading ridge over 'hot mantle'. The stream lines represent corner flow of mantle matrix through the melting region and the boundaries of the triangular melting region represent the mantle solidus. Dashed lines are contours of the increasing melt fraction with decreasing depth within the melting region. Based on Langmuir et al. (1992).

light/heavy REE ratios observed at Iceland (e.g. Maclennan et al., 2001b) are consistent with model predictions that melting must begin deep in the mantle, well within the garnet stability field at depths greater than 100 km (section 2.3.5).

2.3.3 Mode of Melting: Batch versus Fractional

The mode of melting refers to the mechanical process that occurs once melt has formed and is described by two end member processes: perfect batch and perfect fractional melting. Batch melting is the process where the melt and mantle residue remain in contact and in thermal and chemical equilibrium during upwelling. Melt is only extracted at the top of the melting region, once the maximum melt fraction is achieved. Perfect fractional melting describes the other end member of the melting process where melt is extracted as soon as it forms and transported out of the melting region. In the fractional case, melt is only in instantaneous chemical equilibrium with the mantle residue, but is assumed to be in thermal equilibrium throughout the melting region. The intermediate case where melt is only extracted once a threshold (residual) porosity has been reached is known as continuous melting (Langmuir, 1977). The review of mantle melting presented by Kelemen et al. (1997) summarised numerous geochemical, geophysical and experimental studies to show that mantle melting beneath mid-ocean

ridges is near-fractional with a residual porosity of <1%. The compositional variability within the melting region resulting from incremental melting can be observed in melt inclusions, trapped in crystals from MORB samples (e.g. Maclennan, 2008b). Several authors, using melting models to account for the compositional range in melt inclusions and U-series disequilibrium, infer a very small residual porosity for near-fractional melting between 0.05% and 1% (summarised in McKenzie, 2000). Following extraction the incremental melts are mixed together during transport and crustal residence prior to emplacement at the ridge axis. This process has been well studied at Iceland (Maclennan, 2008b).

2.3.4 Melt Transport

The extraction and transport of incremental melts has a significant control on the variability in melt compositions leaving the mantle to form new crust. Early suggestions of diffuse porous flow of melt out of the melting region (Spiegelman and Elliot, 1993; Iwamori, 1994) would result in chemical equilibrium between the residue and the melt at shallow levels (Kelemen et al., 1997). It is clear that from the compositional variability observed in the melt inclusions that chemical equilibrium is not achieved. A study by Spiegelman and Kelemen (2003) summarised the evidence from the literature for distinct melt channels in the mantle including chemical variability in melt inclusions and MORB lavas and field observations of 'replacive' dunite channels in ophiolites. They showed that the fluid dynamics even within simple channels in homogenous systems can produce extreme chemical variability on very small length scales during melt transport.

The range of compositional variability observed for whole rock data is less than that for melt inclusions for MgO compositions above 7 wt.% (Maclennan, 2008a). Once melt has reached the crust, mixing as melt is collected in magma chambers tends to homogenise the small scale heterogeneity produced by incremental melting of a heterogeneous mantle source and melt transport. Primitive melts with high MgO will still have variable compositions of melt inclusions. However, as melts become more evolved this compositional variability is mixed out. Large sample numbers are used to compare different regions in Iceland to reduce the impact of small heterogeneities that may remain from the melting process. By looking at the distribution of compositions erupted from a rift zone, it is hoped that the average composition of the mantle melts can be observed. It must be considered that, following the extraction of melt from the

melting region, it cannot be assumed that all melt fractions will be focused toward the rift axis. This process of melt focusing may not collect the most distal melts from the rift axis (Spiegelman 1996), reducing the contribution of highly enriched incompatible element concentrations from garnet field melting. Therefore, the average composition from the distribution of lava compositions may not reflect the complete melting region, but this must be reasonably consistent on a global scale as global correlations of chemistry and oceanic crustal thickness would not be possible (e.g. Klein and Langmuir, 1987).

Melt extraction, transport and focusing processes, although complex, are likely to be similar for all rifts past and present at Iceland and therefore it is possible to link observations of changes in the geochemical signature between rifts with relative changes in the melting regime. As yet, only one study has been carried out on melt inclusions in the older Tertiary lavas in Iceland, which simply presents the Sr isotope data without interpretation with respect to the melting process at Iceland (Harlou et al., 2009). Further studies of Tertiary melt inclusions could reveal whether the process of incremental melting, mixing and emplacement is relatively similar for the extinct rift axes compared to the neovolcanic zones.

2.3.5 Geochemical Behaviour During Melting

This section will deal predominantly with the behaviour of trace elements during melting. Major element behaviour is simply controlled by the composition of each phase in the melting reaction, which is dependent on the P-T conditions and the composition of the residual mantle. The modelling of major element compositions is discussed in section 6.2.1. Major element compositions of lava flows are strongly influenced by fractional crystallisation trends and it is not as easy to isolate major element variations caused by melting as it is for trace elements.

The equilibrium distribution of any trace element between the mantle melt and matrix is described by a unique bulk partition coefficient. The bulk partition coefficient is calculated from individual partition coefficients, describing the behaviour of each element in each phase present in the solid during melting. Partition coefficients are defined by the ratio of the concentration of an element in the liquid (C_L) compared to the solid (C_S): $D = C_S/C_L$. This value can be estimated using melting experiments of synthetic materials or analysis of natural minerals and glassy matrices in rapidly cooled lavas (Blundy and Wood, 2003). Elements which are compatible in a phase will have $D > 1$

and elements which are incompatible, preferring the liquid to the solid, will have $D < 1$. The bulk partition coefficient, $\overline{D}$, describes the overall compatibility of an element in the mantle solid. For any element it is calculated as the sum of different phase partition coefficients weighted according to their fraction in the solid: $\overline{D} = \Sigma_{n=1}^{N} F_n D_n$, where n represents each phase. With knowledge of the source composition, bulk partition coefficient and the melt fraction at any depth, the concentration of an element in the instantaneous melt can be calculated. These instantaneous melts are accumulated by different methods (sections 2.3.3 and 2.3.4) and therefore, there are numerous ways of calculating the final melt compositions. The new time-dependent model employs perfect fractional melting to calculate trace element compositions in the melt described in section 6.9.

The garnet-spinel transition is a major phase change that occurs in the mantle. It has already been noted that mid-ocean ridge melting, especially at Iceland, begins deep in the mantle within the garnet stability field. This transition causes the most significant variation in the composition of instantaneous melts in the melting region, with major changes in the partition coefficients of certain elements. The Heavy REEs (Lu, Yb, Tm, Er, Ho, Dy) and Y are compatible in garnet and incompatible in spinel (McKenzie and O'Nions, 1991; Johnson, 1994). The depth of the garnet-spinel transition will limit the melt fraction within the garnet stability field and define the level of influence of deep mantle melting on the overall melt composition. The transition depth depends on the mantle potential temperature, increasing for higher temperatures. Robinson and Wood (1998) showed that for higher than normal mantle potential temperatures such as those found beneath Iceland, the transition takes place at approximately 100 km depth.

By looking at element pairs which are only fractionated during melting in the garnet stability field and behave similarly in the spinel and plagioclase fields, it is possible to compare the influence of deep mantle melting for different rift zones and volcanic features at Iceland. If the elements have similar partition coefficients in the plagioclase stability field, the ratio of their concentrations will remain relatively unaffected by fractional crystallisation processes. Useful ratios which essentially behave as described and are used extensively in the geochemical comparison chapters (chapters 4 and 5) to identify changes in the melting regime include: Nb/Y, Zr/Y and Sm/Yb. Slight differences in the shallow depth partition coefficients can cause fractionation of these element pairs during fractional crystallisation. However, this would be evident in variation diagrams using MgO compositions as a proxy for the evolution of magmas and is discussed when necessary. The partition coefficients for the trace elements in these

ratios are discussed in section 4.3.

2.3.6 Temporal Variations: Rift Jumps and Glaciation

At Iceland there are two time-dependent processes which can have significant effects on mantle melting: rift relocations and glaciation. Although the driving force behind rift jumps is likely to be internal in the form of a variable mantle flow (Jones et al., 2002), glaciation is the result of external conditions which must be taken into consideration when comparing lava series which were erupted under different climate regimes.

The effect of a variable spreading rate on the melting regime and the composition of melts could be quite significant. Bown and White (1994) showed using a simple model of upwelling beneath a mid-ocean ridge that 20 mm yr^{-1} full spreading rate is a significant threshold in terms of the shape of the melting region. Lower spreading rates result in conductive cooling becoming a more significant control on the melting regime, lowering the top of the melting region and consequently lowering the final degree of melting. The depth to the top of the melting region is around 10 km for full spreading rates higher than 20 mm yr^{-1} and increases to 30 km depth for lower spreading rates. This is an important observation in relation to Iceland. As described in section 2.1.3, during a rift relocation the extension is partitioned across two parallel rift axes reducing the full spreading rate on the individual axes below the normal Iceland full spreading rate 20 mm yr^{-1}. Therefore during a rift relocation the extent of melting could be significantly affected by conductive cooling. The aim of this project is to estimate the effects of a variable spreading rate on mantle melting and composition of lavas, using a new time-dependent model described in chapter 6.

Hardarson et al. (1997) carried out a detailed geochemical and geochronological study of a palaeorift in northwest Iceland which was active until approximately 15 Ma before the rift relocated to the now extinct Snaefellsnes-Skagi rift. The Tertiary crust is subject to a crustal accretion bias where only lava flows able to flow outside of the main rift zone are preserved (Pálmason and Saemundsson, 1974; Hardarson and Fitton, 1997). It must be remembered that not all features and compositions associated with the extinct rift zone will be represented by sampling the exposed Tertiary crust. Section 5.2 provides detailed background to the formation of the Tertiary crust. Hardarson et al. (1997) concluded that the variable isotopic and trace element signature observed in the dying rift lavas could be related to changes in access to different mantle source components as the rift migrated further from the plume. They also suggested that

the changes in melt productivity associated with rift relocations could cause the V-shaped ridge topography observed on the Reykjanes and Kolbeinsey Ridges. However, Jones et al. (2002) showed that this could not be the case and it is more reasonable to suggest that V-shaped ridges and rift jumps are the result of time-dependent flow in the mantle.

Laterite palaeosol horizons observed between lava flows throughout the exposed Tertiary crust in Iceland (approximately 17–3.3 Ma) provides evidence that Iceland hosted a warm tropical climate during this time. Unconformities observed in northern Iceland (chapter 3) signify the onset of major northern hemisphere glaciation at 3.3 Ma. Sub-glacial eruptions form hyaloclastites, building up over 1000 m in thickness before being capped by a sub-aerial flow to form the classic table mountain structure characteristic of Iceland's glacial volcanic activity (figure 2.13). As the climate warms, rapid deglaciation unloads the crust to the extent that it causes a significant increase in the rate of adiabatic decompression melting, by up to a factor of 30 (Jull and McKenzie, 1996). Early post-glacial eruptions produced unprecedented volumes of lava, forming very large lava shields. For example, Stóravíti in Theistareykir system, Northern Volcanic Zone is approximately 30 km^3 (for geochemistry see section 5.4). An example of a postglacial lava shield is shown in figure 2.14. Early post-glacial (12–7 kyr) volcanism across Iceland has a unique geochemical signature with significant depletion in the incompatible elements compared to sub-glacial eruptions (e.g. Maclennan et al., 2002). High MgO wt% compositions are also characteristic of post-glacial lava flows, with the most mafic picrites from Theistareykir containing over 20 wt% MgO, most likely forming as a result of olivine accummulation (Maclennan et al., 2002). This marked difference in chemistry resulting from deglaciation must be taken into consideration when comparing extinct volcanic zones with the neovolcanic zones.



Figure 2.13: Herdubreid, situated north of Askja central volcano within the Northern Volcanic Zone, central Iceland. A classic example of a table mountain composed predominantly of hyaloclastite flows erupted sub-glacially, capped by a sub-aerial lava flow. The steep sides reveal the much greater susceptibility of hyaloclastite to weathering compared to the capping lava flow.

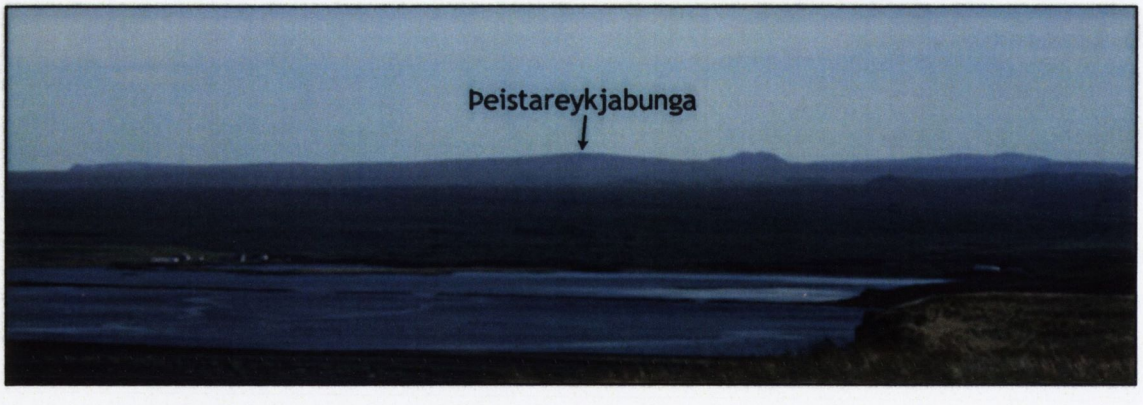

Figure 2.14: Theistareykjabunga, situated in the Theistareykir volcanic system within the Northern Volcanic Zone, north-east Iceland. A classic example of a postglacial lava shield, formed when huge volumes of lava were erupted following rapid deglaciation.

Chapter 3

The Skagafjördur Region, Northern Iceland

3.1 Introduction

The Skagafjördur region of northern Iceland is the location of an extinct rift axis which died after extension transferred to the presently active Northern Volcanic Zone (figure 3.1). Extensive dating of samples from across northern Iceland predicts that the Skagi rift died around 3 Ma (Garcia et al., 2003). However, a substantial suite of Quaternary lavas (i.e. younger than 3.3 Ma) exists on the Skagi peninsula, with other smaller Quaternary lava outcrops present across the Skagafjördur region. There have been several previous studies of these young lavas including Sigurdsson et al. (1978) and Everts (1975). There are two possible origins for these Quaternary lava flows: the final flows from a dying rift axis or a suite of flows produced by a transient rifting episode.

A detailed field study carried out by Everts (1975) focused on the Skagi peninsula. Everts (1975) established a stratigraphy for the Quaternary lava suite and associated glacial sediments (figure 3.2) and mapped the northern half of the Skagi peninsula in detail, identifying individual Quaternary lava flows (appendix A). A petrological and geochemical study of western Iceland was presented by Sigurdsson et al. (1978) and Schilling et al. (1978) and included several samples from the Skagafjördur region. Schilling et al. (1978) describe the Skagafjördur Quaternary lavas as a suite of uniform tholeiitic basalts with unusual geochemical characteristics different to the Western Volcanic Zone. Everts' study (1975) identified a significant unconformity between

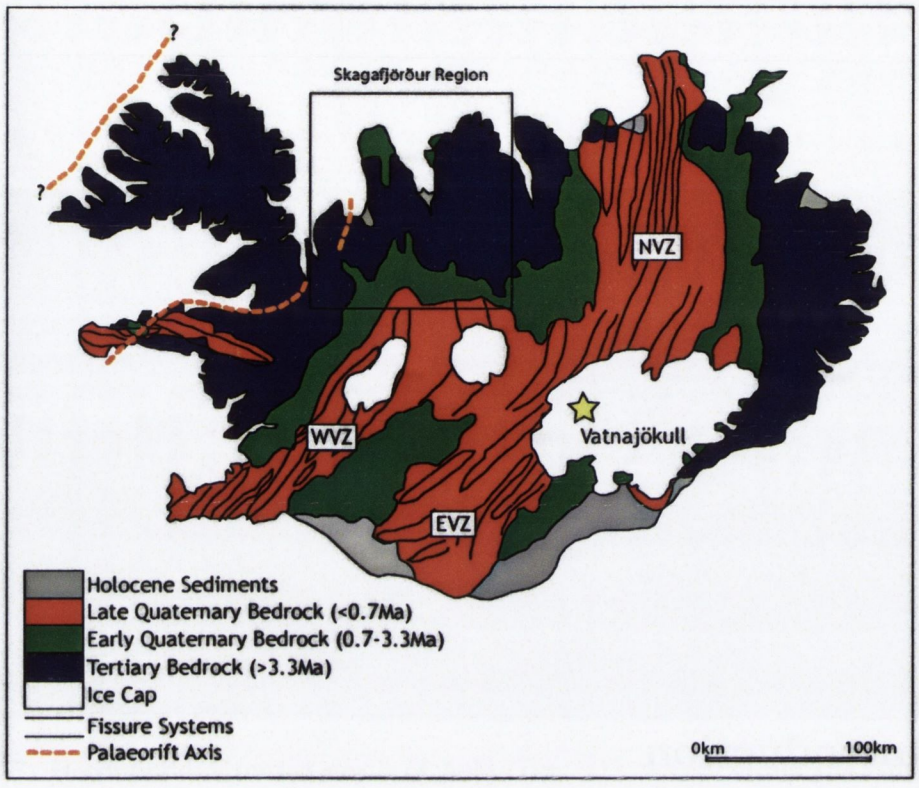

Figure 3.1: A simplified geological map of Iceland. The broad area of the Skagafjördur region (figure 3.3) is outlined on the north coast of Iceland. The approximate location of an extinct rift axis is shown in the western part of the Skagafjördur region. Presently active volcanic zone are shown in red: Northern Volcanic Zone, NVZ; Western Volcanic Zone, WVZ; Eastern Volcanic Zone, EVZ. Adapted from Jóhanesson and Saemundsson, 1998; Palaeorift locations from Hardarson et al. (1997) and Jóhanesson (1980).

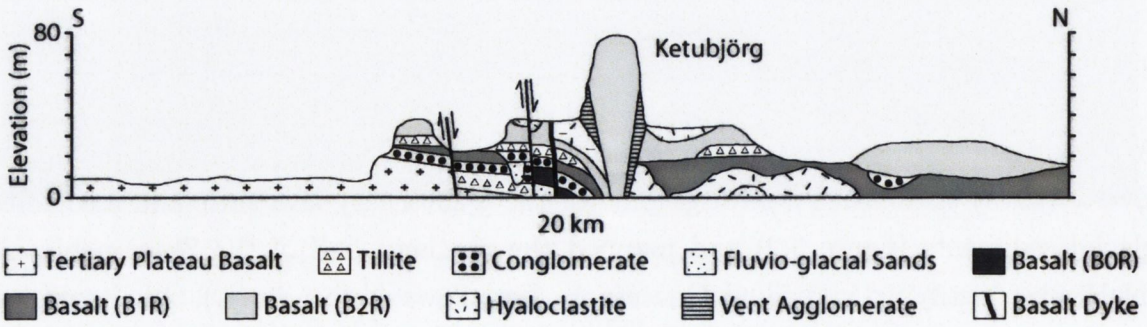

Figure 3.2: Sketch cross section showing the main geological units identified on the Skagi peninsula including individual Quaternary lava flows. The complete sequence of Quaternary flows from oldest to youngest is B0R, B1R, B2R, B3R and B4N, where R and N stand for reverse and normal polarity from magnetic studies (Everts, 1975). B3R and B4N are not shown on this section.

the Tertiary lava flows and a significant section of fluvio-glacial sediments which are overlain by the Quaternary lava suite. One of the aims of the project is to identify any significant changes in geochemistry across the Tertiary-Quaternary unconformity and establish whether the unconformity represents a hiatus in volcanic eruption or is simply a result of the onset of glaciation. The presence of a substantial volcanic hiatus and a significant change in geochemistry would have important implications for identifying the origin of the young lavas emplaced at Skagi.

In order to identify the likely origin of the Quaternary lava flows from the Skagafjördur region, an understanding of the melting regime required to produce these lavas is necessary. The melting regime can be established using geochemical comparisons and modelling. At present there is relatively little geochemical data available for this extinct rift and associated young lavas compared to the main volcanic zones, therefore new samples were required.

Over 50 new samples were collected from the Skagafjördur region to provide the basis for a detailed geochemical study focused on the main Quaternary outcrop on the Skagi peninsula (figure 3.3). The sampling locations, sampling strategy and main field observations are described in sections 3.3 and 3.4. Major and trace element analyses were obtained for the all new samples, in addition to 9 donated samples from previous studies of the region (Hjartarson, 2003; Garcia et al., 2003). REE concentrations were obtained for a subset of the new samples, together with $^{87/86}Sr$ and $^{143/144}Nd$ isotopic values for 12 new samples. This is the first detailed geochemical dataset for the suite of Quaternary lavas from the Skagi peninsula and the first radio-isotope data for the Skagafjördur region. The new data and initial interpretations are presented in section 3.5.

The aim of this chapter is to introduce the geology of the Skagafjördur region and to compare the geochemistry of lavas and dykes of Tertiary and Quaternary age. The outcrop of Quaternary age lava flows is discontinuous within the Skagafjördur region and a comparison of samples from different areas is used to establish whether all these outcrops can be considered to be part of the same episode of volcanic activity. Using field observations and the K-Ar dating results from Everts et al. (1972) it is easy to show that the Skagi rift was active for significantly longer than predicted by Garcia et al. (2003). It is important to establish whether all samples can be considered to be part of the same melting event so that a suitable comparison can be made between the extinct Skagafjördur rift and the neovolcanic zones across Iceland (chapter 4). The new analyses suggest that samples from Austurdalur, Vesturdalur and Tröllaskagi

Quaternary outcrops (figure 3.3 are part of the same rifting episode as the main Quaternary outcrop on the Skagi peninsula because they display very similar geochemical signatures.

One aim of this project is to estimate the degree and depth of melting required to produce the series of Quaternary lava flows and to compare this to other volcanic zones. This chapter uses the new geochemical data to compare the composition of mantle melts for Quaternary and Tertiary lava flows from Skagafjördur and establish whether any major difference in the melting regime exists between these two suites.

Tertiary and Quaternary lava flow comparisons show only a small difference in geochemistry which can reasonably be attributed to a difference in crustal fractionation processes rather than melting. $^{87}Sr/^{86}Sr$ and $^{143}Nd/^{144}Nd$ values are largely consistent with a constant mantle source composition for all the Skagafjördur samples. The lack of significant difference between the Tertiary and Quaternary lava flows may have important implications for the tectonic origin of the young Skagafjördur lavas and crustal accretion processes in general at Iceland (discussed in chapters 5 and 8). It is generally accepted that the Quaternary lavas from Skagafjördur represent a transient rifting episode initiating around 2.5 Ma and lasting for 2 Myrs (Gudmundsson, 2007). However, there is little evidence from the geochemistry to suggest that the major unconformity between the Tertiary and Quaternary is indicative of a break in volcanic eruption, therefore, the Quaternary lava suite may simply be a continuation of the old Tertiary rift.

3.2 Geological Background

This section includes a description of the tectonic history of the area and the main geological features which are covered in further detail in section 3.3. Tertiary age rocks (older than 3.3 Ma) form the largest outcrop adjacent to Skagafjördur (figure 3.3). The Tertiary outcrop is composed of a relatively uniform basalt lava pile, with numerous cross-cutting dyke intrusions, formed by a major rift zone active between 15 and 3 Ma (Hardarson et al., 1997; Garcia et al., 2003). The approximate location of the extinct axis is shown adjacent to the Skagi peninsula on figure 3.1. The location of this extinct rift axis can be inferred from a regional syncline, identified by inwardly dipping lava flows (Saemundsson, 1974). The formation of the syncline in response to the emplacement of lavas at a rift axis is described in section 2.1.3.

Acidic lava suites and intrusions are generally associated with central volcanic complexes, of which several have been identified within the Tertiary in the Skagafjördur region (figure 3.1). Quaternary lavas outcrop across the southern part of the region in association with the currently active Western Volcanic Zone. There are several outcrops of Quaternary lavas which are aged between 0.5–2.5 Ma (Everts et al., 1972) and are thought to have originated from a transient rift axis after the main Tertiary rift became extinct (Sigurdsson et al., 1978). The onset of a major glaciation in northern Iceland occurred approximately 3.3 Ma, prior to the proposed formation of this transient rift. This glaciation is represented by a large unconformity between the Tertiary and Quaternary lava suites identified by the presence of hyaloclastite and fluvio-glacial sediments.

The largest outcrop of Quaternary lavas from the Skagafjördur rift is located on the northern tip of the Skagi peninsula (figure 3.3). The sub-glacial unconformity that exists between the Tertiary and Quaternary lavas is well exposed at several localities on the Skagi peninsula including Selnes Bay on the east coast (figure 3.4), described in detail in section 3.3. The stratigraphy of this area of the Skagafjördur region has been described by Everts (1975). A sketch cross section showing some of the main geological units is given in figure 3.2. This stratigraphy was used as a basis for completing detailed sampling of the Quaternary lava flows.

3.3 Field Observations

This section describes the field relationships between the main geological units observed on the Skagi peninsula. As previously described the stratigraphy consists of a series of Tertiary basalt lava flows unconformably overlain by fluvio-glacial sediments, followed by a series of Quaternary basalt lava flows. These units are cross-cut by intrusions of various ages.

The main study of the stratigraphy on the Skagi peninsula is presented by Everts (1975) and a sketch cross-section is shown in figure 3.2. The majority of good exposure on Skagi is coastal with some small poorly exposed inland locations. Everts (1975) used coastal exposures combined with inland topographic features such as small scarps to identify the extent of individual Quaternary lava flows. Everts (1975) inferred that B1R lava flow extends across the whole of the northern part of the Skagi peninsula. However, with the poor inland exposure and the observation that existing volcanic rifts

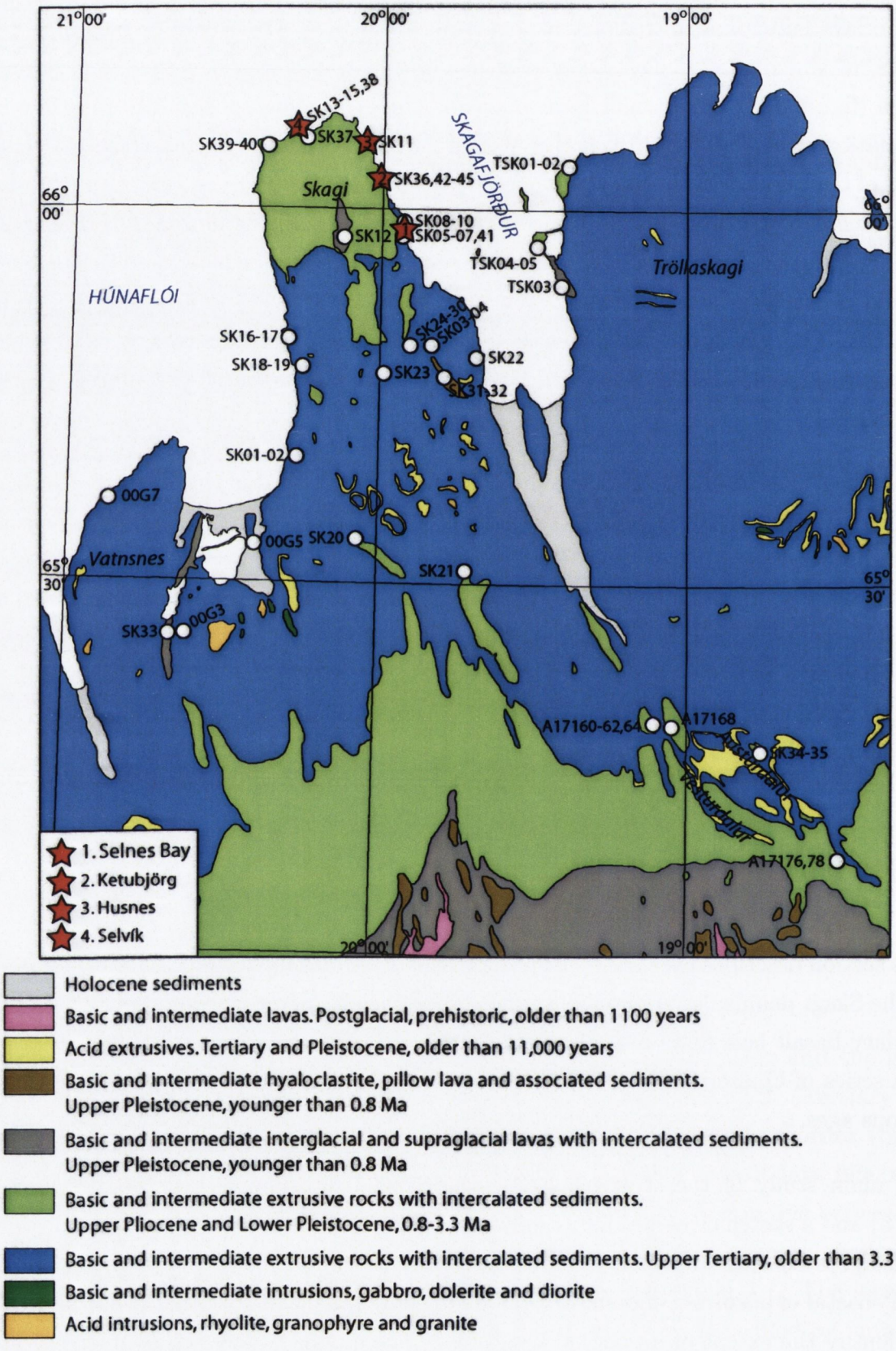

Figure 3.3: Geological map of the Skagafjördur region. Sample localities are shown as white circles. The red stars represent key localities discussed later in the chapter. Acidic lava suites and intrusions are associated with Tertiary age central volcanic complexes. (Adapted from Jóhanesson and Saemundsson, 1998).

on Iceland produce complex lava topography, it is difficult to support Everts' (1975) relatively simple interpretation of the stratigraphy. Compare figure 3.4 and figure 3.7, which both show B1R lava flow according to Everts' (1975) interpretation. These lava flows clearly have very different morphologies.

The following observations are used to show the important field relationships between the three main geological units and provide a geological framework for the interpretation of the geochemical data. The presence of a significant unconformity between the Tertiary and Quaternary lava flows on Skagi may have implications for the tectonic origin of the Quaternary lavas. The majority of geochemical comparisons made in chapters 4 and 5 use the Skagi Quaternary lava flows. It is possible that these lava flows could have flowed from another nearby volcanic zone such as the Western Volcanic Zone and therefore, a further aim of these field observations is to show that Skagi Quaternary lavas are most likely to have erupted from local volcanic vents.

The unconformable relationship between the Tertiary and Quaternary lavas is well exposed at Selnes Bay on the east coast of Skagi (figures 3.3 and 3.4). In the cliffs on the southern side of the bay a series of Tertiary lavas can be identified by characteristic subaerial weathering resulting in red rubbly tops (figure 3.5). This weathering feature is characteristic of Tertiary lavas in Iceland.

On the northern side of Selnes Bay a significant sequence of fluvio-glacial sediments can be observed (figure 3.6). These sediments are identified as fluvio-glacial in origin due to obvious layering and channel-like structures. These structures combined with a variety of clast types and a lack of volcanic glass are good evidence that these sediments have been reworked and do not represent original proximal hyaloclastite deposits. The sediments were deposited unconformably on to the Tertiary lavas and must be younger than 3.3 Ma, the age of the onset of the most recent glaciation in northern Iceland. There is no exposure at Selnes of the unconformable contact between the Tertiary and the sediments, but it must be situated between the two outcrops, and has probably been picked out as a line of weakness where the stream enters the bay in the western corner. The unconformity may simply represent the onset of glaciation, or it may also represent a hiatus in rift activity and lava flows. The distinction between these two has important consequences for the tectonic interpretation of the Quaternary lavas on Skagi (section 3.6).

The fluvio-glacial sediments are overlain by a series of Quaternary basalt lava flows. The detailed stratigraphy of these lavas has been described, and their lateral extent

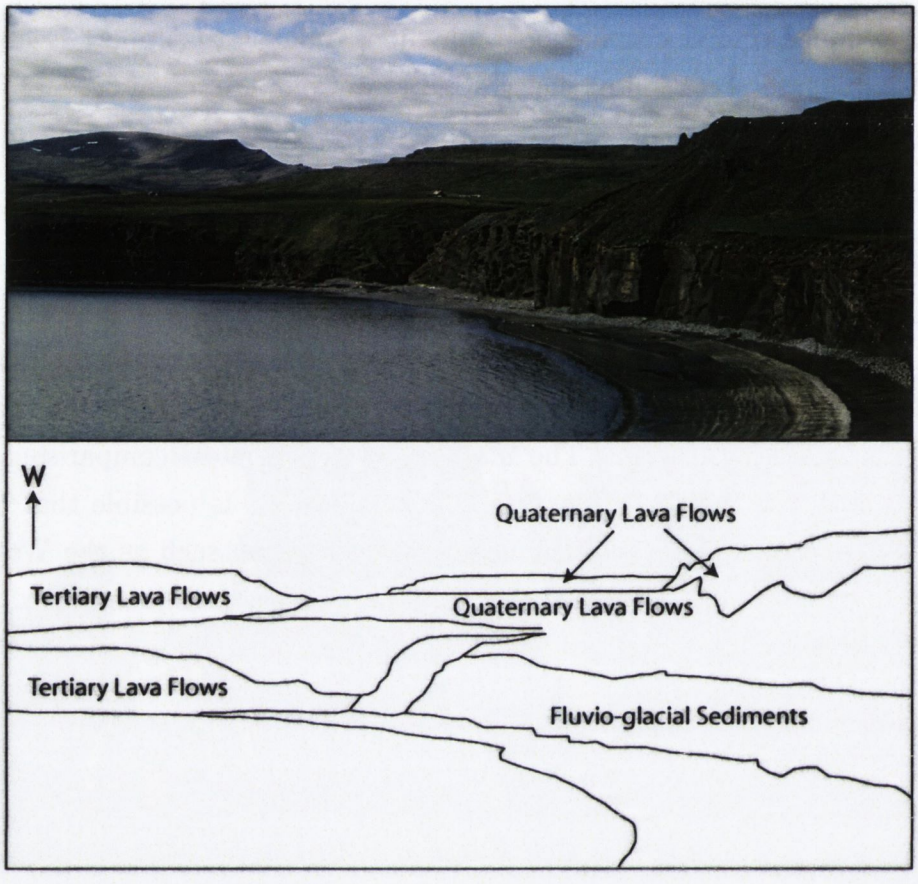

Figure 3.4: Selnes Bay on the east coast of the Skagi peninsula in northern Iceland. A sequence of Tertiary lavas are overlain by fluvio-glacial sediments. Quaternary lavas lie stratigraphically above the fluvio-glacial sediments. The unconformable boundary between Tertiary lava flows and fluvio-glacial sediments lies near the large gully at the centre of the bay, but due to poor exposure the orientation and exact position of this boundary are ambiguous. The oldest Quaternary lava flow identified directly above the fluvio-glacial sediments is B1R according to Everts' (1975) stratigraphy.

mapped, by Everts (1975) (figure 3.2). The young lava suite lies stratigraphically above the glacial sediments, which must themselves be younger than 3.3 Ma, therefore the lavas must be Quaternary in age. The morphology of the Quaternary lava flows varies dramatically from heavily fractured (figure 3.4) and blocky to well developed columnar jointing creating huge 2 m diameter hexagonal columns (figure 3.7).

Everts (1975) identified several volcanic vents on Skagi and Tröllaskagi. One example of a volcanic vent for the B2R lava flow is shown in figure 3.8. A volcanic breccia can be observed lining the edges of the vent, with broken and unoriented columns in the centre unlike the simple morphology of the adjacent lava pile.

Two Quaternary dykes were identified on the Skagi coast. Both were observed to cross-



Figure 3.5: Subaerial weathering of the top of a Tertiary lava flow on the southern side of Selnes Bay. The approximate boundary between the two lava flows is shown as a dashed line. The red rubbly top is characteristic of Tertiary lavas flows across Iceland.

cut fluvio-glacial sediments and therefore must be significantly younger than 3.3 Ma (figure 3.9). Dykes are usually emplaced vertically within a rift system although there are circumstances in relation to central volcanic systems of horizontal emplacement. Dykes are useful because they cannot have flowed from somewhere else. However, dykes can be emplaced laterally and constraining the age of dykes is vague without absolute dating methods. The advantage of sampling lava flows is that they can usually be placed within a stratigraphic framework.

It could be argued that these young Skagi lavas could simply have flowed from the nearby Western Volcanic Zone to the south. The presence of dykes and volcanic vents is good evidence that the Quaternary lavas observed on Skagi resulted from local volcanic activity. It is possible that lateral magma transport from the Western Volcanic Zone could have fuelled the Quaternary volcanic activity on Skagi, however the geochemical observations suggest a local magma source (section 4.3.1).



Figure 3.6: Quaternary fluvio-glacial sediments observed on the northern side of Selnes Bay. Layering and channel-like structures indicate that these sediments have undergone significant reworking in a fluvial environment.



Figure 3.7: Quaternary lava flow at Husnes on the east coast of Skagi. Well developed columnar jointing forming huge columns over 2 m in diameter. This is B1R lava flow according to Everts' (1975) stratigraphy.

3.4 Sample Descriptions

The main sampling area was the Skagi peninsula in northern Iceland (figure 3.3). In total, 81 samples were analysed for geochemical data. 39 new samples were collected from the Skagi peninsula, 5 from the west coast of the Tröllaskagi peninsula, 1 from a very young flow on the Vatnsnes peninsula and 2 from Austurdalur valley south-east of Skagi. The rest of the samples were donated by two previous studies: 7 samples

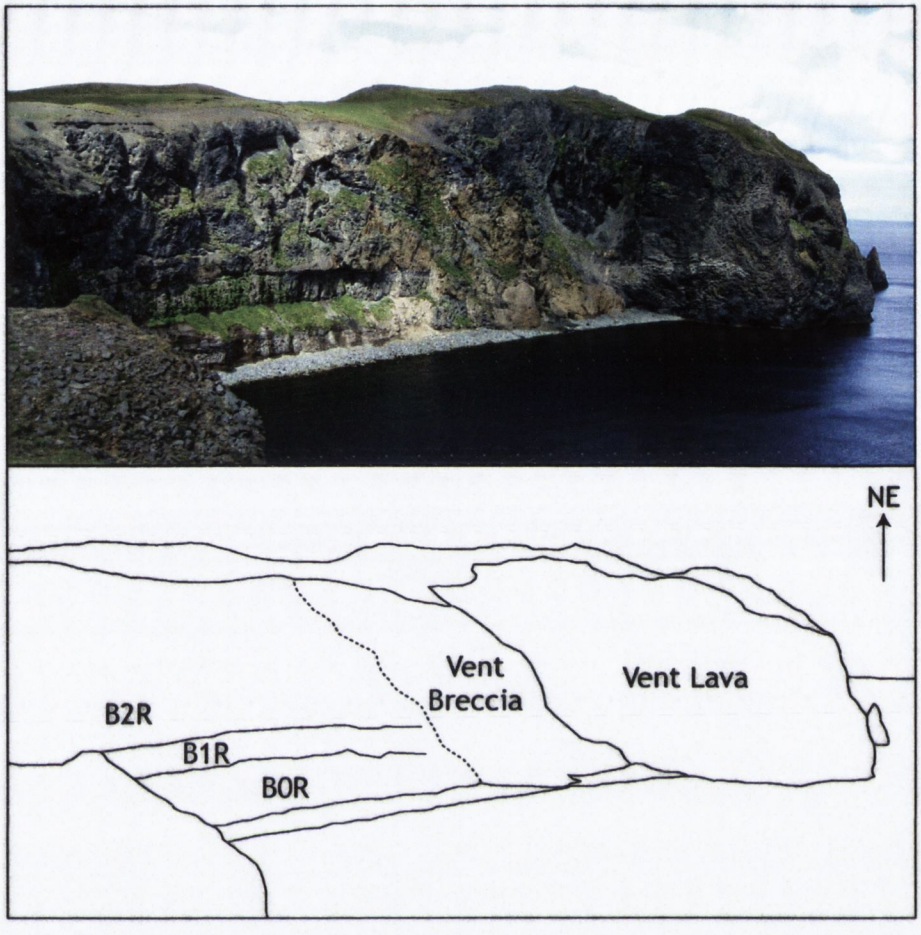

Figure 3.8: A volcanic vent in the Quaternary lava suite, Ketubjörg, east coast Skagi. A volcanic breccia can be observed lining the edges of the vent, with broken and randomly oriented column in the centre of the vent. Adjacent to the vent regular lava flows are observed and labelled according to Everts (1975) stratigraphy.

from Austurdalur and Vesturdalur donated by A. Hjartarson (Hjartarson, 2003) and 24 samples from dykes across northern Iceland donated by S. Garcia (Garcia et al., 2003). Only 3 of the Garcia dykes are located in the Skagafjördur region and only 14 of the dykes have $^{40}Ar/^{39}Ar$ ages. The geochemistry of the rest of the Garcia dykes are discussed in section 5.4. The sample locations are shown on figure 3.3.

The first sampling season aimed to sample any dykes, particularly those cutting the glacial sediments. However, the lack of stratigraphic or absolute dating age constraints on many of the dykes sampled limits the usefulness of the geochemical interpretation. The second field season was primarily aimed at completing detailed sampling of the Quaternary lava stratigraphy using Everts (1975) map and cross section as a basis. Lava flows from recent volcanic zones have flowed up to 100 km away from the eruption site e.g. Laki, Laxarhraun and Thjorsahraun. However, it has already been shown in



Figure 3.9: Looking south at Selvík (figure 3.3) on the north coast of the Skagi peninsula. A Quaternary basalt dyke is observed to cross-cut glacial sediments.

section 3.3 that the young lava flows are likely to have local origin (figure 3.8; Everts, 1975).

The Quaternary basalts are generally characterised by plagioclase phenocrysts in a fine grained groundmass. The thicker, more extensive lava flows such as B1R contain relatively coarse phenocrysts up to a few mm in diameter. It is assumed that these phenocrysts were in chemical equilibrium with the melt. There should be no effect on the validity of the geochemical interpretation for investigating the melting regimes as the chosen trace element ratios minimise the effects of fractional crystallisation. Magnetite is an abundant accessory phase in the ground mass of this suite of rocks, reflecting the high iron content.

3.5 Geochemical Observations

The aim of this section is to establish the broad geochemical characteristics of the Skagafjördur region, identifying any systematic differences between different areas and

between Tertiary and Quaternary age units. The geochemical data are used to show that the Tertiary and Quaternary lava result from similar melting processes. All the data were obtained for whole rock powders. Major and trace element concentrations were obtained for all 81 samples using XRF (X-Ray Fluorescence) at the University of Edinburgh. Rare Earth Element concentrations were analysed for 47 of these samples using ICP-MS at the Scottish Universities Environmental Research Centre (SUERC) and the University of Cambridge. The REE samples were broadly restricted to those with reasonable age constraints, although some Tertiary dykes were analysed for comparative purposes. 12 samples were analysed for Sr and Nd isotopic ratios at the University of Cambridge. This subset of samples were chosen for their location, age constraints and to cover the range of geochemical variation across the suite of Quaternary lavas. The analytical methods used to obtain the geochemical data are described in appendix B. The new geochemical data are presented in appendix C.

The lavas and dykes sampled from the Skagafjördur region are tholeiitic, mostly basalts with some slightly more evolved basaltic andesite samples and one slightly more primitive picro-basalt (figure 3.10). Two of the Skagafjördur samples will be excluded from the geochemical plots: SK20 is a rhyolitic dyke and is likely to have experienced significant crustal contamination and remelting; A17164 contained secondary mineral infills affecting the whole rock chemistry.

Figure 3.11 shows that the few Tertiary lava samples are taken from slightly more evolved flows than the Quaternary lavas. The stratigraphy is not as well constrained for the Tertiary lava samples, therefore it must be taken into consideration that these lava flows may be from central volcanoes and may have undergone different fractionation processes. This is a problem when investigating the melting regime for samples from different ages and areas. To overcome this problem we use trace element ratios whose behaviour is similar during crustal processes such as fractional crystallisation and the two elements are fractionated during melting.

For the other major elements, figures 3.12 and 3.13 compare different areas and Tertiary versus Quaternary respectively. The Quaternary lava flows from the whole of the Skagafjördur region form a well defined geochemical trend when comparing different major elements to MgO wt%. Straight line increasing trends for decreasing MgO for Fe and Ti indicate a lack of crystallisation of magnetite out of the magma prior to eruption. Simple fractional crystallisation trends are shown in MgO vs. CaO and Al_2O_3 representing the evolution of the magma as increasing amounts of clinopyroxene and possibly plagioclase are removed.

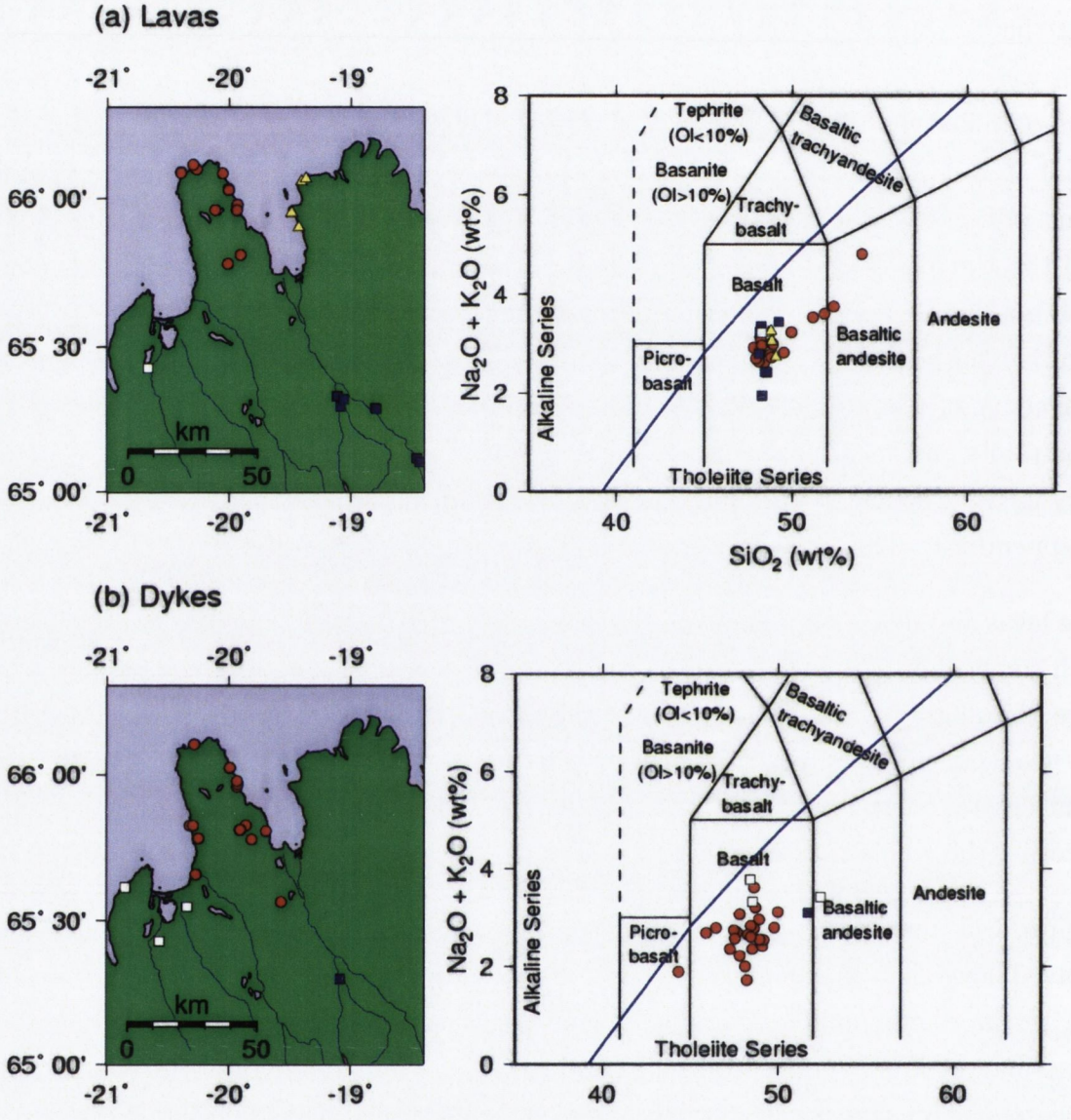

Figure 3.10: Figures showing the location and total alkali-silica classification of the Skagafjördur samples. Lava samples are shown in the top two diagrams, dykes and other intrusions are shown in the bottom two diagrams. Key: Skagi (red circles); Tröllaskagi (yellow triangles); Austurdalur/Vesturdalur (blue squares); Vatnsnes (white squares). Classification: Le Maitre et al. (1989); Alkaline-Tholeiite divide: Irvine and Baragar (1971).

In order to compare Skagafjördur samples with the Neovolcanic zones (section 4.3), it is necessary to establish whether similar age (Quaternary) lavas from different sampling areas across the Skagafjördur region represent the same rifting episode. Lavas erupted from the same rift will result from similar melting regimes. Figure 3.12 shows plots of major elements Fe and Ti; incompatible trace elements Nb and Zr; and incompatible trace element ratios Nb/Y and Sm/Yb. These ratios are useful indicators of variations

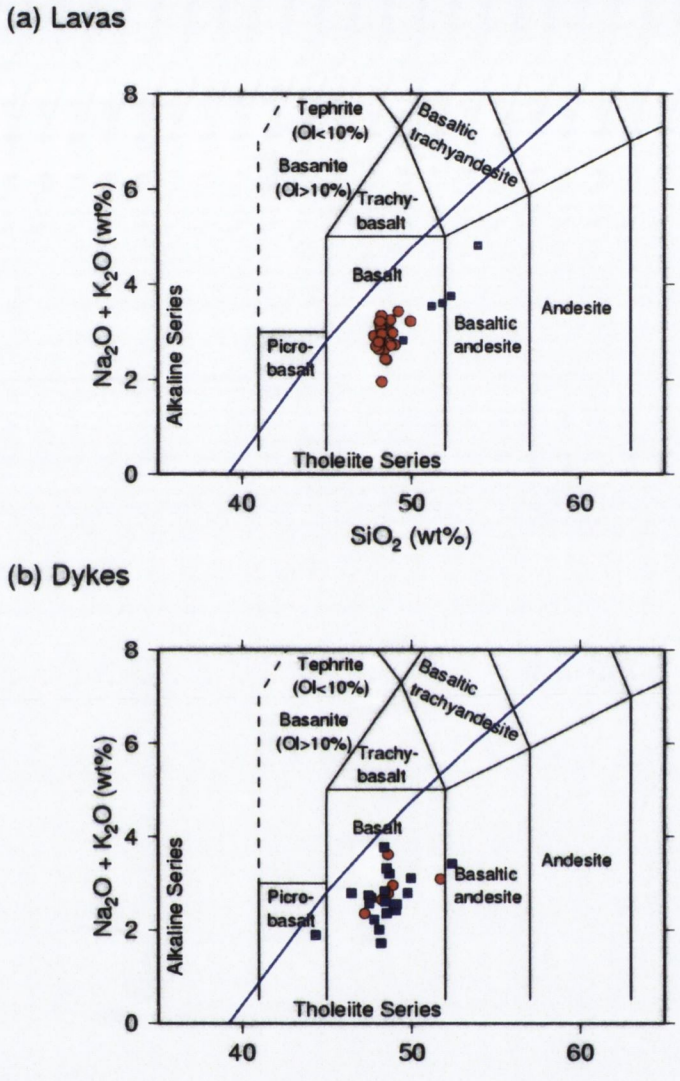

Figure 3.11: Total alkali-silica classification of Skagafjördur (a) lava and (b) dyke samples. Quaternary age samples are marked as red circles and Tertiary age samples are marked as blue squares. It must be noted that many of the Tertiary dyke samples simply cross-cut Tertiary lava flows and do not have absolute ages to confirm that they are Tertiary age. Classification: Le Maitre et al. (1989); Alkaline-Tholeiite divide: Irvine and Baragar (1971).

in the composition of mantle melts as the effects of crustal processes are minimised by the similar behaviour of the element pairs at shallow depths, explained in more detail below. Apart from one exception from Vesturdalur, there are no systematic differences between the different sampling areas for individual major and trace elements (figure 3.12). For Sm/Yb, the Skagi samples plot slightly lower than those from the other sampling areas. For Nb/Y, only Tröllaskagi samples plot higher than Skagi samples, the other areas show similar ratio values. The differences identified in the trace element ratios are not significant compared to variations observed within the Neovolcanic zones

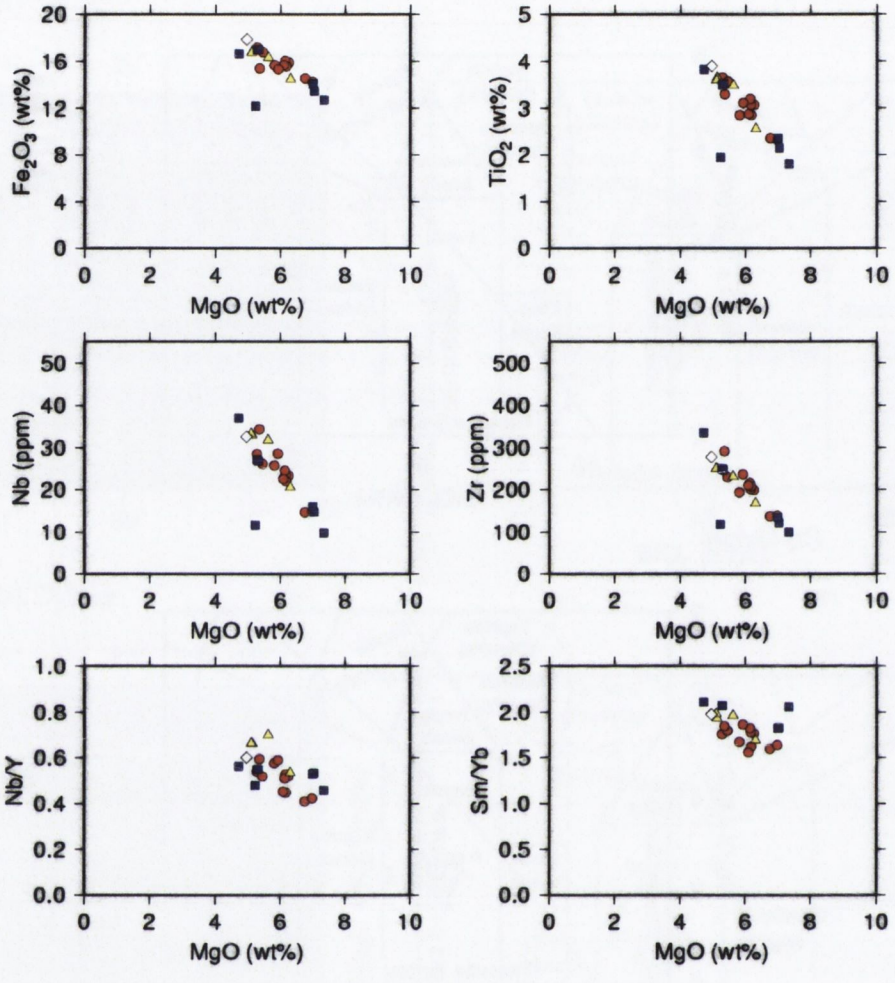

Figure 3.12: Variation diagrams for Quaternary lavas from Skagi (red circles), Tröllaskagi (yellow triangles), Austurdalur/Vesturdalur (blue squares) and Vatnsnes (white diamonds) for various major and trace elements and trace element ratios with MgO wt%. Fe_2O_3 is total Fe.

(section 4.3), suggesting that all the Skagi Quaternary samples can be considered to be related to the same rifting episode. The exception is sample A17168 donated by A. Hjartarson. This sample was described as the central layer of a Quaternary shield volcano located in Vesturdalur. The sample shows significant differences in major and trace element chemistry, but not in the trace element ratios suggesting that the magma source for this lava flow had undergone slightly different crustal fractionation processes. A17168 has an unusually high concentration of Al_2O_3 suggesting that it has accumulated plagioclase feldspar during storage in the crust (figure 3.13), producing the unusual major and trace element chemistry. Some of the Tertiary lavas from Skagi also reflect a difference in fractionation processes to the Quaternary lavas (figure 3.13).

Figure 3.13 shows the major element variations with MgO wt%. The Quaternary lavas form very well defined trends for all the major elements, with incompatible elements Ti, Mn and P increasing in concentration with decreasing MgO as expected from fractional crystallisation. Fe and Ti are increasing in the melt as plagioclase crystallises, with no evidence for the fractionation of magnetite prior to eruption. The generally high Fe-Ti concentrations are reflected in the abundance of groundmass magnetite in thin section in many of these samples. The Tertiary samples show slightly more scatter than the Quaternary lavas, particularly with reference to the incompatible major elements and Fe. Ca and Al show well defined descreasing trends with decreasing MgO concentrations related to fractional crystallisation of clinopyroxene and possibly plagioclase feldspar. There is one exception to these well defined trends in the Quaternary lava flows which is sample A17168 discussed previously. The Tertiary lavas are more scattered for Fe and the incompatible elements Ti, Mn and P. The origin of these lava flows is less well constrained, and some of the samples may be from central volcanic complexes where crustal fractionation processes may be very different to the fissure and vent eruptions that formed the Quaternary lava suite on Skagi.

Figure 3.14 shows some of the incompatible trace element variations with MgO wt% for Quaternary and Tertiary lava flows from Skagfjördur. The single element plots look very similar to the major element plots in figure 3.13, being strongly influenced by fractional crystallisation processes. The Quaternary lavas exhibit well defined trends with decreasing Mg and the Tertiary lavas are generally more scattered. Rb, Ba and Sr are mobile incompatible elements. Rb and Ba show similar trends to the immobile elements Nb, Zr and Y suggesting that hydrothermal alteration has not significantly affected these lavas. However, the Sr values are slightly more scattered, forming a cloud of data points rather than a defined trend. This scattering suggests that some of these samples have undergone fractional crystallisation of plagioclase because Sr is compatible in plagioclase. Rb and Ba are not affected in the same way as Sr because they are incompatible in all phases during fractional crystallisation of gabbroic material.

Certain trace element ratios, such as Nb/Y and Zr/Y, are hardly affected by the effects of crustal processes such as fractional crystallisation and hydrothermal alteration and allow information about the melting processes to be obtained. These element pairs are strongly fractionated by melting in the presence of garnet, but have relatively similar partition coefficients for clinopyroxene and plagioclase. These ratios can be used a reasonable proxy for the influence of deep melting of garnet lherzolite on the overall degree of melting. Further discussion of the partition coefficients is presented in section 4.3. The ratios do not show the same trends as the single element plots. The Tertiary

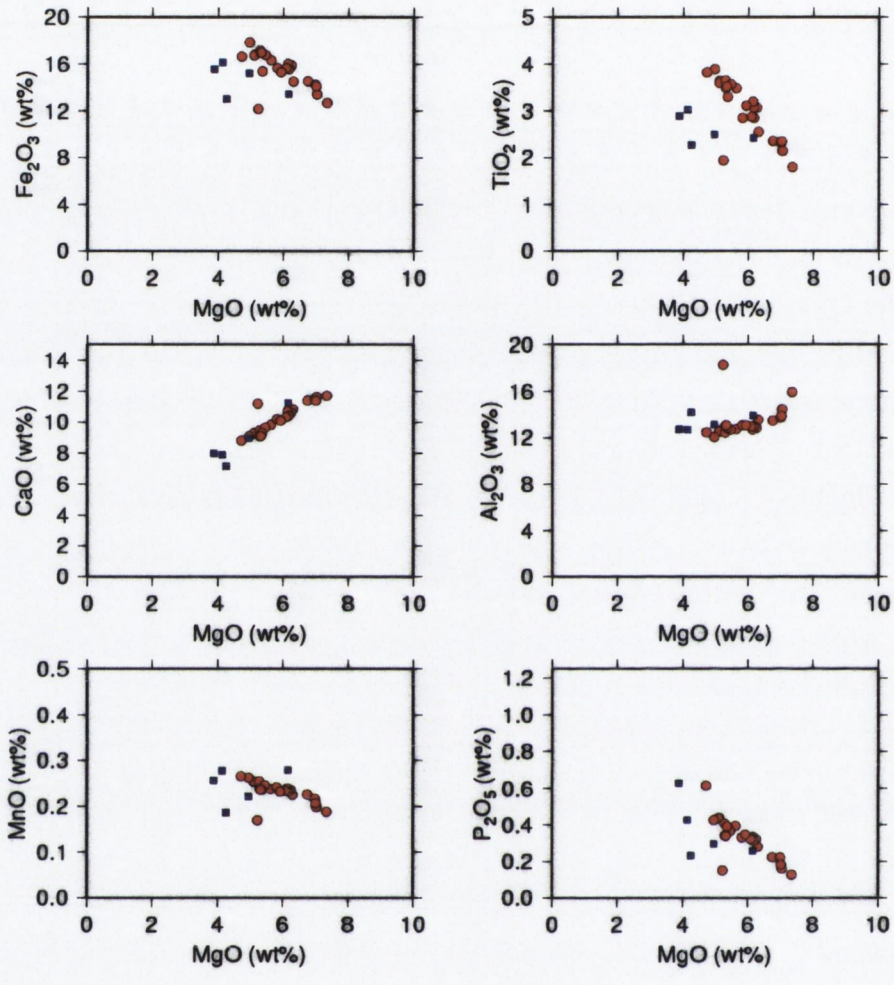

Figure 3.13: Variation diagrams for Quaternary (red circles) and Tertiary (blue squares) lavas from the Skagafjördur region for various major elements with MgO wt%. Fe_2O_3 is total Fe.

lavas plot in the same range of values as the Quaternary lavas suggesting that, despite differences in the major and trace element absolute concentrations, the original melting regimes may be similar.

Figures 3.15 and 3.16 show the REE concentrations for Quaternary and Tertiary lavas and dykes. For all samples shown the REE concentrations exhibit steep patterns, evident from later comparisons with the Northern Volcanic Zone in Iceland (section 4.3.2). The Skagafjördur lavas and dykes show light REE enrichment indicative of a strong influence of deep mantle melting on the melting regime, consistent with the trace element ratio interpretation above. The absolute concentrations of the REE is very high which may reflect a small degree of melting or significant differences in fractional

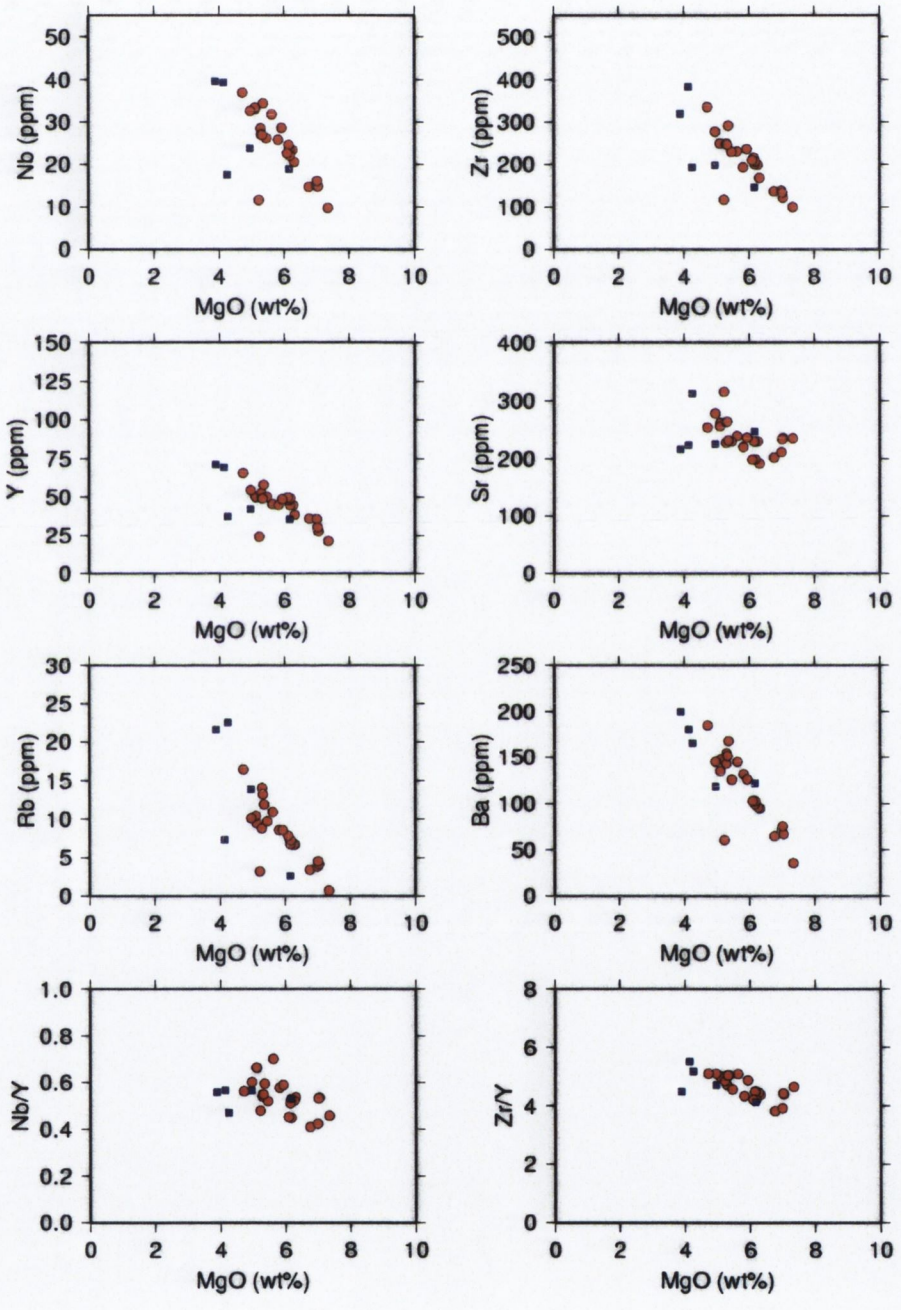

Figure 3.14: Variation diagrams for Quaternary (red circles) and Tertiary (blue squares) lavas from the Skagafjördur region for various trace elements and trace element ratios with MgO wt%. Rb and Ba are mobile elements.

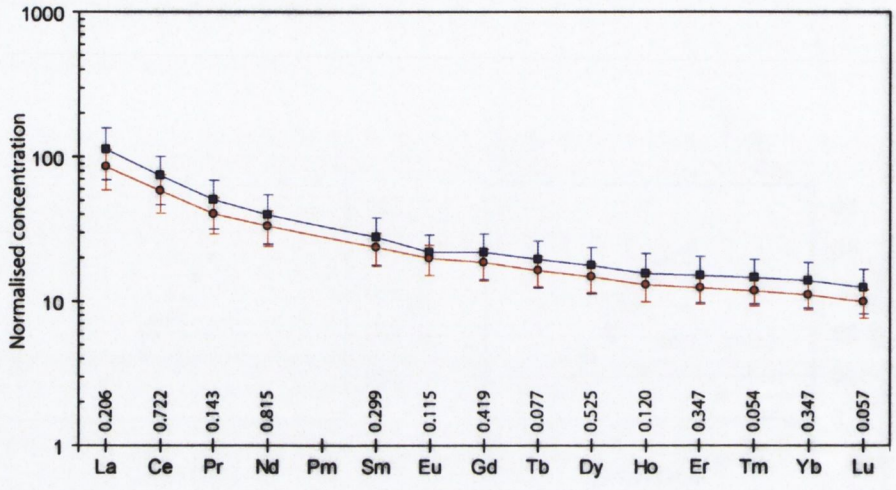

Figure 3.15: Mean REE concentrations from Quaternary (red circles; n=21) and Tertiary (blue squares; n=4) lavas from the Skagafjördur region normalised to the MORB source of McKenzie and O'Nions (1991). The error bars are $\pm 1\sigma$. Normalising values in ppm are shown above the x-axis.

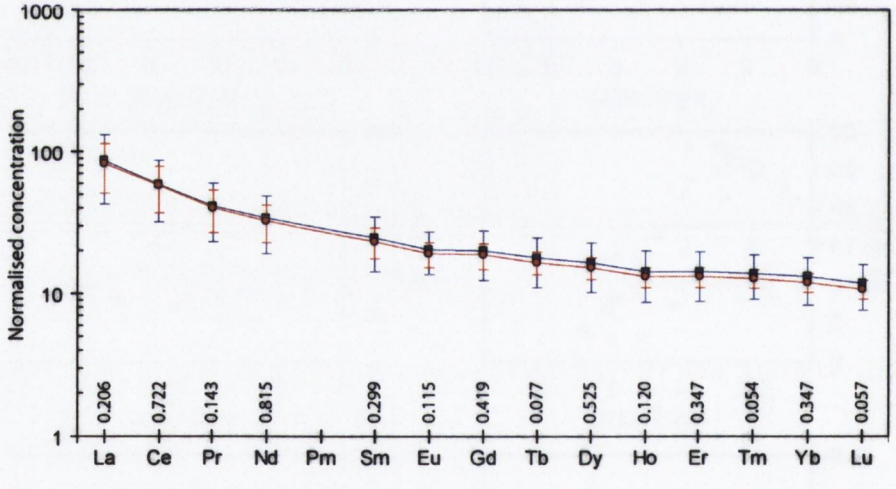

Figure 3.16: Mean REE concentrations from Quaternary (red circles; n=6) and Tertiary (blue squares; n=11) dykes from the Skagafjördur region normalised to the MORB source of McKenzie and O'Nions (1991). The error bars are $\pm 1\sigma$. Normalising values in ppm are shown above the x-axis.

crystallisation processes. The lavas and dykes exhibit very similar patterns with the Tertiary lavas showing slightly higher concentrations, most likely reflecting fractional crytallisation as this is consistent with the scatter observed in the incompatible major and trace element concentrations.

The major and trace elements and REE show that there are no significant differences between Quaternary and Tertiary lava flows from the Skagafjördur region that can-

not be accounted for by a difference in fractional crystallisation processes (figures 3.13 to 3.16). Before a comparison is made to the rest of Iceland, possible variations in source composition within the Quaternary lava suite compared to the Tertiary lavas must be investigated. Figure 3.17 shows that there is no significant difference between the Quaternary lavas for $^{87}Sr/^{86}Sr$ and $^{143}Nd/^{144}Nd$ values indicating little variation in source composition. Only 2 samples from Tertiary lavas and 2 samples from Quaternary dykes were analysed; more samples would need to be analysed for more reliable interpretation. For the $^{143}Nd/^{144}Nd$ values the Tertiary lavas and Quaternary dykes show no significant differences to the Quaternary lava suite. For the $^{87}Sr/^{86}Sr$ values there are two outliers that plot significantly higher than the Quaternary lavas. The high $^{87}Sr/^{86}Sr$ is likely to reflect some hydrothermal alteration or assimilation of hydrothermally altered material rather than a different mantle source and this would be consistent with the scatter shown by the individual Sr concentrations (figure 3.12). The $^{143}Nd/^{144}Nd$ values are also consistent with a constant mantle source composition. The two samples with exceptionally high $^{87}Sr/^{86}Sr$ are excluded from the comparison of the isotope concentrations with the rest of Iceland. Figure 3.18 would normally show an inverse relationship between $^{87}Sr/^{86}Sr$ and $^{143}Nd/^{144}Nd$, where high $^{87}Sr/^{86}Sr$ are correlated with low $^{143}Nd/^{144}Nd$ for the most enriched compositions. However, the range of compositions in the Skagi lavas is so small that no trend is observed. It is important to note that the two exceptionally high $^{87}Sr/^{86}Sr$ do not have exceptionally low $^{143}Nd/^{144}Nd$, consistent with the suggestion that these samples have been affected by hydrothermal alteration or the assimilation of hydrothermally altered material.

3.6 Discussion and Conclusions

Differences in absolute concentrations of elements for Tertiary lavas compared to Quaternary lavas may reflect differing crustal processes. The tectonic setting for the few Tertiary lava samples is not well constrained and the lava flows may be part of central volcanic complexes which will exhibit very different magma storage and transport mechanisms to the fissure and central vent eruptions evident for the Quaternary lava suite. However, similar values for the trace element ratios Nb/Y and Zr/Y suggest that there may be little difference between the partial melting processes or mantle source composition forming the Tertiary and Quaternary magmas. The similar REE patterns for the Tertiary and Quaternary lavas is consistent with similar melting regimes. Slightly higher absolute values in the REE concentrations for the Tertiary compared to the Quaternary may indicate different fractionation processes. The significant glacial

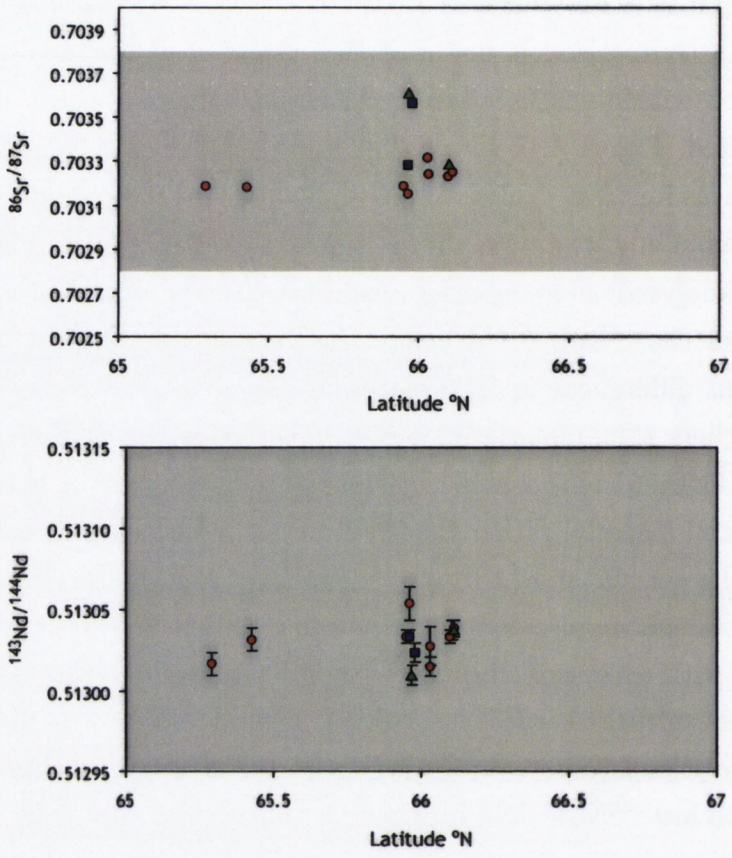

Figure 3.17: Whole rock $^{87}Sr/^{86}Sr$ and $^{143}Nd/^{144}Nd$ ratio values for 12 Skagafjördur samples. Quaternary lava flows (red circles), Tertiary lava flows (blue squares) and Quaternary dykes (green triangles). The 2σ error is shown for $^{143}Nd/^{144}Nd$, and is not shown for $^{87}Sr/^{86}Sr$ because it is a similar size to the data point as on figure 3.18. The range of $^{87}Sr/^{86}Sr$ values for Iceland is shown by the grey area (Kokfelt et al., 2006).

unconformity observed between the Tertiary and Quaternary is not associated with a significant change in the geochemical signature of melting.

The lack of significant difference between the Tertiary and Quaternary lava flows may have important implications for the tectonic origin of the young Skagafjördur lavas and crustal accretion processes in general at Iceland (discussed in chapters 5 and 8). It is generally accepted that the Quaternary lavas from Skagafjördur represent a transient rifting episode (Schilling et al., 1978) initiating around 3.3 Ma and lasting for 1–2 Myrs (Gudmundsson, 2007). However, there is little evidence from the geochemistry to suggest that the major unconformity between the Tertiary and Quaternary is indicative of a break in volcanic eruption. The Quaternary lava suite may simply be a continuation of the old Tertiary rift. Further comparisons of the new geochemical data with published data from the Neovolcanic zones provide further constraint on the tec-

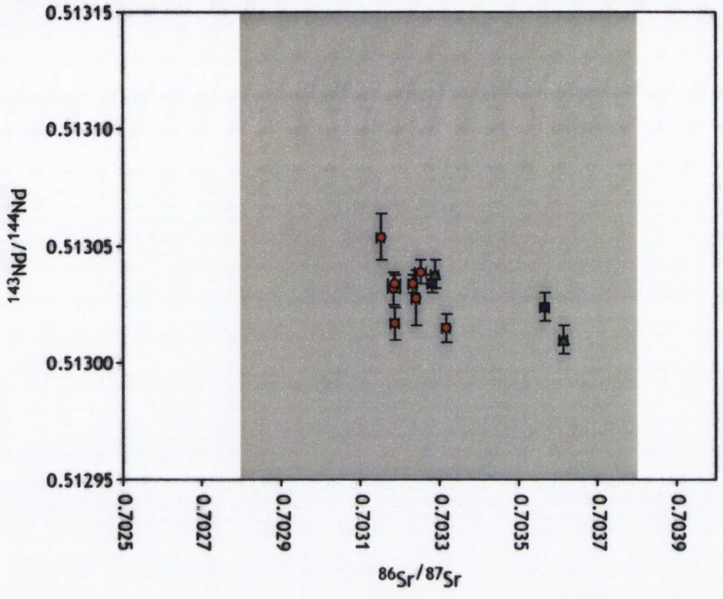

Figure 3.18: Whole rock $^{143}Nd/^{144}Nd$ versus $^{87}Sr/^{86}Sr$ ratio values for 12 Skagafjördur samples. Quaternary lava flows (red circles), Tertiary lava flows (blue squares) and Quaternary dykes (green triangles). The range of $^{87}Sr/^{86}Sr$ values for Iceland is shown by the grey area (Kokfelt et al., 2006); the range of $^{143}Nd/^{144}Nd$ for Iceland is larger than range plotted. The error bars are $\pm 2\sigma$.

tonics discussed in section 4.3. The preservation bias introduced by crustal accretion mechanisms operating at Iceland must also be taken into consideration by comparing the Skagafjördur lavas to Tertiary data from across Iceland as well as data from the Neovolcanic zones (section 5.4).

Chapter 4

Temporal Variations in Geochemical Signature at Iceland

4.1 Introduction

Temporal variations in the geochemistry of rift products at Iceland are controlled by three main processes: glaciation/deglaciation, rift relocations and plume flow. The latter two directly affect mantle flow beneath the spreading ridges and are likely to be linked. The effects of deglaciation on melting and the chemistry have been well documented and modelled so that they can, to a certain extent, be isolated from the effects resulting from mantle flow variability (Maclennan et al., 2002; Jull and McKenzie, 1996). Understanding the changes in melting that occur beneath a spreading ridge during a rift relocation could indicate which processes control the initiation of rift jumps at Iceland. Although rift jumps are thought to be plume-driven, there has been very little evidence to suggest what causes them.

Significant changes in geochemistry have been observed in association with rift jumps and the death of a rift axis at the Phoenix Ridge, Antarctica (Choe et al., 2007). The aim of this chapter to compare the geochemical observations (new and existing) from different rift stages preserved or active at Iceland and relate any significant differences to variations in the melting regime. The neovolcanic zones have been subject to extensive geochemical investigation in isolation, however, little work has been done to compare the different zones and relate geochemical observations with geophysical observations. Geochemical data will be examined in the context of the variations of crustal thickness

across Iceland with the aim of establishing whether the geochemical variations can be linked to the rift relocation cycle or are the result of other temporal processes. It is possible to confidently attribute some geochemical variations to the changes in spreading rate during a rift relocation.

The geochemical signature of the young Quaternary Skagi lavas from the now extinct Skagi rift was characterised in chapter 3. Another aim of chapter 4 is to establish their likely origin by comparing their geochemical signature to that of active rift zones and off-axis volcanism. REE inversion modelling (McKenzie and O'Nions, 1991) is used to quantify differences in the melting regime and show the inconsistency between crustal thickness predictions and observations at Skagi.

4.2 Background

4.2.1 Temporal Processes

The following section contains a description of the effect of the three temporal processes: glaciation, rift relocations and plume flow, on the geochemical signature of the active rifts at Iceland. The geochemical response to glaciation and deglaciation in the Northern Volcanic Zone is observed by Slater et al. (1998) and Maclennan et al. (2002), and for the Western Volcanic Zone by Sinton et al. (2005) and Gee et al. (1998). Samples from the Northern Volcanic Zone show a significant decrease in incompatible element enrichment in early postglacial lavas compared to glacial lavas. Postglacial lavas also show a much greater range in MgO contents than subglacial and recent eruptions, with a whole rock maximum of up to 20 wt% MgO in picrites. Changes in the geochemical signature resulting from glaciation/deglaciation have been linked to differences in the rate of melting, particularly at shallow levels. These are caused by a change in pressure in the mantle from loading/unloading of the crust. Jull and McKenzie (1996) modelled crustal unloading to show that deglaciation can produce an increase in the rate of melting by up to a factor of 30 compared to glacial times. Maclennan et al. (2002) accounted for low REE concentrations associated with early postglacial magmatism by increased melt production rates in the shallow mantle. The high MgO picritic samples are likely to result from the accumulation of olivine. For comparative purposes, samples from all ages (glacial, >12 kyr; postglacial, 12–7 kyr; recent, <7 kyr) where possible are used so that any major differences seen in the geochemical signature between different rift zones can be related to mantle processes

rather than glaciation.

Rift relocation describes the processes of migration of the active rift axes on Iceland in response to the relative migration of Iceland and the Mid-Atlantic Ridge compared to the Iceland plume centre. Garcia et al. (2003) predicted the partitioning of extension across two simultaneously active ridges for around 5 Ma resulting in slower individual spreading rates and the possibility of asymmetric spreading. This decrease in spreading rate may result in a greater influence of conductive cooling on the melting regime, as the threshold full spreading rate is approximately 20 mm yr^{-1} (Bown and White, 1994) and the normal full spreading rate at Iceland is already slightly lower than that at 18 mm yr^{-1} (DeMets et al., 1994). These studies are described in detail in section 2.1.3 and the effects of a variable spreading rate on melting and chemistry are modelled in chapter 7.

The presence of diachronous ridges in the sea floor along the Reykjanes Ridge, south of Iceland and along the Kolbeinsey ridge, north of Iceland represent variations in crustal thickness. Jones et al. (2002) suggest that these V-shaped ridges are related to time dependent flow in the mantle originating from temporal variations in the flow out of the plume stalk, spreading out under Iceland. White et al. (1995) predict temperature variations associated with the melting which causes V-shaped ridges are approximately 30°C. However, there is currently no clear evidence to suggest that the melting variations result from thermal variations alone and they could therefore also be linked to compositional variations in plume flow.

4.2.2 Rift Cycle at Iceland

Four different rift stages are present or preserved at Iceland. The location of these rifts and off-axis volcanic activity are shown on figure 4.1. The fully established rift stage where Iceland's full spreading rate is taken up across one rift is represented by the Northern Volcanic Zone which has been active for approximately 8 Ma (Garcia et al., 2003). There is some doubt over how long the Northern Volcanic Zone has been independently active, in that the timing of the extinction of the Skagi rift is not well constrained. Dual activity in northern Iceland may have extended up to approximately 1 Ma, depending on the exact origin of the young Skagi lavas which is discussed at the end of this chapter in section 4.5. The crustal thickness in the Northern Volcanic Zone varies from 20 km in the northern part (Staples et al., 1997) up to 40 km in central Iceland (Darbyshire et al., 1998). The influence of the plume has significant effects on

melt productivity and chemistry (Maclennan et al., 2001b).

The birth or propagation of a rift axis marking the start of a new rift jump is represented by the Eastern Volcanic Zone and in particular the propagating tip activity in the Vestmannaeyjar system off the south coast of Iceland. The Eastern Volcanic Zone has been propagating southwards for 2–3 Ma and has an average crustal thickness of 20 km (estimated from Darbyshire et al., 2000; figure 4.2) increasing gradually northwards towards the edge of Vatnajökull ice cap. However, the crustal thickness is not well constrained in southeast Iceland.

The decline of a rift as extension gradually transfers to a new adjacent rift is represented by the Western Volcanic Zone which was independently active since 6–7 Ma before the Eastern Volcanic Zone propagated to overlap around 2–3 Ma. The crustal thickness in the Western Volcanic Zone ranges from approximately 35 km in the north down to approximately 16 km at the end of the Reykjanes Peninsula (estimated from Darbyshire et al., 2000; figure 4.2). Maclennan et al. (2001b) showed that similarly thick crust in central Iceland could not be produced by passive upwelling alone, without the addition of active upwelling from the influence of the plume. This observation suggests that the northern end of the Western Volcanic Zone may be subject to influence from plume flow.

Finally, the last eruptions of an extinct rift are thought to be preserved at Skagi. There is some doubt over the origin of the young lava series found on the Skagi peninsula, however, they are clearly related to the extinct Skagi rift, but may be the result of re-activation rather than the final eruptions of the Skagi rift. The average crustal thickness at present beneath Skagi is approximately 25–30 km (Darbyshire et al., 1998), resolved at the base of the peninsula from the ICEMELT seismic refraction profile. An extinct rift is also preserved in Northwest Iceland, studied by Hardarson et al. (1997), see section 4.2.3.

The main rift activity is supplemented by several off-axis volcanic centres or flank zones up to 50 km from the nearest main rift. Grímsnes is a small volcanic centre only 15 km from the Western Volcanic Zone which has produced unusually enriched tholeiitic basalts compared to the Western Volcanic Zone (Sinton et al. 2005). Öraefajökull is a flank zone situated 25 km east of the edge of the Northern Volcanic Zone in central Iceland. Öraefajökull and Snaefell are the two volcanic centres within this flank zone. The Snaefellsnes Volcanic Zone is the final and most active flank zone forming a distinct peninsula in west Iceland. The tectonic origin of the Snaefellsnes Volcanic Zone is

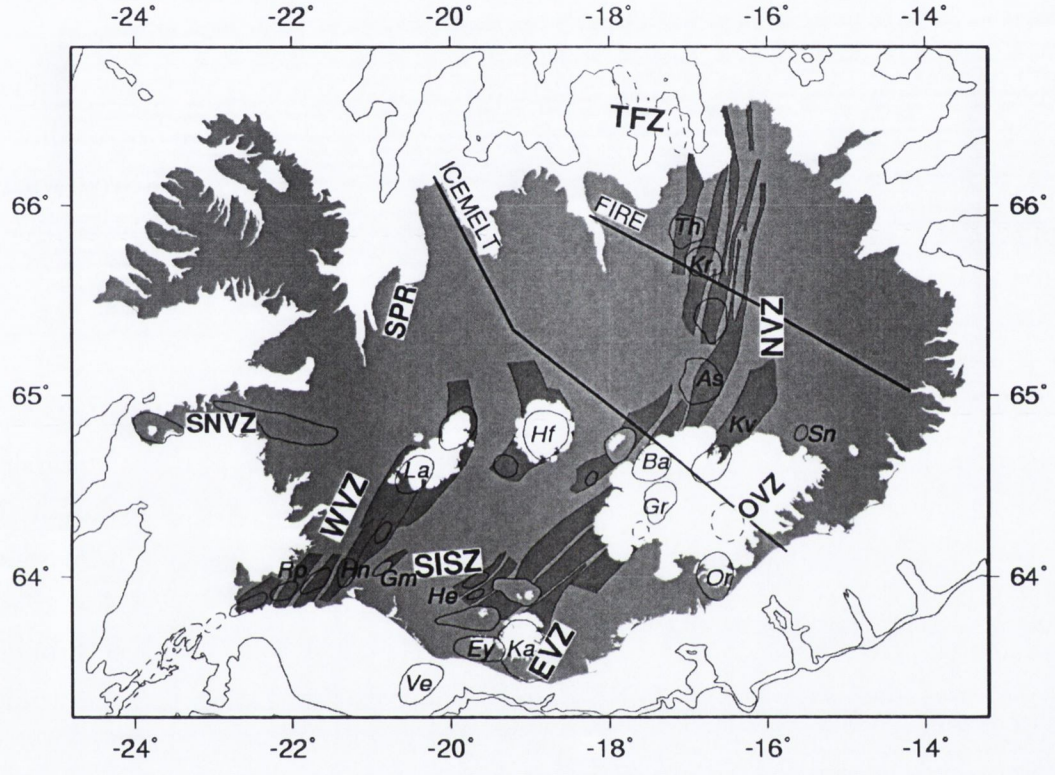

Figure 4.1: Tectonic map of Iceland based on Einarsson & Saemundsson (1987). Fissure swarms associated with volcanic systems forming the three main rift zones are filled dark grey. Central volcanoes are shown as closed circles. The neovolcanic zones are labelled: NVZ, Northern Volcanic Zone; WVZ, Western Volcanic Zones; EVZ, Eastern Volcanic Zone. Active seismic zones: SISZ, South Iceland Seismic Zone; TFZ, Tjörnes Fracture Zone. Flank zones: SNVZ, Snaefellsnes Volcanic Zone; OVZ, Oïaefajökull Volcanic Zone. Extinct rift: SPR, Skagi palaeorift axis. Main volcanic systems labelled as follows: Th, Theistareykir; Kr, Krafla; As, Askja; Kv, Kverkfjöll; Ba, Bardarbunga; Gr, Grímsvötn; Ka, Katla; Ey, Eyjafjallajökull; He, Hekla; Ve, Vestmannaeyjar; Hf, Höfsjökull, La, Langjökull; Hn, Hengill; Gm, Grímsnes; Rp, Reykjanes Peninsula (includes all 3 systems). Sn, Snaefell and Or, Öraefajökull are volcanic centres. Askja and Kverkfjöll form the central Iceland part of the Northern Volcanic Zone as referred to in section 4.3; Theistareykir, Krafla and Fremri-Namur form the northern part of the Northern Volcanic Zone. FIRE and ICEMELT refer to seismic experiments (Staples et al., 1997; Darbyshire et al., 1998).

unclear as there is very little extension associated with this area. The Öraefajökull flank zone may play an important part in the Icelandic rift cycle and rift jump process in the future, as the initiation of the next new rift.

The more recent activity from the Skagi rift may result from a similar melting regime to off-axis volcanism. Therefore it is important to compare the chemistry of the Skagi Quaternary lavas with off-axis activity, as well as with the main rift zones. The compositional map (section 2.1.2) shows that the established volcanic zones (Northern and Western) generally have tholeiitic compositions whereas the propagating tip (Eastern Volcanic Zone) and the Snaefellsnes flank zone are associated with more alkaline lava compositions which indicates a much smaller degree of melting compared with the established zones.

4.2.3 Existing Geochemical Data

To allow comparisons of the extinct rift with the neovolcanic zones, a database of existing data for the active rift zones was compiled. There have been hundreds of geochemical studies carried out across the neovolcanic zones in Iceland and it was not within the scope of the project or necessary to compile them all. Several studies are chosen for each volcanic zone to provide a range of locations and ages throughout the zone, so that the range of basaltic compositions produced at a rift zone would be suitably represented.

Previous studies of the volcanic zones have often been limited to particular systems and volcanoes in that detailed geochemistry has been carried out but only analysed and explained within its own context and not compared to volcanism from other areas of Iceland. There have been a few studies which have considered geochemical variations on an Iceland-wide scale. Sigurdsson et al. (1978) and Schilling et al. (1978) studied variations in Western Iceland from the Reykjanes Peninsula up the Western Volcanic Zone to Skagi on the north coast (figure 4.1). Sigurdsson et al. (1978) compared the composition of basalts from the Skagi rift and the Langjökull volcanic system, Western Volcanic Zone concluding that major element concentrations in Skagi basalts could be reproduced by extensive fractional crystallisation of Langjökull parent magmas, but the REE compositions for Skagi basalts required different melting regimes. Schilling et al. (1978) noted an abrupt petrological and geochemical discontinuity between the Langjökull and Skagi volcanic zones suggesting that they are unlikely to be related by parental melts. Smaller degrees of melting and higher extents of fractional crystalli-

Volcanic Zone	References
Western Volcanic Zone	Sigurdsson et al. (1978) Schilling et al. (1978) Meyer et al. (1985) Hémond et al. (1993) Sinton et al. (2005) Kokfelt et al. (2006)
Northern Volcanic Zone	Meyer et al. (1985) Hémond et al. (1993) Slater et al. (2001) Maclennan (2000) Maclennan et al. (2001a) Maclennan et al. (2001b) Kokfelt et al. (2006)
Eastern Volcanic Zone	Meyer et al. (1985) Steinthorsson et al. (1985) Furman et al. (1991) Sigmarsson et al. (1991) Sigmarsson et al. (1992) Hémond et al. (1993) Mattson and Höskuldsson (2003) Mattson and Oskarson (2005) Kokfelt et al. (2006)
Snaefell Volcanic Centre	Hards (1995)
Snaefellsnes Volcanic Zone	Steinthorsson et al. (1985) Hémond et al. (1993) Kokfelt et al. (2006)

Table 4.1: References used to compile data for comparative purpose for each of the neovolcanic zones. Data from Maclennan (2000) is published in Maclennan et al. (2001b).

sation are predicted for Skagi compared to the Western Volcanic Zone. The degree of melting and fractional crystallisation were modelled to respectively decrease and increase gradually towards the Reykjanes Peninsula from the Langjökull system. Sigurdsson et al. (1978) also observe similarities between Skagi and the Eastern Volcanic Zone. They were both considered to be transient rift zones by Schilling et al. (1978).

Meyer et al. (1985) carried out an extensive geochemical study of the neovolcanic zones across Iceland including the Snaefellsnes flank zone producing over 200 new analyses and compiling data from the literature. The formation of alkaline basalts at the southern tip of the Eastern Volcanic Zone at Vestmannaeyjar, is modelled to result from small degree melts beneath a thick lithosphere. The degree of melting is observed to increase northwards to produce more transitional and high Fe-Ti compositions for

Hekla and Katla systems. High degrees of melting and low cooling rate leading to less evolved magmas are observed in the main axial rift zones in southwest and north Iceland. However, the limited knowledge of rift relocations meant that important geochemical variations were not able to be associated with variations in crustal thickness and spreading rate. Meyer et al. (1985) suggested that the propagation of the Eastern Volcanic Zone was initiated by the ascent of a 'blob' of undepleted mantle from the plume head which spreads out laterally under Iceland 2–3 Ma. Recent work by Jones et al. (2002) has shown that the first V-shaped ridge corresponds to a melting anomaly peak at Iceland around 3 Ma, which is thought to result from time-dependent flow in the mantle plume as described in section 4.2.1. Jones et al. (2002) prefer a thermal rather than compositional link between pulses in the mantle plume and rift relocations.

Geochemical variations associated with the extinct rift in the extreme northwest of Iceland known as the Northwest Rift were published by Hardarson et al. (1997). Broad differences are observed in the Zr/Nb ratio between the Northwest Rift and the younger Skagi-Snaefellsnes Rift, where older lavas beneath the unconformity are more depleted than the young lavas. Hardarson et al. (1997) suggested that source variation may account for these geochemical differences. They also suggest that rift relocation results in restricted access to plume material for the declining rift, resulting in the source being primarily depleted upper mantle material. A marked decrease in depletion of the Zr/Nb ratio is observed just below the unconformity. The NW Iceland rift chemistry is described in chapter 5.

Hémond et al. (1993), Thirwall et al. (2004) and Kokfelt et al. (2006) have presented further data from across the neovolcanic zones in Iceland including extensive isotopic data. The main aim of their studies was to determine the composition of the mantle source beneath Iceland and link variability in isotopic concentrations to a number of different mantle components. Hémond et al. (1993) conclude that the isotopic composition of alkaline magmas reflect a more enriched source than the main tholeiitic fissure eruptions. Low $\delta^{18}O$ and high $^{87}Sr/^{86}Sr$ values from crustal assimilation were found mainly in evolved tholeiitic lavas associated with central volcanoes. Finally, they suggest that all Icelandic lavas have undergone some level of interaction with hydrothermally altered crust, but for high MgO lavas the effect is essentially limited to anomalies in the mobile incompatible elements Sr, Rb and Ba. Isotopic evidence presented by Kokfelt et al. (2006) is consistent with a broadly two component mantle with an enriched and a depleted source, however, these are then broken down into several individual components. A similar conclusion is presented by Thirwall et al. (2004). The validity of this precise interpretation of for example, Pb isotope values, is questionable

as Maclennan (2008a) showed that the complete range of variability of Pb-isotopes at Iceland can be found in melt inclusions taken from one hand sample, indicating high amplitude heterogeneity on small length scales in the mantle. The length scale is estimated at significantly less than 100 km, which is a similar scale to the plumbing system of a single volcano. Kokfelt et al. (2006) model partial melting of off-axis basalts as derived from small degree melts from between approximately 80 and 50 km depth with larger degrees of melting and depth ranges observed in the neovolcanic zones and at the propagating tip of the Eastern Volcanic Zone (Vestmannaeyjar).

Geochemical Links to Crustal Thickness

A crustal thickness map of Iceland is shown in figure 4.2 from Darbyshire et al. (2000) compiled from seismic profiles, receiver function analysis and gravity modelling. There have been several more recent attempts at producing a crustal thickness map using mostly receiver function analysis via different methods, however, there is a wide variety of results and no current consensus on the most accurate map. The main features of thick crust over the plume centre, thinning with distance from the plume along the Northern and Eastern Volcanic Zones; and thickening crust towards central Iceland in the Western Volcanic Zone from the Reykjanes Peninsula remain relatively consistent for each model (Allen et al., 2002; Foulger et al., 2003; Kumar et al., 2007). The location of seismic stations results in poor constraints for the crustal thickness beneath Skagi, with the best estimate of 25–30 km calculated from the ICEMELT seismic refraction profile with the closest bounce point resolving the crustal thickness at the southern end of the peninsula (Darbyshire et al., 1998).

The distinction is made between the northern part of the Northern Volcanic Zone and the southern part which will be referred to as central Iceland. Theistareykir, Krafla and Fremri-Namur are the main fissure systems in the northern part, while Askja and Kverkfjöll are the main systems in central Iceland (figure 4.1). Maclennan et al. (2001b) showed that melting in the central systems is significantly influenced by active upwelling from the plume, producing up to half of the observed crustal thickness. Greater light REE enrichment is observed in the central part of the Northern Volcanic Zone compared to Theistareykir and Krafla. REE inversion models of Theistareykir reproduce the observed crustal thickness of 20 km based on passive upwelling of hotter than normal mantle. However, the predicted 40 km thick crust cannot be reproduced by REE inversion modelling of central Iceland compositions. Maclennan et al. (2001b) reproduced the observed crustal thickness from the REE inversion by introducing active

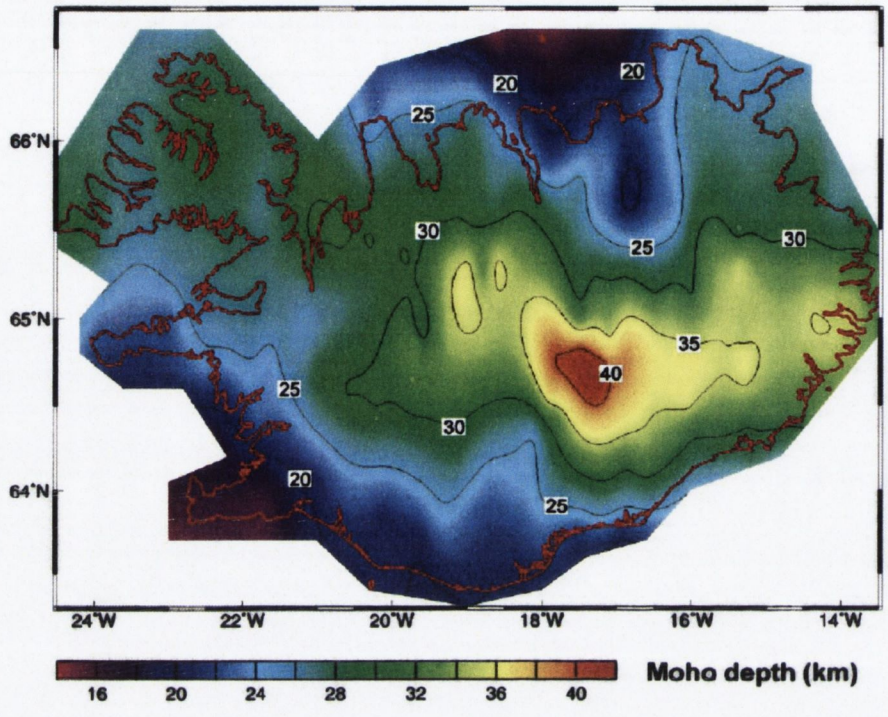

Figure 4.2: Contour map of depth to the Moho, using a combination of results from seismic profiles, receiver function analysis and gravity modelling. The contour interval is 5 km. From Darbyshire et al. (2000).

upwelling in the deepest parts of the melting region. Fluxing material through the deep mantle i.e. garnet field melting (>80–100 km) produces a more enriched composition than would be expected from the very large degrees of melting required to produce 40 km thick crust. The effect of the plume on melt productivity and the resultant chemistry must be taken into account when analysing the geochemical comparisons in order to gain a consistent understanding of geochemical variations associated with rift relocations.

In the Western Volcanic Zone, Sinton et al. (2005) observed systematic depletion in incompatible elements moving northwards through the zone. The exceptions to this are high MgO and highly depleted samples from the Reykjanes Peninsula and highly enriched samples from Grímsnes. The Reykjanes Peninsula samples are related to early postglacial eruption following rapid decompression melting after deglaciation as discussed previously (section 4.2.1). Grímsnes is located approximately 15 km off-axis from the main volcanic systems in the Western Volcanic Zone (figure 4.1). It is described as volcanically anomalous, composed of small volume lava flows that have the most enriched incompatible element signatures of the Western Volcanic Zone. Sinton et al. (2005) assign the geochemical signature at Grímsnes to small degrees of melting

associated with off-axis volcanism. The systematic changes in Nb/Y and Zr/Y with latitude in the Western Volcanic Zone are attributed to either long range mantle source variation or variations in the melting processes along axis. The estimated crustal thickness variations across Iceland by Darbyshire et al. (2000), figure 4.2 show a gradual increase in the crustal thickness from the Reykjanes Peninsula (16 km) to the Langjökull system (35 km). The correlation between incompatible element chemistry, melting and crustal thickness is discussed in section 4.3.1. Sinton et al. (2005) conclude from the postglacial record that there is no evidence of decline of the Western Volcanic Zone in the geochemistry despite a distinct decline in the melt production rate. This observation is discussed in section 4.5.

4.3 Geochemical Observations

The following section will present new comparisons of the compiled published data with the new Skagi data presented in chapter 3. The aim is to observe any key similarities or differences between the different rift zones which could be attributed to the rifts being at different stages of the rift cycle as described in section 4.2. The geochemical signature of each of the volcanic zones has been well documented, the aim here is not to repeat observations of major and trace element trends, but to use trace element ratios and selected single element variations to compare melting processes across different rift stages. Detailed comparisons are made between young Skagi lava flows and the active volcanism on Iceland in order to better constrain their relationship to the extinct Skagi rift.

The ratios chosen to assess melting differences are Nb/Y, Zr/Y and Sm/Yb. They are all relatively good indicators of degree and depth of melting. Table 4.2 provides the partition coefficients for Nb, Zr, Y, Sm and Yb for garnet, clinopyroxene and plagioclase. Garnet and clinopyroxene are the primary reservoirs of REE and high field strength elements (HFSE) in upper mantle peridotite and therefore, the partitioning of elements between these phases and the melt has the greatest influence on the overall composition of the mantle melt. Clinopyroxene and plagioclase are important phases during fractional crystallisation. Sm/Yb is the most robust ratio during fractional crystallisation with very similar partition coefficients for Sm and Yb in clinopyroxene and plagioclase. Sm and Yb are strongly fractionated by melting in the presence of garnet because Yb is highly compatible, whereas Sm is mildly incompatible. This difference causes enrichment in Sm and depletion in Yb to produce a very high Sm/Yb

ratio. The Sm/Yb ratio is a very good proxy for the degree of deep mantle melting. The partition coefficients for garnet for Zr, Nb and Y meant that they are also strongly fractionated during melting in the presence of garnet. Zr and Y have similar partition coefficients for clinopyroxene, but could be fractionated slightly by the removal of plagioclase during fractional crystallisation. This fractionation would appear as a gentle increasing trend for decreasing MgO. Nb and Y could be fractionated slightly by the removal of clinopyroxene and plagioclase during fractional crystallisation. Again, this fractionation would produce a gentle increase in the ratio for decreasing MgO. It must be noted that there are a wide range of partition coefficient estimations presented by numerous authors. The main feature of strong fractionation by melting in the presence of garnet is present throughout for the elements discussed here.

	Nb	Zr	Y	Sm	Yb
D_{gnt}	0.0031	0.27	3.1	0.25	6.6
D_{cpx}	0.004	0.119	0.412	0.293	0.4
D_{plag}	0.002	0.0013	0.023	0.044	0.03

Table 4.2: Partition coefficients for garnet, clinopyroxene and plagioclase for trace elements and REE used for geochemical comparisons in this chapter and chapter 5. All values are from experimental data. Garnet and clinopyroxene values are from Johnson (1998), plagioclase partition coefficients for Nb, Zr and Y are from Bindeman et al. (1998) and Sm and Yb are from Aigner-Torres et al. (2007).

The REE pattern is shown to provide further indications of differences in melting. Fractional crystallisation of plagioclase and clinopyroxene causes the REE absolute concentrations to increase, but does not affect their relative concentrations. Changes in the depth and degree of melting can be identified by the steepness and curvature of the REE pattern. Light REE enrichment over the heavy REEs results from melting in the deep mantle in the presence of garnet.

4.3.1 Skagi versus Western Volcanic Zone

The origin of the young series of Skagi basalts has in the past been associated with Western Volcanic Zone activity (Sigurdsson et al., 1978). Field observations described in chapter 3 indicate that the young Skagi lava flows were erupted at Skagi and did not flow from the northern part of the Western Volcanic Zone. The aim of this comparison is not only to characterise the Western Volcanic Zone geochemical signature in relation to its tectonic situation, but also to show that the Skagi melts are produced in situ and have not resulted from extreme lateral transport from the Western Volcanic Zone.

It has been suggested that young Skagi lavas could be derived from melts produced by the Langjökull volcanic system (Sigurdsson et al., 1978). Langjökull is located directly south of the Skagi volcanic zone and therefore, the significant lateral transport of melt that is required to supply Skagi is possible because it would be parallel to the regional tectonic weakness from plate motion at Iceland. Firstly, it should be noted that the Quaternary lavas from Skagi form extremely well defined groups and trends throughout all the major and trace element variation diagrams with MgO suggesting that they have all been formed by the same series of processes. Melts subject to a series of different evolution processes will produce a variety of different trends causing significant scatter in the data. The lateral transport of melt over 100 km is clearly possible from studies of the Askja system (Maclennan et al., 2001b) and this transport could result in further interaction with the surrounding crust. The two possible scenarios which need to be eliminated are the derivation of Skagi lavas by fractional crystallisation of Langjökull melts or the assimilation of crust during transport of Langjökull melts.

The variation of TiO_2 and trace element ratios with MgO wt% (figure 4.3) are chosen to show that the geochemical differences observed between Langjökull lavas and Skagi lavas represent differences in the melts coming out of the mantle. For the purpose of eliminating crustal assimilation, andesitic and rhyolitic samples from the Northern Volcanic Zone are also plotted, together with the only acidic sample from Skagi. No highly evolved samples were available for the Western Volcanic Zone, however, since the major element chemistry is similar to that of the Northern Volcanic Zone it is hoped that samples from the Northern Volcanic Zone will provide a reasonable comparison. The extremely high TiO_2 concentrations in the Skagi lavas are matched only by the Eastern Volcanic Zone (figure 4.13) with essentially no overlap of values with the Langjökull lavas. This automatically rules out crustal assimilation to produce high TiO_2 as there is no higher end member in the local crust to contaminate the Langjökull melts with. Also, likely assimilants, such as rhyolite, have very low TiO_2. The two Skagi samples which have the same MgO concentrations as some Langjökull samples at 7 wt% have slightly higher (approximately 0.3 wt%) TiO_2 than the average Langjökull concentration. Fractional crystallisation models run at 5 kbars (Maclennan et al., 2001a) show that is possible to reproduce the high TiO_2 concentrations in the Skagi lavas by crystallising Langjökull magmas. Beyond 4–5 wt% MgO, TiO_2 starts to decrease in concentration as it is highly compatible in magnetite. Magnetite becomes stable in the crystallising assemblage at this later stage and is clearly removed from the melt to produce the low TiO_2 values exhibited by the andesite and rhyolite samples from the Northern Volcanic Zone.

The Sm/Yb observations confirm that the geochemical difference between Skagi and Langjökull cannot be resolved by fractional crystallisation processes. Unfortunately, only 13 of the Langjökull samples have published REE concentrations, however of those 13, only 2 samples plot just within the lowest range of the Skagi Sm/Yb values. The rest are significantly lower. As discussed above, the Sm/Yb ratio is very robust and is essentially immune to fractional crystallisation processes. Therefore the high Skagi values cannot be produced by fractional crystallisation of Langjökull magmas. The other possibility is crustal assimilation. Northern Volcanic Zone andesites and rhyolites show a relatively constant value of Sm/Yb between 1.2 and 1.4 with one slightly higher sample at 1.6, compared to the Skagi values from 1.5 to 2.0. It is clear that no crustal assimilation processes could reproduce the high Sm/Yb values from Skagi by a combination of Langjökull and compositions similar to the highly evolved samples from the Northern Volcanic Zone. If a rhyolitic crust with high enough Sm/Yb did exist near the Western Volcanic Zone, it is still clear from the TiO_2 concentrations that little crustal assimilation has occurred in these Skagi melts, because any contamination with rhyolitic material would produce decreasing tails from the TiO_2 crystallisation trend towards the low TiO_2 rhyolites. The Skagi TiO_2 trend is so well defined with no deviations, that significant crustal assimilation has clearly not occurred.

The Nb/Y and Zr/Y reflect the same pattern as seen in the Sm/Yb values, however, there is slightly more overlap between Skagi and Langjökull. For Nb/Y, again it is clear that crustal assimilation of rhyolitic material could not reproduce the higher range of Skagi values. However, this is not true for Zr/Y but, because of the previous observations and interpretations of Sm/Yb and TiO_2 it is more likely that the higher Skagi values result from melting processes rather than crustal assimilation. The higher Zr/Y values for the Northern Volcanic Zone andesites and rhyolites probably result from the fractional crystallisation of clinopyroxene from the melt and crustal assimilation. REE concentrations are presented in figure 4.4, showing greater light REE enrichment for Skagi compared to Langjökull and much higher absolute concentrations for Skagi. The steeper pattern for young Skagi lavas is indicative of a difference in the melting regime to Langjökull, consistent with the trace element ratio observations. The significantly higher concentrations observed for Skagi reflect a combination of a smaller degree of melting and greater extents of fractional crystallisation.

One problem still remains: the increasing trends for the trace element ratios for decreasing MgO for the young Skagi lavas. Zr/Y and Nb/Y can be increased by the fractional crystallisation of clinopyroxene. However, Sm and Yb are essentially not partitioned by any phases that may be stable during the crystallisation of basaltic

magma. The correlation between MgO and Sm/Yb is not as distinct as for the other trace element ratios. The most likely explanation is that high MgO and high Sm/Yb melts from Skagi were not emplaced at the surface and therefore could not be sampled. If the complete range of MgO compositions were sampled at Skagi, the Sm/Yb values would form a band of points between 1.5 and 2 across all MgO compositions. The range of Sm/Yb from 1.5 to 2 is the range of compositions coming out of the mantle. High Sm/Yb are usually associated with small degree melts in comparison to the main rift zones (see REE inversion results, section 4.4.2).

Following the above observations and interpretations it is reasonable to conclude that the difference observed between Langjökull and Skagi can be linked to mantle processes rather than later crustal processes. Therefore, it can be assumed that Skagi lavas were formed 'in situ' in the mantle beneath the Skagi peninsula.

The next task is to observe the variations in the geochemical signature across the Western Volcanic Zone and link this to the melting process using a comparison with crustal thickness estimates (figure 4.7). The data shown in figures 4.5 and 4.7 for the Western Volcanic Zone cover glacial to historic age flows (younger than 0.8 Ma). TiO_2 has a general increasing trend for decreasing MgO broadly reflecting fractional crystallisation. There is clearly a relatively wide range of composition coming out of the melting region as the Ti concentration varies by more than 1 wt% for some MgO concentrations. A few samples are affected by crustal assimilation, as shown by lower TiO_2 tails at approximately 6 wt% MgO. The range of MgO concentrations is much smaller than that observed for the Northern Volcanic Zone, with the bulk of data plotting between 7 and 10 wt%. This is consistent with the extent of fractional crystallisation being less than other volcanic zones (Meyer et al., 1985). As with the Langjökull samples, there is very little overlap between the TiO_2 concentrations and trace element ratios in the Western Volcanic Zone and Skagi Quaternary lavas. It has already been shown in the interpretation of figure 4.3 that these differences must come out of the mantle. The relatively constant Sr and Nd isotope ratios indicate that the average composition of the mantle source is relatively constant and therefore, the differences observed in the trace element ratios are likley to be the result of variable melting processes.

Skagi average REE concentrations show greater light REE enrichment than the Western Volcanic Zone resulting in a steeper REE pattern (figure 4.6). These observations are consistent with significant differences in the degree and depth of melting in the Western Volcanic Zone and Skagi. The extent of light REE enrichment is a very good indicator

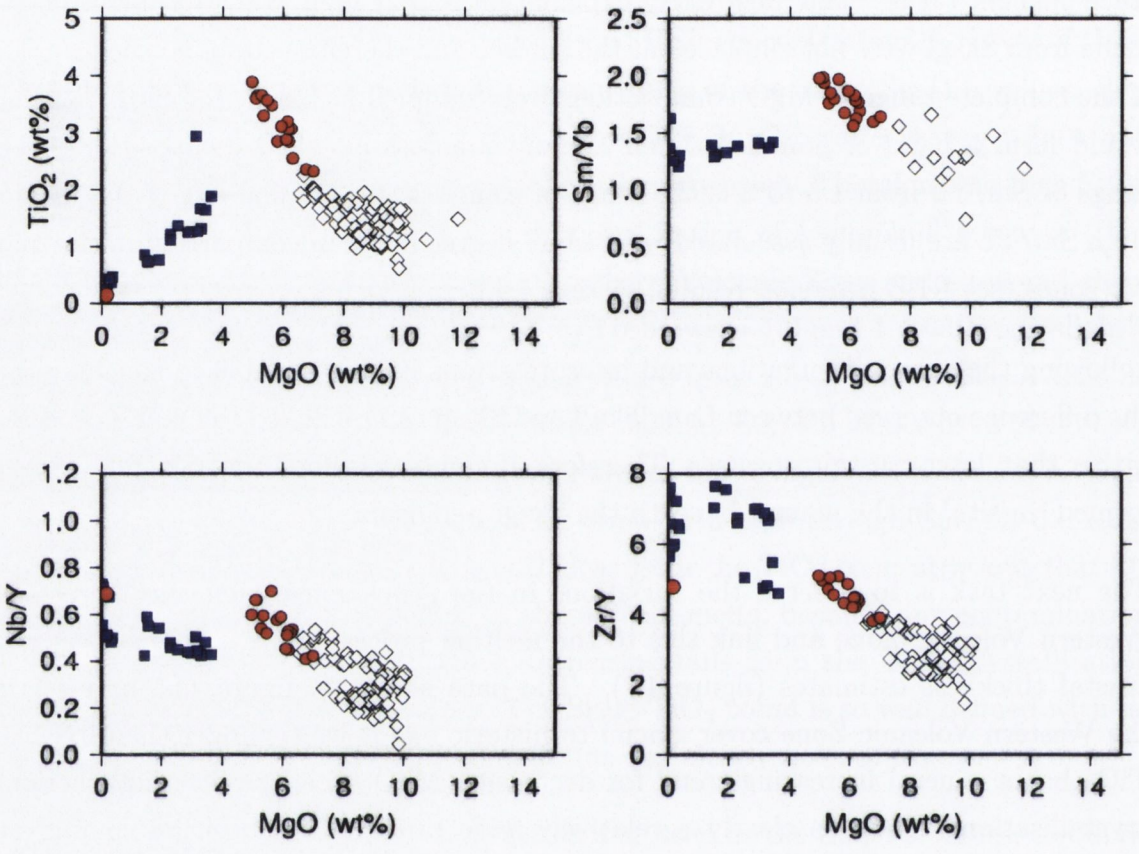

Figure 4.3: Variation diagrams for TiO_2, Sm/Yb, Nb/Y and Zr/Y to compare Skagi Quaternary lava flows (red circles) and Quaternary flows from the Langjökull volcanic system, Western Volcanic Zone (white diamonds). No samples have less than 4 wt% MgO for Skagi and Langjökull. For the case of crustal assimilation, andesitic and rhyolitic samples from the Northern Volcanic Zone are shown (blue squares) for comparison, together with the only acidic sample from a Skagi dyke (large red circle at 0 wt% MgO). Data sources are listed in table 4.1.

of the influence of deep mantle melting in the garnet stability field as light REEs are incompatible whereas heavy REEs are compatible in garnet.

A comparison of Skagi Sr and Nd isotope ratios with the Western Volcanic Zone is shown in figure 4.8. Compared to the Icelandic range of Sr and Nd isotope ratios, the values for Skagi and the Western Volcanic Zone can be considered relatively constant. Skagi has slightly higher Sr isotope ratios than all except one of the Western Volcanic Zone samples. Nd isotope ratios are similar between the two zones, with a higher range exhibited by the Western Volcanic Zone. All of the samples from Skagi and Western Volcanic Zone lie within the Icelandic range ($^{87}Sr/^{86}Sr$: 0.7030–0.7037; $^{143}Nd/^{144}Nd$: 0.51289–0.51308; summary of published values from Kokfelt et al., 2006). Sr isotope

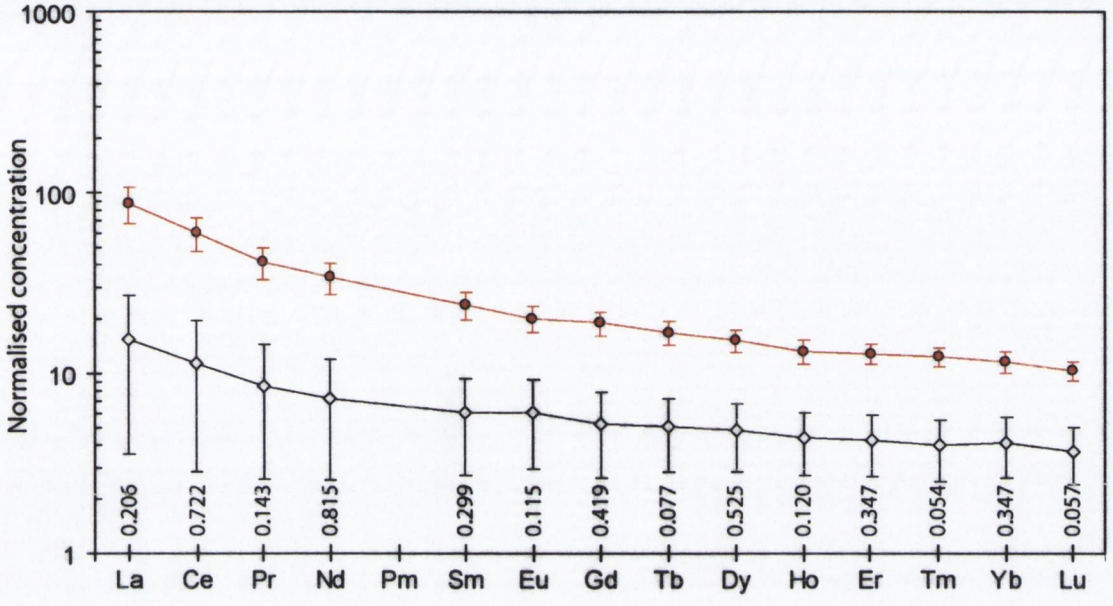

Figure 4.4: Average REE concentrations (±1 S.D.) for Quaternary lavas from Skagi (red circles; n=17) compared to Langjökull basalts (white diamonds; n=7) data from Kokfelt et al. (2006). The data set includes only basalts with greater than 4 wt% MgO. REE concentrations are normalised to MORB source mantle, McKenzie and O'Nions (1991).

ratios can be subject to hydrothermal alteration to a much greater extent than Nd isotope ratios, which may account for the consistently higher Sr-isotope values at Skagi. Hydrothermal alteration will not significantly affect the incompatible elements used in this chapter as they are essentially immobile.

One other possible explanation for the higher Sr-isotope ratios for Skagi is to consider the small scale heterogeneous mantle model presented by Maclennan (2008a), with enriched veins in a relatively depleted ambient mantle matrix. Small degrees of melting, as predicted for Skagi (section 4.4.2), would result in a greater contribution by the enriched veins as they preferentially melt compared to the ambient mantle. Sr is slightly more incompatible than Nd, so there would be some partitioning at very small degree of melting of these enriched veins. For larger degrees of melting such as beneath the Western Volcanic Zone, the preferential melting of fusible veins deep in the mantle would not be as visible in the chemistry due to large degrees of shallow melting where both veins and ambient mantle melt would effectively drown out the deep isotope signature. Since the distinct difference shown by Skagi Sr-isotopes compared to the Western Volcanic Zone is not reflected in the Nd-isotope ratios, and could be explained by a change in the depth and degree of melting or hydrothermal alteration, it is reasonable to assume that the geochemical differences coming out of the mantle can

be attributed to variable melting processes, rather than significant changes in average mantle source composition.

The variation of TiO_2 and trace element ratios (Nb/Y, Zr/Y and Sm/Yb) with latitude (figure 4.7) for the Western Volcanic Zone show very broad decreasing trends from south to north. Data from Grímsnes is excluded as it is considered to be an off-axis centre and is compared to the young Skagi lavas in section 4.3.4. The consistently depleted samples at the southern end of the Western Volcanic Zone are from early postglacial lava shields associated with systems on the Reykjanes Peninsula which are clearly showing the geochemical signature associated with rapid decompression melting following deglaciation (Maclennan et al., 2002). These very depleted (and relatively high MgO) samples were excluded from the straight line fit. The straight line was produced using trend1d in GMT employing a robust 2-term polynomial fit. There is obviously a wide range of compositions for any particular latitude location however, there are very broad decreases in the incompatible element ratios moving northwards through the Western Volcanic Zone to central Iceland. These are more distinct in the trace element ratios as TiO_2 is also sensitive to changes in fractional crystallisation processes. Sinton et al. (2005) comments that this may result from different melting processes or a long wavelength source variation. No consistent trend is observed in the Sr and Nd isotope ratios with latitude from the Western Volcanic Zone suggesting that there is no significant horizontal variation in the average mantle source composition on a wavelength of 10's of km. This is consistent with isotopic observations from the Northern Volcanic Zone interpreted by Maclennan et al. (2001b). A crude estimate of crustal thickness variations with latitude for the Western Volcanic Zone and north towards Skagi was taken from the map presented by Darbyshire et al. (2000). The gradual increase in crustal thickness indicates a general increase in the degree of melting from south to north consistent with the observations of depleting trace elements.

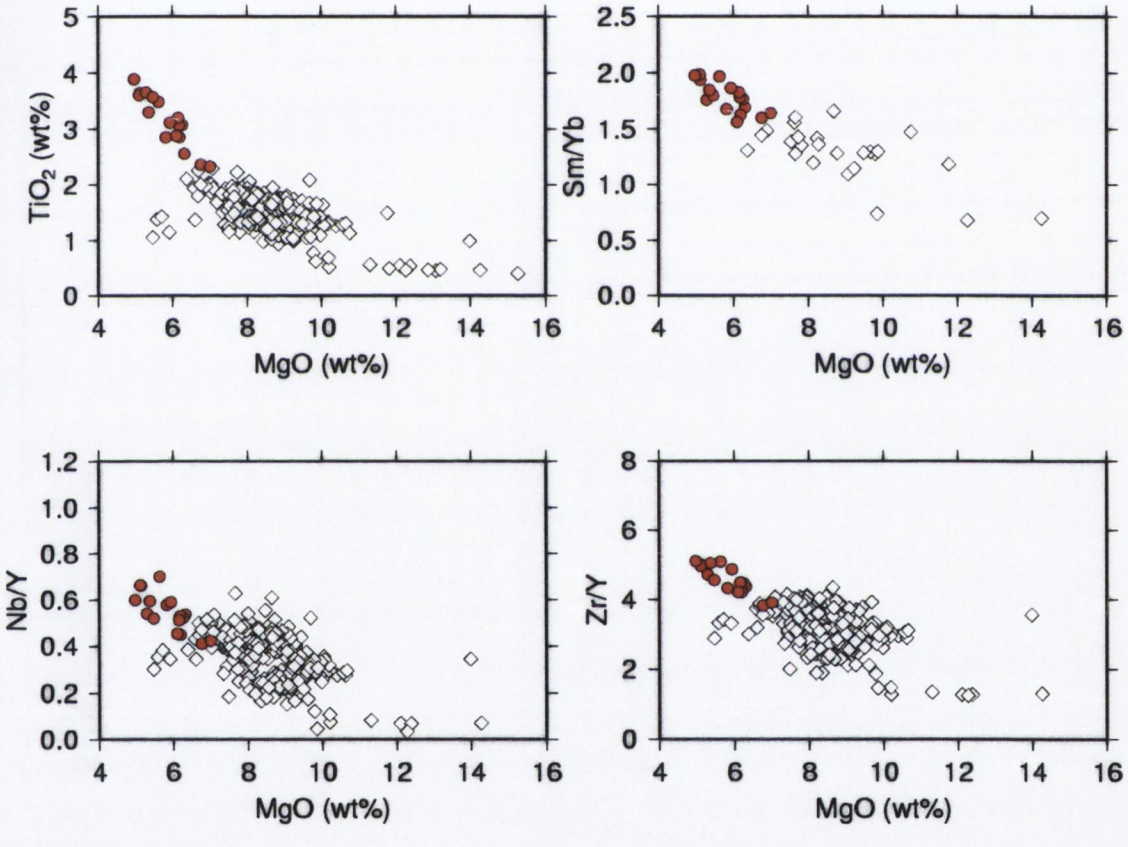

Figure 4.5: Variation diagrams for TiO_2, Sm/Yb, Nb/Y and Zr/Y to compare Skagi Quaternary lava flows (red circles) and Quaternary flows from the Western Volcanic Zone (white diamonds), excluding the Grímsnes volcanic system. No samples have less than 4 wt% MgO for Skagi and Western Volcanic Zone. Data sources are listed in table 4.1.

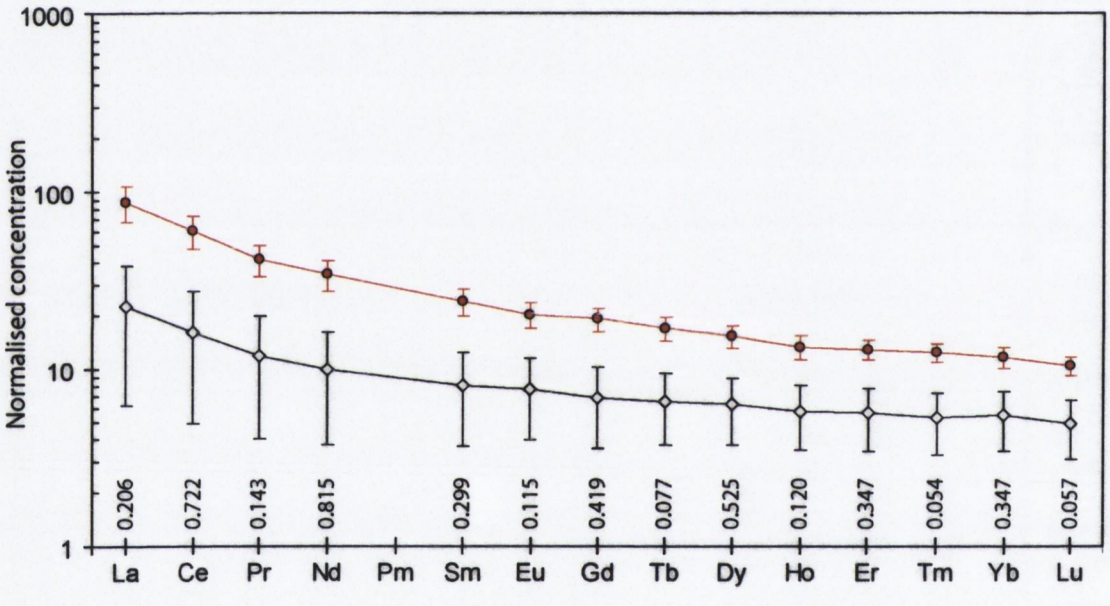

Figure 4.6: Average REE concentrations (±1 S.D.) for Quaternary lavas from Skagi (red circles; n=17) compared to the Western Volcanic Zone (white diamonds; n=20) excluding the Grímsnes system (see figure 4.6). Data for the Western Volcanic Zone from Kokfelt et al. (2006). The data set includes only basalts with greater than 4 wt% MgO. REE concentrations are normalised to MORB source mantle, McKenzie and O'Nions (1991).

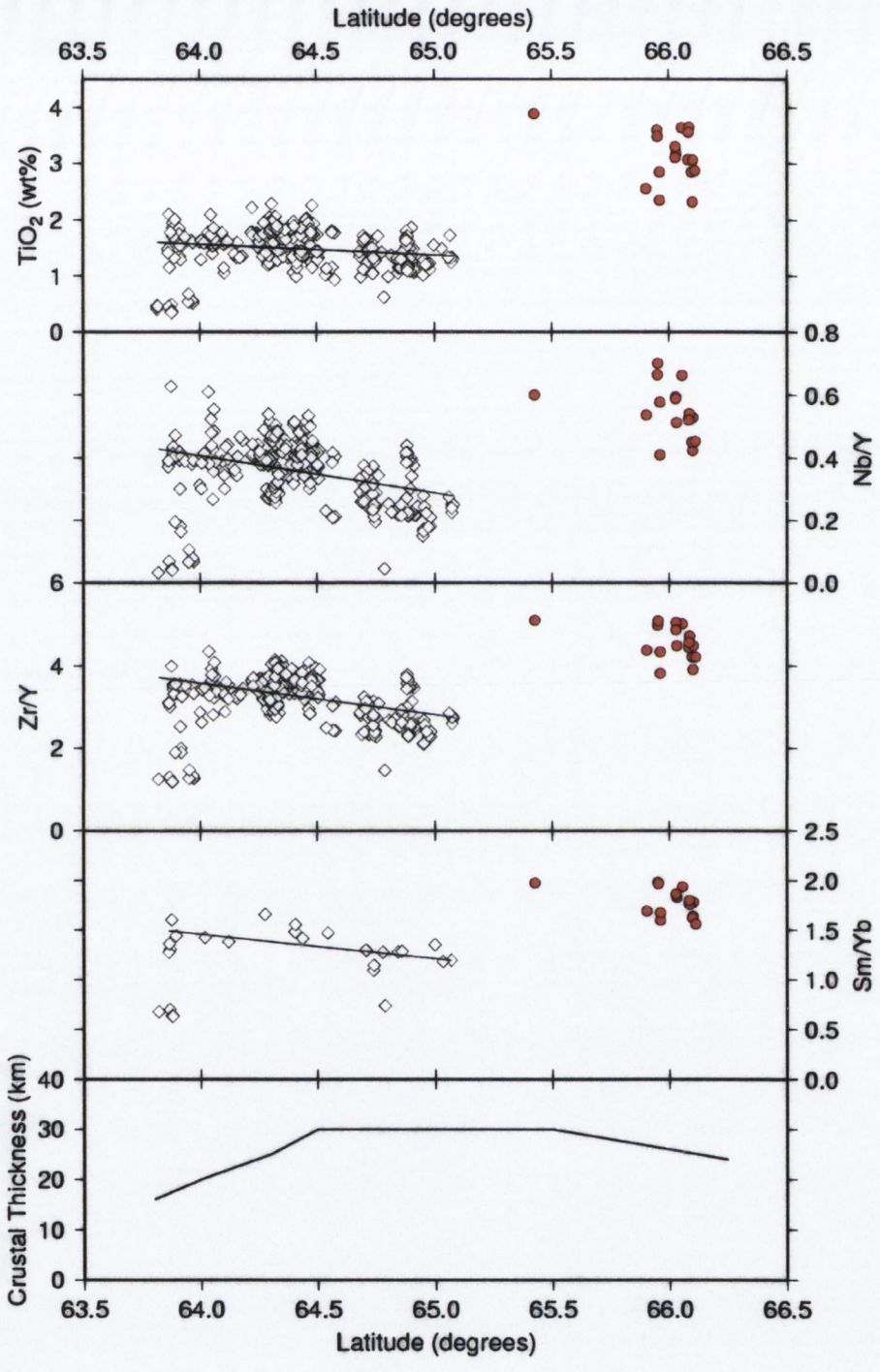

Figure 4.7: Variation of TiO_2, Nb/Y, Zr/Y and Sm/Yb with latitude for Quaternary lava flows from the Western Volcanic Zone (white diamonds) and Skagi (red circles). Crustal thickness is a crude straight line estimation from the map presented by Darbyshire et al. (2000). Data from the Grímsnes volcanic system, located off-axis, but associated with the Western Volcanic Zone is not included here, but is shown in section 4.3.4. The extremely depleted samples at the southern end of the Western Volcanic Zone are located on the Reykjanes Peninsula, from early postglacial lava shields. These depleted samples from the Reykjanes system are not included in the calculation of the trend line. The trend line is calculated using a robust straight line fit - trend1d in GMT. Data sources for the Western Volcanic Zone are listed in table 4.1.

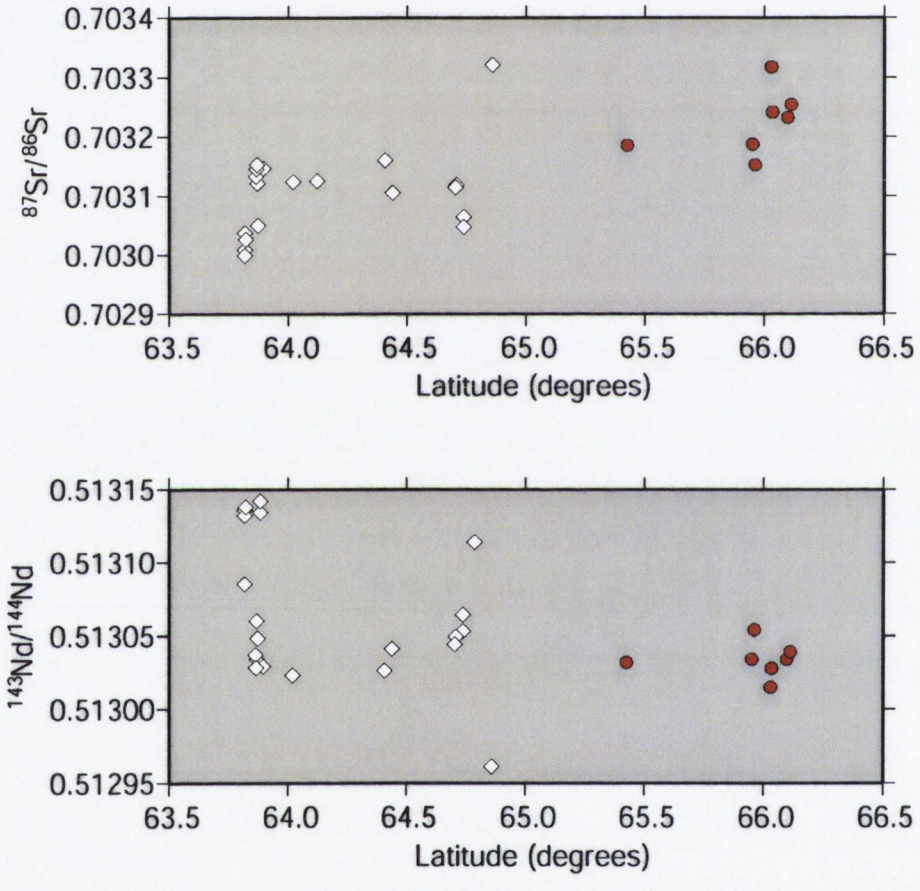

Figure 4.8: Variation of $^{87}Sr/^{86}Sr$ and $^{143}Nd/^{144}Nd$ with latitude for Quaternary lava flows from the Western Volcanic Zone (white diamonds) and Skagi (red circles). Data is whole rock and for the Western Volcanic Zone is from Kokfelt et al. (2006). The range of values for Iceland is shown in grey (Kokfelt et al., 2006).

4.3.2 Skagi versus Northern Volcanic Zone

The Northern Volcanic Zone is the only active rift at present in northern Iceland and therefore accommodates the full spreading rate of approximately 18 mm yr^{-1} (DeMets et al., 1994). Data from the Theistareykir and Krafla volcanic systems are compiled to represent the northern part of the Northern Volcanic Zone. The central Iceland part of the Northern Volcanic Zone is represented by data from Askja and Kverkfjöll systems combined with data from Herdubreid, which all show geochemical evidence of interaction with the Iceland plume. A comparison of the geochemical signature of this well developed rift with the young Skagi lavas is used to further constrain the origin of the young lavas and identify any differences in the melting regime between an established rift and possibly the death of a rift axis.

Theistareykir and Krafla

The variation of TiO_2 and trace element ratios with MgO for Theistareykir and Krafla volcanic systems are shown in figure 4.9. Maclennan et al. (2002) suggested that the higher values of MgO in postglacial samples up to 20 wt% result from accumulated olivine. The most primitive postglacial samples have less than 1 wt% TiO_2, which increases as a result of fractional crystallisation between 10 and 7 wt% MgO. These postglacial samples form relatively well defined trends for decreasing MgO for Ti and the trace element ratios, compared to the glacial samples which are much less well behaved. The bulk of the Sm/Yb data form increasing trends for decreasing MgO (10–7 wt%) for the postglacial samples. The glacial samples show a wide range of Sm/Yb values at 10 wt% MgO, with the range decreasing towards the Northern Volcanic Zone average of approximately 1.3 below 7 wt% MgO. Maclennan (2008b) suggests that this trend in glacial samples is produced by progressive mixing in magma chambers as the melt evolves from 10–7 wt% MgO. Consequently, as new postglacial melts are transported into the crust, mixing between these new melts and residual glacial melts could result in the steady increasing Sm/Yb trend for decreasing MgO from 10 to 7 wt%. In order to create this increasing trend by the assimilation of rhyolitic crust, highly enriched compositions would be required, similar to the Eastern Volcanic Zone and these have not been found in the northern part of the Northern Volcanic Zone (see figure 4.3 for evolved Northern Volcanic Zone chemistry).

Similar trends to Sm/Yb versus MgO for glacial compared to postglacial lavas are observed for Nb/Y and Zr/Y. However, the trends in Nb/Y and Zr/Y could be produced

by contamination with more evolved crust (figure 4.3). Slater et al. (1998) suggest that the trace element ratios (Nb/Y and Zr/Y) are only likely to be affected by crustal assimilation and fractional crystallisation for samples with less than 6 wt% MgO. The values observed for higher MgO are therefore, likely to reflect the range of compositions produced by mantle melting and differences in crustal storage during the glacial cycle.

As observed by Slater et al. (1998) and Maclennan et al. (2002), glacial samples show a more enriched chemistry than the postglacial samples. Glacial samples show a much greater range of TiO_2 and trace element ratio values for the same MgO composition than the postglacial samples as described previously. Young Skagi lavas plot significantly higher for Ti and trace element ratios compared to all the postglacial samples. Despite the enriched nature of the glacial lavas, young Skagi lavas still plot consistently higher in general. TiO_2 is as much as a factor of 2 higher than the most enriched glacial samples for the same MgO composition. There is some overlap with 2 glacial samples plotting well within the range of Sm/Yb values for Skagi. However, the bulk of Skagi data still plots higher than most of the glacial samples. This pattern is similar for the Nb/Y and Zr/Y ratios, with more overlap between the most enriched glacial samples and the most depleted Skagi samples.

The enriched incompatible element signature of the glacial lavas compared to the postglacial lavas is attributed to deeper melting on average for the glacial samples (Maclennan et al., 2002). The slight overlap between the glacial samples and Skagi lavas is consistent with Skagi lavas being strongly influenced by deep mantle melting within the garnet stability field. Melting at Theistareykir is estimated at approximately 22% total melting with less than a quarter of that within the garnet field, from REE inversion modelling (Maclennan et al., 2001b). This model reproduces the observed 20 km thick crust and therefore, the average geochemical signature from these systems represents the steady-state chemistry of a normal established rift at Iceland. For a discussion of the variation of Ti and trace element ratios with latitude see section 4.3.3.

The REE comparison reflects the difference in melting between Skagi and the northern part of the Northern Volcanic Zone (figure 4.10). Young Skagi lavas show greater light REE enrichment than Theistareykir and Krafla systems and higher absolute concentrations, similar to the comparison of Skagi with the Western Volcanic Zone. The light REE enrichment indicates smaller degree a significant influence of garnet field melting for Skagi Quaternary lavas; greater than the northern part of the Northern Volcanic Zone.

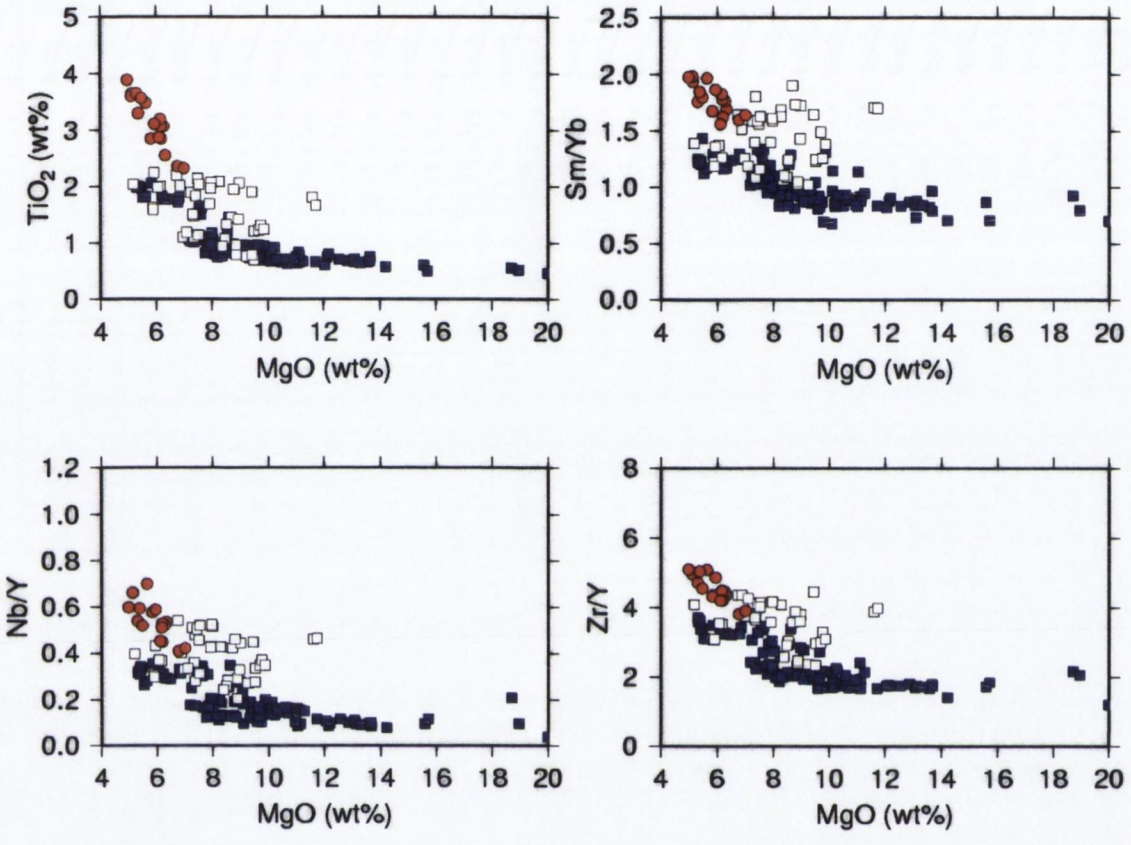

Figure 4.9: Variation diagrams for TiO_2, Sm/Yb, Nb/Y and Zr/Y to compare Skagi Quaternary lava flows (red circles) and Quaternary flows from the Theistareykir and Krafla systems, Northern Volcanic Zone (blue and white squares). Glacial age samples from Theistareykir and Krafla have been specifically highlighted as white squares; the rest of the sample are largely postglacial with only a few recent samples included. The data has been filtered to remove any sample with less than 4 wt% MgO as there are no samples for Skagi below 4 wt%. Data sources are listed in table 4.1.

Central Iceland: Askja, Kverkfjöll and Herdubreid

The bulk of the central Iceland data comes from glacial table mountains and postglacial lava shields situated up to 100 km north of the plume centre. Maclennan et al. (2001b) showed that active upwelling has significant effects on the melt chemistry in central Iceland resulting in more enriched compositions than would be expected from the large degrees of melting required to produce the 40 km thick crust. The variation of TiO_2 and trace element ratios: Nb/Y, Zr/Y and Sm/Yb with MgO for central Northern Volcanic Zone and Skagi are shown in figure 4.11.

For TiO_2 the central samples are much more consistent than the northern samples

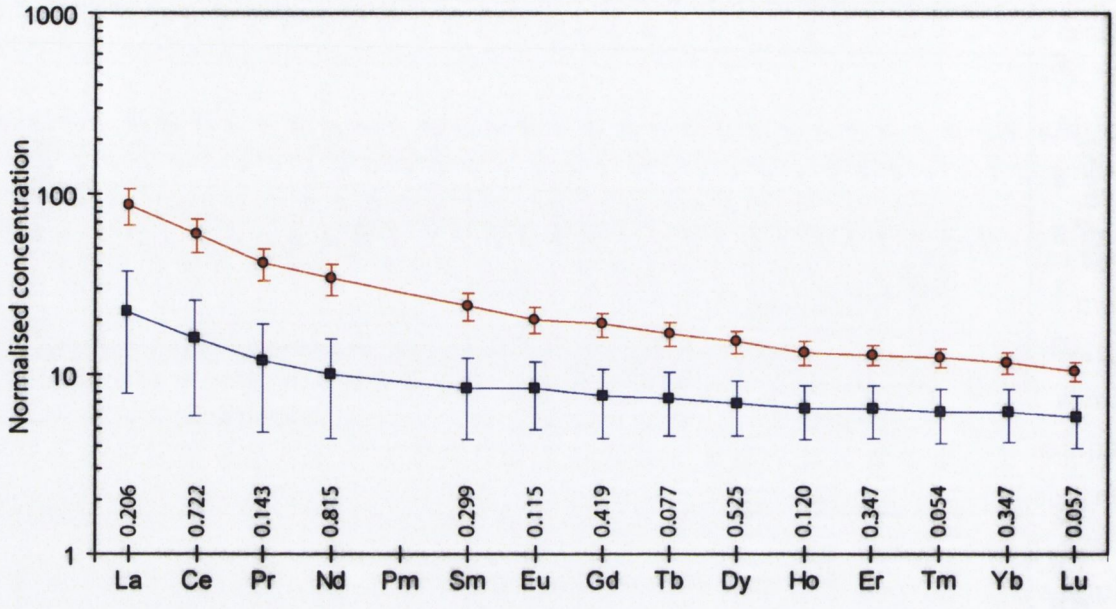

Figure 4.10: Average REE concentrations (±1 S.D.) for Quaternary lavas from Skagi (red circles; n=17) compared to the Theistareykir and Krafla volcanic systems, Northern Volcanic Zone (blue squares; n=145). Data sources for the Northern Volcanic Zone are listed in table 4.1. The data set includes only basalts with greater than 4 wt% MgO. REE concentrations are normalised to MORB source mantle, McKenzie and O'Nions (1991).

shown in figure 4.9, with less scatter in the data. Glacial and postglacial samples form similar, well constrained, increasing trends for decreasing MgO as would be expected from fractional crystallisation. Again young Skagi lavas plot consistently higher than the Northern Volcanic Zone samples, however, for central systems the maximum difference for the same MgO composition is only a factor of 1.3. This is much less than for Theistareykir and Krafla systems, where young Skagi lavas are up to a factor of 2 more enriched in TiO_2.

Significant similarities are observed for the trace element ratios, with Sm/Yb showing almost complete overlap for Skagi with the central Northern Volcanic Zone. There are clearly several early postglacial samples with low MgO and depleted Sm/Yb values; and a few high MgO glacial samples with depleted Sm/Yb compositions. The low Sm/Yb postglacial samples may be the result of crustal assimilation of rhyolitic material, however, this would cause a decreasing tail in the TiO_2 concentrations toward low MgO which is not observed. The depleted Sm/Yb values for low MgO could be produced by extensive fractional crystallisation reducing the MgO concentrations of more depleted high MgO melts, while keeping the Sm/Yb compositions the same. The depleted glacial samples are from Herdubreidatögl, described by Maclennan (2000).

The Nb/Y and Zr/Y variation diagrams show similar comparisons to the Sm/Yb values for Skagi and central Northern Volcanic Zone, with significant overlap between the zones. Only a few samples plot with higher Nb/Y at the lower MgO compositions, which may result from fractional crystallisation of clinopyroxene. The range of values for central Northern Volcanic Zone samples does extend lower than Skagi lavas which would suggest that the influence of deep mantle melting on the overall degree of melting and chemistry is not always as strong as Skagi. This is consistent with having more extensive shallow melting as well as active upwelling in the deepest parts of the melting region, as modelled by Maclennan et al. (2001b).

The REE pattern (figure 4.12) for Skagi is very similar to central Iceland, as expected from the trace element ratios. Similar light REE enrichment indicates that the strong influence of deep mantle melting predicted for central Iceland by Maclennan et al. (2001b) is also occurring beneath Skagi, but not necessarily resulting from the same process. The absolute concentrations for young Skagi lavas are higher than for central Iceland which could reflect a likely smaller degree of melting and/or greater extents of fractional crystallisation for Skagi. Maclennan et al. (2001b) conclude that up to half of the melt generation under central Iceland results from active upwelling, with the rest caused by plate-driven passive upwelling in order to reproduce the 40 km thick crust. The total degree of melting is equivalent to 35% from passive upwelling models, however, the maximum melt fraction is only approximately 25% because there is a greater flux of mantle material through the deeper parts of the melting region. The relative contribution of deep melting to the overall melting beneath Skagi is likely to be similar however, the discussion at the end of this chapter (section 4.5) considers whether this could be the result of active upwelling related to the plume.

There is no systematic difference in incompatible element enrichment observed between the glacial and postglacial samples for the same MgO composition for samples from the central Northern Volcanic Zone, as seen in the Theistareykir and Krafla samples. This observation would be consistent with the much larger degree of melting required to produce 40 km thick crust compared to the northern end of the Northern Volcanic Zone where the crust is only 20 km thick. The effects of glaciation and deglaciation on the degree and depth of melting would not have the same impact on the central Northern Volcanic Zone when the amount of melting is approximately twice that required for the Theistareykir and Krafla chemistry.

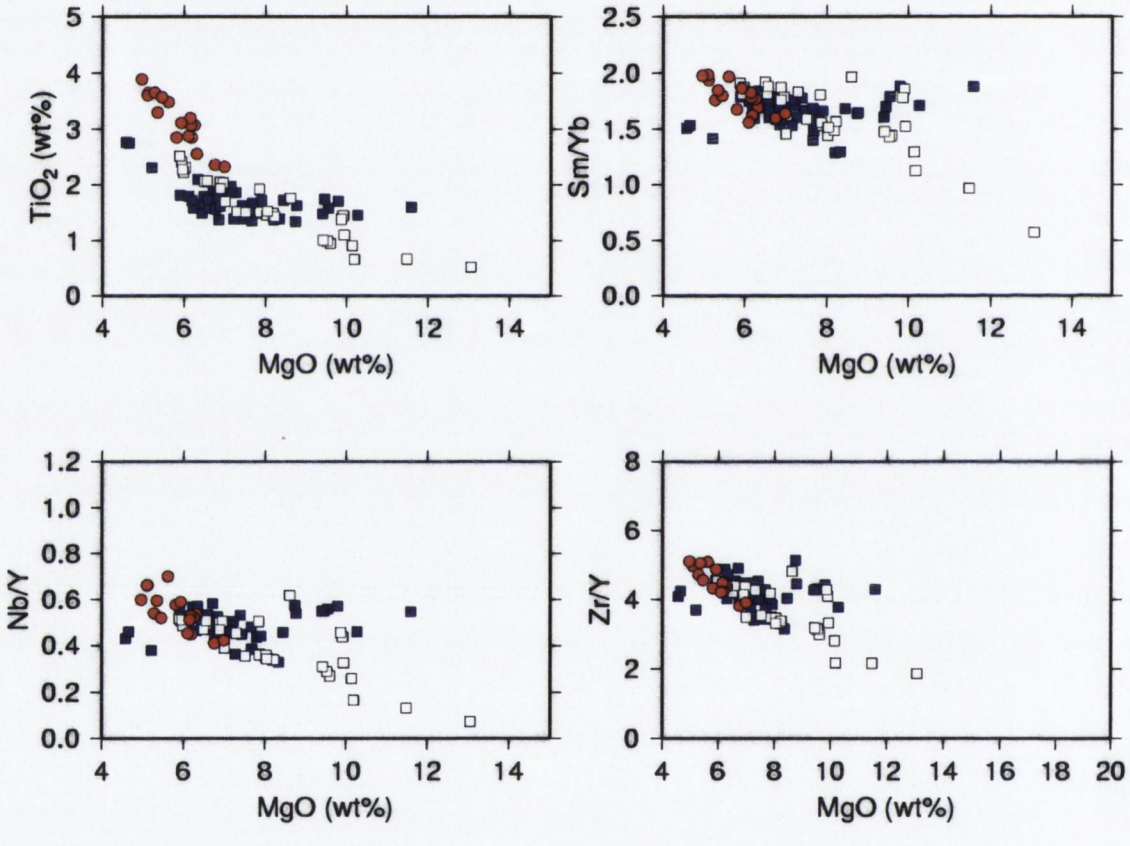

Figure 4.11: Variation diagrams for TiO_2, Sm/Yb, Nb/Y and Zr/Y to compare Skagi Quaternary lava flows (red circles) and Quaternary flows from the central systems in the Northern Volcanic Zone (blue and white squares). Glacial age samples have been specifically highlighted as white squares; the rest of the sample are largely postglacial with only a few recent samples included. The data has been filtered to remove any sample with less than 4 wt% MgO as there are no samples for Skagi below 4 wt%. Data sources are listed in table 4.1.

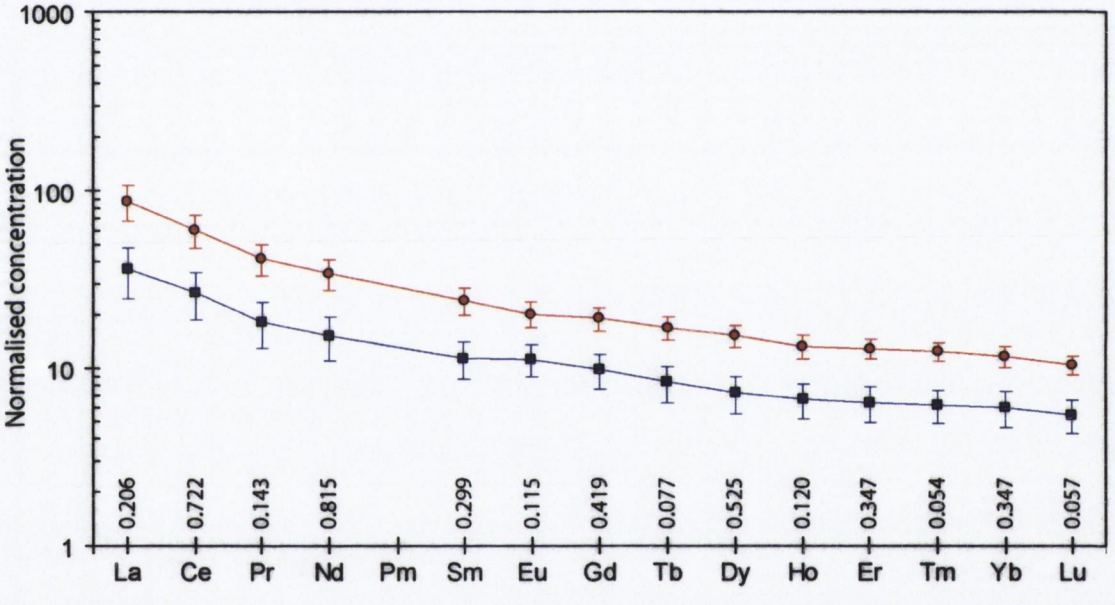

Figure 4.12: Average REE concentrations (±1 S.D.) for Quaternary lavas from Skagi (red circles; n=17) compared to the central volcanic systems (Askja and Kverkfjöll) of the Northern Volcanic Zone and Herdubreid (blue squares; n=79). Data sources for the Northern Volcanic Zone are listed in table 4.1, but a large proportion of the data is from Maclennan et al. (2001b). The data set includes only basalts with greater than 4 wt% MgO. REE concentrations are normalised to MORB source mantle, McKenzie and O'Nions (1991).

4.3.3 Skagi versus Eastern Volcanic Zone

The Eastern Volcanic Zone includes data from the following volcanic systems: Vestmannaeyjar, Eyjafjallajökull, Hekla, Katla, Grímsvötn and Bardarbunga. Similarities between Skagi and the Eastern Volcanic Zone have been noted by Schilling et al. (1978), suggesting that they were both transient rift stages. Despite the trace element similarities presented, Eastern Volcanic Zone basalts are transitional to alkaline compositions where as the young Skagi basalts are tholeiitic. It is an important observation that no alkaline volcanism is observed in association with the extinction of the Skagi Rift, discussed in section 4.5. The comparison of trace elements for Skagi and the Eastern Volcanic Zone will still highlight any similarities in the melting regimes.

The Eastern Volcanic Zone exhibits extremely high TiO_2 up to 5 wt% (figure 4.13), more enriched than the established volcanic zones (Western and Northern Volcanic Zones) and the highest values found in Iceland. For an MgO concentration of 10 wt%, the TiO_2 value is approximately 2 wt% whereas for the same MgO in the Western and Northern Volcanic Zone the average TiO_2 is approximately half the value at 1 wt%. The Skagi TiO_2 values are matched in range by the Eastern Volcanic Zone reflecting similar fractional crystallisation trends. However for the Eastern Volcanic Zone, crustal assimilation of more evolved rocks such as rhyolites (low TiO_2) has resulted in several decreasing tails towards the low MgO compositions. For the same MgO composition Eastern Volcanic Zone lavas are slightly more enriched than the young Skagi lavas by a factor of approximately 1.25.

The extremely enriched incompatible element compositions produced by the Eastern Volcanic Zone are also observed in the trace element ratios: Sm/Yb, Nb/Y and Zr/Y (figure 4.13). The range of Sm/Yb values (between 1.0 and 3.5) for a particular MgO composition is much greater than that observed for the Northern and Western Volcanic Zones where the greatest range is between 1 and 1.5 for glacial samples from Theistareykir and Krafla systems. This greater range is related to the fact that the amount of extension on the Eastern Volcanic Zone varies dramatically. The lithosphere is significantly thicker at the propagating tip in the south where the amount of extension is small compared to the northern end of the zone. The effect of a thick lithosphere on melting is discussed below. Many of the Eastern Volcanic Zone Sm/Yb values are clearly more enriched than the young Skagi lavas with up to a factor of 1.75 difference for the same MgO composition. The Skagi samples overlap with the lower Sm/Yb compositions, with only a few samples from the Eastern Volcanic Zone plotting below the lowest Skagi Sm/Yb values for the same MgO composition. The most depleted samples

from the Eastern Volcanic Zone belong to the most northerly systems (Grímsvötn and Bardarbunga) located in central Iceland. This observation is shown more clearly in figure 4.15. The amount of spreading in the northern Eastern Volcanic Zone is close to full spreading rate at Iceland and, being close to the plume centre, the melting regime is likely to be similar to that indicated by compositions from the central part of the Northern Volcanic Zone (discussed in section 4.3.2). It is very unlikely that the high Sm/Yb values for the Eastern Volcanic Zone have resulted from crustal assimilation, as no obvious trends with increasing MgO are observed (figure 4.13). Also, to produce the extreme values of Sm/Yb up to 3.5 from the Eastern Volcanic Zone, the rhyolitic assimilant would require an exceptionally enriched Sm/Yb composition which is not produced anywhere at Iceland.

Similar comparisons of Skagi and the Eastern Volcanic Zone are observed for Nb/Y and Zr/Y as for Sm/Yb. However, the Zr/Y values form a much tighter range of values for the Eastern Volcanic Zone with a maximum value only a factor of 1.4 greater than the maximum Skagi values for the same MgO composition. The Zr/Y values also show a broad increasing trend for decreasing MgO which may result from the fractional crystallisation of clinopyroxene or the crustal assimilation of rhyolite shown in the TiO_2 concentrations. More trace element compositions for evolved samples (rhyolites) would be required to illustrate which processes control the trace element ratio values.

The REE patterns for the Eastern Volcanic Zone compared to Skagi Quaternary lavas are shown in figure 4.14. The Eastern Volcanic Zone samples on average have a slightly steeper REE pattern, where although the light REE concentrations are similar to Skagi Quaternary samples, the heavy REE concentrations are significantly lower for the Eastern Volcanic Zone. This steepness indicates a greater fractionation of the heavy REEs from the light REEs for the Eastern Volcanic Zone and therefore a stronger influence of garnet field melting compared to Skagi. These observations are consistent with the more enriched chemistry interpreted from the trace element ratios.

The greater enrichment in incompatible elements and fractionation of the REEs for the Eastern Volcanic Zone compared to Skagi show that the influence of deep mantle melting is likely to be greater in the Eastern Volcanic Zone. The Eastern Volcanic Zone has similar estimated crustal thickness to the northern part of the Northern Volcanic Zone and therefore, must have a similar overall melting rate. The fact that the Eastern Volcanic Zone is dominated by transitional to alkaline volcanism compared to the solely tholeiitic volcanism of Theistareykir and Krafla indicates that there must be distinct differences in the melting regime.

Meyer et al. (1985) predicted small degrees of deeper on average melting for the Eastern Volcanic Zone, increasing as you move northwards. Furman et al. (1991) predict a maximum degree of melting of 6%, with a minimum of 1% for the propagating tip of the Eastern Volcanic Zone at Vestmannaeyjar. More recent modelling by Kokfelt et al. (2006) suggests an average of 7–8% melting for Vestmannaeyjar, with a depth range of 40–90 km. The northern end of the Eastern Volcanic Zone is within the estimated maximum 150 km radius of plume-driven active upwelling estimated by Maclennan et al. (2001b). One possibility is that a significant proportion of the melting rate is confined to deep mantle melting resulting from the fluxing of material through the deepest part of the melting region. The overall degree of melting for any packet of mantle rising through the whole melting region via plate-driven upwelling could still be relatively small. This would explain the extreme values observed for the Sm/Yb ratio and the intense light REE enrichment observed from the REE pattern. However, it is possible that the estimate for the Eastern Volcanic Zone by Darbyshire et al. (2000) may be too high as it is not constrained by a seismic refraction profile as for the Northern Volcanic Zone. The low degrees of melting predicted for the Eastern Volcanic Zone suggest that the real crustal thickness is much smaller. It may be the case that the average 20 km thick crust remains from before the propagation of the Eastern Volcanic Zone, with a limited amount of extension across the Eastern Volcanic Zone, particularly near the propagating tip where the spreading rate at present is approximately 8 mm yr^{-1} (LaFemina et al., 2005). The enriched incompatible element signature would in that case result from smaller degree melting with a stronger influence of deep mantle melting compared to Skagi. Large scale crustal redistribution via lower crustal flow for example, could also explain thicker than expected crust (Jones and Maclennan, 2005).

The variation of Ti and trace element ratios with latitude for the Northern and Eastern Volcanic Zones is shown in figure 4.15. A crude estimate of crustal thickness variation with latitude is provided from Darbyshire et al. (2000). The crustal thickness is well constrained beneath central Iceland and northern Iceland where the seismic refraction profiles FIRE and ICEMELT intersect the Northern Volcanic Zone (figure 4.1). The exact variation outside of these locations is not well constrained, but is useful for broad trends in the crustal thickness. The straight lines for composition were produced using trend1d in GMT employing a robust 2-term polynomial fit to give an indication of the average compositional variation along the volcanic zone. There is a wide range of compositions for any particular latitude location so these observations and associated interpretations are very tentative particularly for the Eastern Volcanic Zone where

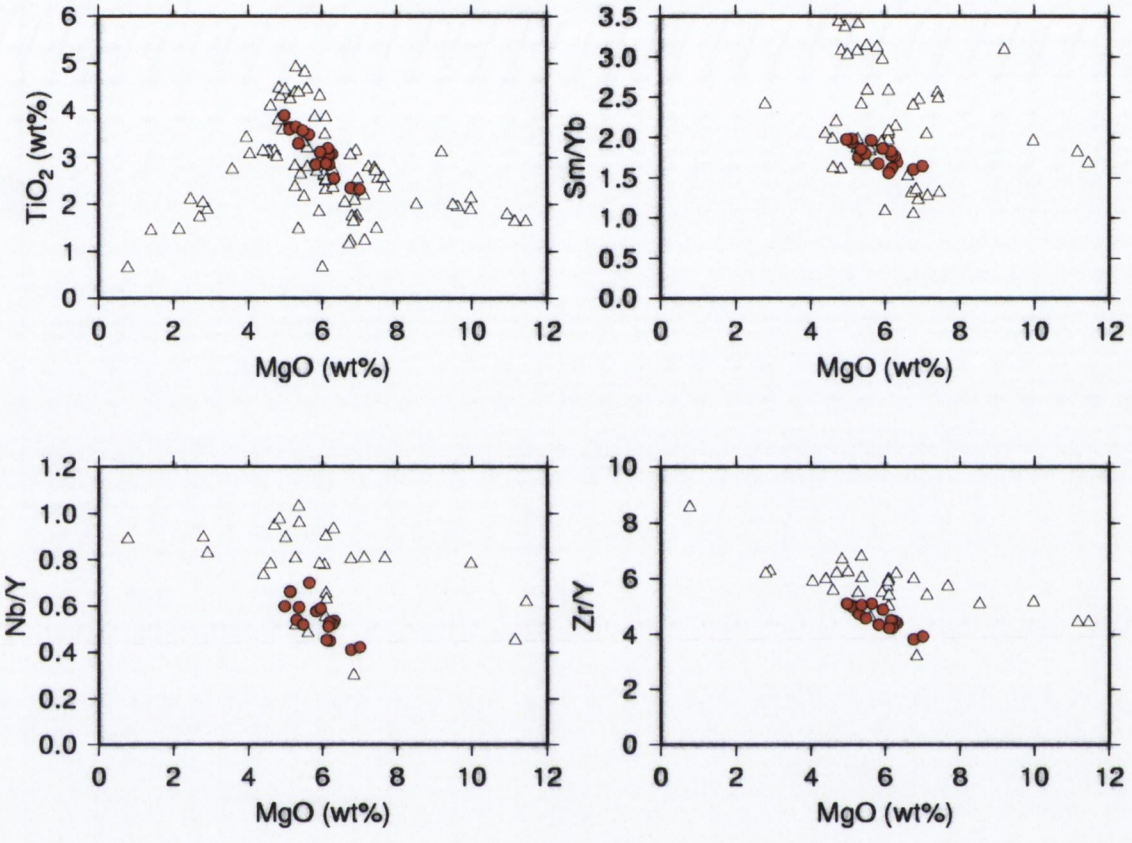

Figure 4.13: Variation diagrams for TiO_2, Sm/Yb, Nb/Y and Zr/Y to compare Skagi Quaternary lava flows (red circles) and Quaternary flows from the Eastern Volcanic Zone (white triangles). Rhyolitic and andesitic compositions are included for the Eastern Volcanic Zone so that any trends that may result from difference in crustal assimilation rather than melting can be identified. Data sources are listed in table 4.1.

the greatest scatter is observed and more data would be essential to make robust conclusions.

There are very broad increases in incompatible element enrichment towards the centre of Iceland along the Northern Volcanic Zone. This trend is shown particularly well by the trace element ratios and correlates with a significant increase in crustal thickness from 20 km to 40 km. This correlation is opposite to the Western Volcanic Zone where depletion is observed for greater crustal thicknesses. The relatively enriched compositions for higher melting rates beneath central Iceland are attributed to the flux of mantle material through the deepest parts of the melting region by active upwelling from the plume, as previously discussed (Maclennan et al., 2001b). These increases are unlikely to be the result of gradual source variation through the Northern

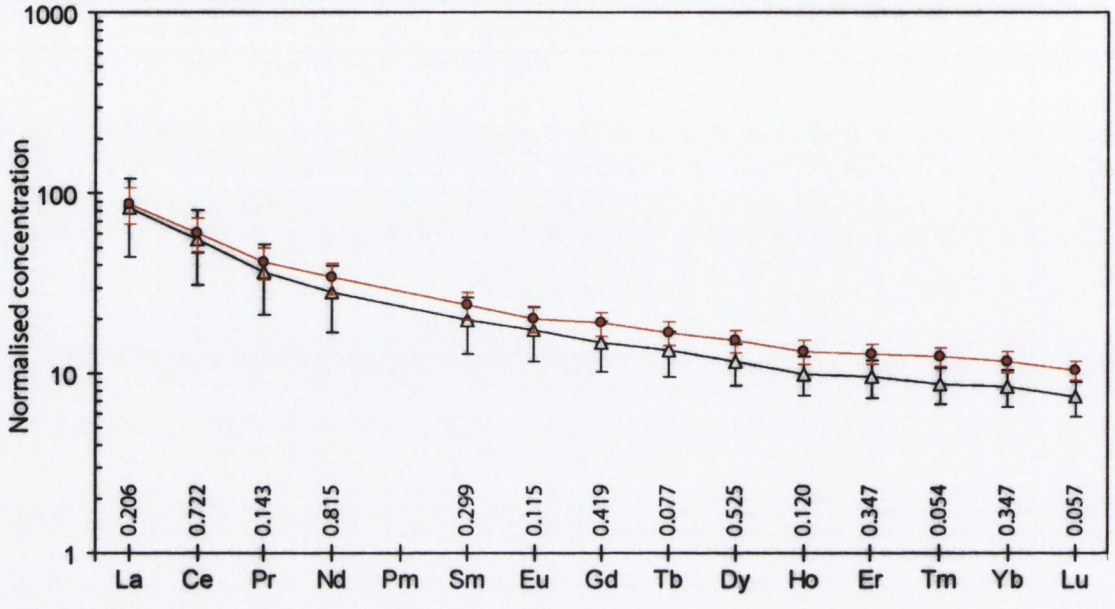

Figure 4.14: Average REE concentrations (±1 S.D.) for Quaternary lavas from Skagi (red circles; n=17) compared to the Eastern Volcanic Zone (white triangles; n=26). Data sources for the Eastern Volcanic Zone are listed in table 4.1. The data set includes only basalts with greater than 4 wt% MgO. REE concentrations are normalised to MORB source mantle, McKenzie and O'Nions (1991).

Volcanic Zone as no systematic variation in the Sr and Nd-isotope ratios with latitude is observed (Maclennan et al., 2001b; figure 4.16).

The correlation of geochemistry with latitude for the Eastern Volcanic Zone is very poor for TiO_2, Nb/Y and Zr/Y. Any differences in these values created by mantle melting processes are likely to have been over-printed by crustal processes following the behaviour with variation in MgO (figure 4.13). However, Sm/Yb shows a distinct and significant increase in enrichment from central Iceland towards the southern end of the Eastern Volcanic Zone. This has also been observed by Sigmarsson et al. (2008). This is correlated by a decrease in the crustal thickness from 40 km to 20 km. From the previous discussion it is not clear whether the melting rate at the Eastern Volcanic Zone could produce the observed crustal thickness, however the enriched compositions are as expected for a decrease in the crustal thickness requiring smaller degrees of melting. The extreme Sm/Yb compositions produced at the propagating tip are clearly the result of very small degrees of melting, as predicted by Furman et al. (1991), Meyer et al. (1985) and Kokfelt et al. (2006). The lithosphere is much thicker at the propagating tip compared to the northern part of the Eastern Volcanic Zone because the spreading rate is significantly less. Using GPS measurements, LaFemina et al. (2005) observed a

steady decrease in the spreading rate from 19±2 mm yr^{-1} in the northeast to 8 mm yr^{-1} near the propagating tip (Vestmannaeyjar system, figure 4.1). Thicker lithosphere results in deeper melting and therefore, a stronger influence of garnet field melting.

The Sm/Yb values near central Iceland for the Eastern Volcanic Zone have a similar range to those from the southern (central) part of the Northern Volcanic Zone. It is likely that melting at the top of the Eastern Volcanic Zone is affected by active upwelling in a similar way to the central Northern Volcanic Zone, discussed in section 4.3.2.

Overall the Eastern Volcanic Zone compositions are more enriched than the Northern Volcanic Zone suggesting a smaller degree of melting and greater extent of fractional crystallisation (Meyer et al., 1985). The higher trace element ratios are consistent with a greater influence of deep mantle melting on the total melt fraction compared to the Northern Volcanic Zone.

Figure 4.16 shows the variation of Sr and Nd isotope ratios with latitude for the Eastern and Northern Volcanic Zones. There is no systematic variation in the isotope ratios for the Northern Volcanic Zone. Maclennan et al. (2001b) suggest that the simplest interpretation of this lack of variation is that over a scale of 10's of km there is little change in the average composition of the mantle source. More recent work suggests that the mantle is heterogeneous on small length scales (Maclennan, 2008a), however extensive mixing of melts in the crust results in constant range of isotope ratio values produced at the Northern Volcanic Zone (Maclennan, 2008b).

There are not enough samples for the Eastern Volcanic Zone to make a reasonable conclusions about the variation of the isotopic ratios. It appears as though Sr isotope ratios do not show any systematic variation with latitude. However, Nd isotope ratios seem to decrease towards the southern end of the Eastern Volcanic Zone i.e. the propagating tip, indicating that melting of a more enriched source may be contributing to the enriched trace element compositions as described above. The Sr isotope ratios will be preferentially affected by hydrothermal alteration and interaction with hydrothermally altered crust compared to Nd isotope ratios. This may explain why no systematic variation is observed in the Sr isotope ratios. All the samples except 1 from the Northern Volcanic Zone lie within the Icelandic range: $^{87}Sr/^{86}Sr$: 0.7028–0.7037; $^{143}Nd/^{144}Nd$: 0.51289–0.51308 (Kokfelt et al., 2006). The enriched Nd isotopic ratios found at the propagating tip of the Eastern Volcanic Zone are also observed in the Northern Volcanic Zone. Following these two observations the trend observed in the

Eastern Volcanic Zone is consistent with a heterogeneous mantle on relatively small length scales (Maclennan, 2008a). The degree of melting in the Eastern Volcanic Zone is so small that only the enriched and fusible areas of the mantle are melted, where as in the more established Northern Volcanic Zone both enriched and depleted mantle materials are melted to produce a wide range of isotopic values.

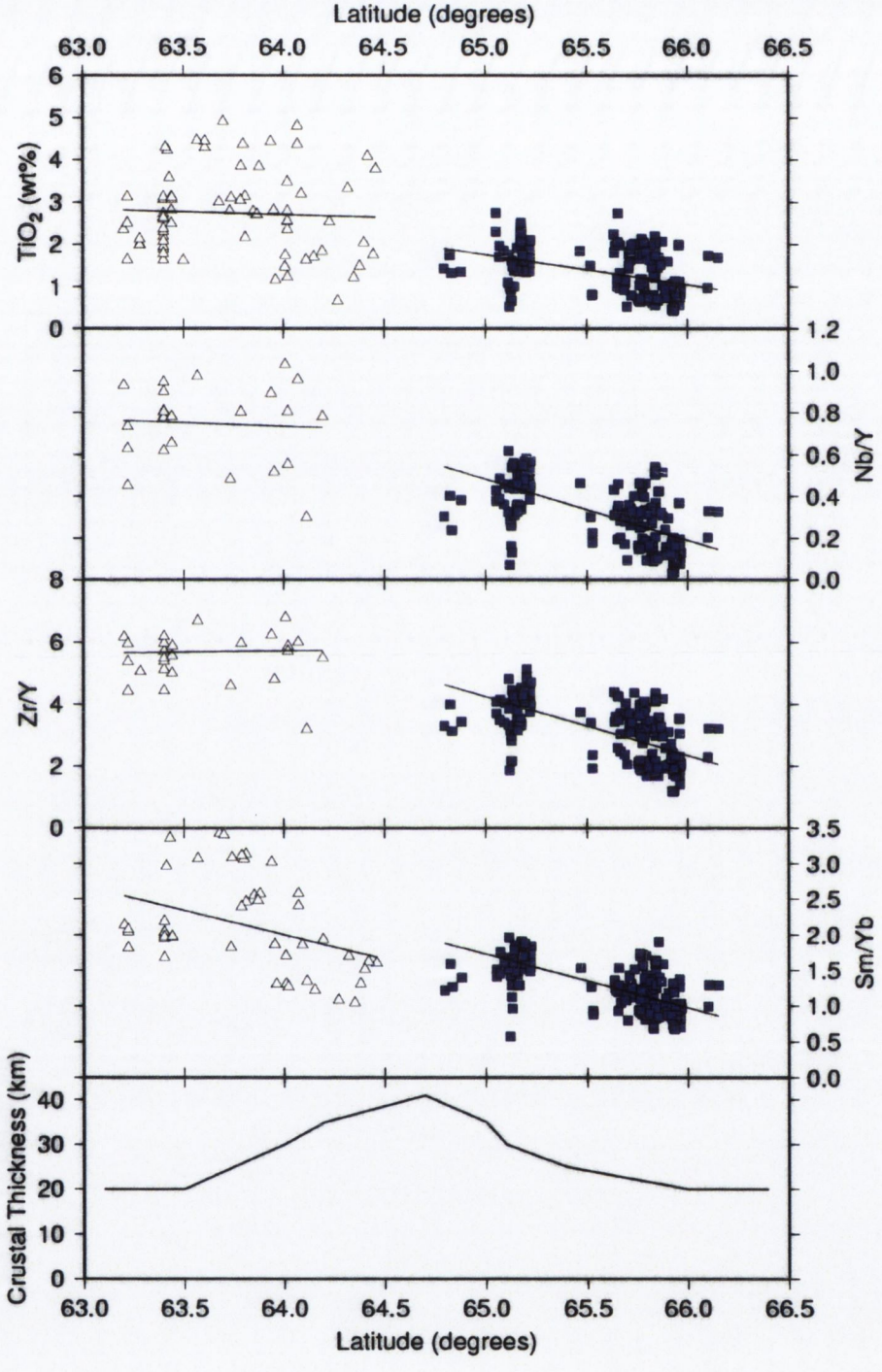

Figure 4.15: Variation of TiO_2, Nb/Y, Zr/Y and Sm/Yb with latitude for Quaternary lava flows from the Theistareykir and Krafla systems, Northern Volcanic Zone (blue squares) and Quaternary lava flows from the Eastern Volcanic Zone (white triangles). The data has been filtered to remove any sample with less than 4 wt% MgO so that comparisons are restricted to basaltic compositions. Crustal thickness is a crude straight line estimation from the map presented by Darbyshire et al. (2000). The trend line is calculated using a robust straight line fit - trend1d in GMT. Data sources are listed in table 4.1.

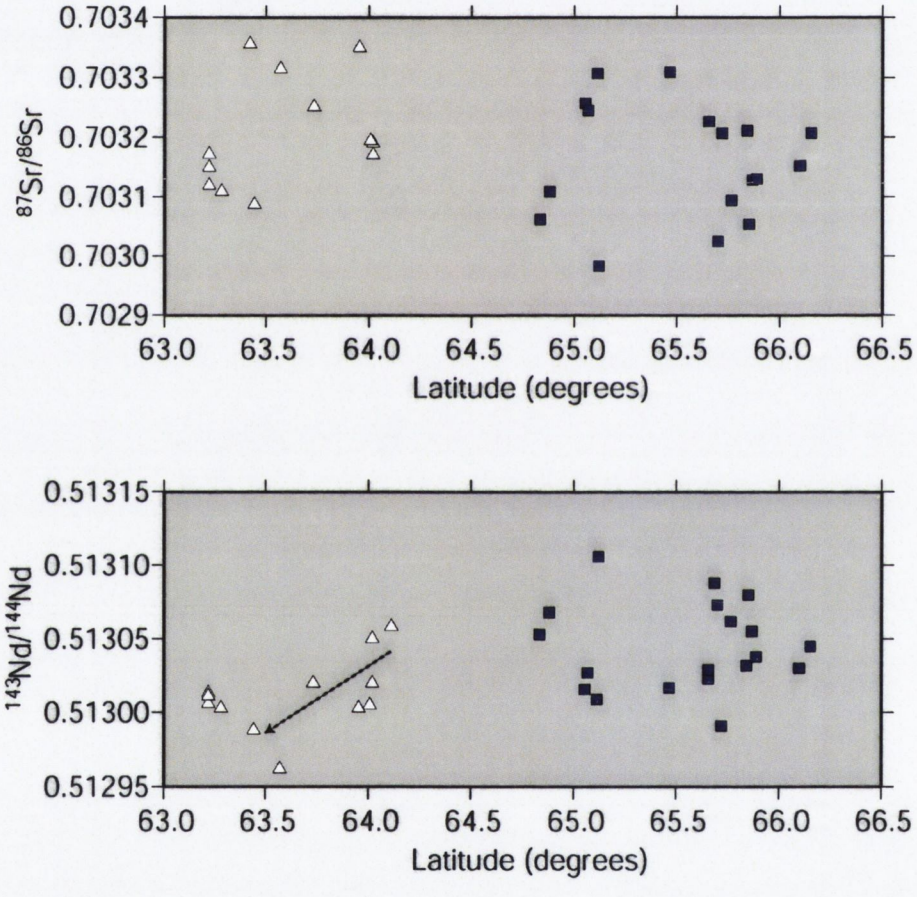

Figure 4.16: Variation of $^{87}Sr/^{86}Sr$ and $^{143}Nd/^{144}Nd$ with latitude for Quaternary lava flows from the Northern Volcanic Zone (blue squares) and Eastern Volcanic Zone (white triangles). Data is whole rock and sources are listed in table 4.1. The range of values for Iceland is shown in grey (Kokfelt et al., 2006).

4.3.4 Skagi versus Off-axis Volcanism

Young Skagi lavas are clearly associated with an extinct rift axis, however a useful comparison can be made with present off-axis and flank zone volcanism as the Skagi lavas may have an off axis signature if they were not related to the main active rifts at the time. Three features considered to be off-axis or flank zones are used for comparison with Skagi: Grímsnes volcanic system, Snaefell volcanic centre and Snaefellsnes Volcanic Zone. These areas are situated progressively further off-axis.

Grímsnes is a very small volcanic system located approximately 15 km east of the main volcanic systems of the Western Volcanic Zone. Off-axis volcanism is commonly associated with alkaline basalt compositions, however, Grímsnes is tholeiitic like the young Skagi lavas. The geochemical signature of Skagi lavas compared with Grímsnes is shown in figure 4.17. Similar to the Western Volcanic Zone as a whole, the MgO composition of the Grímsnes samples is higher than Skagi and over a limited range (8–10 wt%). This distinction between the MgO compositions of the most primitive lavas from each series indicates that the crustal processes may be slightly different.

However, the range of values for the Nb/Y and Zr/Y trace element ratios is very similar to young Skagi lavas suggesting that the average depth of melting relative to the degree of melting is similar. Only one sample from Grímsnes has REE data with MgO, which is more enriched than the Skagi samples and if more samples were consistent with that observation that would probably indicate more garnet field melting relative to the overall degree of melting compared to Skagi. There are a few samples plotting with very slightly higher Nb/Y and Zr/Y ratios. Crustal assimilation of rhyolitic material could not have produced the higher values for Grímsnes as that process would also result in a trend towards lower MgO compositions which is clearly not observed. The TiO_2 concentrations are much lower as would be expected for more primitive melts. Fractional crystallisation models of Grímsnes primitive high MgO composition would reproduce Skagi values as magmas evolve to lower MgO. It is reasonable to expect that, like the rest of the Western Volcanic Zone, Grímsnes lavas have not been subject to the same extents of fractional crystallisation as the rest of Iceland. Grímsnes lavas could result from melt from the corners of the melting region being transported to the surface without mixing with melt fractions from higher up in the centre of the melting region (figure 4.18). The similarity in enrichment of incompatible elements between the Grímsnes off-axis volcanism and young Skagi lavas may suggest that Quaternary volcanism on Skagi is not produced by normal axial melting regimes.

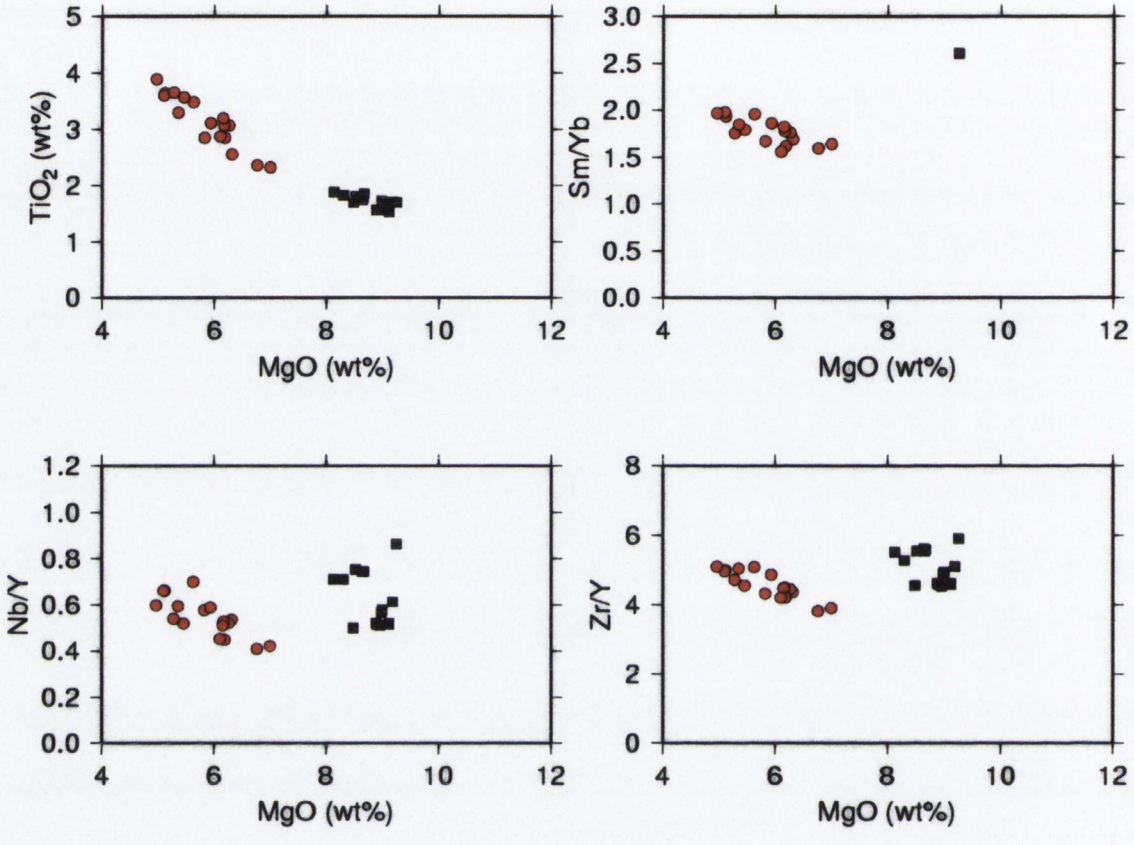

Figure 4.17: Variation diagrams for TiO_2, Sm/Yb, Nb/Y and Zr/Y to compare Skagi Quaternary lava flows (red circles) and Quaternary flows from the off-axis Grímsnes system in the Western Volcanic Zone (black squares). No samples have less than 4 wt% MgO for Skagi and Grímsnes. Data sources are listed in table 4.1.

Snaefell is a volcanic centre located in central-east Iceland at the northern tip of a flank volcanic zone known as the Öraefajökull Volcanic Zone. It is situated approximately 25 km off-axis from the edge of the Northern Volcanic Zone. Snaefell has bi-modal volcanism with mildly alkaline basalt flows and a significant amount of rhyolitic volcanism, approximately 10% of the whole suite (Hards et al., 2000). The variations of TiO_2 and trace element ratios with MgO for Skagi Quaternary lavas and Snaefell lava flows are presented in figure 4.19. Snaefell and Skagi basalts have similar TiO_2 concentrations for the same MgO compositions, with patterns clearly controlled by fractional crystallisation. However, there are several samples producing descending tails towards low Mg and low Ti rhyolitic composition showing clear evidence of some mixing or crustal assimilation as observed by Hards et al. (2000) from the isotopic characteristics. The higher range of MgO values for the most primitive lavas produced by Snaefell indicates that the parent magmas are probably the result of a greater overall degree of melting

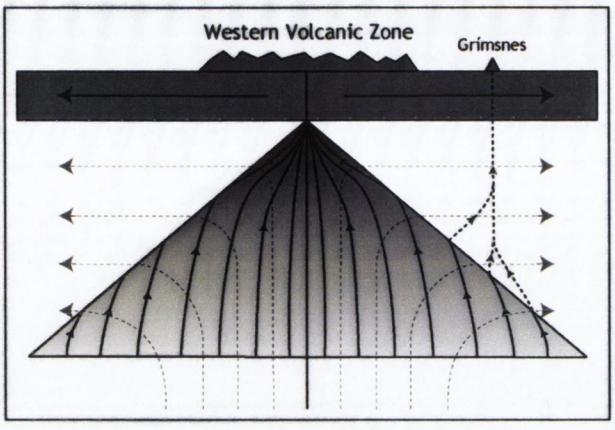

Figure 4.18: A sketch of how melt transport beneath the Western Volcanic Zone could result in off-axis volcanic activity at Grímsnes. The dashed arrows indicate the flow of the mantle through the melting region. The solid melt flow lines within the melting region are based on a model of melt transport by Spiegelman and McKenzie (1987). The transport of melt through the lithosphere from the outer corners of the melting region may be very complex in reality due to extension.

than the young Skagi lavas.

There are a wide range of trace element ratio values with a distinctly low group at MgO compositions similar to the Skagi range of MgO: 7–4 wt%. These low concentrations must be coming out of the mantle as they do not correlate with the samples affected by crustal assimilation observed from the TiO_2 trends. However, observing the average range of trace element composition at any particular MgO composition (except the relatively small group of depleted samples) it is consistently higher than the young Skagi lavas. The highest trace element ratio values for the same MgO compositions as Skagi are between 1.25 (Sm/Yb) and 1.7 (Nb/Y) times higher for Snaefell suggesting that the percentage of deep mantle melting beneath Snaefell, relative to the total melt fraction, is greater than Skagi. The Snaefell trace element compositions are very similar to the Eastern Volcanic Zone as would be expected from their tectonic situations as an incipient rift and propagating rift respectively. The mantle at Snaefell will be well within the maximum 150 km sphere of influence of active upwelling driven by the plume and this would have significant effects on the incompatible element chemistry as discussed in section 4.3.3.

Snaefellsnes Volcanic Zone is the furthest off-axis, situated a minimum of 50 km from the nearest axial zone and is the largest off-axis feature on Iceland consisting of three individual volcanic systems. The incompatible element comparison with young Skagi lavas is shown in figure 4.20. Significantly more data exists for the Snaefellsnes Volcanic Zone and further compilation of published data is required to establish any distinct

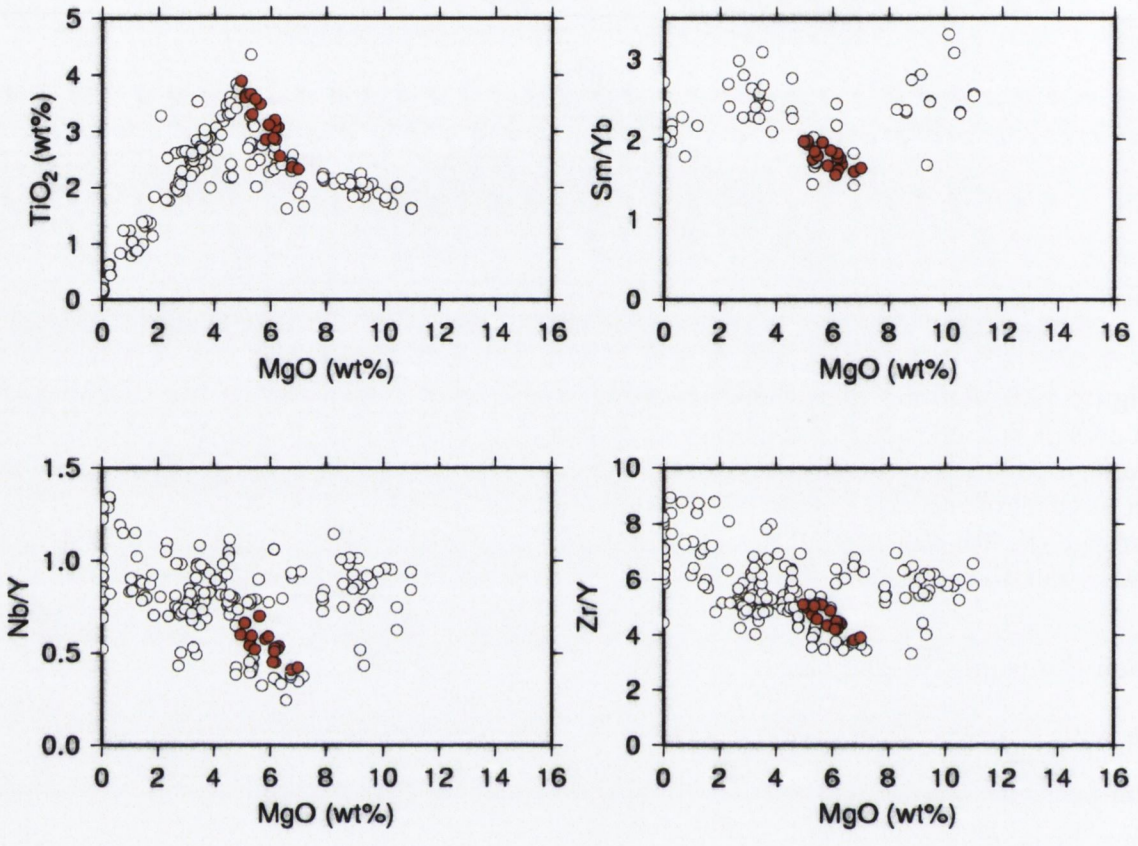

Figure 4.19: Variation diagrams for TiO_2, Sm/Yb, Nb/Y and Zr/Y to compare Skagi Quaternary lava flows (red circles) and Quaternary flows from Snaefell volcanic centre (white circles), located at the northern end of the Öraefajökull Volcanic Zone. Data sources are listed in table 4.1.

trends, however, the main purpose of this comparison is to establish if there is any similarity with young Skagi lavas. TiO_2 concentrations form a general increasing trend for decreasing MgO, but is not as well defined as the trend in the Skagi lavas. For the same MgO composition the TiO_2 concentration is similar for Skagi and Snaefellsnes. The trace element ratios plot consistently higher for the same MgO compositions for Snaefellsnes compared to Skagi except for two Snaefellsnes samples with depleted Zr/Y compositions at 4–5 wt% MgO. For Nb/Y, Snaefellsnes samples are up to 4 times more enriched. Sm/Yb and Zr/Y are up to 1.4 times more enriched for Snaefellsnes compared to Skagi. Kokfelt et al. (2006) modelled Snaefellsnes melting with a very limited depth range between 50 and 80 km of a small scale heterogeneous mantle, all within the presence of garnet bearing source material. Young Skagi lavas are not as enriched as Snaefellsnes lavas in general and therefore, Snaefellsnes lavas may result from slightly smaller degrees of melting compares to Skagi.

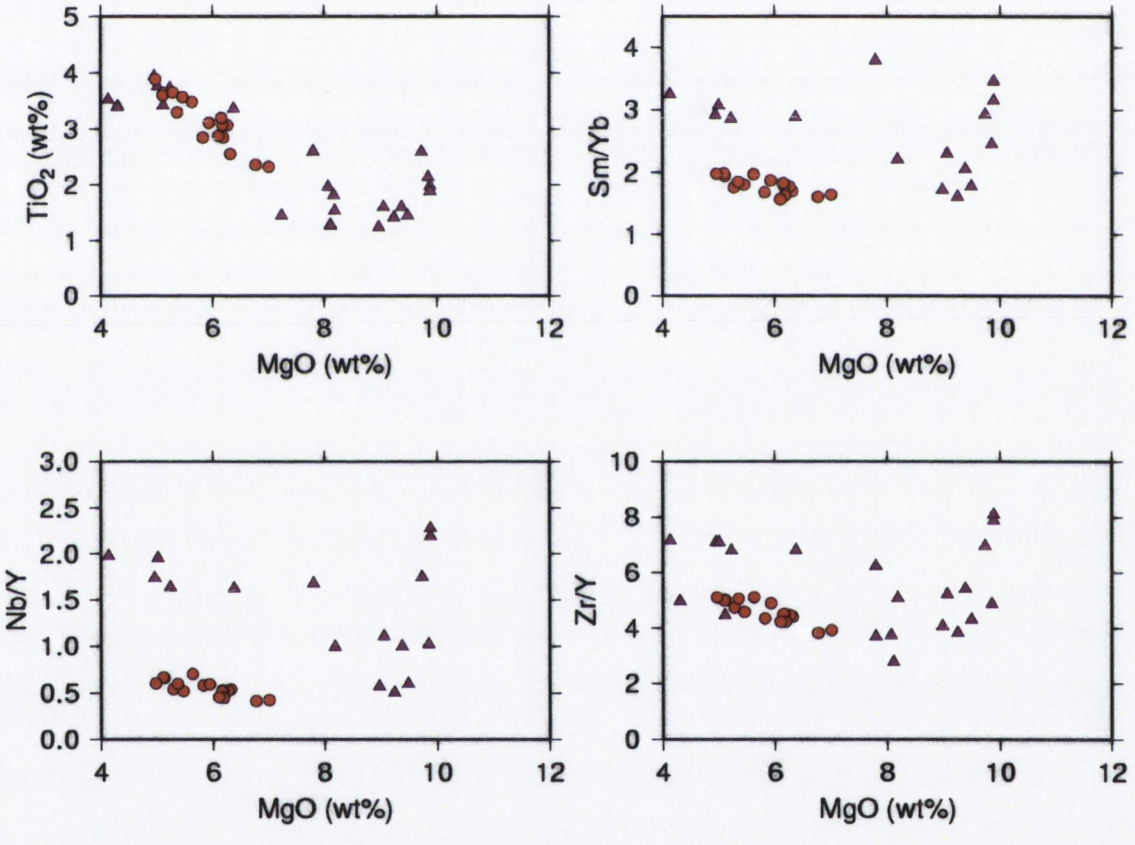

Figure 4.20: Variation diagrams for TiO_2, Sm/Yb, Nb/Y and Zr/Y to compare Skagi Quaternary lava flows (red circles) and Quaternary flows from Snaefellsnes Volcanic Zone (purple triangles). Snaefellsnes samples are filtered to exclude samples with less than 4 wt% MgO as these evolved compositions are not comparable to the Skagi range of MgO compositions. Data sources are listed in table 4.1.

4.4 REE Inversion Modelling

4.4.1 Background

The REE inversion model of McKenzie and O'Nions (1991) is used to investigate the mantle melting behaviour associated with the geochemistry of young Skagi lavas. Under the assumption of passive upwelling at a mid-ocean ridge, their model allows the prediction of crustal thickness given REE concentrations. This section will provide an introduction to the main theories and variables used in the model. For full details of the mathematical theory refer to McKenzie and O'Nions (1991) and White et al. (1992). The model predicts the melt fraction against depth relationship, $X(z)$, for fractional melting of a constant homogenous mantle source. The computer program is known as INVMEL, written by D. McKenzie. An algorithm is used to find $X(z)$ by minimising the misfit between observed and calculated normalised REE concentrations. The melt fraction is calculated at given number points at 10 km intervals. Smoothing methods are used to limit the melt fraction against depth profile estimates to physically reasonable forms with melt fractions between 0 and 1.

There are several independent variable inputs to the model which must be considered. The composition of the mantle source is the most poorly constrained. In reality, the mantle beneath Iceland is almost certainly heterogeneous on small length scales (e.g. Maclennan, 2008a). However, the inversion model is restricted to a homogenous source composition and the best estimate is probably a mixture of primitive mantle and depleted MORB source, defined by the average ε_{Nd} value (White and McKenzie, 1995). The more enriched the source composition the greater the melt fraction required to reproduce the observed REE concentrations.

The partition coefficients determine the trace element concentration in the melt according to the mineral phase assemblage in the mantle. For simplicity, the bulk partition coefficient for a trace element is constant in the INVMEL program. In reality partition coefficients may vary with pressure, temperature and composition of melt or crystal, however, McKenzie and Blundy (1999) showed that the use of variable partition coefficients in an inversion model does not have a significant effect on the predicted melt fraction against depth relationship (Maclennan, 2000).

The final independent variable is the spinel-garnet transition depth. This variable simply influences the absolute depth of melting and does not affect the overall degree

of melting or the proportion of melt within the garnet stability field predicted by the REE inversion. McKenzie and O'Nions (1991) use a transition range of 60–80 km for a mantle potential temperature of 1300°C and 80–100 km for a potential temperature of 1500°C. The mantle potential temperature at Iceland is approximately 1500°C (White et al., 1995) so 80–100 km transition range is used for Skagi REE inversions.

The final melt fraction versus depth profile is dependent on the initial melting model employed to run the inversion. The execution of the INVMEL program is repeated with various reasonable initial melting models, based on geochemical observations until a very good fit is achieved for the final melting profile and the associated fit to REE observations. The compositions are based on a point and depth average calculation; the mean composition of all the melt extracted from the melting region. An assumption is made that lavas represent the combination of all melt fractions from the whole of the melting region. The geophysical model assumed by McKenzie and O'Nions (1991) and White et al. (1992) is that melting is the result of passive upwelling. This may not be the case for Skagi, therefore the model results are simply considered as an indication of the degree of melting and the contribution of melting within the garnet field. The final consideration is the correction of the final melt fraction profile and REE concentrations for fractional crystallisation. INVMEL bases fractional crystallisation correction on the Mg and Fe compositions of the observed lavas and the predicted melt compositions. Therefore the inversion only predicts the amount of olivine and clinopyroxene fractionation. The amount of plagioclase fractionation is not accounted for, however the influence of plagioclase fractionation on melt composition is minimised by modelling reasonably mafic magmas. Accounting for plagioclase fractionation would be considerably more important for acidic magmas.

4.4.2 Application to Skagi

The McKenzie and O'Nions (1991) REE inversion model was run for all Skagi data with more than 4wt% MgO. There is little difference in the REE pattern between the Tertiary and Quaternary data as shown in section 3.5. The garnet stability field is set according to mantle potential temperature estimated at 1500°C for Iceland corresponding to a garnet-spinel transition at 80–100 km. The source composition used is primitive mantle, the most enriched source possible resulting in the largest degree of melting possible to reproduce the Skagi REE concentrations. Depth to the top of the melting region is set to 56 km, well below the base of the crust. This value is

comparable with the predicted depth to the top of the melting region during the final stages of decline of the rift (section 7.5). The final melting model as a melt fraction versus depth profile is shown together with the final fit to the REE concentrations in figures 4.21 and 4.22. The inversion predicts a total degree of melting of approximately 1.4% with about one third of that melting occuring within the garnet stability field. This is consistent with the geochemical observations from comparisons presented and discussed in section 4.3. However, the resulting estimate of crustal thickness of approximately 1.5 km is not consistent with the observed 25–30 km thick crust. This mis-match is discussed in section 4.5. The dip in the curve around 90 km results from the smoothing constraints and is not significant in real terms.

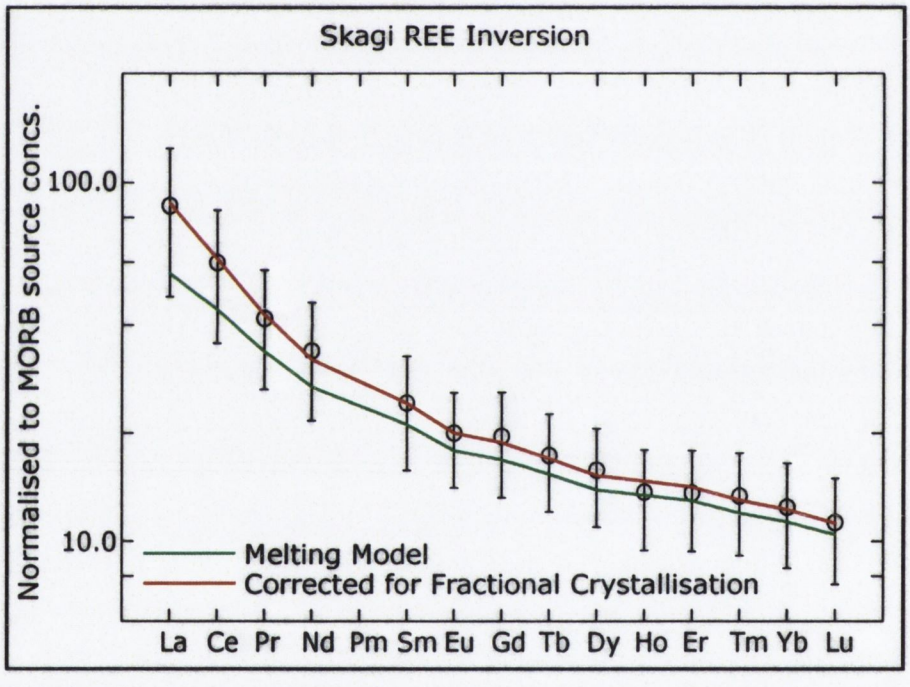

Figure 4.21: Result of REE inversion model (McKenzie and O'Nions, 1991): fit of model compositions to observed REE concentrations. The green line represents the compositions resulting directly from the melting model shown in figure 4.22. The red line estimates the change in absolute REE concentrations according to fractional crystallisation processes estimated from the Fe and Mg content of the melt.

4.5 Discussion and Conclusions

The aim of this chapter was to establish the likely origin of the young Skagi lavas in relation to the extinct rift and describe geochemical variations associated with different stages of the rift cycle. By combining the different rift stages, an artificial record of

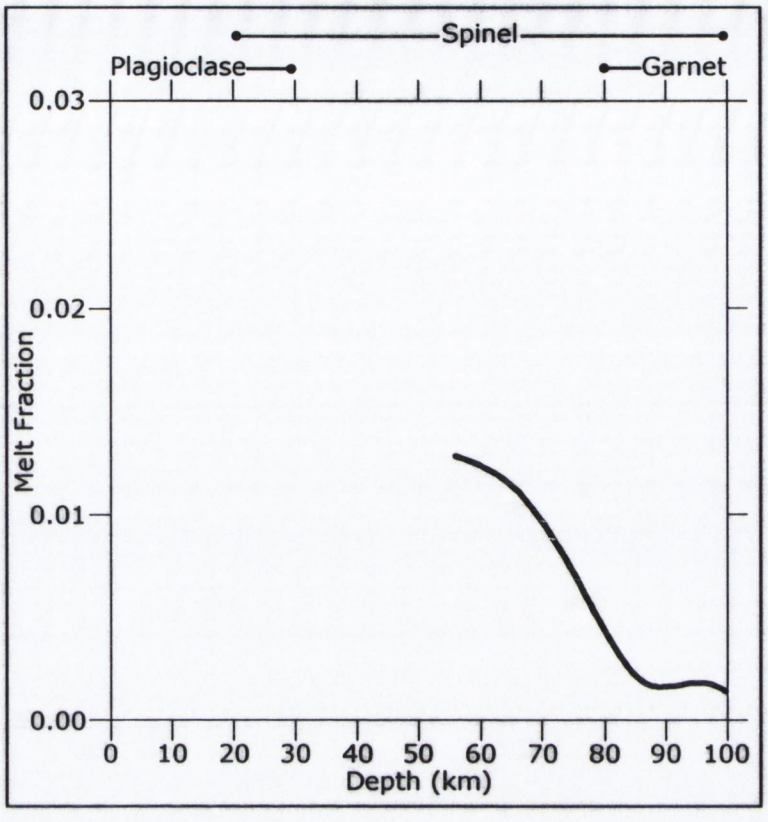

Figure 4.22: Result of REE inversion model (McKenzie and O'Nions, 1991): predicted melt fraction versus depth curve. The total melt fraction is approximately 1.4% with about 0.5% (a third of the total) melting within the garnet stability field (<80 km).

temporal variations during one rift cycle can be produced to compare with the time-dependent model results of variable spreading rate at a rift axis presented in chapter 7.

The Quaternary lavas on Skagi are aged between 2.5 and 0.5 Ma according to Everts et al. (1972) K-Ar study. This is much younger than the estimated death of the Skagi rift at approximately 3 Ma (Garcia et al., 2003). The first question is to establish whether the young lavas represent the last eruptions of a dying rift or whether they are the result of a transient melting episode. This is an important distinction to make as in the declining Western Volcanic Zone, no geochemical change has been observed as extension transfers to the Eastern Volcanic Zone. If the Skagi lavas are not from a dying rift, then the lack of change in the Western Volcanic Zone may be further evidence that the chemistry of rift products does not react to spreading rate variations at the end of a rift cycle before the rift becomes completely extinct.

Skagi Quaternary lavas have a similar chemistry to the local Tertiary lavas (section 3.5) and the Tertiary in general from the whole of Iceland (section 5.3). The obser-

vations in chapter 5 suggest that existing Tertiary samples have a similar enriched incompatible element signature to those in central Iceland (Northern Volcanic Zone) where enrichment is the result of active upwelling contributing half the total melt production (Maclennan et al., 2001b). Very large degree melting in central Iceland forms up to 40 km thick crust (Darbyshire et al., 1998). The comparison of Skagi with central Iceland flows (section 4.3.2) shows a close similarity between incompatible element compositions. However, the enrichment at Skagi is probably the result of small degrees of melting and not active upwelling.

The REE inversion model predicts less than 2% melting for young Skagi lavas and the field observations indicate that these lava flows are not the large volume, laterally extensive for a 100 km, flows erupted by central Iceland and preserved in the Tertiary. Significant geochemical effects of active upwelling are restricted to a maximum of 150 km from the plume centre (Maclennan et al., 2001b). At 0.5 Ma the plume centre was very close to its present position under the northwest corner of Vatnajökull, especially with the apparent slow down of Iceland-plume migration over the last few Ma (Jones, 2003). This is also consistent with the widely accepted notion that rift relocations are driven by the migration of Iceland over the plume centre and the plume centre will therefore need to have migrated away nearly 8 Ma prior to young Skagi lava emplacement, to cause the initiation of the Northern Volcanic Zone. Therefore, the melting processes are different between Skagi and the surrounding Tertiary. This change in melting regime could still be part of the shut-down of an active rift. However, very little faulting is observed on the Skagi peninsula suggesting that the young Skagi volcanism was not associated with any significant extension and plate separation. This would explain the mis-match between the INVMEL crustal thickness (approximately 1.5 km) and the observed crustal thickness (25–30 km). If very little extension occurs, the crustal thickness must remain from the old rift activity. The young Skagi lavas are most likely to be the result of a transient melting episode or renewed impulse of melting on a deactivating rift. Dating of the youngest Tertiary lava flows directly beneath the glacial unconformity in Skagi would determine whether a significant hiatus in eruptions exists which would suggest the shut-down of the rift, prior to a transient melting episode or constant activity on the rift.

Exceptionally high TiO_2 values from the Quaternary lavas on Skagi and the Eastern Volcanic Zone are some of the highest for oceanic volcanism. Prytulak et al. (2007) show that such high TiO_2 compositions cannot be made by melting normal mantle peridotite source, even with very small degrees of melting. They suggest that the most reasonable explanation involves a small (<10%) contribution of recycled oceanic crust

to the mantle. The recycled mafic crust starts melting deeper than the host peridotite mantle so that small degree melts below a thick lithosphere will preferentially sample this source heterogeneity and result in enriched Ti melt compositions. This explanation is consistent with the small length scale heterogeneities in the mantle beneath Iceland predicted by Maclennan (2008a) and the various isotopic studies predicting essentially a two-layer mantle beneath Iceland with an enriched set of components and a depleted set of components (e.g. Hémond et al., 1993; Thirwall et al., 2004; Kokfelt et al., 2006).

The unusual origin of Skagi melting and the Sinton et al. (2005) study of the Western Volcanic Zone indicate that the decline of a rift axis may not result in significant changes in geochemistry of rift products similar to the difference observed from the birth of a rift axis. The lack of alkaline volcanism at Skagi and the Western Volcanic Zone is consistent with this theory. The time-dependent model shows that it is difficult to achieve more enriched compositions at the end of rift activity compared to the growth of a rift axis (section 7.5). The possible causes of Quaternary activity on the Skagi rift are discussed in chapter 8.

The temporal variations in geochemical signature and melting associated with rift relocations can be summarised as follows:

- Very enriched compositions for the birth of a rift axis similar to the propagating tip of the Eastern Volcanic Zone, evolve into relatively depleted compositions for normal rifting such as the Theistareykir and Krafla systems of the northern part of the Northern Volcanic Zone.
- Eastern Volcanic Zone compositions are significantly more enriched than the more established rift zones indicating smaller degree of melting and a greater contribution of garnet field melting.
- Sm/Yb values for the Eastern Volcanic Zone are up to a factor of 2 greater than the most enriched compositions from Theistareykir and Krafla.
- Melt fractions evolve from as little as 1–6% for the propagating tip of a new rift (Furman et al., 1991) to 22% in a fully established rift producing 20 km thick crust.
- The decline of the Western Volcanic Zone shows no obvious geochemical change yet (Sinton et al., 2005).
- Young Skagi lavas are unlikely to represent the simple death of a rift axis and the

enriched compositions compared to the established rifts cannot be assumed to be caused by the slow down of plate separation as extension transfers to a new rift.

The main conclusions from the comparison of young Skagi lavas to neovolcanic activity on Iceland and REE inversion modelling:

- Skagi Quaternary lavas, most likely, have been produced in the mantle directly beneath Skagi and are not related to Langjökull magmas. The trends observed for increasing trace element ratios with decreasing MgO must be coming out of the mantle and are probably associated with small degree partial melting.
- Skagi compositions are distinct from the Western Volcanic Zone and the northern part of the Northern Volcanic Zone, being more enriched in incompatible elements.
- Basalt compositions from the Northern Volcanic Zone in central Iceland are very similar to young Skagi lavas indicating that the relative contribution of deep mantle melting compared to the total melt fraction is similar. However, the process of active upwelling that has been inferred for the enriched compositions in central Iceland is not likely to have contributed to the Quaternary melting beneath Skagi.
- Eastern Volcanic Zone and significantly off-axis (Snaefell and Snaefellsnes) compositions are more enriched than the young Skagi lavas suggesting that the relative contribution of garnet field melting is greater in these places than at Skagi.
- The off-axis Grímsnes system shows similar enrichment to Skagi lavas for tholeiitic basalts, suggesting similar melting regimes and indicating that the Skagi volcanism may not be associated with normal axial melting processes.
- Young Skagi lava compositions are consistent with very small degrees of melting (1–2%) with a significant contribution of garnet field melting (approximately 30–35% of the total).

Chapter 5

Geochemical Insights into Crustal Accretion at Iceland

5.1 Introduction

Crustal accretion refers to the mechanical processes that occur during and immediately after the emplacement of dykes and lava flows at rift zones in Iceland. This post-emplacement crustal drift creates a bias as to which features of the rift zone are preserved at the surface as extension continues. The Tertiary age crust at Iceland provides a unique record (up to 17 Ma) of volcanic activity and geochemical variations associated with a ridge-hotspot interaction. The interpretation of existing geochemical data has been restricted, in part, due to a limited understanding of the preservation bias introduced by crustal accretion mechanisms.

The wealth of existing Tertiary data could provide significant insights into the impact of Iceland's active tectonic history on the geochemical signature of ridge products. Reliable interpretation of Tertiary geochemical data is very complex because all the factors which affect the chemistry of recent rift products, including source composition, partial melting, fractional crystallisation, mixing, crustal contamination and hydrothermal alteration, must be considered together with the bias created by crustal accretion processes and temporal variations in spreading rate and glaciation.

A previous study showed that the geochemical variability that exists in the neovolcanic zones is not reflected in the Tertiary (Hardarson and Fitton, 1997) and related

this homogeneity to the Pálmason model of crustal accretion described in section 5.2 (Pálmason and Saemundsson, 1974). Hardarson and Fitton (1997) observed that according to Pálmason's model only large axial flows able to escape the rift axis will be preserved at the surface in the Tertiary. Pálmason's model does not account for off-axis volcanism, the presence of dykes and Tertiary central volcanoes at the surface, and does not consider the effect of rift relocations on the crustal structure. The contribution made by off-axis volcanic centres and dying rift axes to the Tertiary crust has not previously been considered and is investigated in this chapter using new geochemical comparisons. Gaining a more consistent understanding of what exactly is represented in the Tertiary crust in terms of extinct rift zones may allow geochemical variations to be linked to the rift relocation cycle.

The aim of this chapter is to present a more detailed geochemical comparison using existing Tertiary data donated by G. Fitton (unpublished) and Kitagawa et al. (2008), published data from the neovolcanic zones and the new Skagi rift data presented in chapter 4. New geochemical data is presented for 24 dyke samples donated by S. Garcia and is used to discuss the validity of Garcia et al. (2003) plate spreading velocity model which describes the most recent rift relocation in northern Iceland. The Tertiary shows significant geochemical similarities with the extinct Skagi rift, off-axis volcanic centres and central Iceland. Comparisons with the Northern Volcanic Zone indicate the effects of glaciation on the geochemistry of rift products, showing that not all large lava flows have a chemistry that is consistent with the Tertiary. These new observations indicate that the Tertiary lava pile is not solely composed of the largest axial flows as suggested by Hardarson and Fitton (1997). Although the largest lava flows will form a large proportion of the Tertiary, the contribution from off-axis volcanism and dying rift axes must also be considered. This investigation into the geochemical signature of the Tertiary places better constraints on the bias introduced by the surface preservation process during crustal accretion and improves the interpretation of existing geochemical data. It also allows a qualitative assessment of the impact of Iceland's active tectonic evolution (via rift relocations) on the geochemistry of ridge products and provides new insights into the temporal evolution of ridge-hotspot interactions in general.

5.2 Background

The Tertiary crust formation includes the oldest rocks in Iceland at 16 Ma until the onset of major glaciation in the northern hemisphere around 3 Ma. The Tertiary lava

pile is characterised by red palaeo-soil horizons at the top of lava flow units indicating a much warmer climate compared to Quaternary times and there is little evidence for significant glaciation during the Tertiary. Steep-sided glaciated valleys in north, east and west Iceland have exposed up to 2 km of the upper Tertiary crust. Further evidence of exhumation can be found in the zeolite minerals precipitated as amygdales within Tertiary lavas. Following detailed mapping of zeolite zones in eastern Iceland, Walker (1960) calculated an approximate figure of 1.8 km for the amount of exhumation relative to the original elevation of the top of the lava pile. There are two main components which make up the exposed Tertiary crust: 'trap' type basalt lava piles (figure 5.1) and complex central volcano structures (figure 5.2). The presence of central volcanic complexes at the surface is discussed in section 5.5. In eastern Iceland a study by Watkins and Walker (1977) showed that the eruption rate represented by the Tertiary lavas is significantly lower than that observed in the neovolcanic zones today, suggesting that only a small proportion of erupted rift products are actually preserved at the surface. This is consistent with the idea that only the large volume lava flows can be preserved at the surface in the Tertiary (Hardarson and Fitton, 1997). In order to interpret geochemical data from the Tertiary correctly we must first establish which elements of rift activity have the potential to be preserved in the Tertiary. The formation of the Tertiary is also subject to the effects of the tectonic arrangement of the active rift(s); the history of rift locations and jumps is discussed in section 2.1.3.



Figure 5.1: Tertiary 'trap' type basalt lava flows in northwest Iceland. This regular layering of laterally extensive flows forms most of the coastline in the Northwest Fjörds, northern Iceland including Tröllaskagi and Flateyjarskagi and the east Iceland Fjörds.

The first, and widely accepted, model of mechanical crustal accretion processes at Iceland was developed by Pálmason (Pálmason and Saemundsson, 1974) and is shown in figure 5.3. The model describes the accumulation and transportation of axial material. There is a narrow zone of dyke injection 50 km wide which defines the rift zone, with minor eruptive activity outside this zone known as off-axis volcanism. Lava flows and



Figure 5.2: Part of Reykjadalur Tertiary central volcano in west Iceland. Observe the lack of regular layering compared to the Tertiary 'trap' lavas, with smaller capping lava flows at the top of the caldera. The discolouration in the hillside represents the caldera infill composed of some acidic volcanic components.

dykes emplaced on-axis are subject to rapid burial by subsequent lava flows resulting in subsidence. Extension at the ridge axis causes this buried material to move out laterally as shown by the trajectories in figure 5.3. Any material emplaced within the rift zone will therefore not be exposed at the surface in older crust. Because glacial erosion in the Tertiary crust reveals only a maximum of 2 km of the upper crust, the only elements of rift activity that will be preserved and accessible will be those emplaced more than 25 km from the rift axis (Hardarson and Fitton, 1997). Centrally focused subsidence in the rift zone creates an inward dip of the rift zone flanks towards the axis forming a regional syncline. Regional synclines have been observed in several locations in Iceland and have therefore been interpreted as extinct rift axes (see figure 2.5, chapter 2); Hardarson et al., 1997; Jóhanesson, 1980).

Hardarson and Fitton (1997) is the only existing geochemical study of Tertiary crustal accretion processes at Iceland. They showed that Tertiary basalts (>5 wt% MgO) have a relatively uniform Zr/Nb ratio compared to a dramatic variability that exists for basalts from the neovolcanic zones (figure 5.4). It was inferred from Pálmason's model that the only lava flows that will be preserved at the surface to form the Tertiary are those large enough to flow outside of the rift zone. Hardarson and Fitton showed using the Zr/Nb ratio that large volume lavas from the neovolcanic zone have a relatively uniform composition compared to very small volume (<0.5 km^2) eruptions (figure 5.5) and that the greatest variability in Zr/Nb is found closest to the rift axis.

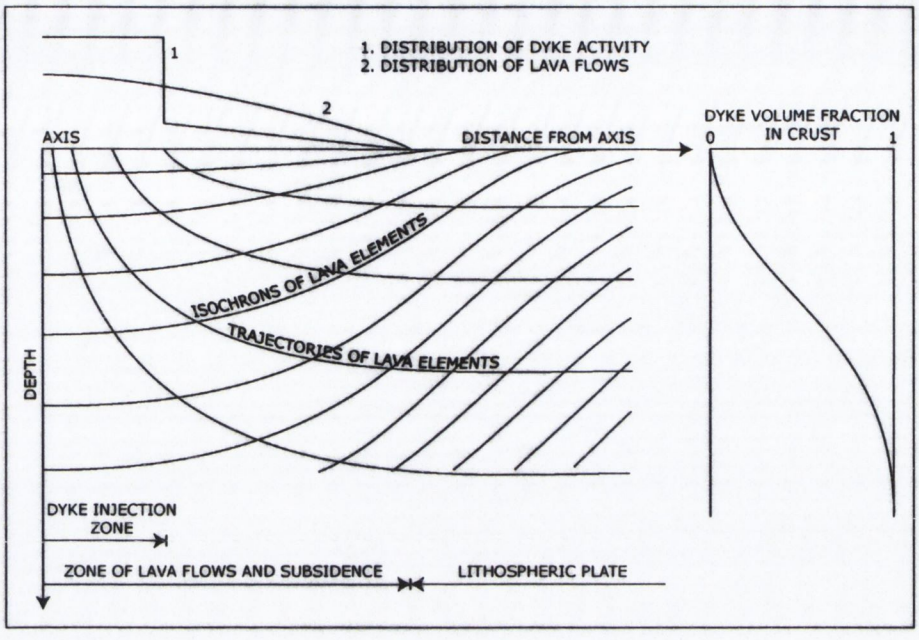

Figure 5.3: The Pálmason model of crustal accretion at Iceland. Rapid burial and subsidence caused by subsequent emplacement of lava flows results in any material emplaced within the rift zone being transported downwards and away from the rift axis as shown by the trajectories (Pálmason and Saemundsson, 1974).

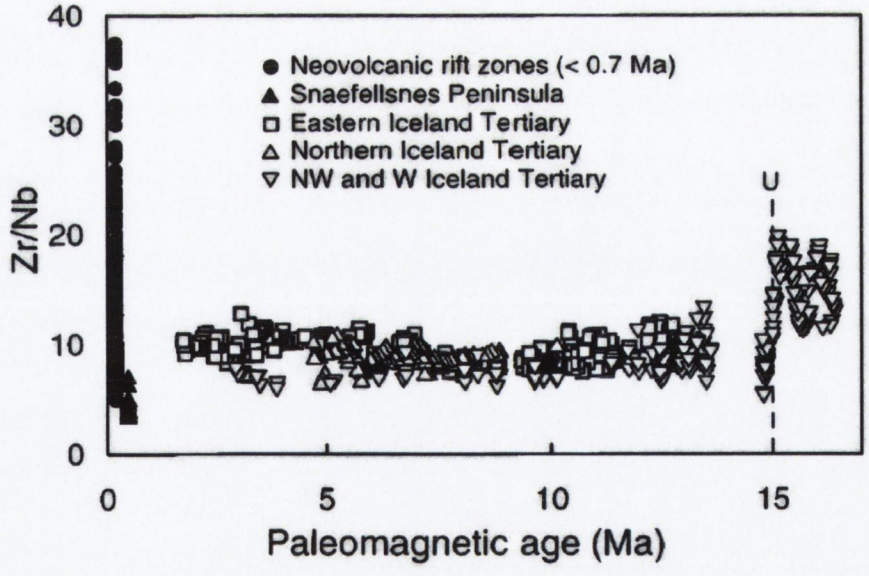

Figure 5.4: The variation of Zr/Nb with palaeomagnetic age in basalts (>5 wt% MgO) from Iceland. Neovolcanic basalts were assigned arbitary ages, with Snaefellsnes samples offset for clarity. From Hardarson and Fitton (1997).

Hardarson and Fitton (1997) assume that large volume lava flows represent the bulk composition of the rift axis because of significant mixing processes in large axial magma chambers. If it is true that only large axial lava flows form the Tertiary lava pile and that they record the bulk composition of the rift zones then it is possible to associate

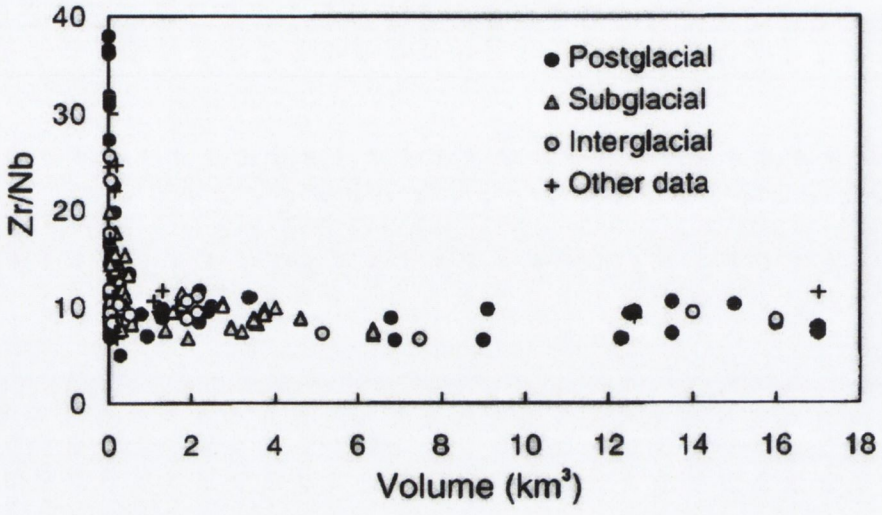

Figure 5.5: The variation of Zr/Nb with volume of eruption in basalts (>5 wt% MgO) from the neovolcanic zones in Iceland. Other data are from Wood et al. (1979), Nicholson (1990), and Hémond et al. (1993). From Hardarson and Fitton (1997).

any geochemical variations in the Tertiary lavas through time with temporal variations in the rift zone e.g. rift relocations and their associated spreading rate variations. Further geochemical investigation of the similarities between the Tertiary crust and neovolcanic zones is presented in section 5.4.1 and suggests that the accumulation of the Tertiary is more complicated than suggested by Hardarson and Fitton (1997).

Garcia et al. (2003) produced a kinematic model of the northern Iceland rift relocation from the now extinct Skagi rift to the presently active Northern Volcanic Zone, described in detail in section 2.1.3. The model is based on $^{40}Ar/^{39}Ar$ dating of dyke intrusions exposed in northern Iceland (figures 2.8 and 2.9) and provides important plate spreading velocity constraints for the formation of the crust in northern Iceland from 11 Ma to present. The model is based on dyke ages and positions and relies on the assumption that the analysed dykes are all on-axis intrusions. However, according to Pálmason's model of crustal accretion any on-axis intrusions will never be exposed at the surface. This problem is investigated in section 5.4.5.

5.3 Geochemical Observations of Tertiary Lavas

The aim of this section is to describe the main geochemical characteristics of the Tertiary lavas and identify any significant differences between the regional data sets. The Tertiary lava data comes from 3 regions in Iceland: North (~100 samples), Northwest

(~700 samples) and East (~500 samples). The sample locations are shown in figure 5.6. Most of the data was produced by G. Fitton at the University of Edinburgh. Data from a small subset of samples from the Northwest Tertiary data set has been published by Hardarson et al. (1997). The East Iceland data is supplemented by a recent published study by Kitagawa et al. (2008; ~100 samples). The aim of comparing the major and trace elements signatures for each of the Tertiary regions is to establish whether it is valid to use all the regional data as one dataset to represent the geochemical signature of the Tertiary.

A variety of rock types exist in the Tertiary in association with several central volcanic complexes, but the data presented here are biased by sampling 'trap' lavas only. Further work is in progress on a series of samples collected from a central volcanic complex in western Iceland (chapter 8). The Northwest and East (G. Fitton) data sets contain several hundred samples whereas the other two datasets only include up to 100 samples. These Tertiary lavas are predominantly tholeiitic basalts with only a small number of samples plotting with alkaline compositions (figures 5.6 and 5.7). The greatest variability in composition is shown in the Northwest Tertiary and East Tertiary data from G. Fitton, but these are also much larger data sets compared to the North Tertiary and East (Kitagawa et al., 2008) data. There are a few slightly more evolved samples in the East and Northwest data sets and these are excluded for geochemical comparison by specifying that MgO wt% is greater than 4%. There are relatively few samples classified as part of the alkaline series. This is an important observation indicating that either there was relatively little alkaline volcanism during the Tertiary or relatively few alkaline lava flows are preserved as a result of the process of crustal accretion (see discussion section 5.5).

The North Tertiary and East (Kitagawa et al., 2008) Tertiary data produce well defined trends for the major elements (figures 5.8 and 5.10), very similar to those observed in the Skagafjördur Quaternary lavas. Fe, Ti, Mn and P all show straight line increasing trends for decreasing Mg produced by fractional crystallisation. The high Fe and Ti concentrations indicate that magnetite has not crystallised out of the melt. Mn and P are incompatible and behave as expected, increasing in concentration with decrease in Mg. Straight line decreasing trends for decreasing Mg are observed for Ca and Al, produced by the removal of gabbro during fractional crystallisation.

The North Tertiary data has very few outlying samples from the crystallisation trends described above. The most notable exception are several samples that have high Al and low Ti and Fe compositions. These characteristics are associated with the accumulation

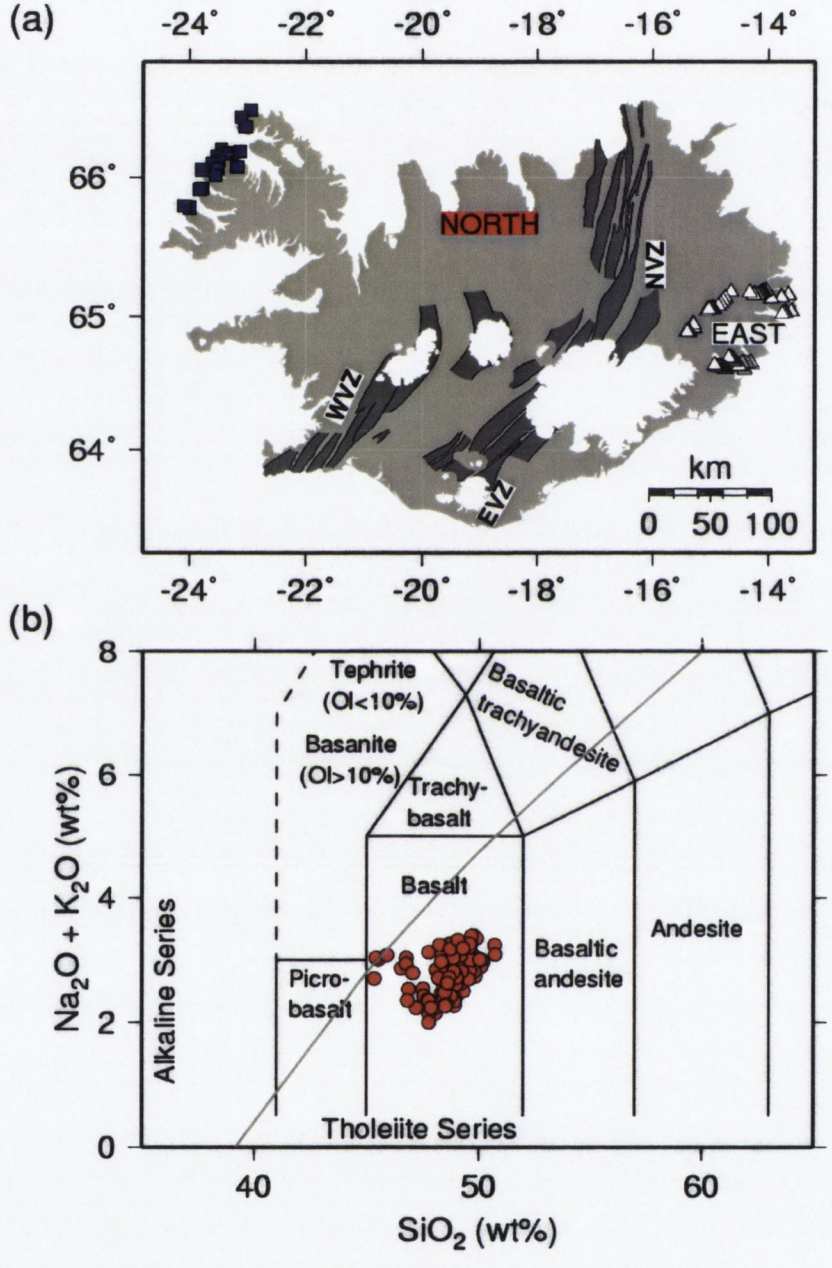

Figure 5.6: (a) shows sample locations for Northwest Tertiary data (G. Fitton) and East Tertiary data (Kitagawa et al., 2008). The North and East Tertiary data from G. Fitton do not have exact locations - the labels are placed in the regions sampled. The total alkali-silica classification for north Tertiary samples (G. Fitton) is shown in (b). Key: Northwest (blue squares), North (red circles), East (G. Fitton - black triangles, Kitagawa et al., 2008 - white triangles). Classification: Le Maitre et al. (1989); Alkaline-Tholeiite divide: Irvine and Baragar (1971).

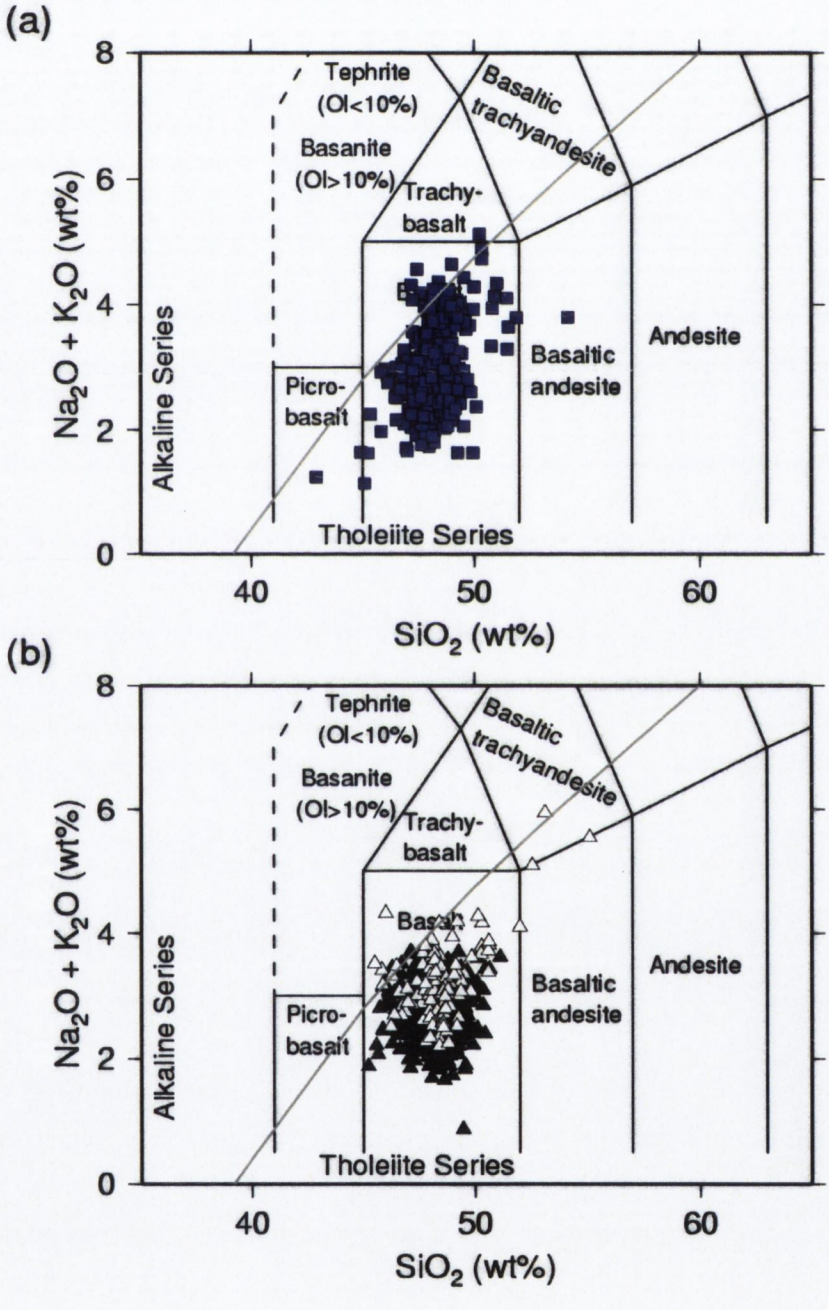

Figure 5.7: (a) and (b) show the total alkali-silica classification for Northwest and East Tertiary data respectively. Key: Northwest (blue squares), East (G. Fitton - black triangles, Kitagawa et al., 2008 - white triangles). Classification: Le Maitre et al. (1989); Alkaline-Tholeiite divide: Irvine and Baragar (1971).

of plagioclase feldspar during storage in the crust. Significant effects on trace element compositions of plagioclase accumulation are essentially limited to increases in Sr and Eu concentrations. Neither of these elements are used for comparison with the rest of Iceland. A few samples show evidence of mixing with evolved, low Ti compositions such as during crustal assimilation of rhyolites.

As noted for the total alkali-silica diagrams the greatest variability in composition is observed in the two larger datasets from northwest and east Iceland (G. Fitton). The Northwest data shows the most scatter, with a significant number of samples influenced by mixing with rhyolitic compositions. A large number of samples show evidence of accumulated plagioclase with high Al and low Fe and Ti. Several samples from the Northwest, that are associated with the extinct Skagi rift, exhibit exceptionally high P compositions. It is not clear why these samples are so high in P, but the trend cannot be made by fractional crystallisation or crustal assimilation of evolved compositions.

The East Tertiary data does not show as much scatter as the Northwest data, but there is still a reasonable number of samples showing evidence of the assimilation of rhyolitic material. Mixing is observed as decreasing trends in Ti and Fe compositions for decreasing MgO. High Al compositions indicate the accumulation of plagioclase as observed in the other Tertiary data. Several samples have exceptionally high MnO concentrations.

Figures 5.11 to 5.13 show some of the incompatible trace element variations with MgO wt%. The single element plots of the immobile incompatible elements (Nb, Zr and Y) produce increasing trends for decreasing MgO for all the Tertiary regions, as would be expected from partial melting and fractional crystallisation. Again the greatest scatter is observed in the larger datasets from Northwest and East Iceland (G. Fitton), however the scatter is less pronounced than in the major element data. The only significant excursion from the main trend lines is a group of samples from the upper part of the Northwest Tertiary, related to the extinct Skagi rift. These Northwest samples show very high Nb values compared to the rest of the Northwest data. This trend cannot be made by fractional crystallisation or by crustal assimilation of more evolved material; it is not clear how these compositions were made.

For the mobile incompatible elements Sr, Rb and Ba, significant scatter is observed for all data sets. This scatter is much more than is observed for the Skagafjördur lavas in section 3.5. Again, the larger datasets from Northwest and East Iceland exhibit the greatest variability. The mobile element concentrations in the Tertiary lavas have

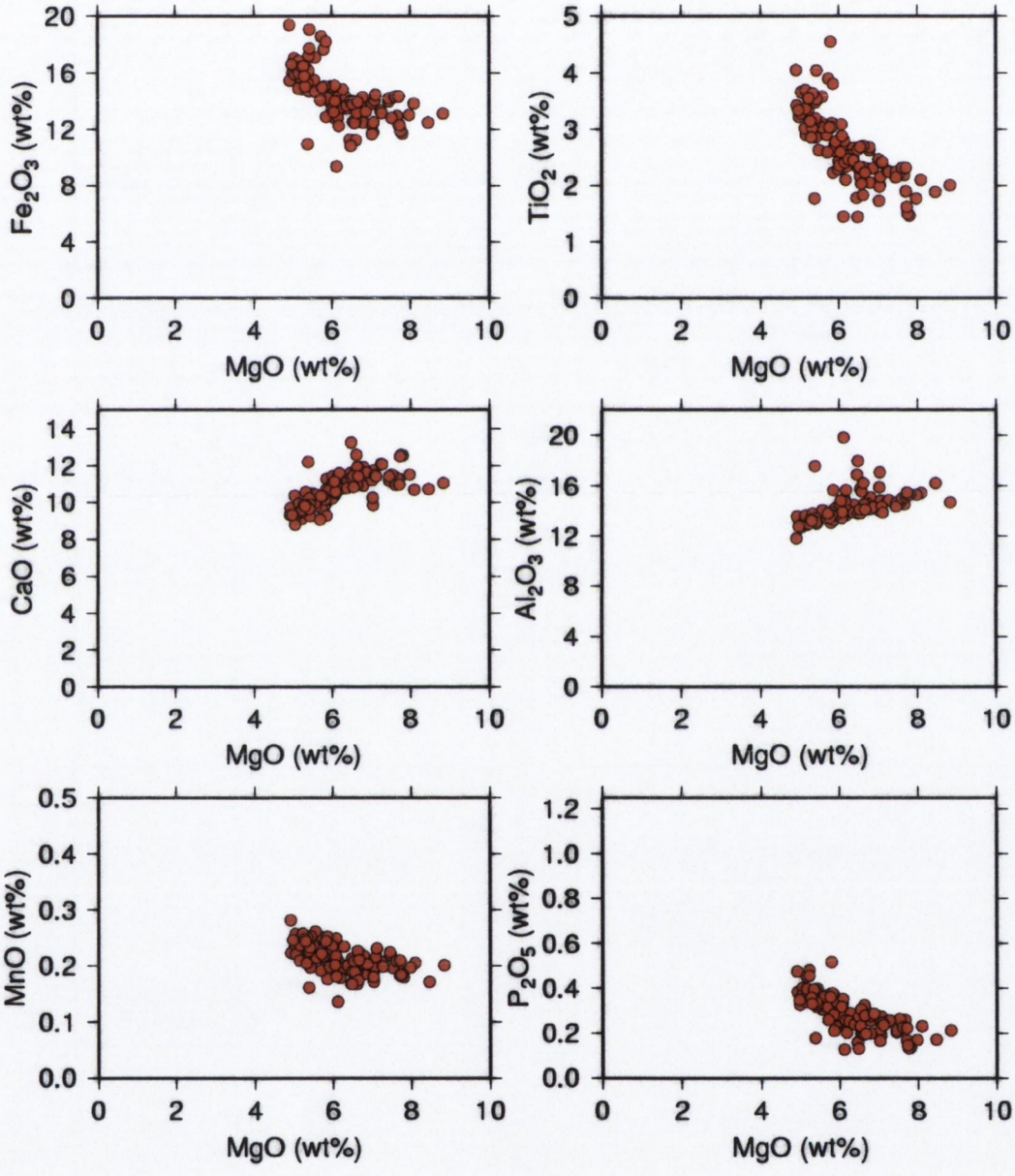

Figure 5.8: Variation diagrams for Tertiary lavas from North Iceland (red circles) for major elements versus MgO wt%. Fe_2O_3 is total Fe. Mg is used as opposed to Si for the base of the variation diagrams because the variation in Mg tends to be more pronounced than Si in basalts.

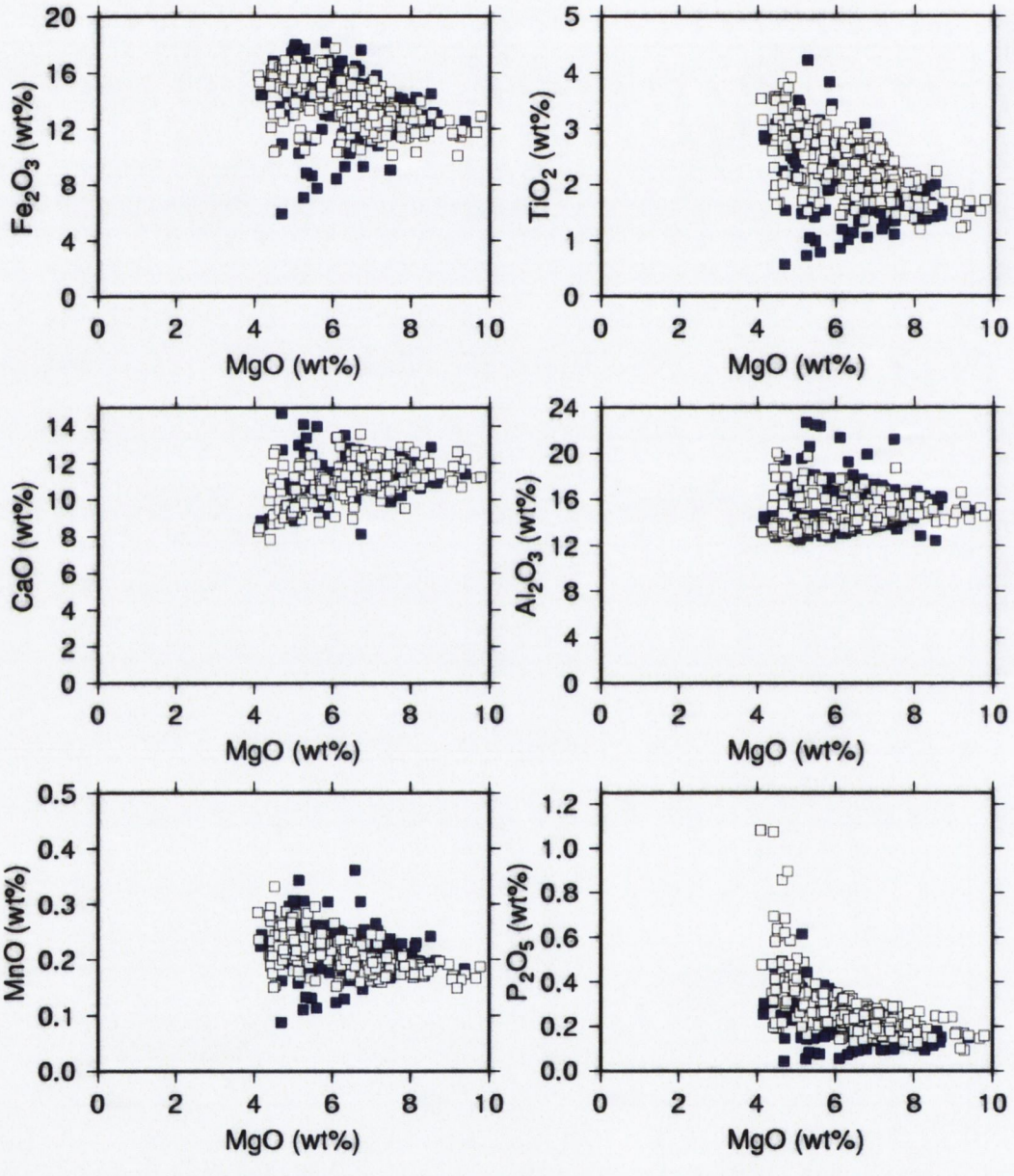

Figure 5.9: Variation diagrams for Tertiary lavas from Northwest Iceland for major elements versus MgO wt%. Fe_2O_3 is total Fe. The data are separated into samples from below the unconformity and therefore related to the older Northwest Iceland Rift (blue squares) and samples from above the unconformity, related to the younger extinct Skagi rift (white squares).

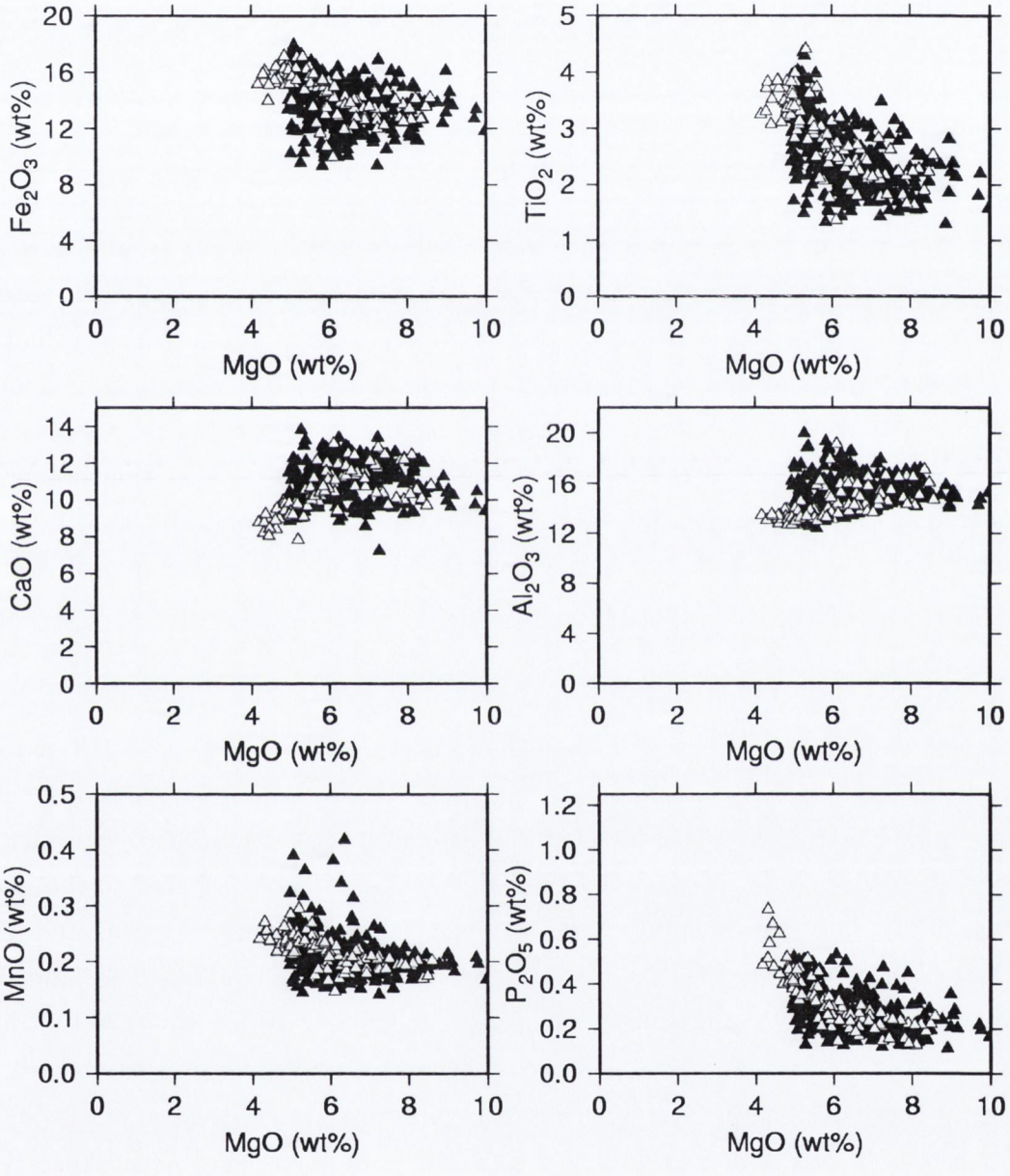

Figure 5.10: Variation diagrams for Tertiary lavas from East Iceland (G. Fitton - black triangles, Kitagawa et al., 2008 - white triangles) for major elements versus MgO wt%. Fe_2O_3 is total Fe.

been strongly influenced by hydrothermal alteration or interaction with hydrothermally altered crust. The large amount of scatter compared to young lavas from Skagi is consistent with Tertiary lavas having undergone burial following emplacement, and therefore being exposed to more episodes of hydrothermal alteration before being exposed at the surface. Excursions to very high Sr concentrations reflect the accumulation of plagioclase feldspar. Significant scatter for mobile elements in the Tertiary is expected from Walker's (1960) observations of abundant zeolite filled vesicles in Tertiary lavas from the northwest and far east Iceland.

The trace element ratios Nb/Y and Zr/Y can be used to minimise the effects of crustal processes such as fractional crystallisation and hydrothermal alteration and allow information about melting processes to be obtained (section 4.3). A slight increase is observed in both ratio values for decreasing MgO and this is particularly evident in the Zr/Y ratio for the North Tertiary data. The North Tertiary shows little evidence of crustal assimilation of rhyolites and therefore, this increasing trend is probably the result of a slight difference in the partition coefficients of Zr and Y during fractional crystallisation. The same increasing trend is observed in Northwest and East tertiary data, however in this case part of this increase could be attributed to crustal assimilation of rhyolites, particularly for the Northwest Tertiary. Zr/Y exhibits a relatively narrow range of values with most Tertiary data plotting between 3 and 5. East Iceland has some samples with higher Zr/Y, up to 6, which are likely to reflect the range of compositions from mantle melting rather than crustal processes. For Nb/Y a relatively narrow range of values is observed for North Tertiary, however there are some significant differences in the Northwest and East data sets. The Nb concentrations are slightly higher for East Tertiary data donated by G. Fitton compared to the Kitagawa et al. (2008) data, and slightly higher for the Northwest samples associated with the extinct Skagi rift compared to samples associated with the Northwest Iceland rift. These differences are particularly clear when calculating the Nb/Y ratio. The two data sets from east Iceland cover a similar range of ages so the difference in Nb cannot be attributed to temporal variations. The East Iceland data from Kitagawa et al. (2008) is obtained by ICP-MS whereas the G. Fitton data is obtained using XRF. Analytical problem related to the ICP-MS method could have caused the offset in the Nb data. Hardarson and Fitton (1997) attribute the offset in northwest Iceland to a change in the mantle source. They suggest that N-MORB source dominates over relatively enriched plume mantle in the older Northwest Rift. Because of the inconsistencies shown in the Nb/Y ratios for the Tertiary, the Zr/Y ratio is used to compare melting processes with other data from Iceland.

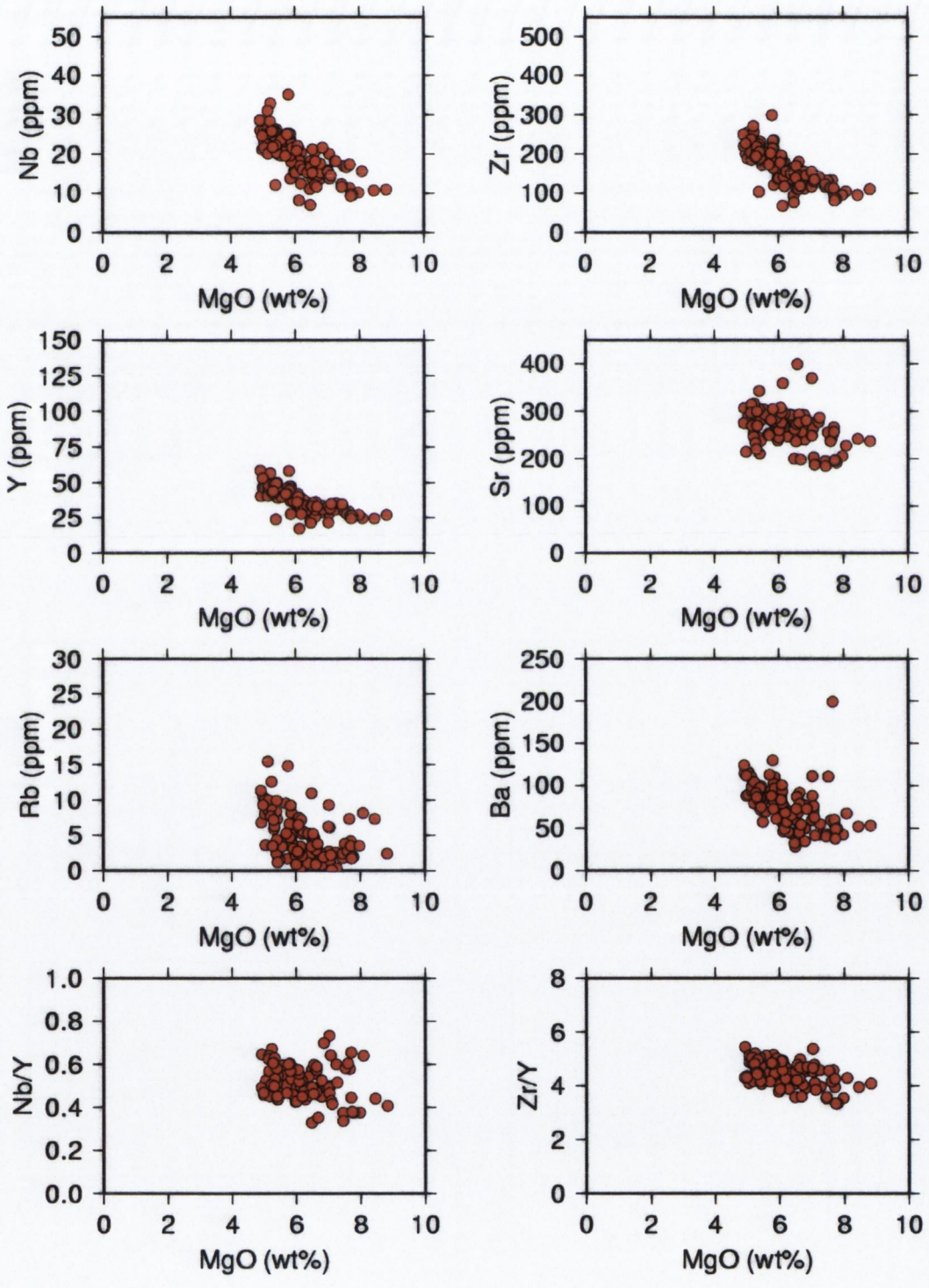

Figure 5.11: Variation diagrams for Tertiary lavas from North Iceland (red circles) for incompatible trace elements and trace element ratios versus MgO wt%. Nb, Zr and Y are immobile elements where as Sr, Rb and Ba are mobile. All data has been filtered to remove any samples with less than 4 wt% MgO.

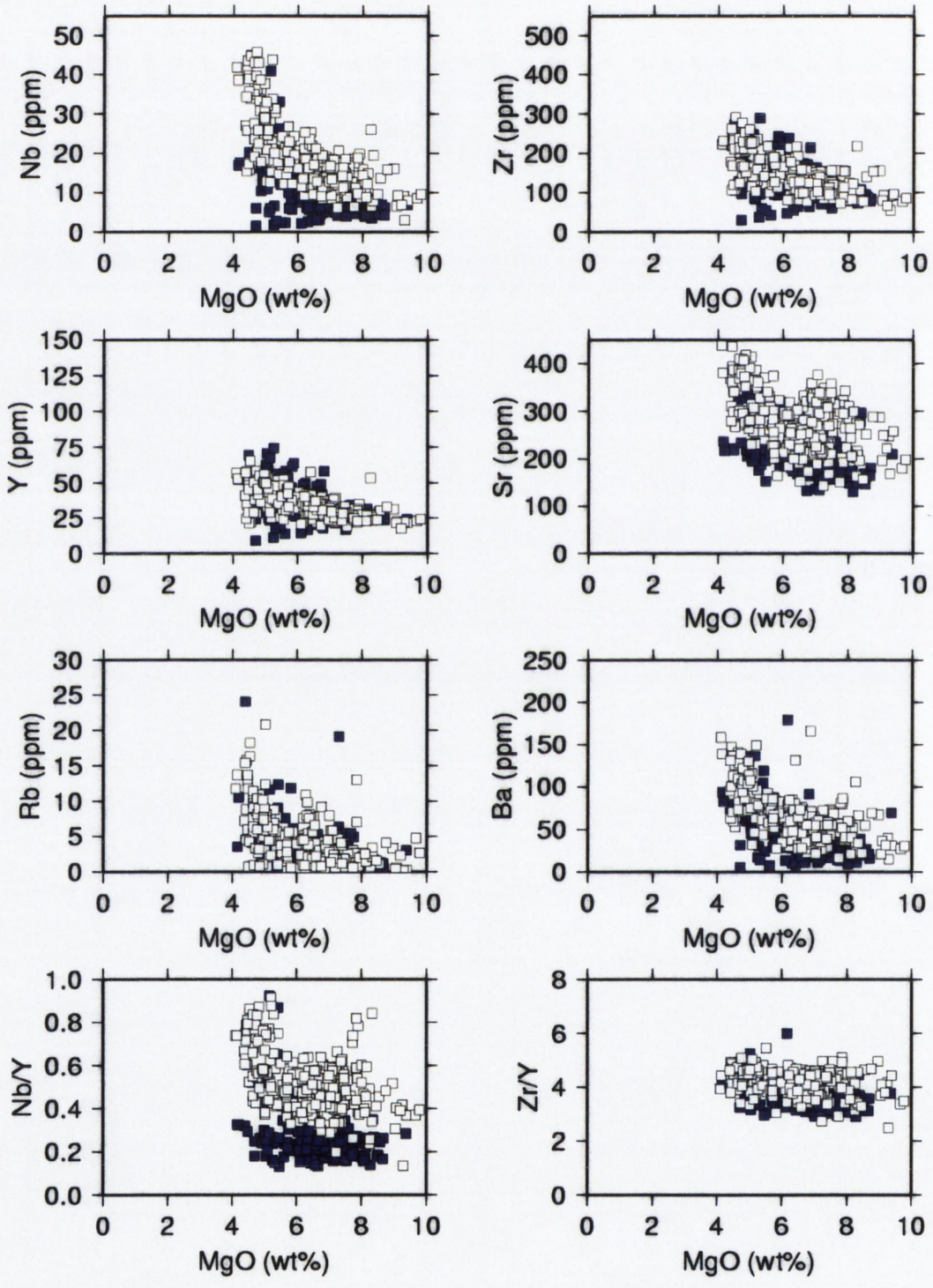

Figure 5.12: Variation diagrams for Tertiary lavas from Northwest Iceland for incompatible trace elements and trace element ratios versus MgO wt%. The data is seperated into those samples from below the unconformity and therefore related to the older Northwest Iceland Rift (blue squares) and those samples from above the unconformity, related to the younger extinct Skagi rift (white squares).

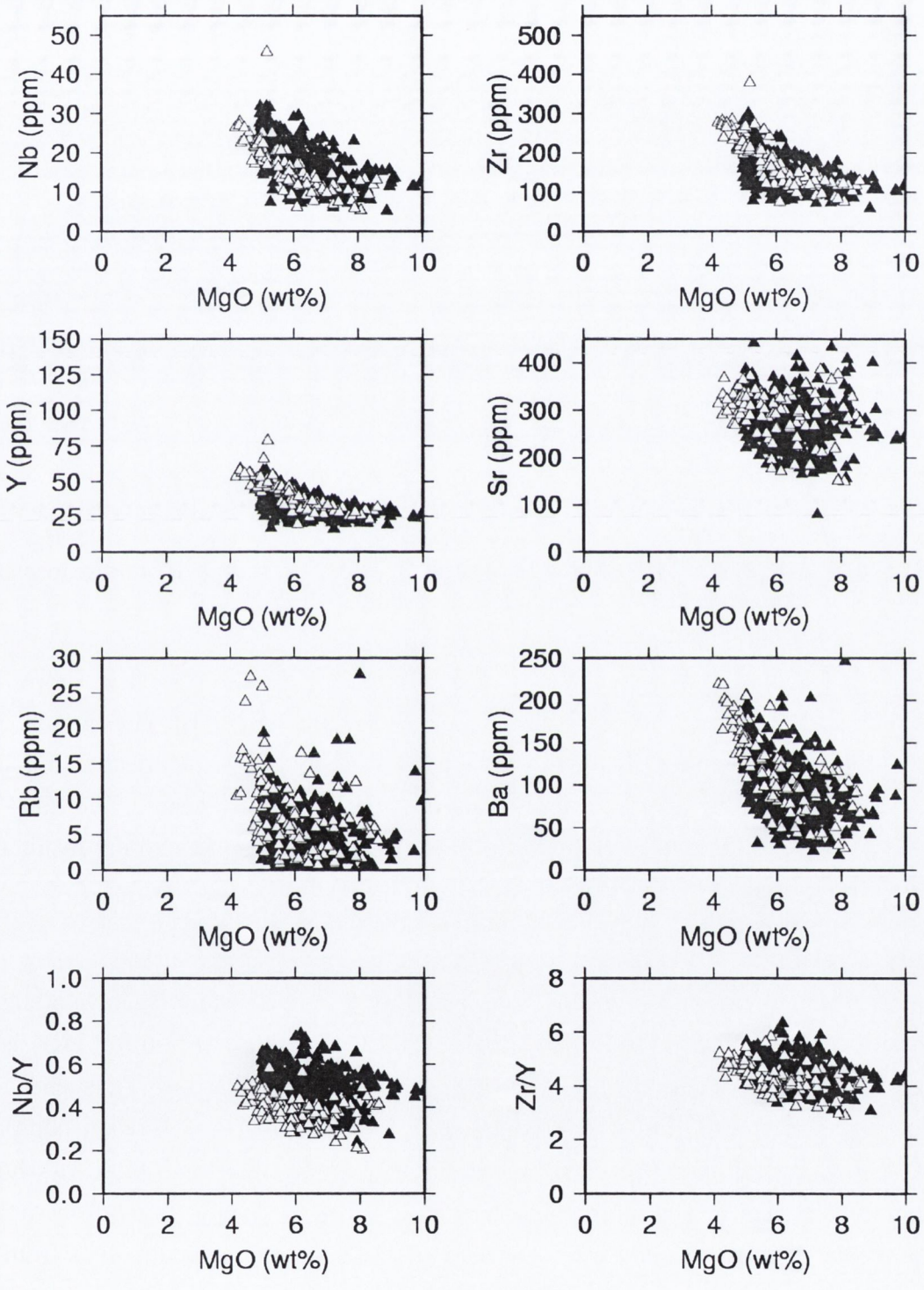

Figure 5.13: Variation diagrams for Tertiary lavas from East Iceland (G. Fitton - black triangles, Kitagawa et al., 2008 - white triangles) for trace elements and trace element ratios versus MgO wt%.

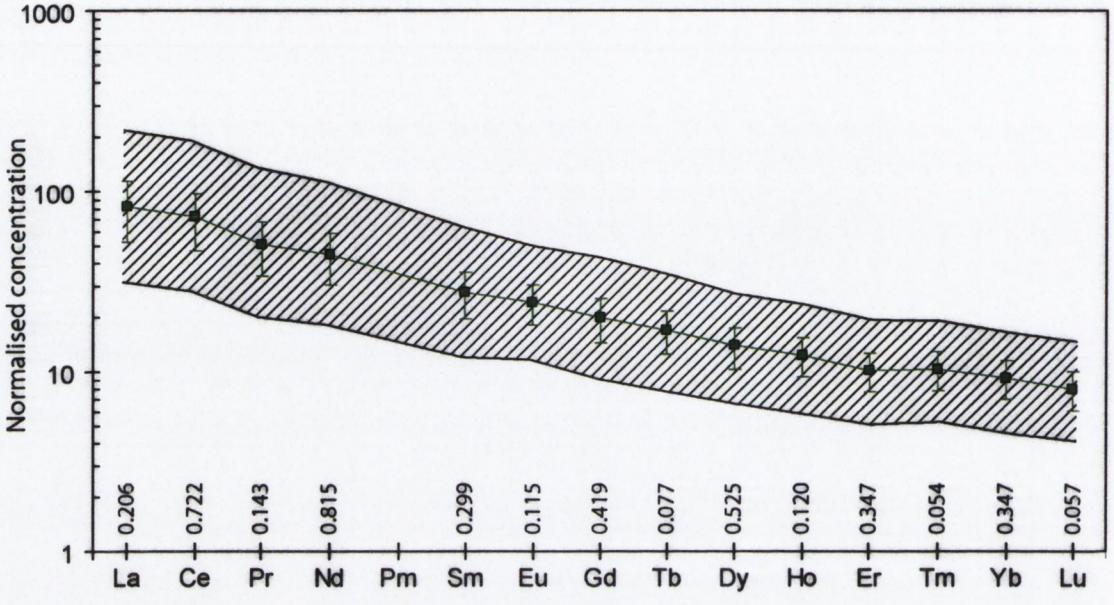

Figure 5.14: Average REE concentrations (n=96; ±1 S.D.) for East Tertiary samples from Kitagawa et al. (2008). The data set includes only basalts with greater than 4 wt% MgO. The shaded region covers the range of individual data values. REE concentrations are normalised to MORB source mantle, McKenzie and O'Nions (1991).

Rare Earth Element concentrations for East Tertiary data are shown in figure 5.14 (Kitagawa et al., 2008). The East Tertiary lavas exhibit light REE enrichment, producing a relatively steep REE pattern (section 5.4). Light REE enrichment is indicative of a strong influence of deep mantle melting in the presence of garnet. The East Tertiary REE also exhibit relatively high absolute concentrations, which may result from small degrees of melting or significant fractional crystallisation.

Figure 5.15 compares the distribution of TiO_2 and Zr/Y values for the Tertiary data from different regions across Iceland. The Northwest Tertiary samples have a slightly depleted distribution compared to the other regions. This observation for TiO_2 is the result of a mixing process involving evolved compositions with low Ti, such as the assimilation of rhyolites. The difference in Zr/Y for the Northwest Tertiary compared to other Tertiary samples is caused by consistently lower values exhibited by the set of samples from the Northwest Iceland rift (figure 5.12). Following these observations, and the large amount of scatter observed in major and trace element data from the Northwest Tertiary, the Northwest data is not included in the data set for comparison with Quaternary data from different features across Iceland.

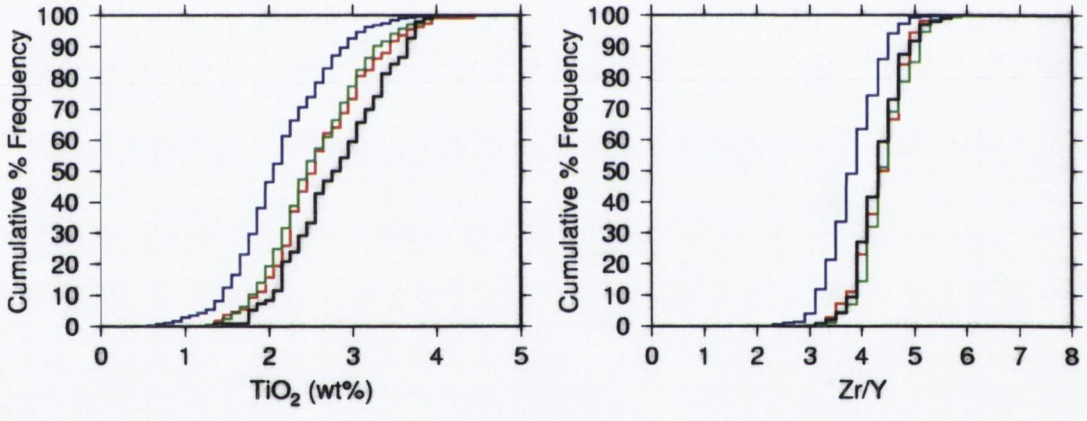

Figure 5.15: Cumulative % frequency for TiO_2 and Zr/Y for different regions of the Tertiary: Northwest (blue), North (red), East (G. Fitton, green; Kitagawa et al., 2008, black).

5.4 Geochemical Comparisons

The aim of this section is to compare the geochemical signature from Tertiary lava flows with more recent activity on Iceland, including the main rift zones, off-axis features, Skagi Quaternary lavas and dykes from across northern Iceland. Our understanding of the variation in the melting process beneath the presently active volcanic zones is significantly better than our understanding of which mantle processes were influential in the formation of Tertiary lava flows. The geochemical comparisons provide new insights into the composition of mantle melts and the melting regime in the Tertiary.

The major and trace element investigation into the Tertiary data sets in the previous section showed that they all have similar geochemical signatures, with the Northwest and East Tertiary data showing more scatter than the North. With consideration of the density of samples plotting outside of the main trend and the comparison between the three regions it was concluded that the North and East Tertiary data would provide a useful representation of Tertiary compositions for the purposes of a general comparison with the rest of Iceland. Only Nb exhibits significant differences between data sets, therefore the Nb/Y ratio will not be used in the comparative study. For the purposes of a preliminary study of crustal accretion processes only general similarities and differences between the Tertiary and other areas from across Iceland will be considered. The data will therefore not be analysed in the same detail as the new Skagi data.

The geochemical comparisons are shown in figures 5.17 to 5.37. Each comparison shows sample locations, the total alkali-silica diagram, cumulative percentage frequency diagrams for TiO_2 concentration and Zr/Y ratio, and the variation of TiO_2 and Zr/Y with MgO. The data are filtered to remove any samples with less than 4 wt% MgO so that only basaltic samples are included. The total-alkali silica diagram is important to show which series (alkaline or tholeiitic) the comparative samples are associated with because the majority of the Tertiary samples plot as tholeiitic basalts as shown in the previous section. High Fe-Ti basalts are characteristic of several areas in Iceland including Skagi and the Eastern Volcanic Zone reflecting a melting and fractional crystallisation signature. Comparison of the TiO_2 concentrations is used to identify major similarities or differences that may exist in the melting and fractional crystallisation processes. Ti is incompatible during melting and fractional crystallisation and is only removed from the melt by the crystallisation and removal of magnetite, a phase with a high partition coefficient for Ti. Zr and Y are incompatible elements with similar partition coefficients in all phases during melting and fractional crystallisation except

garnet. The distribution of Zr/Y ratio values is therefore used to compare the degree of melting and the influence of deep mantle melting. Section 5.4.6 presents the results of a simple statistical test on the similarity between the distribution of Tertiary data and the distribution of the comparative dataset for TiO_2 and Zr/Y as shown in the cumulative % frequency diagrams. The REE concentrations are plotted for each area compared to the East Tertiary data (Kitagawa et al., 2008) again to compare the melting process.

Before differences in melting are identified using trace element and REE signatures, the possible effects of source variation must be addressed. It is now widely accepted that the MORB source mantle is heterogeneous on short length scales (Maclennan, 2008a) with no significant correlation with isotopes and distance from the plume centre for example. The important observation in terms of isotopes is to ensure that the data plots within the Icelandic range. Figure 5.16 taken from Hardarson et al. (1997) shows that the bulk of the Tertiary (west, north and east) plot within the range of the neovolcanic zones, with just a few samples plotting with higher $^{87}Sr/^{86}Sr$. $^{87}Sr/^{86}Sr$ can be subject to hydrothermal alteration so this is not a significant difference. The Northwest Tertiary samples associated with the old Northwest Iceland Rift (below the unconformity) again plot within the range of neovolcanic $^{143}Nd/^{144}Nd$, but have higher $^{87}Sr/^{86}Sr$ for those values. From the Nb concentrations in section 5.3, there may a differing source for the older Northwest Iceland Rift. However, the higher $^{87}Sr/^{86}Sr$ could reflect a greater chance of hydrothermal alteration associated with older rocks that have undergone slightly deeper burial, exposed due to longer erosion and weathering.

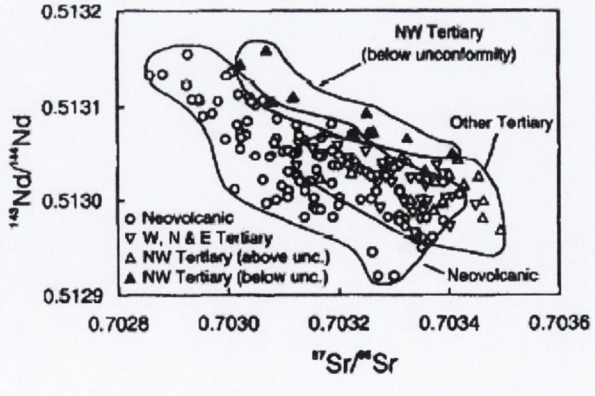

Figure 5.16: Variation in $^{144}Nd/^{143}Nd$ and $^{87}Sr/^{86}Sr$ in lavas from different areas of Tertiary crust and the neovolcanic zones in Iceland. Taken from Hardarson et al. (1997), including data from Hémond et al. (1993), Nicholson (1990), Furman et al. (1991), Elliot et al. (1991), Hardarson (1993) and Zindler et al. (1979).

A comparison is made between the Tertiary and several different areas across Iceland

with the aim of showing that the established neovolcanic zones, including the northern part of the Northern Volcanic Zone and the Western Volcanic Zone, have a broadly different chemistry to the Tertiary. Tertiary lavas have a very similar trace element signature to central Iceland and off-axis volcanism. The similarities with central Iceland are probably the result of a similar plume influence on the Tertiary rift and present Northern Volcanic Zone. Refer to section 4.2.3 for a table of compiled published data used for the geochemical comparisons.

5.4.1 Tertiary versus Neovolcanic Zones

The first comparison is made with the well established neovolcanic Zones: Northern Volcanic Zone (northern and central) and Western Volcanic Zone. Both these zones have been active for several million years (6–8 Ma) and therefore have a fully established temperature structure and melting region. The Western Volcanic Zone (figure 5.17) samples are largely postglacial with most of the data from Sinton et al. (2005). The Grímsnes system is excluded from the Western Volcanic Zone data as it is situated off-axis from the Western Volcanic Zone and is compared to the Tertiary in section 5.4.2. All the Western Volcanic Zone samples plot as tholeiitic basalts. The Western Volcanic Zone exhibits much lower concentrations of TiO_2 compared to the Tertiary and a lower distribution of Zr/Y values. The lower skew to both these distributions represents samples from the Reykjanes peninsula which is known to erupt lavas very depleted in incompatible elements. The variation of TiO_2 and Zr/Y with MgO shows that the Western Volcanic Zone samples generally have higher MgO concentrations. For the same MgO composition, the Tertiary has a similar range of TiO_2 values, with only a few samples plotting higher, but has a distinctly higher range of values of Zr/Y compared to the Western Volcanic Zone. The difference in Zr/Y reflects a change in the composition of the mantle melts.

The REE from the Western Volcanic Zone (Kokfelt et al., 2006) are also very different from the Tertiary with a less inclined pattern than the Tertiary. This pattern could result from a greater influence of deep mantle melting in the Tertiary melting regions compared to the Western Volcanic Zone or the result of a heterogeneous mantle source (figure 5.18). The overall concentrations are much lower for the Western Volcanic Zone, especially for light REE, which is consistent with a lesser influence of deep mantle melting. It is unlikely that the enriched compositions observed for the Tertiary compared to the Western Volcanic Zone are the result of a significantly smaller degree of

melting because the samples are in general taken from large volume lava flows associated with old established volcanic zones similar to the presently active Northern Volcanic Zone.

The northern part of the Northern Volcanic Zone (figure 5.19) comprises data from the Theistareykir and Krafla volcanic systems. The data show a similar geochemical signature to the Western Volcanic Zone. The Northern Volcanic Zone samples plot as part of the tholeiite series with nearly all samples plotting as basalts on the TAS diagram and 4 samples plotting as basaltic andesites. The TiO_2 concentrations provide a much lower distribution in general than the Tertiary with a skew towards lower values which reflects postglacial samples. The Zr/Y ratio distribution has a similar distribution to the Ti concentrations, again lower than the Tertiary, probably indicating a significant difference in the degree and increase in the depth of melting. However, the possible contribution of source variation must be considered. The variation of TiO_2 and Zr/Y with MgO shows that the Tertiary plots with a significantly higher range of TiO_2 values for the same MgO, particularly at low MgO compositions <6 wt%. Many of the samples from the Northern Volcanic Zone plot with lower Zr/Y compared to the Tertiary for the same MgO composition. However, a significant number of samples overlap with the lower range of Zr/Y from the Tertiary. The depleted high MgO samples from the Northern Volcanic Zone belong to postglacial volcanism, as discussed in section 4.3.2. The REE, similar to the Western Volcanic Zone, show a less inclined pattern for the Northern Volcanic Zone compared to the Tertiary, with lower concentrations overall (figure 5.20). However, there is slightly more overlap with the Tertiary compared to the Western Volcanic Zone comparison. The lower concentrations and lack of light REE enrichment are clearly influenced by the postglacial geochemical signature (section 4.3.2).

The southern part of the Northern Volcanic Zone (central Iceland) comprises data from the Askja and Kverkfjöll volcanic systems and Herdubreid, situated up to 100 km north of the plume centre (figure 5.21). All the samples plot as tholeiitic basalts on the total alkali-silica diagram. The TiO_2 concentrations show a slightly lower distribution for central Iceland than the Tertiary and this is also observed in the variation of TiO_2 with MgO. The Zr/Y ratio distribution is very similar for the Tertiary and central Iceland samples, with central Iceland samples plotting slightly lower. The variation of Zr/Y with MgO clearly shows the central Iceland samples plotting in the middle of the range of Tertiary data. The difference in the TiO_2 concentrations may therefore reflect difference in the fractional crystallisation process since the Zr/Y ratios indicate similar mantle melting regimes. The REE for central Iceland exhibit a more inclined

pattern than the northern part of the Northern Volcanic Zone, which is similar to the Tertiary (figure 5.23). The absolute concentrations are lower than the Tertiary which again may reflect a difference fractional crystallisation.

Further comparisons between central Iceland and the Tertiary for Sm/Yb and Nb/Y are shown in figure 5.22. For the same MgO composition, the central Iceland samples plot within the range of values for the Tertiary for both Sm/Yb and Nb/Y. It is not surprising to see that the East Iceland Sm/Yb values correlate exceptionally well with central Iceland because much of the East Tertiary samples come from lava flows erupted during the first 5 million years of activity on the Northern Volcanic Zone. The Tertiary samples also come from a comparable latitude to central Iceland i.e. in line with the spreading direction (figure 5.40). The Nb/Y values for central Iceland plot within the top half of the range of values from the Tertiary, for the same MgO composition. The significant range of samples plotting lower is caused by the significant difference in Nb between the two East Tertiary data sets, discussed in section 5.3. It is still useful to observe that central Iceland correlate with a significant proportion of the East Tertiary data. The strong similarity between central Iceland and the Tertiary samples is discussed further in section 5.5.

The Eastern Volcanic Zone is relatively young (approximately 3 Ma) compared to the Northern and Western Volcanic Zones and therefore, the melting region is not yet fully developed. This results in a significantly different geochemical signature to the established neovolcanic zones. The Eastern Volcanic Zone is compared to the Tertiary data in figure 5.24. Most of the Eastern Volcanic Zone samples plot as basalts, with around 50% plotting as part of the alkaline series and many of the tholeiitic samples plot close to the boundary and would be described as transitional. The alkaline nature of the volcanism is not in agreement with the flows sampled by the Tertiary data which are almost all tholeiitic basalts. It is therefore clear that the initial flows erupted by a new rift axis are not preserved at the surface in the top 2 km. The Eastern Volcanic Zone exhibits a similar range of TiO_2 values to the Tertiary and higher values of Zr/Y for the same MgO composition. The REE patterns are very similar, showing light REE enrichment and a strong influence of deep mantle melting (figure 5.25). The significantly higher Zr/Y for the Eastern Volcanic Zone may result from much smaller degrees of melting, confirmed by the generally alkaline/transitional nature of the volcanism. There are a few Tertiary samples which overlap with the high Zr/Y values from the Eastern Volcanic Zone. These Tertiary samples are the few alkaline basalts from the East Tertiary dataset shown in figure 5.7.

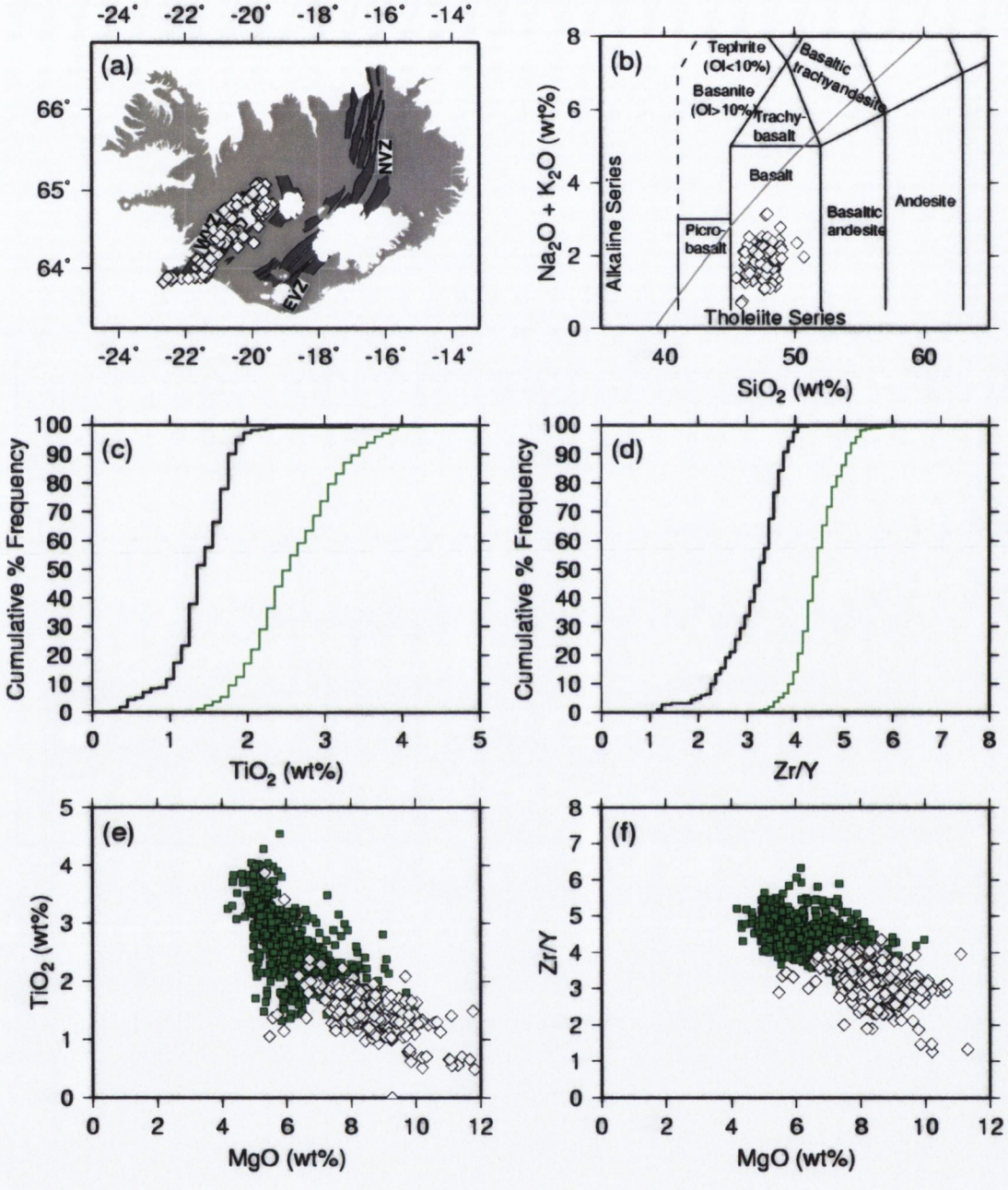

Figure 5.17: Diagrams comparing Tertiary data with the Western Volcanic Zone. (a) and (b) show the sample locations and total alkali-silica diagram for the Western Volcanic Zone. (c) and (d) are cumulative % frequency diagrams for TiO_2 wt% and Zr/Y ratio: Tertiary - green, Western Volcanic Zone - black. (e) and (f) show the variation in TiO_2 wt% and Zr/Y with MgO wt% for the Western Volcanic Zone (white diamonds) and the Tertiary (green squares).

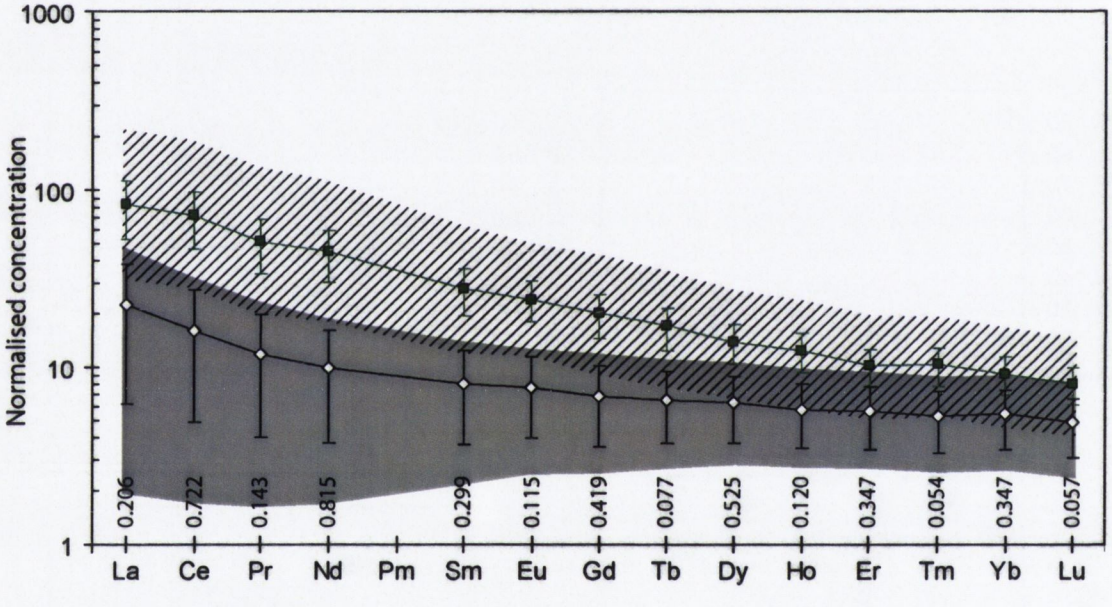

Figure 5.18: The average REE concentrations (±1 S.D.) for East Tertiary (green squares; Kitagawa et al., 2008; n=96) and Western Volcanic Zone (white diamonds; Kokfelt et al., 2006; n=20), normalised to MORB source mantle (McKenzie and O'Nions, 1991). The striped area covers the range of East Tertiary data and the solid grey area covers the range of Western Volcanic Zone data.

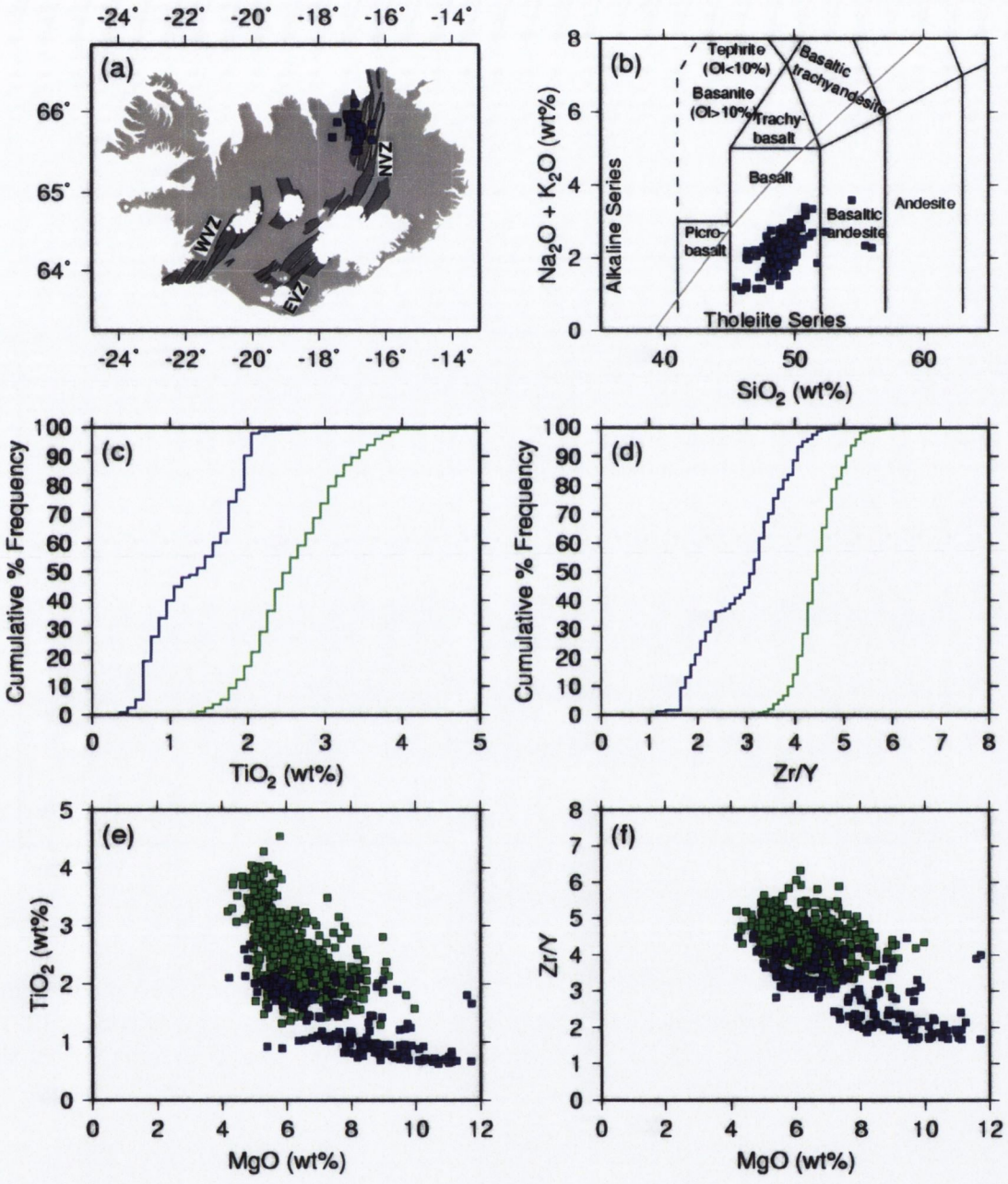

Figure 5.19: Diagrams comparing Tertiary data with the Northern Volcanic Zone (Theistareykir and Krafla systems). (a) and (b) show the sample locations and total alkali-silica diagram for the Northern Volcanic Zone. (c) and (d) are cumulative % frequency diagrams for TiO_2 wt% and Zr/Y ratio: Tertiary - green, Northern Volcanic Zone - blue. (e) and (f) show the variation in TiO_2 wt% and Zr/Y with MgO wt% for the Northern Volcanic Zone (blue squares) and the Tertiary (green squares).

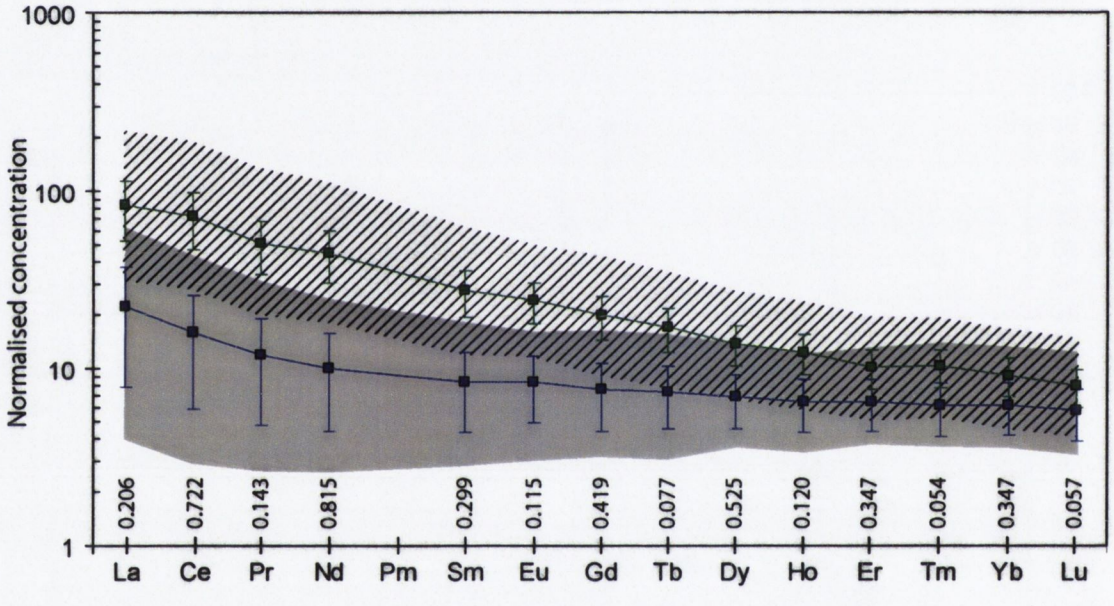

Figure 5.20: The average REE concentrations (±1 S.D.) for East Tertiary (green squares; Kitagawa et al., 2008; n=96) and Northern Volcanic Zone (Theistareykir and Krafla systems; blue squares; n=145), normalised to MORB source mantle (McKenzie and O'Nions, 1991). The striped area covers the range of East Tertiary data and the solid grey area covers the range of Northern Volcanic Zone data.

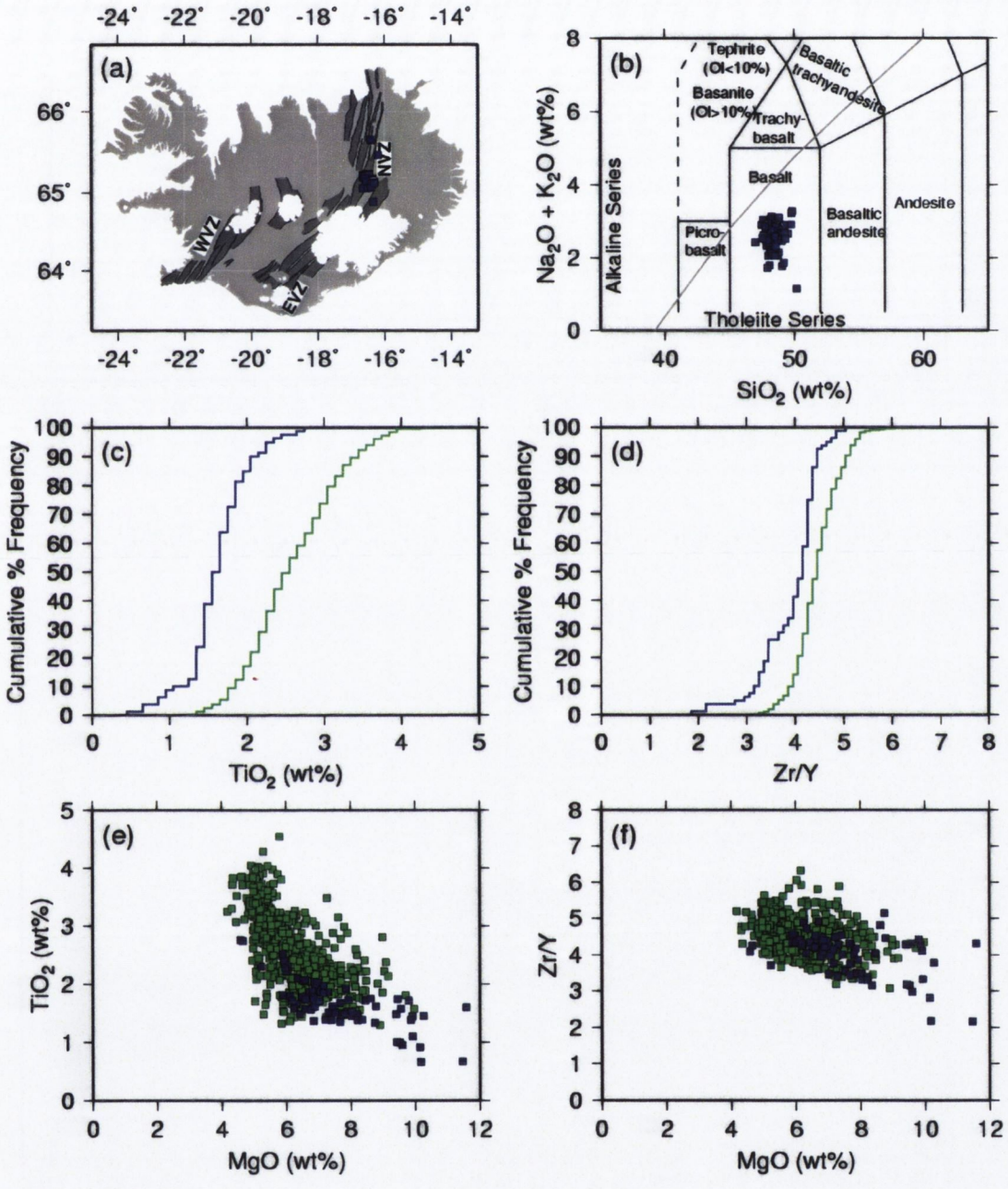

Figure 5.21: Diagrams comparing Tertiary data with the central Northern Volcanic Zone. (a) and (b) show the sample locations and total alkali-silica diagram for the central Northern Volcanic Zone. (c) and (d) are cumulative % frequency diagrams for TiO_2 wt% and Zr/Y ratio: Tertiary - green, central Northern Volcanic Zone - blue. (e) and (f) show the variation in TiO_2 wt% and Zr/Y with MgO wt% for the central Northern Volcanic Zone (blue squares) and the Tertiary (green squares).

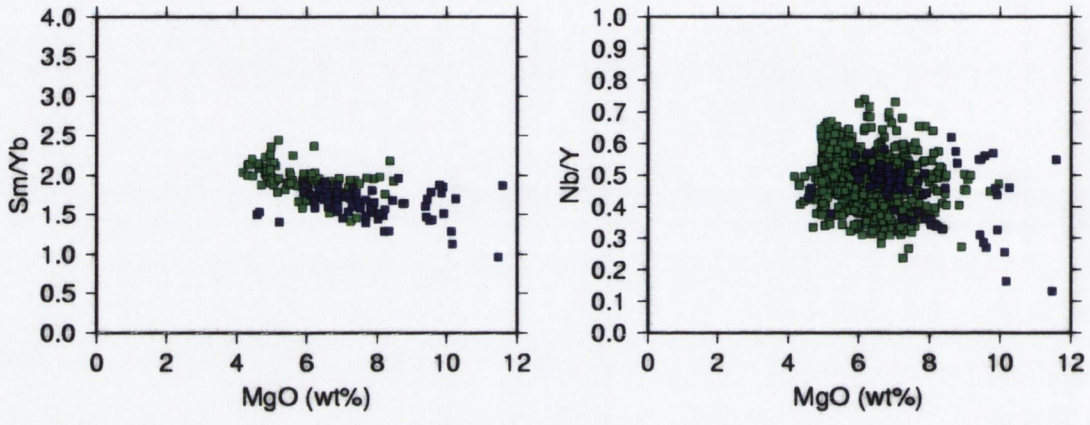

Figure 5.22: Sm/Yb and Nb/Y variations with MgO wt% for the central Northern Volcanic Zone (blue squares) and the Tertiary (green squares). The Sm/Yb data for the Tertiary is only available for East Iceland (Kitagawa et al., 2008).

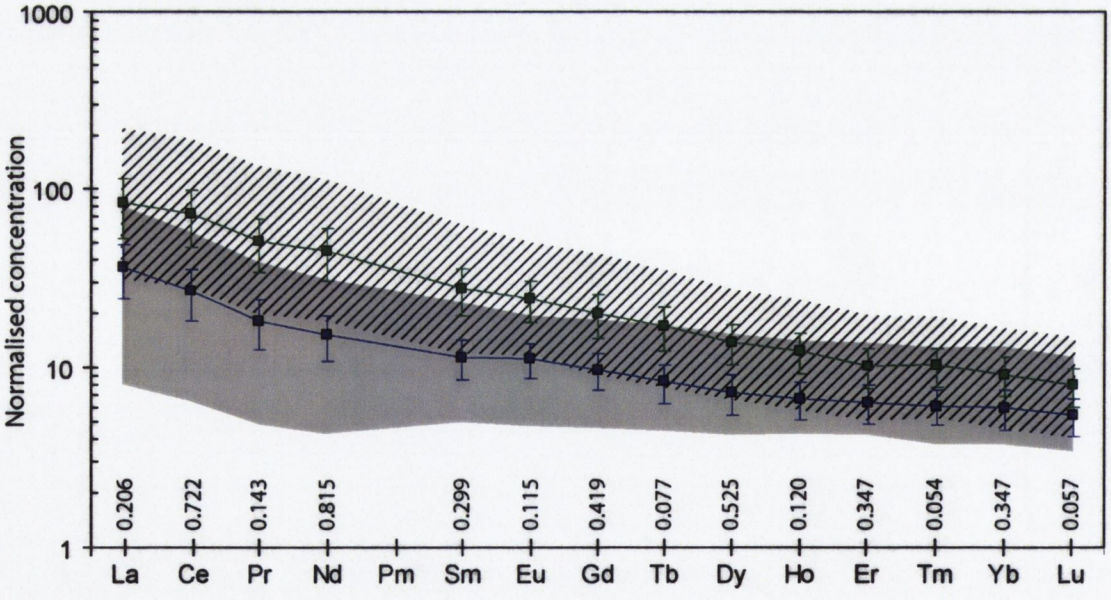

Figure 5.23: The average REE concentrations (±1 S.D.) for East Tertiary (green squares; Kitagawa et al., 2008; n=96) and central Northern Volcanic Zone (blue squares; n=79), normalised to MORB source mantle (McKenzie and O'Nions, 1991). The striped area covers the range of East Tertiary data and the solid grey area covers the range of central Northern Volcanic Zone data.

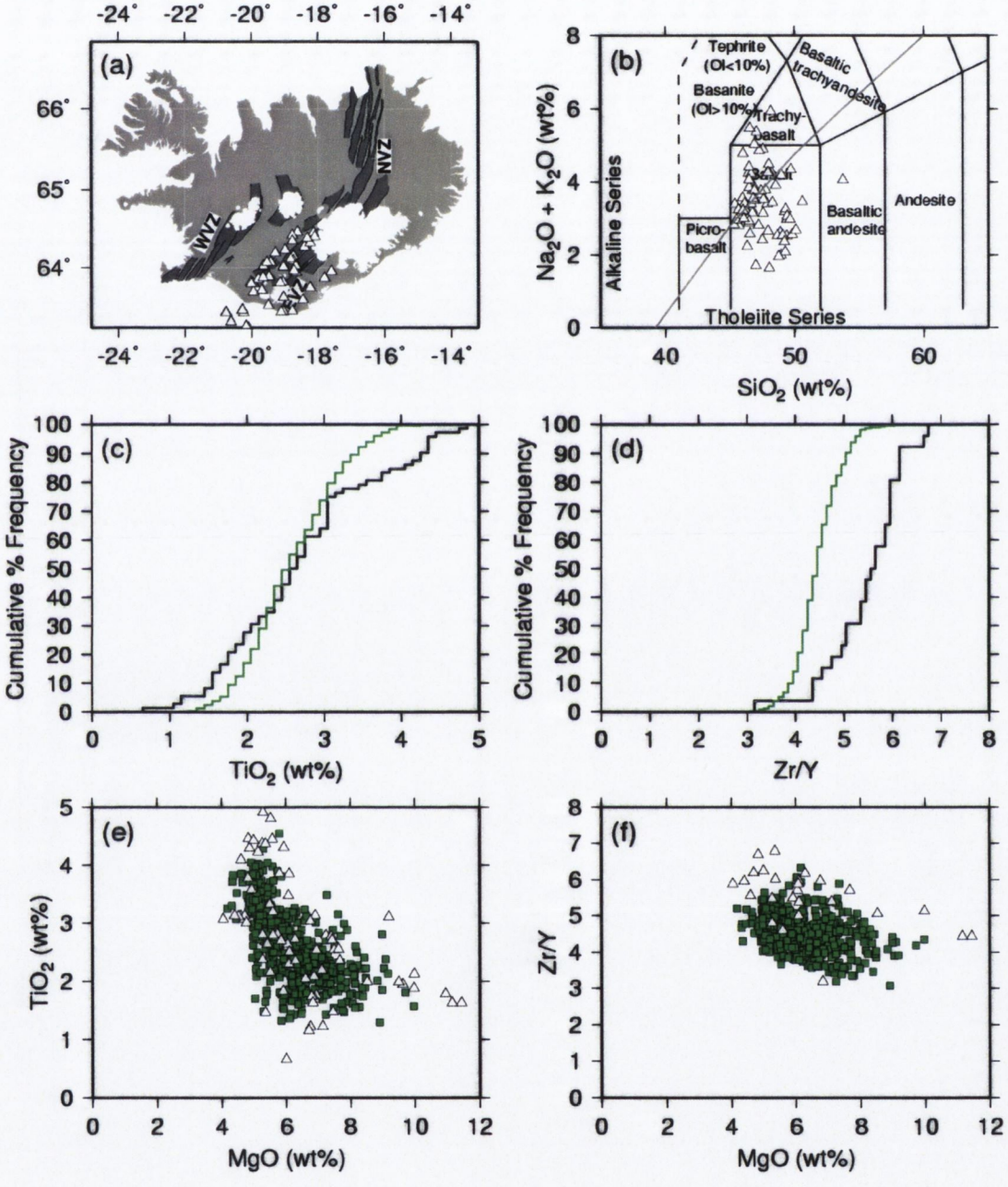

Figure 5.24: Diagrams comparing Tertiary data with the Eastern Volcanic Zone. (a) and (b) show the sample locations and total alkali-silica diagram for the Eastern Volcanic Zone. (c) and (d) are cumulative % frequency diagrams for TiO_2 wt% and Zr/Y ratio: Tertiary - green, Eastern Volcanic Zone - black. (e) and (f) show the variation in TiO_2 wt% and Zr/Y with MgO wt% for the Eastern Volcanic Zone (white triangles) and the Tertiary (green squares).

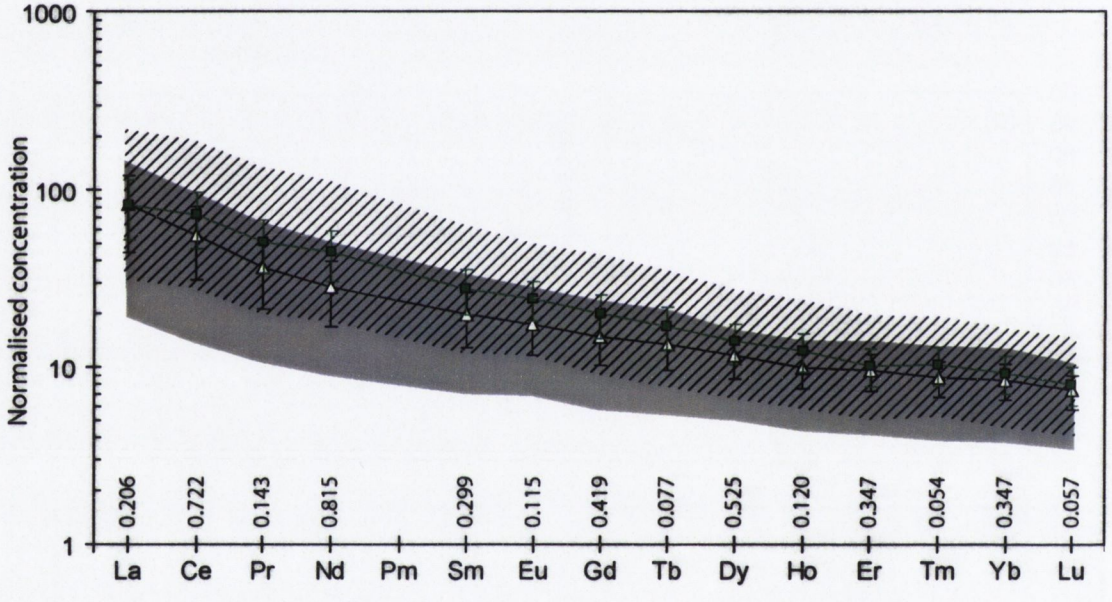

Figure 5.25: The average REE concentrations (±1 S.D.) for East Tertiary (green squares; Kitagawa et al., 2008; n=96) and Eastern Volcanic Zone (white triangles; n=26), normalised to MORB source mantle (McKenzie and O'Nions, 1991). The striped area covers the range of East Tertiary data and the solid grey area covers the range of Eastern Volcanic Zone data.

5.4.2 Tertiary versus Off-axis Volcanism

A comparison is made between the Tertiary data and off-axis volcanic systems and features to assess the preservation potential and possible contribution to the Tertiary lava pile off-axis volcanism could make. Off-axis volcanism is not addressed in the Pálmason model of crustal accretion at Iceland. Considering the predicted transport of material downwards and outwards from the centre of the rift axis it suggests that present day off-axis volcanic centres will not be easily buried by subsequent lava flows and will remain at the surface as the crust spreads away from the axis. The preservation of these volcanic centres will be controlled by erosion.

Grímsnes is an off-axis volcanic feature associated with the Western Volcanic Zone, situated approximately 15 km east of the main volcanic systems. It is characterised by tholeiitic basalts as shown by the total alkali-silica diagram (figure 5.26). There are relatively few (16) samples for Grímsnes that have been analysed for geochemistry with only two samples that have REE concentrations analysed. The distributions of Ti concentrations and Zr/Y ratios for Grímsnes lie well within the Tertiary data. The Ti concentrations from Grímsnes are at the lower end of the range of values shown by the Tertiary, correlating well with the variation with MgO. The Zr/Y ratio from Grímsnes covers the higher Zr/Y values shown by the Tertiary, however, Grímsnes plots significantly higher for Zr/Y for the same MgO composition from the Tertiary. The two sets of REE data for Grímsnes show slightly more light REE enrichment compared to the Tertiary (figure 5.27). The two Grímsnes samples have low absolute values within the range of the Tertiary and, together with the low Ti concentrations, this observation may reflect differing fractional crystallisation processes compared to the bulk of the Tertiary. These geochemical characteristics provide good evidence that any material that was produced just off-axis may be preserved in the exposed Tertiary crust and this conclusion is consistent with the observation of the potential transport of off-axis material according to Pálmason's model.

Snaefellsnes volcanic belt is a much larger off-axis volcanic system than Grímsnes located on the Snaefellsnes peninsula in western Iceland. Snaefellsnes activity is separated from the main rift zones by a minimum of 50 km. The 27 basalt samples plot mostly as tholeiitic basalts with just 6 samples plotting within the alkaline series (figure 5.28). Snaefellsnes is well known for its alkaline volcanism suggesting that the samples in the database may be biased towards tholeiites. The TiO_2 concentrations for Snaefellsnes exhibit a very similar distribution to the Tertiary data and correlate well with the variation in TiO_2 with MgO. The Zr/Y ratios are significantly different

with much higher skew than the Tertiary data and a much wider range of values. The higher Zr/Y values will reflect the more alkaline samples as they represent small degree deep melts. The REE concentrations are also skewed by the alkaline nature of some of the samples showing a more pronounced light REE enrichment than the Tertiary producing a steeper REE pattern on average indicating a strong influence by deep mantle melting (figure 5.29). The Snaefellsnes REE values remain within the Tertiary range. These observations suggest that it is entirely reasonable that this distinctly off-axis material may be preserved at the surface. However, since it is known that Snaefellsnes is dominated by alkaline volcanism and this is not the case for the Tertiary; off-axis material, if preserved, may only form a small part of the exposed Tertiary crust.

Snaefell is a volcanic centre located in central-east Iceland at the northern tip of a flank volcanic zone stretching down to Öraefajökull. It is situated approximately 25 km off-axis, east of the central part of the Northern Volcanic Zone (Kverkfjöll system). It is characterised by a bi-modal distribution of lavas with a broadly alkaline-transitional and a broadly tholeiitic-transitional group of basalts as shown in figure 5.30 by the total alkali-silica diagram. The TiO_2 concentrations and the trace element signature are very similar to Snaefellsnes. The TiO_2 distribution is very similar to the Tertiary, with a similar range of values for the same MgO composition. The bi-modal distribution of compositions at Snaefell is reflected in the Zr/Y values, with very high values for the alkaline series and similar values to the Tertiary for the tholeiitic series. The REE for Snaefell show slightly more light REE enrichment than the Tertiary data, but the values remain broadly within the Tertiary range (figure 5.31). This REE pattern is consistent with the effects of the alkaline samples on the whole data set from Snaefell. Again, these observations are consistent with the idea that off-axis material can be preserved, but may only form a small proportion of the exposed Tertiary crust.

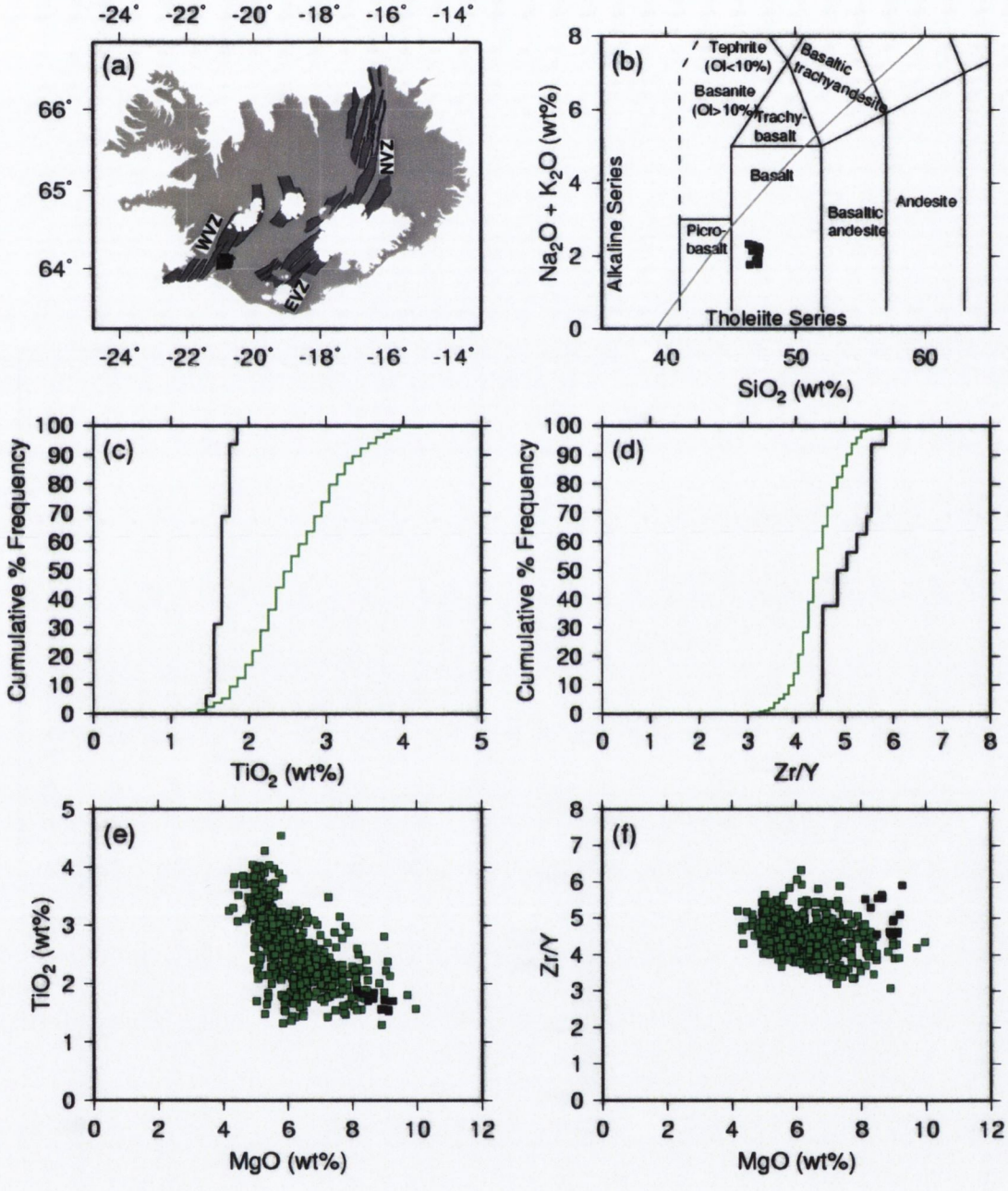

Figure 5.26: Diagrams comparing Tertiary data with the Grímsnes system associated with the Western Volcanic Zone. (a) and (b) show the sample locations and total alkali-silica diagram for Grímsnes. (c) and (d) are cumulative % frequency diagrams for TiO_2 wt% and Zr/Y ratio: Tertiary - green, Grímsnes - black. (e) and (f) show the variation in TiO_2 wt% and Zr/Y with MgO wt% for Grímsnes (black squares) and the Tertiary (green squares).

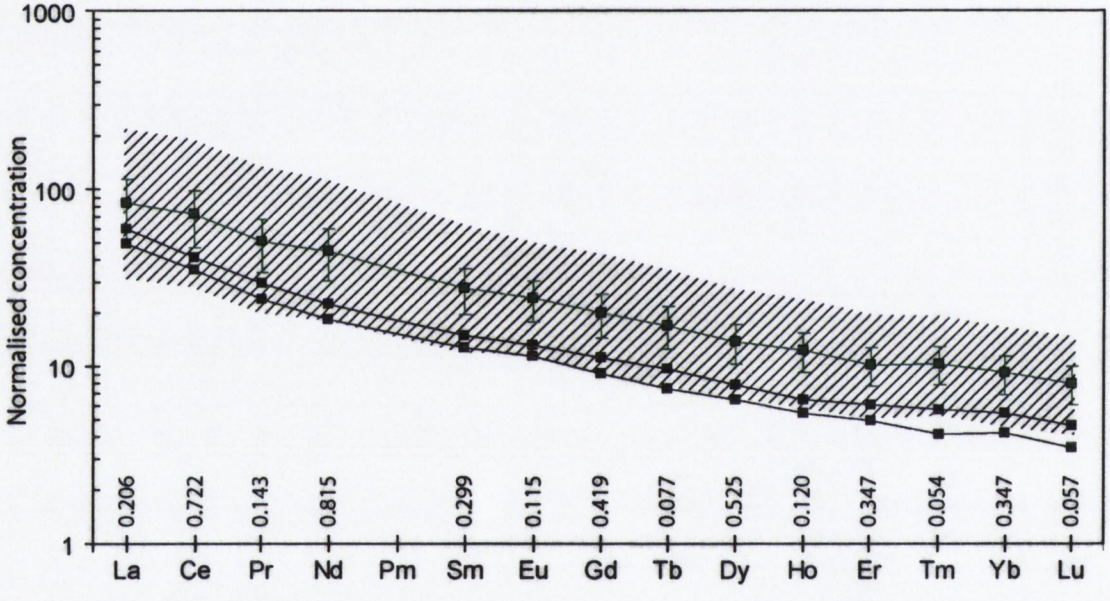

Figure 5.27: The average REE concentrations (±1 S.D.) for East Tertiary (green squares; Kitagawa et al., 2008; n=96) and Grímsnes (black squares; n=2), normalised to MORB source mantle (McKenzie and O'Nions, 1991). The striped area covers the range of East Tertiary data and the solid grey area covers the range of Grímsnes data.

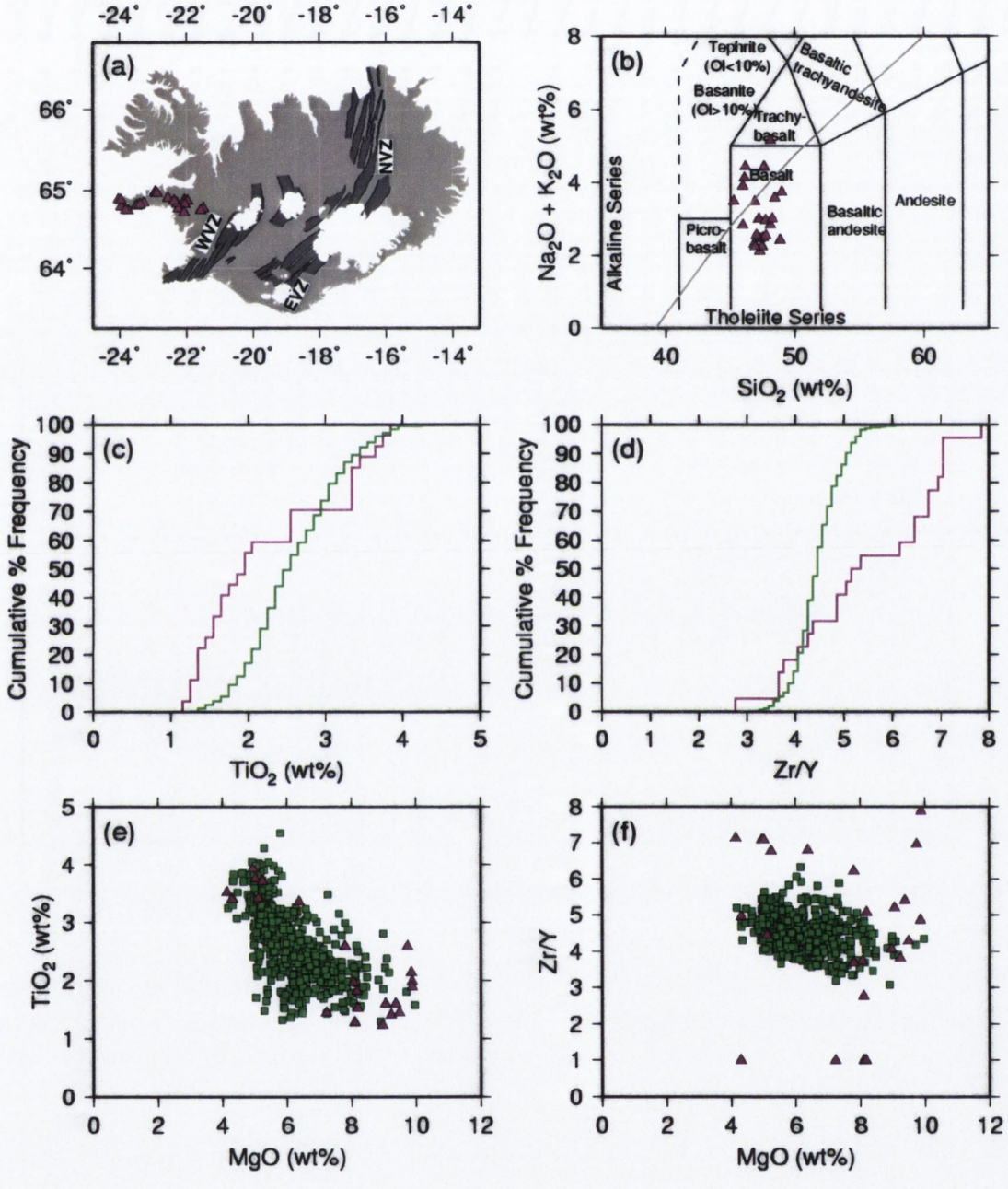

Figure 5.28: Diagrams comparing Tertiary data with the Snaefellsnes volcanic zone. (a) and (b) show the sample locations and total alkali-silica diagram for the Snaefellsnes volcanic zone. (c) and (d) are cumulative % frequency diagrams for TiO_2 wt% and Zr/Y ratio: Tertiary - green, Snaefellsnes volcanic zone - purple. (e) and (f) show the variation in TiO_2 wt% and Zr/Y with MgO wt% for the Snaefellsnes volcanic zone (purple triangles) and the Tertiary (green squares).

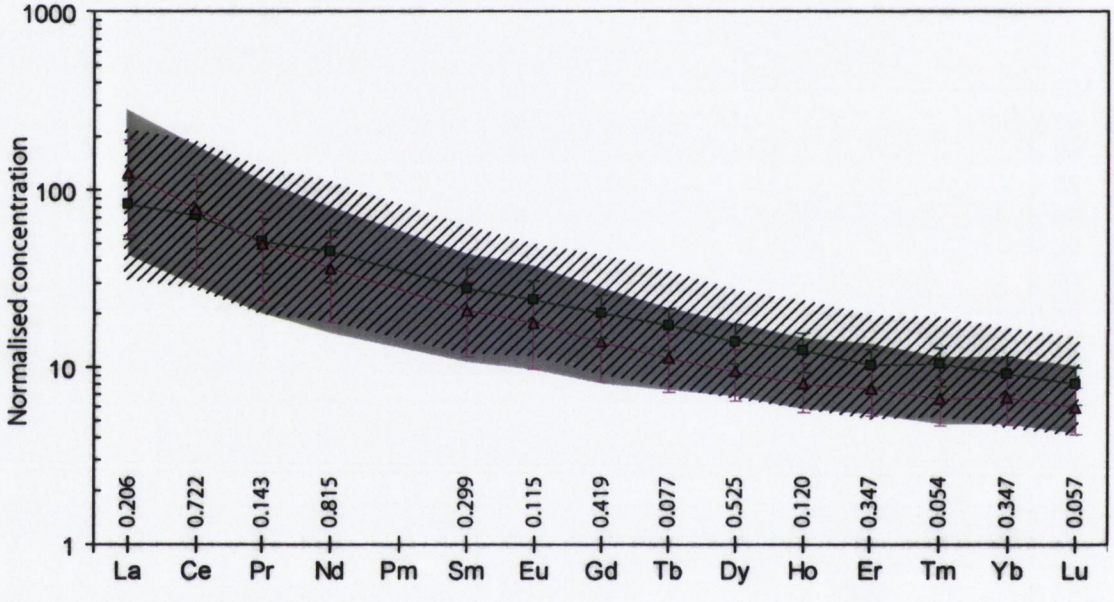

Figure 5.29: The average REE concentrations (±1 S.D.) for East Tertiary (green squares; Kitagawa et al., 2008; n=96) and Snaefellsnes volcanic zone (purple triangles; n=17), normalised to MORB source mantle (McKenzie and O'Nions, 1991). The striped area covers the range of East Tertiary data and the solid grey area covers the range of Snaefellsnes volcanic zone data.

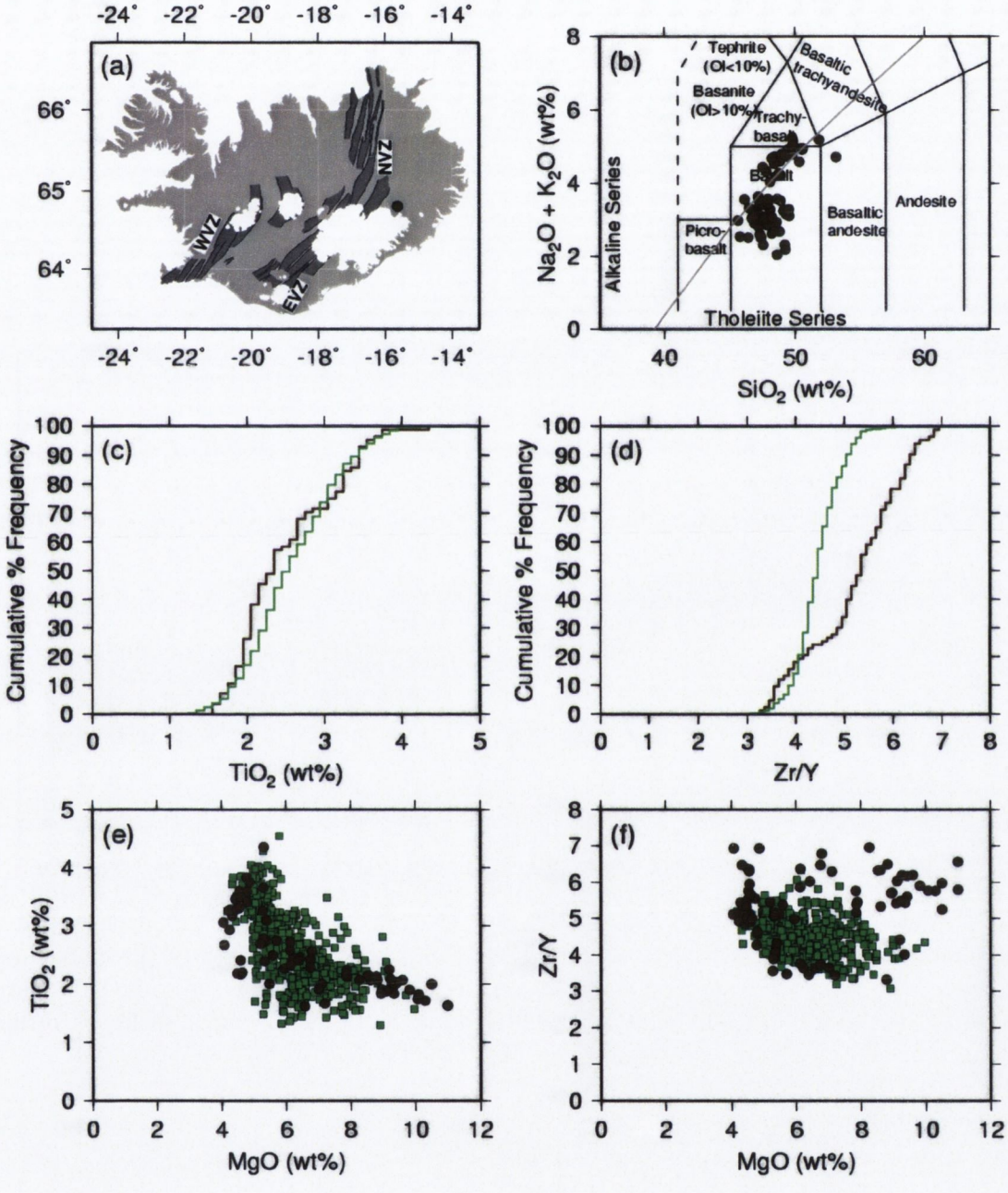

Figure 5.30: Diagrams comparing Tertiary data with the Snaefell volcanic centre associated with the Öraefajökull system. (a) and (b) show the sample locations and total alkali-silica diagram for Snaefell. (c) and (d) are cumulative % frequency diagrams for TiO_2 wt% and Zr/Y ratio: Tertiary - green, Snaefell - brown. (e) and (f) show the variation in TiO_2 wt% and Zr/Y with MgO wt% for Snaefell (brown circles) and the Tertiary (green squares).

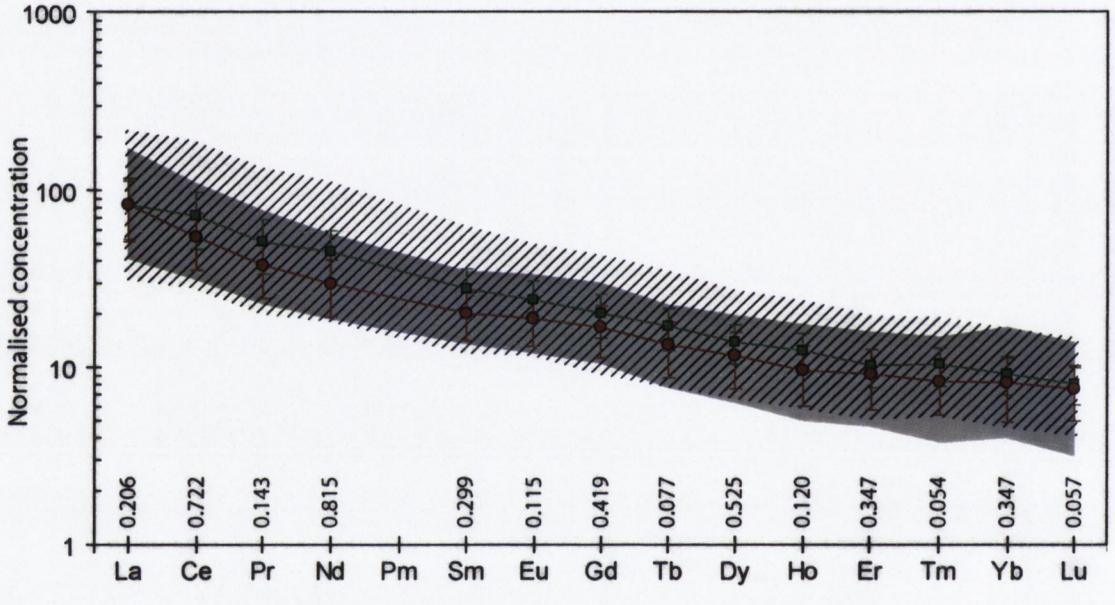

Figure 5.31: The average REE concentrations (±1 S.D.) for East Tertiary (green squares; Kitagawa et al., 2008; n=96) and Snaefell (brown circles; n=26), normalised to MORB source mantle (McKenzie and O'Nions, 1991). The striped area covers the range of East Tertiary data and the solid grey area covers the range of Snaefell data.

5.4.3 Tertiary versus Stóravíti

Stóravíti is one of the largest lava flows from the neovolcanic zones at Iceland, forming a post-glacial lava shield associated with the Theistareykir system in the Northern Volcanic Zone. The geochemical signature compared to the Tertiary data is shown in figure 5.32. All the samples plots as tholeiitic basalts. The TiO_2 and Zr/Y distributions and variations with MgO are clearly much lower than the Tertiary data, indicating that Stóravíti is much more depleted in incompatible elements. The absolute REE concentrations are much lower and exhibit a much flatter REE pattern than the East Tertiary data with a distinctive positive Europium anomaly (figure 5.33). The Eu anomaly probably reflects accumulated plagioclase during melt residence and transport.

Hardarson and Fitton (1997) observed that only the largest lava flows that escape the rift axis will be preserved in the exposed Tertiary crust according to Pálmason's model of crustal accretion (section 5.2). Although Hardarson and Fitton concluded that any large lava flows from the neovolcanic zones show consistent chemistry with Tertiary lavas, such consistency is not observed between the Tertiary and Stóravíti. This issue is discussed further in section 5.5.

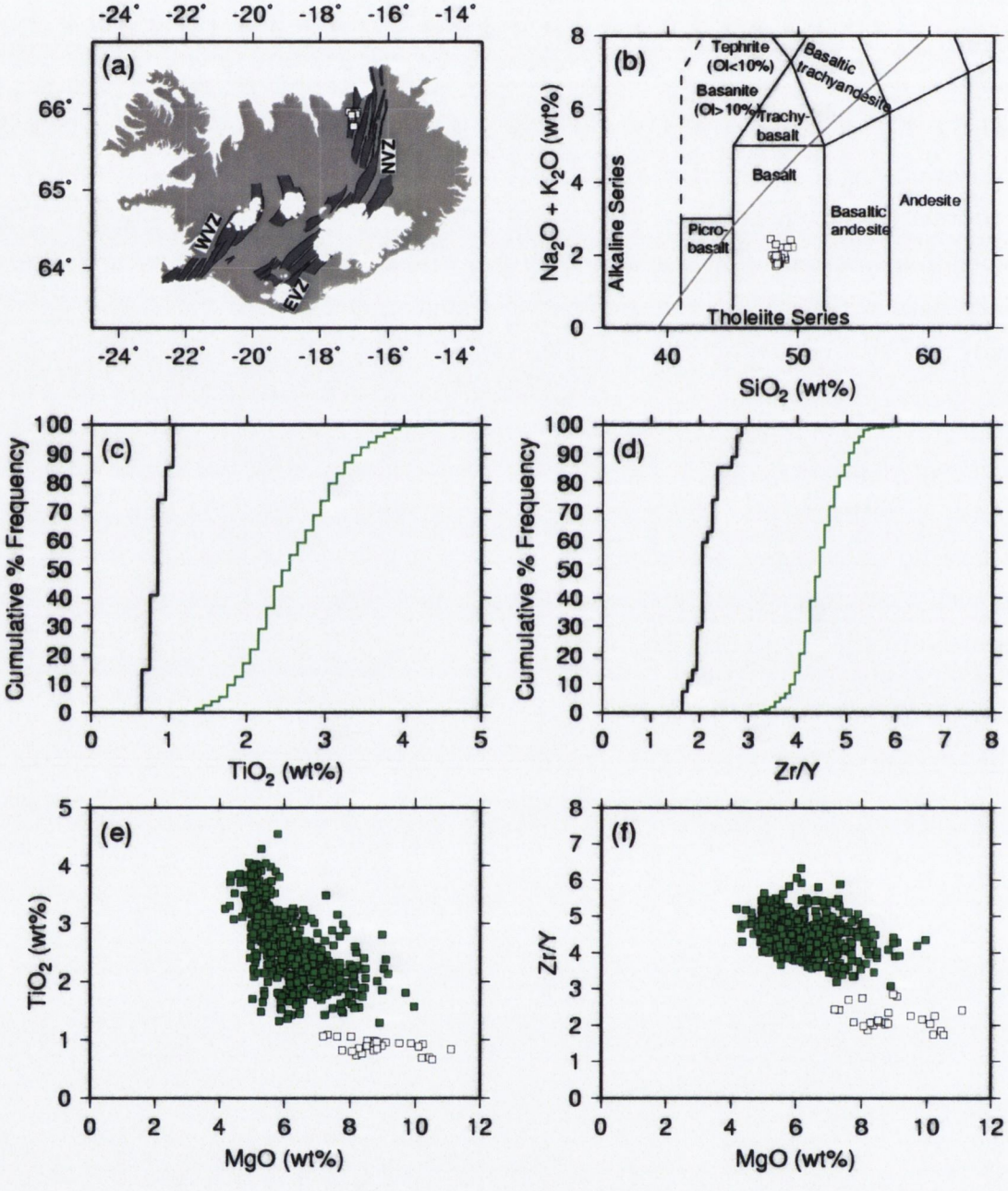

Figure 5.32: Diagrams comparing Tertiary data with Stóravíti lava shield from the Theistareykir system. (a) and (b) show the sample locations and total alkali-silica diagram for Stóravíti. (c) and (d) are cumulative % frequency diagrams for TiO_2 wt% and Zr/Y ratio: Tertiary - green, Stóravíti - black. (e) and (f) show the variation in TiO_2 wt% and Zr/Y with MgO wt% for Stóravíti (white squares) and the Tertiary (green squares).

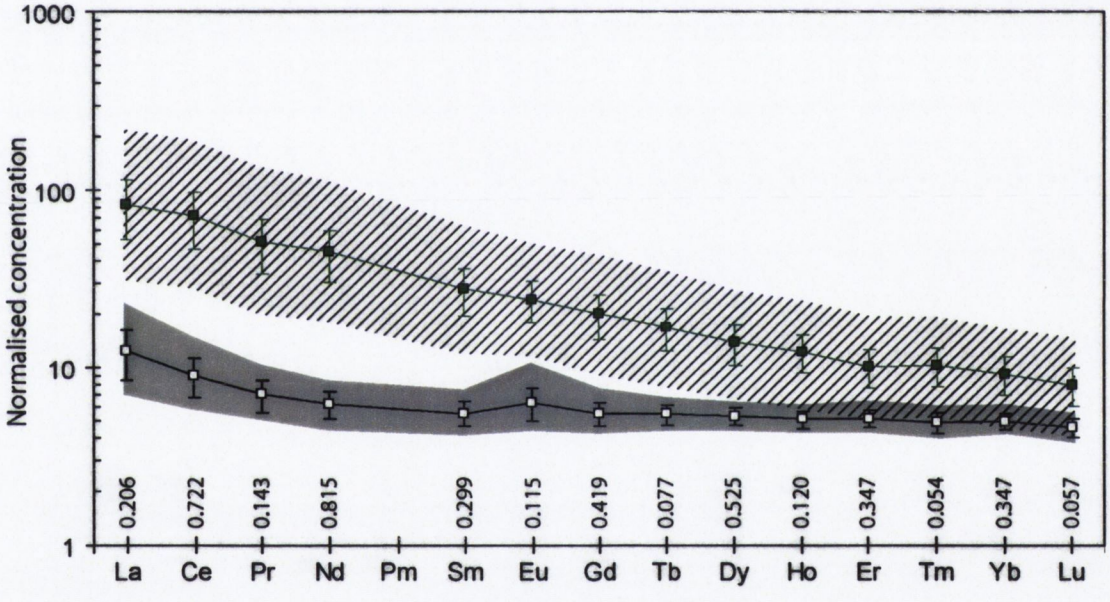

Figure 5.33: The average REE concentrations (±1 S.D.) for East Tertiary (green squares; Kitagawa et al., 2008; n=96) and Stóravíti (white squares; n=25), normalised to MORB source mantle (McKenzie and O'Nions, 1991). The striped area covers the range of East Tertiary data and the solid grey area covers the range of Stóravíti data.

5.4.4 Tertiary versus Extinct Skagi Rift

The new data obtained from the Quaternary lava flows associated with the late stages of activity of the extinct Skagi rift are compared to the Tertiary data (figure 5.34). It has already been in observed in section 3.5 that there is negligible difference in the geochemical signature between the few Tertiary samples collected from the Skagi peninsula and the Quaternary flows. This comparison is used to show that the similarity between the Skagi Quaternary and Tertiary extends to the whole of the Tertiary dataset.

The tholeiitic basalts from Skagi have a TiO_2 distribution well within that of the Tertiary data, plotting at the higher end of the values. The Skagi samples also have a very similar distribution of Zr/Y values. The TiO_2 and Zr/Y values for Skagi plot within the Tertiary range of data at the same MgO composition. The Skagi REE pattern is also very similar to the Tertiary data (figure 5.35). The later stages of a rift will be preserved at the surface in older crust according to Pálmason's model. The preservation of the last eruptions will be limited by location i.e. they will only be found in close proximity to extinct rift axes. The only recognised on-shore extinct rift axis is the Skagi-Snaefellsnes rift. The similarity of the geochemical signatures of the Tertiary and Skagi Quaternary lavas is discussed in section 5.5.

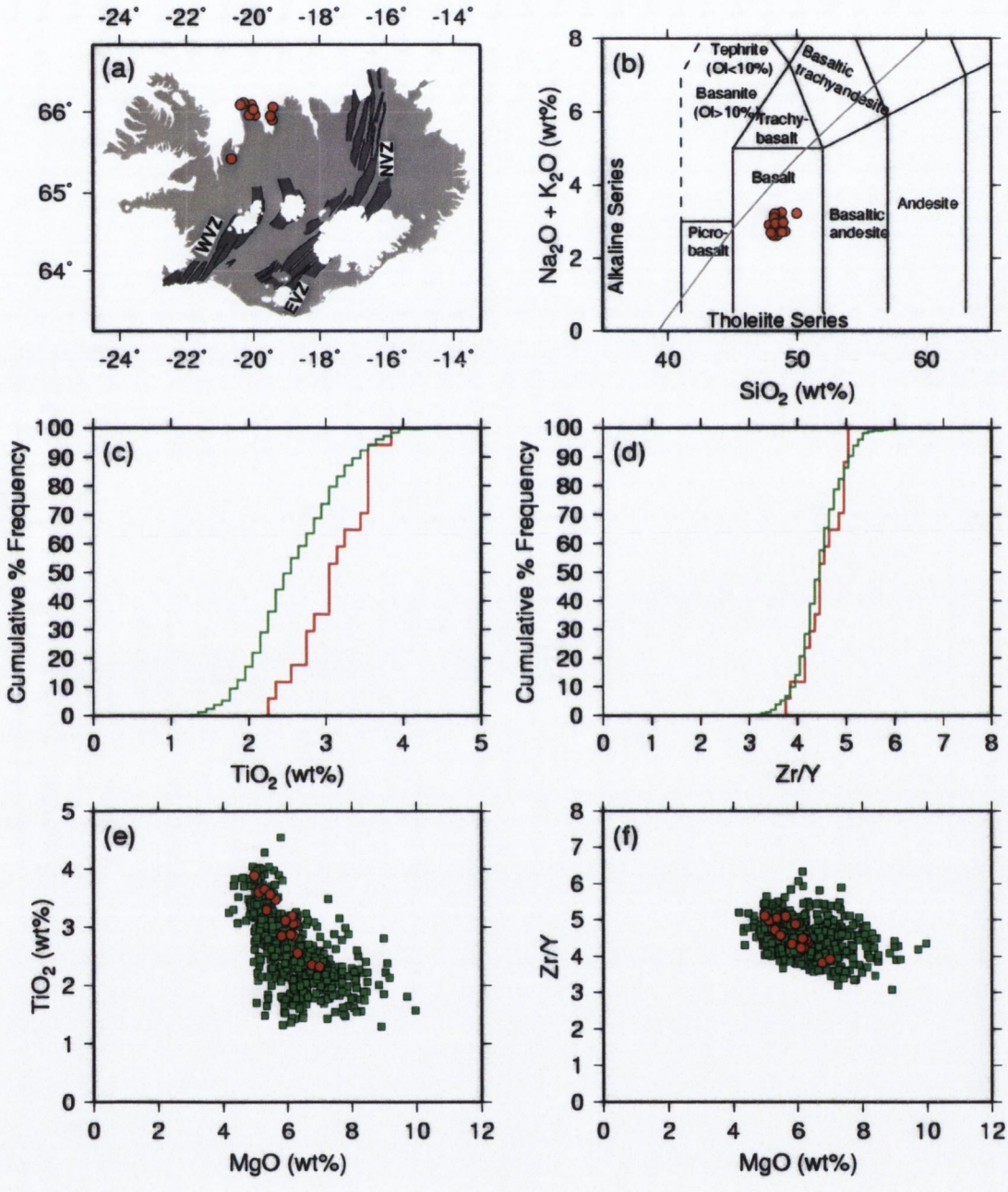

Figure 5.34: Diagrams comparing Tertiary data with Quaternary lava flows from the extinct Skagi rift. (a) and (b) show the sample locations and total alkali-silica diagram for Skagi. (c) and (d) are cumulative % frequency diagrams for TiO_2 wt% and Zr/Y ratio: Tertiary - green, Skagi - red. (e) and (f) show the variation in TiO_2 wt% and Zr/Y with MgO wt% for Skagi (red circles) and the Tertiary (green squares).

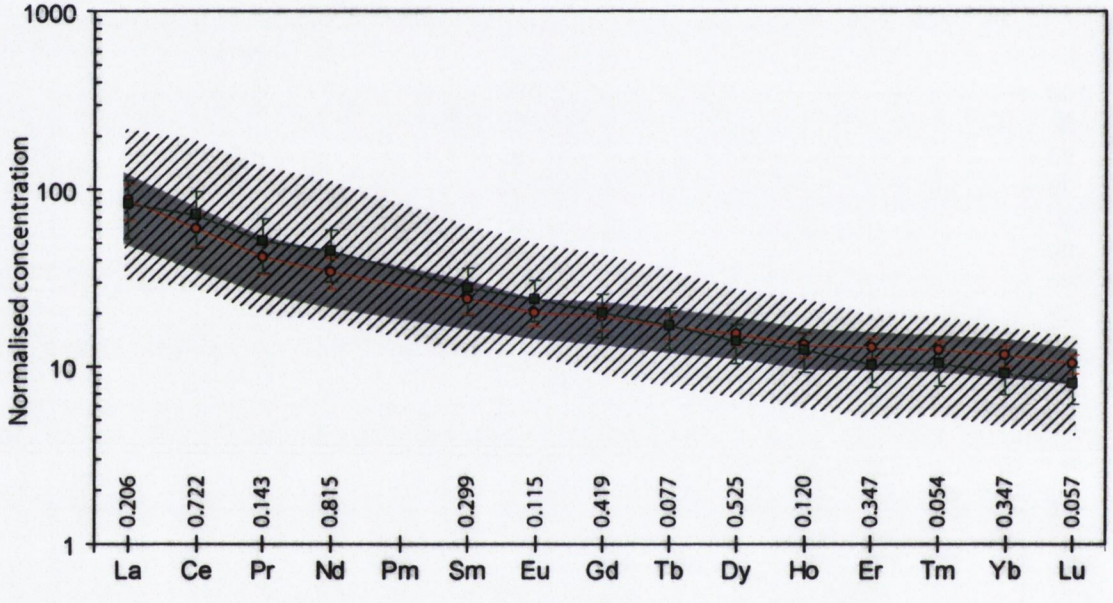

Figure 5.35: The average REE concentrations (±1 S.D.) for East Tertiary (green squares; Kitagawa et al., 2008; n=96) and Skagi Quaternary lavas (red circles; n=17), normalised to MORB source mantle (McKenzie and O'Nions, 1991). The striped area covers the range of East Tertiary data and the solid grey area covers the range of Skagi data.

5.4.5 Dyke Chemistry

New major and trace element data were obtained using XRF at the University of Edinburgh for 24 dyke samples donated by S. Garcia from the Garcia et al. (2003) study. This new data is combined with 22 dyke samples from the Skagi region and 10 samples from the Northwest Tertiary to investigate the variability in dyke chemistry in northern Iceland, compared with the Tertiary and the Northern Volcanic Zone. Only 14 samples from Skagi and the surrounding region were analysed by ICP-MS for REE concentrations and these are compared to the East Tertiary data from Kitagawa et al. (2008). The exposure of dykes at the surface in older crust is not explained by the Pálmason model. Most on-axis intrusions will according to the Pálmason model be advected downwards and outwards from the spreading axis, and will only be exposed by erosion if they are intruded and remain within the top 2 km of the crust.

Firstly, the dyke data set is separated by region to show any major differences in dyke chemistry that may be related to location (figure 5.36). Fe_2O_3, TiO_2, Zr and Nb all exhibit broad incompatible element trends showing increase in concentration with decreasing MgO as would be expected from fractional crystallisation processes. The Northwest samples in particular for Fe_2O_3, TiO_2 and Zr plot slightly below the main trend from the rest of northern Iceland dykes, which may indicate the effects of mixing in these samples. Again we see a difference in Nb for the Northwest, plotting within the main data trend for single element concentration, and significantly higher for Nb/Y than the rest of the data. This Nb problem is discussed in section 5.5. The Zr/Y ratio plots similar to the range shown by the Tertiary data with values between 3 and 6 (section 5.3). However, there is a significant group of central northern Iceland samples plotting with lower Zr/Y values which may indicate that they represent slightly higher degrees of melting than those samples related to the Northern Volcanic Zone (northeast Iceland) and those from the Northwest. For comparison with the Tertiary the samples are treated as a one dataset.

Most of the dykes plot as tholeiitic basalts with one picro-basalt sample (figure 5.37). This observation indicates that they are not intruded widely off-axis as the dykes would then have an alkaline chemistry like Snaefell volcanic centre and Snaefellsnes. The geochemical comparison shows that the dykes' TiO_2 concentrations and Zr/Y ratio compares well with the Tertiary data. This correlation indicates a similar melting regime; not unexpected as more than two thirds of the dyke samples have Tertiary ages. The dykes' REE concentrations show light REE enrichment similar to the Tertiary. On average the Tertiary REE pattern is slightly steeper, but the dyke REE concentrations

still lie within the range of the Tertiary (figure 5.38). The similarity in the geochemical signature may be due to the fact that many of the dykes are Tertiary age or it could be a slightly off-axis signature. This similarity is discussed in section 5.5.

11 dyke samples from Garcia et al. (2003) study are related to the Northern Volcanic Zone according to the plate spreading velocity model and age constraints (section 2.1.3). Considering the assumption these dykes are all on-axis intrusions providing the basis for the validity of the rift relocation model, it would be expected that they would have a similar chemical signature to the Northern Volcanic Zone rift products. Figure 5.39 shows that this is not the case. The distribution of values for TiO_2 concentrations and Zr/Y values are much higher for the Northern Volcanic Zone dykes compared to lava flows from the Theistareykir and Krafla systems.

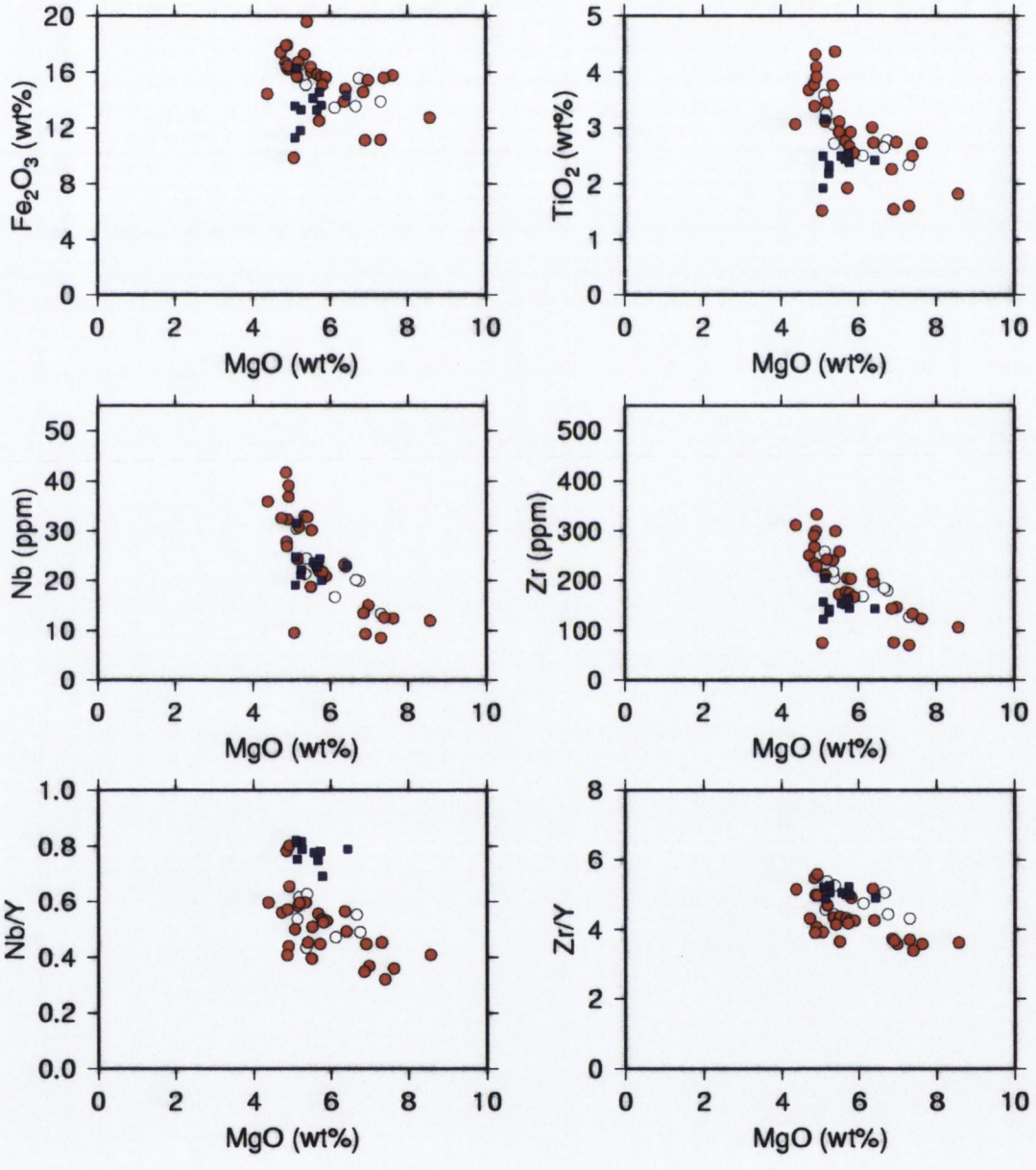

Figure 5.36: Variation diagrams showing MgO wt% versus incompatible major and trace element concentrations and ratios for dyke samples from across northern Iceland. Northwest samples - blue squares (G. Fitton), central North Iceland - red circles and Northeast Iceland - white circles.

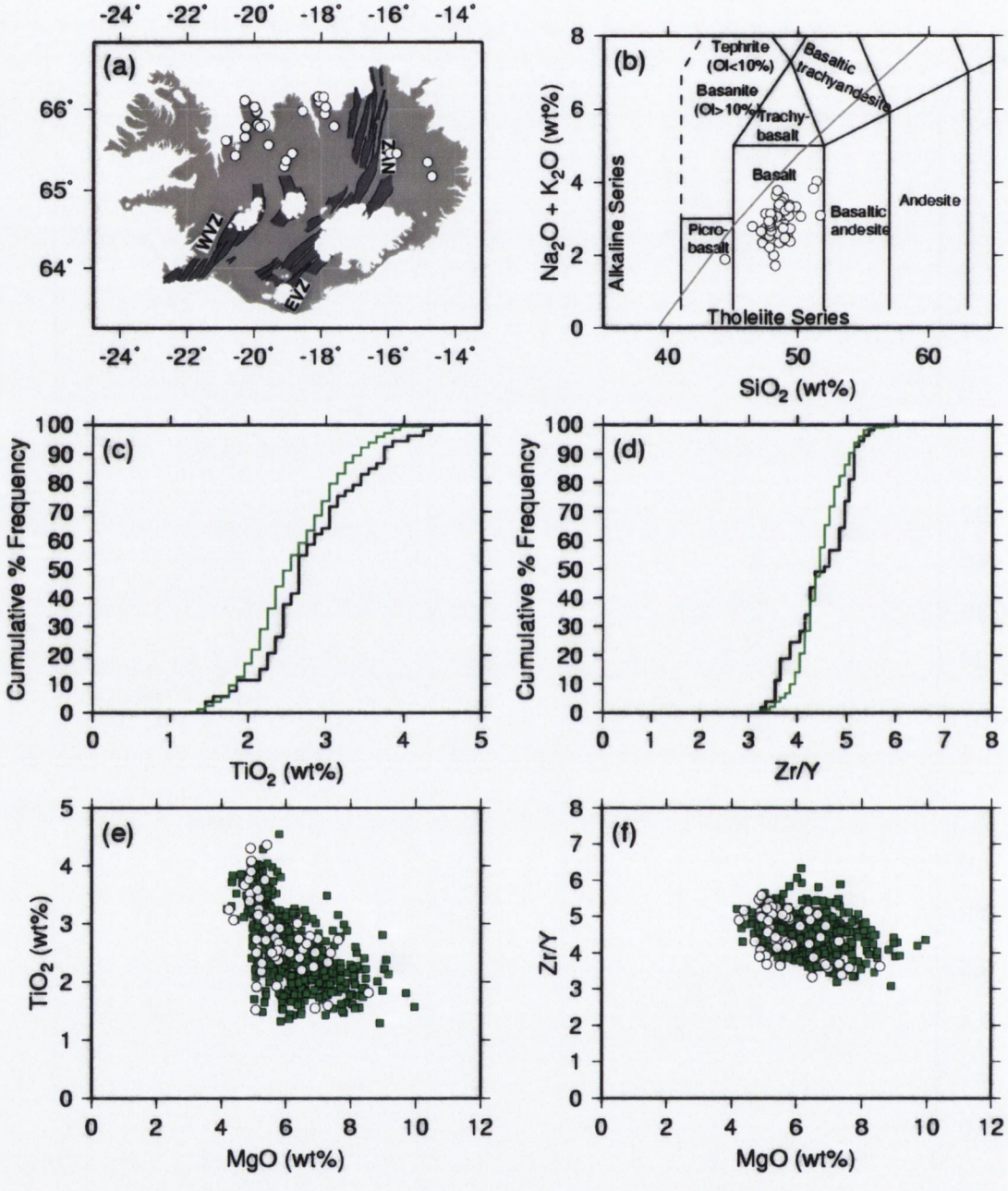

Figure 5.37: Diagrams comparing Tertiary data with dyke intrusions from across northern Iceland. (a) and (b) show the sample locations and total alkali-silica diagram for dyke intrusions. (c) and (d) are cumulative % frequency diagrams for TiO_2 wt% and Zr/Y ratio: Tertiary - green, dykes - black. (e) and (f) show the variation in TiO_2 wt% and Zr/Y with MgO wt% for dyke intrusions (white circles) and the Tertiary (green squares).

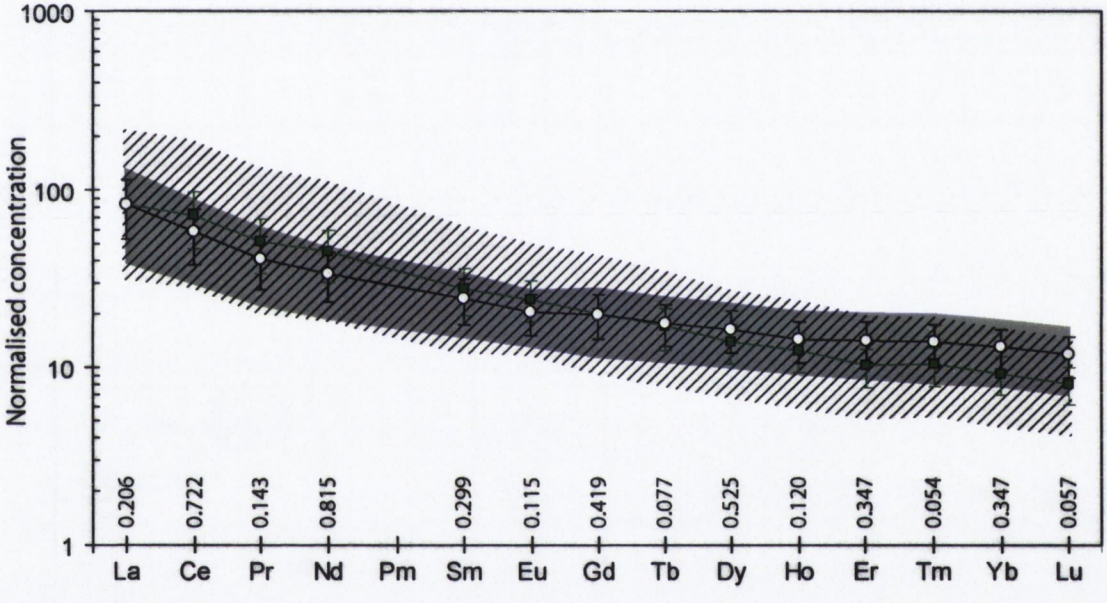

Figure 5.38: The average REE concentrations (±1 S.D.) for East Tertiary (green squares; Kitagawa et al., 2008; n=96) and dyke intrusions from across northern Iceland (white circles; n=29), normalised to MORB source mantle (McKenzie and O'Nions, 1991). The striped area covers the range of East Tertiary data and the solid grey area covers the range of the dyke data.

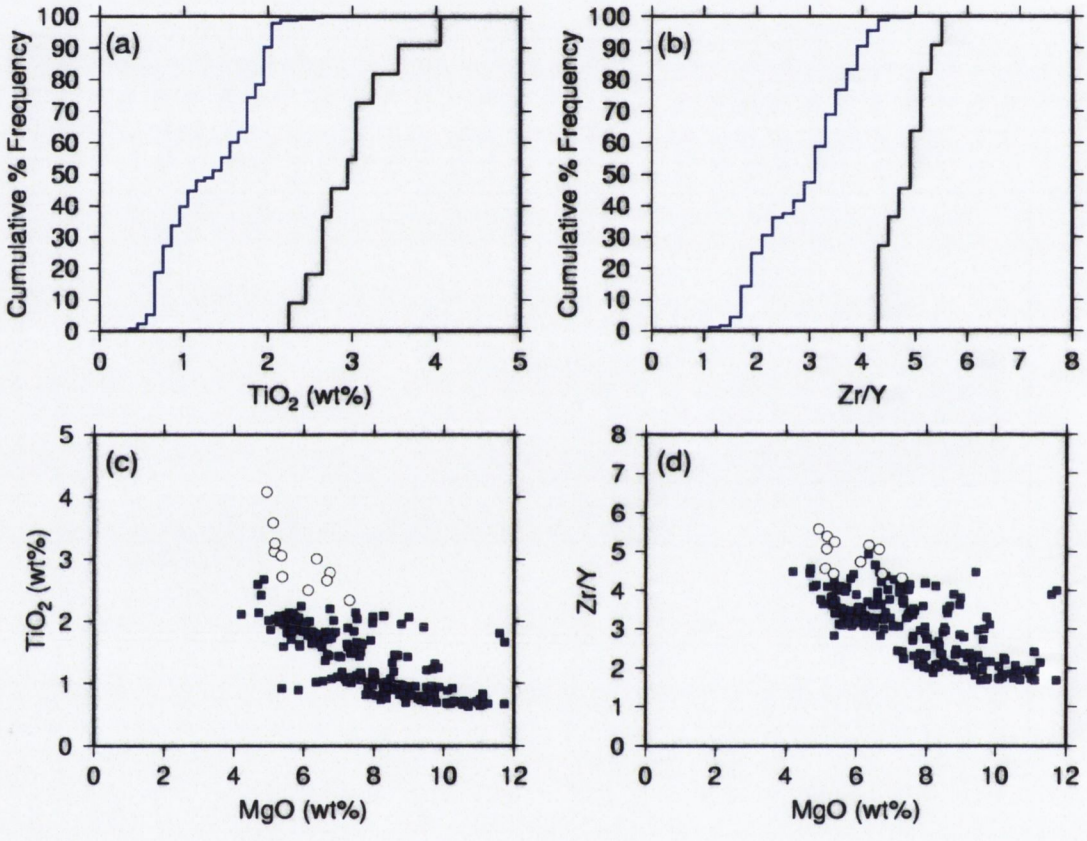

Figure 5.39: Cumulative % frequency diagrams comparing (a) TiO_2 and (b) Zr/Y values for the Theistareykir and Krafla volcanic systems from the northern part of the Northern Volcanic Zone with dykes associated with the Northern Volcanic Zone according to Garcia et al. (2003) velocity model. (c) and (d) show the variation of TiO_2 wt% and Zr/Y with MgO wt% for dyke intrusions (white circles) and the Northern Volcanic Zone (Theistareykir and Krafla systems; blue squares).

5.4.6 Statistical Analysis

A quantitative analysis of the comparison between the Tertiary and volcanic zones and features across Iceland is provided in table 5.1. The Kolmogorov-Smirnov (K-S) statistical test is used to determine the probability that one distribution of values has the same distribution as another. The D value is the maximum vertical distance between two cumulative % frequency distributions and a measure of the difference between the two distributions. Small probabilities indicate that the two distributions are significantly different. The K-S statistical test is good at finding shifts in the probability distribution, but not at detecting changes in the spread of the distribution.

Data 1	n1	Data 2	n2	Element	D	Probability
Western Volcanic Zone	339	Tertiary	650	TiO_2	0.83	0.
	332		650	Zr/Y	0.86	0.
Northern Volcanic Zone	246	Tertiary	650	TiO_2	0.78	0.
Theistareykir & Krafla	245		650	Zr/Y	0.76	0.
Northern Volcanic Zone	80	Tertiary	650	TiO_2	0.71	5.90×10^{-33}.
Central Systems	80		650	Zr/Y	0.39	2.29×10^{-10}
Eastern Volcanic Zone	72	Tertiary	650	TiO_2	0.16	7.68×10^{-2}.
	28		650	Zr/Y	0.68	9.13×10^{-12}
Grímsnes	16	Tertiary	650	TiO_2	0.90	3.61×10^{-12}.
	16		650	Zr/Y	0.56	5.29×10^{-5}
Snaefell	84	Tertiary	650	TiO_2	0.18	1.44×10^{-2}.
	83		650	Zr/Y	0.54	2.67×10^{-19}
Snaefellsnes	27	Tertiary	650	TiO_2	0.42	1.26×10^{-4}.
	23		650	Zr/Y	0.49	2.26×10^{-5}
Skagi Quaternary	17	Tertiary	650	TiO_2	0.46	1.12×10^{-3}.
	17		650	Zr/Y	0.15	0.81
Stóravíti	27	Tertiary	650	TiO_2	1.00	3.27×10^{-24}.
	27		650	Zr/Y	1.00	3.27×10^{-24}
Dykes	53	Tertiary	650	TiO_2	0.23	2.24×10^{-2}.
	53		650	Zr/Y	0.23	8.77×10^{-3}
Dykes	11	NVZ	246	TiO_2	0.99	3.24×10^{-10}.
Northern Volcanic Zone	11		245	Zr/Y	0.96	1.18×10^{-9}

Table 5.1: Kolmogorov-Smirnov statistical test results for the Tertiary data compared to different volcanic zones and features across Iceland. The probability is the probability of the null hypothesis, and the null hypothesis is that both distributions are the same. The D value is a fraction between 0 and 1.

In general, the results from the K-S test are consistent with the observations presented throughout this section. Focusing on the distribution of Zr/Y values as reasonable proxy for the range of compositions of mantle melts from a particular region the best

comparison with Tertiary lavas is given by the Skagi Quaternary lavas. Skagi Quaternary lavas have a D value of 0.15 and a probability of 0.81 of having the same distribution as the Tertiary. Despite having a similar range of melt compositions it is unlikely that they result from the same melting regime, this is discussed in section 5.5. The probabilities for the neovolcanic zones and off-axis volcanism are very small indicating that the overall distributions are significantly different. However, the huge difference in sample size must be taken into account. The central systems from the Northern Volcanic Zone clearly plot well within the range of Tertiary data for the same MgO composition (figure 5.21, but have a very low probability from the K-S test due to the low Zr/Y values associated with high MgO compositions not represented in the Tertiary. Central Iceland does have a reasonably low D value of 0.39 for Zr/Y, when compared to the other neovolcanic zones. The probability for central Iceland is exceptionally small despite the variation with MgO showing that there is a considerable overlap with the Tertiary data. The K-S statistic may not be the most appropriate test for this comparison.

5.5 Discussion

The aim of this section is to discuss the implications of the geochemical investigation shown in sections 5.3 and 5.4 with a view to gaining a better understanding of the preservation bias introduced by mechanical crustal accretion processes.

The preliminary assessment of the different regions of the Tertiary, used to identify any major geochemical differences, indicated a systematic difference in the Nb concentrations for the Northwest and East Iceland datasets. The two data sets from east Iceland cover a similar range of ages so the difference cannot be attributed to a temporal variation. The G. Fitton data may be from a different location to the Kitagawa et al. (2008) data in which case the difference could be related to a difference in melting regime or source composition. The other possibility is a systematic error in the precision of the data from one of the laboratories because the G. Fitton data was obtained using XRF and the Kitagawa et al. (2008) data was obtained using ICP-MS. Errors may have been introduced during the preparation of samples for ICP-MS. The difference is also observed between the two sets of data from the Northwest which were both analysed at the University of Edinburgh. The two datasets from the Northwest relate to different rifts which were active over two different time periods. It may be that the two rifts had access to slightly different source compositions as suggested by Hardarson and Fitton

(1997). This Nb difference is also observed within the dyke data with several Northwest samples plotting distinctly higher than the bulk of the data from across northern Iceland (figure 5.36). There is currently no satisfactory explanation for this difference and hence, Nb/Y was not used for comparative purposes.

The Tertiary lavas in general plot as tholeiitic basalts with very few alkaline samples preserved in the exposed crust. This may be because there was very little alkaline volcanism during the Tertiary, or very little alkaline volcanism was preserved from the Tertiary in the exposed crust. However, it could simply be the result of sampling bias by location for example, which may have excluded alkaline flows. The Tertiary samples are taken from the 'trap' type lava flows which clearly represent a large proportion of the exposed Tertiary crust, and it is important that we understand how these large tholeiitic lava flows were formed in the old rift zones.

The lack of substantial alkaline samples from the Tertiary is consistent with the extent of active alkaline volcanism present on Iceland today. The largest volume is produced in the Eastern Volcanic Zone, which represents the birth of a rift axis. It is unlikely that many of the lava flows from early rift axis volcanism will be exposed at the surface as there would be very few if any large lava flows that would escape burial by the more voluminous tholeiitic volcanism which follows once the rift has been established for a few million years. Therefore the few alkaline lava flows which were sampled from the Tertiary (Northwest data) are most likely to be from off-axis volcanism such as Snaefell volcanic centre or Snaefellsnes.

Hardarson and Fitton (1997) suggested that lava flows large enough to escape the rift axis would be preserved in the exposed Tertiary crust and showed using the Zr/Nb ratio that the largest flows from the neovolcanic zones have the same chemistry as the Tertiary. (Figures 5.4 and 5.5). However, many of the highest (depleted) values of Zr/Nb defining the high variability described for small volume lava flows and flows within 5 km of the rift axis are found in postglacial lava flows (and other undefined data). Stóravíti is one of the largest postglacial lava flows erupted as a lava shield from the Northern Volcanic Zone. It is clear from figure 5.32 that the geochemical signature is very different to the Tertiary data. Postglacial volcanism is dominated by lava shield morphology essentially formed by one single massive lava flow which can be up to 8 km^2 in volume. The geochemical signature is generally high MgO, but with a dramatically depleted incompatible trace and REE element signature as shown by the Stóravíti data. This depleted signature results from rapid melting of the upper parts of a depleted melting region following rapid decompression caused by deglaciation

rather than being a function of volume or location. Postglacial volcanism and related chemistry is unique to the neovolcanic zones as there is no evidence of significant icecap and glacier formation prior to the Quaternary glaciation. The Stóravíti observations merely discount postglacial lava flows from Hardarson and Fitton's study (1997). It is still very likely that the largest lava flows from the old rift zones were preserved to form the exposed Tertiary crust. Further investigation is required to compare other non-postglacial large volume eruption from the neovolcanic zones to determine whether the recent large volume eruptions are similar to the Tertiary large volume flows. The effects of glaciation must be taken into consideration when comparing the Tertiary with the neovolcanic zones and analysing major differences.

The most significant observation from this study is the similarity in the geochemical signature between the Tertiary and central Northern Volcanic Zone data (referred to as central Iceland). These volcanic systems from the Northern Volcanic Zone are located within the sphere of influence of the plume centre. Maclennan et al. (2001b) studied a series of samples from the Askja system north of the Vatnajökull icecap. The trace element signature is similar to off-axis alkaline volcanism however, the melt production rate must be the highest in Iceland as the crustal thickness is approximately 40 km (Darbyshire et al., 1998). Using REE inversion modelling (based on McKenzie and O'Nions, 1991), Maclennan et al. (2001b) concluded that this central Iceland geochemical signature results from active upwelling related to the plume, which fluxes material through the deepest parts of the melting region. This active upwelling is in addition to passive plate-driven upwelling. The influence of deep mantle melting on the trace element composition is much greater than would be expected for solely passive upwelling. The geochemical effect of plume upwelling is limited to approximately 150 km away from the plume centre (Maclennan et al., 2001b). The similarity between central Iceland chemistry and Tertiary chemistry suggests that the bulk of the Tertiary data represents lava flows that have been erupted by volcanic systems within the radius of influence of the plume centre. Plotting the locations of the Tertiary samples shows that this is not an unusual outcome. Figure 5.40 shows a map of Iceland projected so that the horizontal axis is parallel to the localised spreading direction. The east Iceland samples from Kitagawa et al. (2008) are roughly located along the line of spreading from the Askja system and particularly in relation to the samples shown as red squares which represent data from Maclennan et al. (2001b). The Northwest samples, which have known locations, are all 14 to 16 Ma and are located within the 150 km along axis radius of the 15 Ma position of the plume centre. The plume centre at 15 Ma was 100 km north of its current position according to the plume track (Jones, 2003).

Locations will need to be obtained for the rest of the Tertiary data to ensure that this proximity to the plume is the case for all existing Tertiary samples.

These qualitative observations suggest that the thorough sampling of the Tertiary to date has unfortunately been biased by the general sampling region. In order to confirm whether or not this is the case, further samples should be collected from areas of the Tertiary crust that could not have had any influence from the plume such as the southerly exposures of the western Tertiary that should be related to the pre-glacial Western Volcanic Zone and the most northerly exposures of the eastern Tertiary that should be associated with the pre-glacial northern part of the Northern Volcanic Zone. The geochemical signature of these Tertiary regions should show a more depleted signature than that exhibited by central Iceland as there is no active upwelling beneath that part of the volcanic zone. The limited effect of active upwelling in the northern part of the Northern Volcanic Zone is clear from the 20 km thick crust (Staples et al., 1997) compared to a central crustal thickness of 40 km (Darbyshire et al., 1998). A reconstruction of plate spreading and a correction of the plume track is required to properly assess how the plume could have influenced the active ridges through time.

The comparison of off-axis volcanism with the Tertiary shows a good correlation of trace element signature. Snaefell and Snaefellsnes are composed of mostly alkaline volcanism and therefore these more extreme off-axis features cannot have made significant contributions to the Tertiary, which is broadly tholeiitic. Grímsnes is situated only 15 km off-axis and exhibits tholeiitic volcanism with a similarly enriched trace element signature to the Tertiary. It is reasonable to expect, as an extension to Pálmason's model, that any off-axis volcanism will be preserved in the exposed Tertiary crust as there is little chance of burial by axial lava flows. Off-axis flows are likely to be small volume lava flows that are not laterally extensive compared to the big 'trap' flows erupted by the central rift system which have a similar chemistry to the small off-axis flows as described above.

It is also observed that there is a broad increase in the alkalinity and the distribution of Zr/Y values of lava flows from off-axis centres with increasing distance from a rift axis. This is observed in the Tertiary comparisons with Grímsnes (15km), Snaefell (25km) and Snaefellsnes (>50km). The light REE enrichment reflects a strong influence of deep mantle melting in the presence of garnet. The relative light REE enrichment is caused by depletion in the heavy REEs rather than an increase in the light REE concentrations. The strong influence of deep mantle melting is consistent with off-axis volcanism tapping only the edges of a triangular melting region (see figure 4.18, section

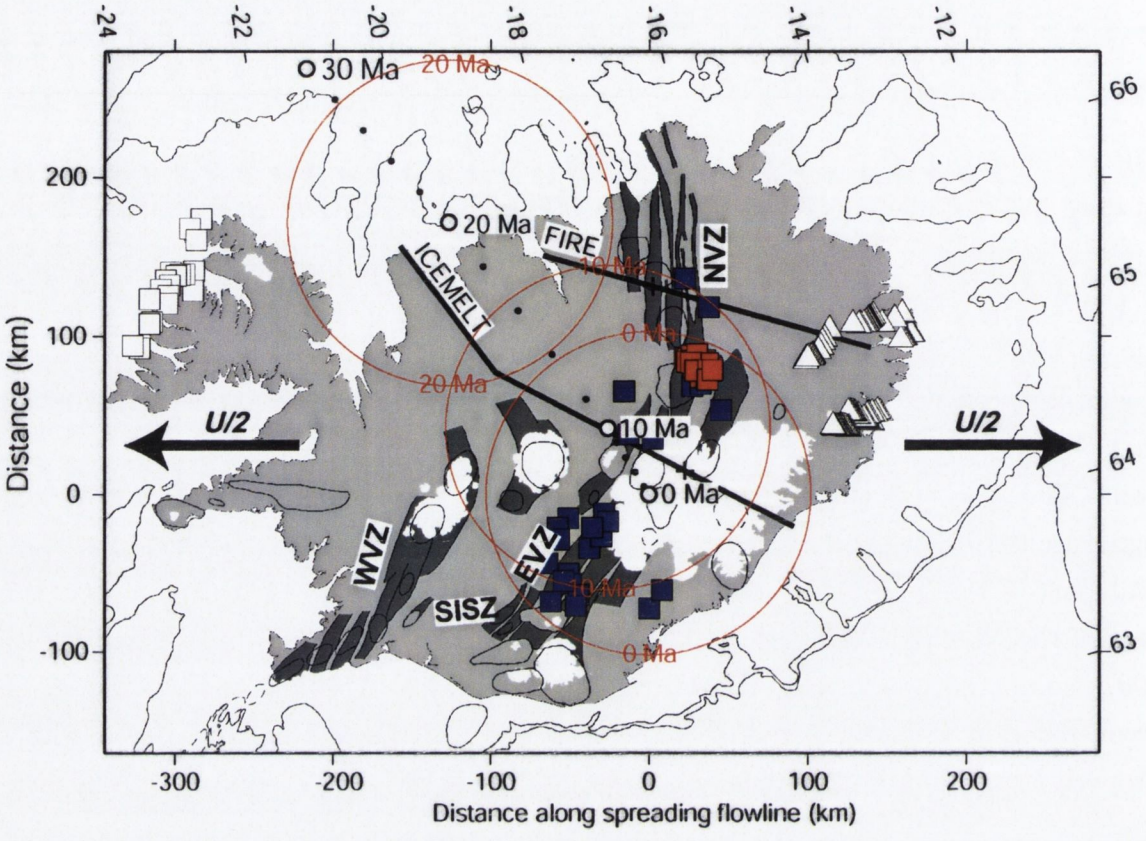

Figure 5.40: Map of Iceland and the surrounding bathymetry showing the location and extent of the active volcanic zones and their individual volcanic systems (As - Askja system); data from Einarsson and Saemundsson (1987). The map is projected obliquely so that the horizontal axis represents the local spreading direction. Sample locations are shown for central Iceland (Blue Squares), East Tertiary (Kitagawa et al., 2008 - White Triangles) and Northwest Tertiary (White Squares). The central Iceland samples studied by Maclennan et al. (2001b) are shown as red squares. The approximate location of the plume centre over the past 30 Ma is also shown (Jones, 2003); in the reference frame of the present day spreading axis. Three red circles represent the estimated minimum radius of the geochemical effect of the plume for 0, 10 and 20 Ma. FIRE and ICEMELT refer to seismic experiments, and the small cross located within the Northern Volcanic Zone on each line is the position of greatest crustal thickness (Staples et al., 1997; Darbyshire et al., 1998).

4.3.4). The further the distance from the main melting region, the smaller the degree of melting with a greater influence of deep mantle melting. Also, lithosphere thickness increases with age resulting in an increase in the average depth of melting. Snaefellsnes is clearly a more complex situation because it is not even in the orientation of the main rifting and is not thought to exhibit any passive extension.

There are also distinct similarities observed between the youngest lavas from the extinct Skagi rift and the Tertiary. From the present day geometry of the extinct Skagi rift axis and exposed Tertiary crust, it is clear that the last eruptions from a dying rift axis will

remain at the surface and will not be buried as there are no subsequent eruptions from the rift. Therefore, axial lava flows from dying rifts will be preserved in the surface exposure of old crust. The contribution of dying rifts will be limited by location to small volume lava flows, close to the know extinct rift axes. The only on-shore case at present is at the Skagi-Snaefellsnes rift. It is likely that another extinct rift axis lies off-shore from the Northwest Iceland Rift, but this has not been observed yet.

At least two features present in the exposed Tertiary crust are not explained by the Pálmason model of crustal accretion at Iceland: dykes and central volcanoes. Central volcanoes only occur in association with fissure systems in present day Iceland. Therefore, Pálmason's model suggests that they should be buried by subsequent lava flows from the rift axis. The Tertiary central volcanoes could remain from the death of a rift axis, however several centres exist in the exposed Tertiary crust that are apparently unrelated to extinct rift axes. Another suggestion is that they are off-axis volcanic centres which have escaped burial by subsequent axial lava flows. However, there are numerous centres preserved, particularly in northwest Iceland, and although one or two may be off-axis this cannot be the correct explanation for them all. For example, Reykjadalur Tertiary central volcano in west Iceland (figure 5.2) is composed of tholeiitic lavas (Jóhanesson, 1975), where as off-axis centres would have a predominantly alkaline chemistry similar to Snaefell depending on their distance from the main rift. Further geochemical investigation is required to determine the likely tectonic origin of these central volcanoes.

The exposure of Tertiary and Quaternary dykes occurs frequently across northern Iceland. However, according to Pálmason's model any on-axis intrusions would be subject to downward and outward crustal drift following emplacement and therefore should not be exposed in the Tertiary crust. There are young dykes exposed in Skagi, located relatively close to an extinct rift axis and considering the estimated width of a rift zone is up to 50 km, the dykes can be assumed to be on-axis intrusions. Because they are relatively young (less than 3.3 Ma), they cannot have been subject to 2 km of erosion as is the case for older Tertiary lavas and central volcanoes. Therefore, it must be true that on-axis dykes can be exposed by erosion especially considering many of the Garcia et al. (2003) dykes are much older (5 to 9 Ma) and will have had the opportunity to under go more erosion than the young Skagi dykes. However, it may also be the case that some of the Garcia et al. (2003) dykes are intruded slightly off-axis in a Grímsnes type setting, and have more chance of exposure by erosion as they are not buried by axial lava flows. The dykes definitely cannot be widely off-axis intrusions as they plot as tholeiitic basalts and not alkaline like the Snaefell volcanic centre. It is difficult to

distinguish between a near off-axis signature like Grímsnes and the general Tertiary signature observed in section 5.4. The fact that the dykes have a similar geochemistry to the Tertiary (figure 5.37) is an important observation.

The Garcia et al. (2003) dykes associated with the Northern Volcanic Zone, according to the velocity model, do not have the same geochemical signature as the lava flows from the northern part of the Northern Volcanic Zone. It is very likely that this is related to the effects of glaciation creating a depleted incompatible element signature in the northern part of the Northern Volcanic Zone. The dykes are predominantly Tertiary in age and will therefore reflect the chemistry of the rift zone prior to glaciation. However, it it possible that although the chemistry may have been more enriched for the northern part of the Northern Volcanic Zone prior to glaciation it is also possible that these dykes may have been intruded slightly off-axis recording a chemical signature similar to that of Grímsnes from the Western Volcanic Zone. If it can be shown that the dykes are not intruded within the main rift zone, this would have significant implications for the validity of the Garcia et al. (2003) velocity model as it relies very much upon the dykes being on-axis intrusions.

In order to establish whether these dykes are on-axis or off-axis, new samples from the younger Tertiary (3–8 Ma) related to the northern part of the Northern Volcanic Zone would need to be collected, in line with the spreading direction. This would indicate the geochemical signature of the main rift products prior to glaciation and a good correlation with the Tertiary dykes from the Northern Volcanic Zone would indicate shallow on-axis intrusion. The intrusions must be shallow in order to be exposed by erosion after a few Ma.

It is reasonable to expect that although the Garcia et al. (2003) assumption that all dykes are on-axis intrusion may not be wholly true for all samples it is likely that they are intruded within approximately 15 km of the main volcanic zone activity. This is because beyond 15 km the off-axis chemistry becomes more alkaline and the Tertiary chemistry is generally tholeiitic. The good correlation of data shown by Garcia et al. (2003) plate spreading velocity model, together with the geochemical evidence suggests that although it may not be 100% accurate, it is still likely to be a very good approximation for the northern Iceland rift relocation 8–3 Ma.

This study has investigated general geochemical similarities and differences to establish which elements of rift activity in Iceland are represented by the Tertiary data. Further investigation is required to break down the data by age and location to make more

specific assessments of the effect of temporal variations in spreading rate and tectonic arrangement on geochemistry, than has been possible in this preliminary study of the Tertiary.

5.6 Conclusions

The main conclusion from the preliminary geochemical comparisons of the Tertiary with different volcanic features across Iceland is the very good correlations with the central part of the Northern Volcanic Zone. This suggests the extensive sampling of the Tertiary has been biased towards plume influenced volcanism. The majority of samples represent large volume lava flows that have escaped the rift axis (Hardarson and Fitton, 1997) and have been buried to less than 2 km and therefore, have the potential to be exhumed to make up the exposed Tertiary crust. Off-axis volcanism is likely to provide a small contribution to the exposed Tertiary in the form of small volume lava flows. These may be tholeiitic in the case of near off-axis volcanism and more rarely alkaline in the case of widely off-axis volcanism. Axial lava flows from dying rifts are also preserved in the Tertiary crust, but their contribution is limited to small volume lava flows near the know extinct rift axes. The difference between the Tertiary and the general established neovolcanic zone chemistry (northern part of Northern Volcanic Zone and Western Volcanic Zone) is probably related to the effect of glaciation in the neovolcanic zone chemistry. The Tertiary dykes have been intruded within 15 km of the rift axial zone and the good correlation of data in Garcia et al. (2003) model suggests that they are shallow axial or very nearby off-axis intrusions.

Chapter 6

Model Theory and Development

6.1 Introduction

Numerical modelling of mid-ocean ridges can provide significant insights into the formation of new oceanic crust, its production rate and composition. Several authors have presented time-dependent models of mid-ocean ridge melting, but have not considered changes in spreading rate or the impact of temporal variations on the chemistry of lava flows (e.g. Mittelstaedt et al., 2008, Bown and White, 1995). The composition and thickness of oceanic crust are not constant and variations can in some cases be qualitatively linked to time-dependent tectonic variations at the mid-ocean ridge (Choe et al., 2007). Tectonic variations include changes in the spreading rate associated with the growth and decline of ridges, and changes in the geometry of the melting region following continental break up. In order to understand how these tectonic variations may influence the volume and composition of new oceanic crust an appropriate time-dependent model of upwelling beneath a spreading ridge is required.

The main geological focus of this project is the study of the effects of rift relocations on the amount of melting and composition of melts at Iceland. Rift relocations cause variations in the spreading rate as the transfer of extension is completed between the old and the new rift (Garcia et al., 2003). Rift relocations occur globally in association with plume-ridge interactions and complex transform zones (e.g. Small, 1995). A new time dependent model of mid-ocean ridges will have global applications and may provide new insights into the effects of plume-ridge interaction. The model may also be applied to the initial development of mid-ocean ridges following continental break up, where

re-focusing of the melting region may have a significant influence on the time scale and volume of crust production (section 7.6).

Previous mid-ocean ridge models have mainly been concerned with two-dimensional steady-state mantle melting varying from relatively simple mathematical parameterisations of the temperature and melt fraction with respect to the mantle solidus, to models encompassing phase equilibria where the melting reaction and composition of the mantle are tracked throughout the melting region. Section 6.2 describes the range of existing numerical models relevant to this project. It has been shown that observations of oceanic crust, such as crustal thickness, can be reproduced by relatively simple numerical models based on parameterisations of the solidus, liquidus and melt fraction with respect to temperature as constrained by experimental data (McKenzie and Bickle, 1988; Watson and McKenzie, 1991; Bown and White, 1994; Katz et al., 2003).

One of the main aims of this project is to develop a new time-dependent model of melting beneath a spreading ridge. The new model is based on a melting parameterisation developed by Katz et al. (2003) and the basic structure of mid-ocean ridge models employed by Bown and White (1994) and Bown and White (1995). The aim of this chapter is to describe in detail the melting parameterisation, mathematical methods and program structure used in the new time-dependent model. The chapter also aims to highlight the limitations of the model and indicate how improvements could be made.

6.2 Background

This section will outline existing research in numerical modelling of mid-ocean ridge processes relevant to this project and include a discussion of the validity of simplifications and assumptions made in the development of the new model. A brief introduction to mantle melting is provided in section 2.3.

6.2.1 Existing Numerical Models

There have been numerous models of melt generation and melt transport starting with Ahern and Turcotte (1979), who were the first to quantify the amount of melt gener-

ated by decompression of the mantle by fitting an analytical expression to a series of experimental results. Various improvements have been made using the same process of fitting analytical expressions to experimental melting results to quantify changes in the melt fraction with respect to mantle temperature and pressure, as more results were published. McKenzie and Bickle (1988) were the first to use a large database of experimental melting results from several different authors. They produced an anhydrous parameterisation for the variation of the solidus and liquidus temperatures with pressure, the variation of melt fraction with pressure and temperature, and the variation of major element compositions of melts with respect to melt fraction and pressure.

Various authors throughout the 1990s published slightly different parameterisations as more experimental data became available to constrain the analytical expressions and with small refinements to the parameterisation process (Davies and Bickle, 1991; Langmuir et al., 1992; Kinzler and Grove, 1992; Jha et al., 1994; Iwamori et al., 1995; Iwamori, 1997; Kinzler, 1997; as summarised in Katz et al., 2003). Iwamori et al. (1995) produced a fractional melting parameterisation estimating a reduction in the degree of melting by 5–15% of the total compared to those produced by batch melting for the same mantle potential temperature. They also developed a preliminary hydrous parameterisation of melting, which suggested that mantle melting in the presence of water may start at depths greater than 150 km. This depth is confirmed by Hirth and Kohlstedt (1996), who predicted that hydrous melting will lower the onset of melting by approximately 40 km. Katz et al. (2003) predicted the amount of extra melt produced by deep hydrous melting before the onset of anhydrous melting to be approximately 2 wt% for mantle with 0.02 wt% H_2O.

A full thermodynamically consistent model was developed by Asimow et al. (1997) based on the MELTS algorithm (Ghiorso and Sack, 1995). The model calculates the melt fraction versus depth relationship for fractional and batch melting based on the thermodynamic properties of phases participating in peridotite melting in the mantle. The accuracy of this type of modelling depends on the accuracy of the estimates of the thermodynamic and mixing properties of different phases. There are several problems associated with the MELTS algorithm, resulting in a poor prediction of the melt fraction-temperature relationship and certain major element-melt fraction relationships, which are unresolved (Hirschmann et al., 1998).

Katz et al. (2003) developed a new parameterisation of anhydrous and hydrous mantle melting based on an updated experimental database. This parameterisation provides the basis for the new time-dependent model described in this chapter. The evidence

summarised in section 2.3.2 clearly shows that melting at mid-ocean ridges is influenced by the presence of water in the mantle. The presence of water increases the depth that melting initiates and this increased depth has a significant impact on the composition of melts. Katz et al. (2003) used experimental results from Grove (2001) and Kawamoto and Holloway (1997) to constrain the solidus for different bulk water contents up to the water saturated solidus. Theoretical variations based on thermodynamic behaviour are incorporated into the melt fraction versus temperature relationship for both anhydrous and hydrous melting. The result is that melt fraction is dependent on the weight fraction of clinopyroxene in the mantle as well as temperature, pressure and water content. The melting rate decreases once clinopyroxene has been exhausted from the mantle. The Katz et al. (2003) model has the advantage that latent heat is not fixed in the parameterisation as is the case in the Watson and McKenzie (1991) parameterisation employed by Bown and White (1994).

There are several advantages of analytical parameterisations of experimental observations over thermodynamically consistent models. Firstly, simple parameterisations are computationally fast and efficient compared to the more complex models, which is an important feature for the development of a time dependent model in which hundreds of time steps will each require a melting calculation. Secondly, using melting parameterisations allows relatively simple incorporation of different tectonic models, so that for example, the new model can be applied to a variety of tectonic situations once a mantle flow model has been obtained. Finally, because the parameterisations are based on experimental results, the models tend to reproduce the observations much more reliably than the fully consistent thermodynamic models.

Bown and White (1994) used the Watson and McKenzie (1991) parameterisation of temperature, melting rate and major element composition to calculate the volume (crustal thickness) and composition of the products of melting under rifts. Expressions for the solidus and liquidus, and expressions used in the calculation of the melting rate are from McKenzie and Bickle (1988). Bown and White (1994) observed significant variation in the geometry of the melting region, in particular the depth to the top of the melting region, for different spreading rates. Abrupt decreases in melt generation are observed at full spreading rates below 20 mm yr^{-1} with significant increases in the depth to the top of the melting region. Bown and White (1994) explain this abrupt decrease by conductive cooling becoming a greater control on the extent of melting, resulting from significantly reduced upwelling rates at slow spreading rates. The significant changes in melt generation are also reflected in the composition at slow spreading rates where compatible elements decrease in concentration and incompatible

elements increase in concentration to a greater extent relative to faster spreading rates. For normal mantle potential temperature (approximately 1300°C) an average 6 km crustal thickness is produced for spreading rates greater than 20 mm yr^{-1}. This value compares well with a global range of seismic measurements. These results presented by Bown and White (1994) are used as a basis for comparison of the results from the new time-dependent model at steady-state.

Bown and White (1995) developed a time-dependent model of melt generation at rifted margins. The melting calculation is based on Watson and McKenzie (1991) and McKenzie and Bickle (1988), as with Bown and White (1994). However, the calculation of the melting rate is based on Lagrangian derivatives of temperature and pressure with respect to time. The time-dependent expressions for melting rate from Bown and White (1995) are used in the new time-dependent model and are described in section 6.8.

Forward modelling of the melt composition consistent with the results of the melting calculation was first described by McKenzie and Bickle (1988). McKenzie and Bickle presented a mathematically simple parameterisation of the concentration of major element oxides as a function of dimensionless temperature, based on compositions obtained from batch melting experiments. A further modification to this parameterisation was presented by Watson and McKenzie (1991). Langmuir et al. (1992) showed that inconsistencies exist in the application of this parameterisation with the original experimental results for certain elements (CaO, Na_2O, FeO). The advantage of calculating the major element composition of melt and residue within the melting region is that the major element composition of the residue can be used to estimate the phase proportions involved in the melting reaction. Phase proportions are required to calculate consistent trace element concentrations throughout the melting region. This method of calculating melt composition would be an ideal addition to the new time-dependent model.

The MELTS algorithm (Ghiorso and Sack, 1995) described previously estimates the composition of rift products from the phase proportions predicted by the algorithm. This is clearly a step forward from the parameterisation method of McKenzie and Bickle (1988); however, the problems associated with the prediction of the melt fraction-temperature relationship limit the usefulness of this model for the aims of this project until improvements are made to the melting calculation.

Trace element compositions of the melt have been estimated without calculating the

major element compositions and phase proportions using estimated bulk partition coefficients. The definition of the partition coefficient is given in section 2.3.5. The trace element composition of the melt is dependent on the total melt fraction with standard equations for batch and fractional melting (Schilling, 1966; Gast, 1968; Shaw, 1970). The calculation of trace element concentrations in the melt using constant bulk partition coefficients is a relatively simple process because only one value, the total melt fraction, must be tracked through the melting region. However, it is clear from geochemical studies of mid-ocean ridges that phase changes in the mantle residue are an important control on the final melt chemistry. The transition from the garnet to spinel phase during melting has the most significant impact on the bulk partition coefficient of certain elements and, consequently, has a significant impact on the final melt composition. Spiegelman (1996) employed a 2-layer mantle model to simulate the impact of the garnet-spinel phase transition on REE concentrations. This method provides a useful estimation of trace element compositions, without the added complexity of calculating major element concentrations and phase proportions. At present the new time-dependent model simply estimates relative changes in the trace element concentration using constant bulk partition coefficients for the mantle (see section 6.10). However, it is then only possible to compare the model results with qualitative changes observed in real data. For a more robust comparison a 2-layer mantle would be a relatively straight forward extension to the program and would allow consideration of the garnet-spinel phase change.

All the models described above are based on steady-state mid-ocean ridge settings with the exception of Bown and White (1995) which is concerned with rifted continental margins. This steady-state approach is generally appropriate for established mid-ocean ridges and has provided significant insights into the formation of new oceanic crust. However, in order to understand more complex mid-ocean ridge processes where spreading rate and ridge position may vary through time it is necessary to develop a time-dependent model.

6.2.2 Limitations

The velocity model used to calculate the flow of the mantle is based on the assumption that ridges operate symmetrically. This may not always be the case, with particular consideration of the application of the model to Iceland. Garcia et al. (2003) used $^{40}Ar/^{39}Ar$ dating to show that asymmetrical spreading may occur during a rift reloca-

tion on Iceland. When two rifts are active simultaneously the resultant activity across an individual rift is asymmetrical with faster spreading rates occurring on the outer limb compared to the central limb of the rift. The effect of asymmetrical spreading on the melting region cannot be estimated without a suitable asymmetrical velocity field (e.g. Katz et al., 2004). The half-spreading rates from the model presented by Garcia et al. (2003) are not well constrained, therefore for simplicity asymmetrical spreading is not employed in the new model. The possible effect of simultaneous rift activity on the volume and composition of mantle melts is discussed in chapter 7. Another important limitation of the application of the velocity field to Iceland is that it is 2D, whereas rift relocations at Iceland are 3D processes. New rifts propagate laterally through the mantle from an initial rifting point. LaFemina et al. (2005) shows that the spreading rate varies along axis for the growing Eastern Volcanic Zone and the declining Western Volcanic Zone.

The current consensus on the mode of mantle melting is that it is near-fractional melting with a very small residual porosity less than 1% (Kelemen et al., 1997; section 2.3.3). A suitable simplified numerical model should therefore employ fractional melting. However, the majority of experimental data used to constrain the pressure-temperature-melt fraction (P-T-X) relationship comes from batch melting experiments. Batch requires a relatively simple parameterisation to estimate the P-T-X relationship at any point in the melting region. However, due to the chemical isolation involved in fractional melting, the parameterisation of the P-T-X relationship will change as the composition of the residue is depleted by melt extraction. The development of realistic numerical models will be limited until more experimental data for fractional melting becomes available. Iwamori et al. (1995) estimated a 5–15% reduction in the total amount of melting. This project is primarily concerned with relative changes in melting and composition that can be linked to significant variations in spreading rate so although the effect of fractional melting on the absolute results may be significant, the comparison between different rift stages will still be valid. It has been shown by several authors (e.g. Bown and White, 1994; Klein and Langmuir, 1987) that despite the unrealistic nature of batch melting models, the reproduction of observed global data is still very good.

Compaction of the mantle residue occurs as melt is extracted and must be taken into consideration when calculating the volume of melt produced at a mid-ocean ridge. A realistic incorporation of compaction into a numerical model would require a variable velocity field. However, White et al. (1992) introduced a simple compaction correction into the final integration of the melt volume and resulting crustal thickness. This

is used by Bown and White (1994) and the predicted crustal thickness for various spreading rates compares well with global observations of mid-ocean ridges. Therefore, this simple compaction correction is used in the new model.

It is now clear that the mantle beneath mid-ocean ridges is heterogeneous on small length scales significantly less than 100 km (Maclennan, 2008a) and possibly down to a few metres (Kogiso et al., 2004). The new model only employs an over-simplified method of estimating trace element compositions using constant bulk partition coefficients. Further work could extend the model to incorporate more realistic compositional calculations, in which case the composition of the mantle source will be extremely relevant. The possible effect of a heterogeneous mantle source on the composition of mantle melts is discussed in section 7.6. Despite the significant short length scale scatter of Sr and Nd isotopes at Iceland, there is no evidence for systematic variation along the rift zones. Therefore, it is reasonable to suggest that the upwelling mantle beneath Iceland has a relatively uniform average composition on a long length scale (Maclennan et al., 2001b). The use of a constant mantle source composition to model changes in rift product compositions through time is a reasonable simplification in order to compare model predictions of geochemical variations with observations from different rift stages at Iceland. Bown and White (1994) show that a simple parameterisation of the composition using a constant mantle source produces a good comparison with global mid-ocean ridge data. In the future, if the model is to predict absolute concentrations, a heterogeneous source composition will be required to predict exceptionally incompatible signatures such as those observed for small degree melting at Iceland.

Existing research into the effects of melt transport on geochemical variability is discussed in section 2.3.4. For the purposes of the new model it is assumed that all the increments of melt from the melting region are extracted, transported and homogenised before being emplaced as new crust. Spiegelman and Kelemen (2003) show that variable transport processes can produce extreme chemical variability from a homogeneous input. The important part of the model assumption, whether chemical variability is produced by fractional melting or by channelised flow, is that the mixing of melts prior to eruption is 100% efficient. Efficient mixing must be a reasonable assumption, otherwise global correlations of composition and crustal thickness of oceanic crust such as those observed by Klein and Langmuir (1987) would not be possible.

6.3 Model Outline

This section will provide a simple overview of the methods used in the new model, details of the equations are provided in sections 6.4 to 6.9. The aim of the new model is to identify significant changes in the melting regime and resultant lava chemistry that can be associated with spreading rate variations. It is a relatively simple approach to a complex problem and there are many straight-forward additions which could be made with further resources and these are discussed in chapters 7 and 8. Despite this simple approach, the results presented in section 7.5 compare well with melt fraction and relative compositional variations observed during a rift jump at Iceland.

The basic structure of the model is based on the steady-state model of melting beneath a spreading ridge presented by Bown and White (1994). The following describe the main steps in the computer program (figure 6.1) and the basis of all the equations used. Tables 6.1 and 6.2 provide a reference for all the parameters used in the model, their values where constant and their units.

A: The first task of the program is to read in starting values and set constant parameters. Some parameters are fixed within the code, and several independent parameters can be varied.

B: The area of calculation is kept to a minimum by assuming that the ridge behaves symmetrically. This area is divided into numerous regular squares, each centred on a node. The speed of the program is controlled by the number of nodes. The grid size used in the application of the model in chapter 7 is 0.5 km, since grid spacings less than 0.5 km require excessive computational time and larger grid spacings introduce significant error (appendix D). The value at the node is assumed to prevail over the whole grid square.

C: The horizontal and vertical velocity of the mantle at each grid node is calculated using Cartesian equations (Jull, 1997) based on Batchelor (1967) and Spiegelman and McKenzie (1987) simple 2-D corner flow velocity models (section 6.4).

D: The initial temperature field is calculated according to a conductive geotherm (section 6.5.2). The basal boundary condition is controlled by by the mantle potential temperature. A half-space cooling model can also be used if a steady-state thermal structure is required for the calculation (appendix D). However, it must be noted that the initial residue field must be set accordingly.

E: Having established a starting temperature field, the temperature before melting is calculated using the standard advection-diffusion equation (section 6.5.3). The advection-diffusion is calculated using the control volume formulation method outlined in Patankar (1980), see appendix D. Temperature is treated in a similar way to a mass fraction so that the flux through each grid square is internally consistent over the whole grid within a tolerance level of 0.1°C.

This method automatically introduces diffusion on the scale of the grid size because the value of the central node in each grid square is assumed to prevail over the whole square, known as a step-wise profile calculation. The grid size and the time-step control the amount of error introduced by artificial diffusion. The grid size of 0.5 km and time step of 0.1 Ma used in the model application produce a very small error of 3%. The error was estimated by advecting a 2D Gaussian distribution around the grid.

F: The mass fraction of mantle residue at the start of calculations is simply assumed to be completely undepleted. As melting occurs the residue is gradually depleted as it moves through the melting region until no more melting is possible (section 6.6). The advection of the mass fraction of mantle residue is also calculated using the Patankar (1980) control volume formulation (appendix D).

G: The amount of melt produced in the mantle over the time step is calculated using the Katz et al. (2003) parameterisation of anhydrous and hydrous melting (section 6.7). The melt fraction and the temperature are implicitly linked by the correction for the latent heat of melting and therefore, have to be solved using a root bisection method (section 6.7.2).

H: Melt is assumed to be extracted from the mantle as soon as it forms, i.e. perfect fractional melting. The melting rate is calculated using Lagrangian derivatives (section 6.8). The melting rate is then integrated over the whole region to calculate the melt volume produced during that time step. The melting volume leads simply on to the crustal thickness (section 6.8).

I: With knowledge of the depth and degree of melting, the composition of ridge products can be calculated. At present, the new model employs an over-simplified method using trace elements with constant bulk partition coefficients (section 6.9).

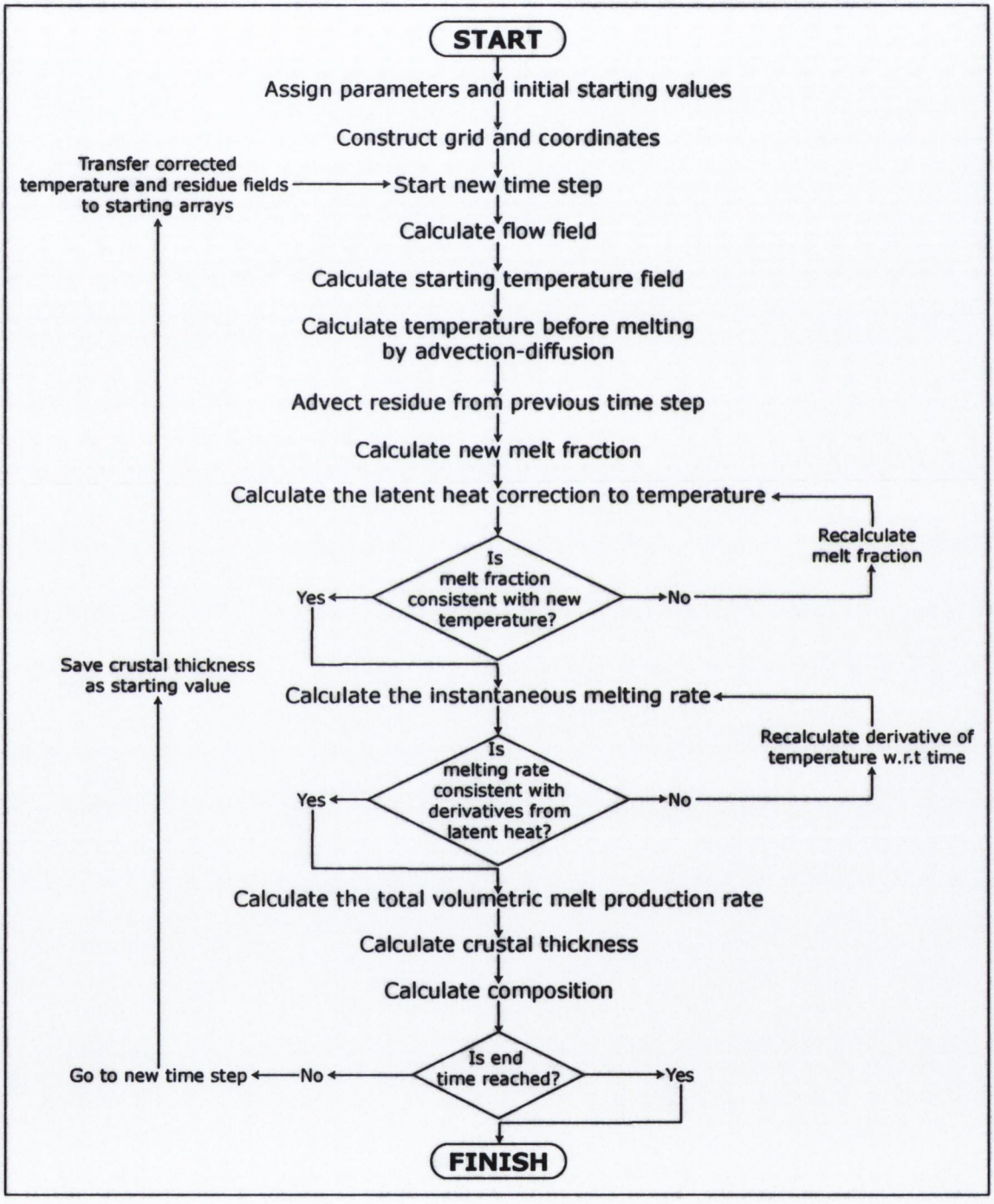

Figure 6.1: Flowchart to summarise the main steps in the numerical model.

Parameter	Symbol	Value	Units
Full spreading rate	u_f	-	$m\ s^{-1}$
Half spreading rate	u_h	-	$m\ s^{-1}$
Horizontal velocity of matrix	v_x	-	$m\ s^{-1}$
Vertical velocity of matrix	v_z	-	$m\ s^{-1}$
Horizontal distance from the rift axis	x	-	m
Depth	z	-	m
Acceleration due to gravity	g	9.81	$m\ s^{-2}$
Wedge angle	θ	-	radians
Mantle potential temperature	T_p	-	°C
Thermal expansion coefficient	α	$3.2x10^{-5}$	$°C^{-1}$
Specific heat capacity at constant pressure	C_p	$1x10^3$	$m^2\ s^{-2}\ °C^{-1}$
Adiabatic temperature gradient	h	-	$°C\ m^{-1}$
Time	t	-	s
Density of mantle matrix	ρ_s	$3.3x10^3$	$kg\ m^{-3}$
Mean density of oceanic crust	ρ_c	$2.8x10^3$	$kg\ m^{-3}$
Residue mass fraction	R	-	-
Total melt fraction	F_t	-	-
Thermal diffusivity of the mantle	κ	$8.04x10^{-7}$	$m^2\ s^{-1}$
Change in melt fraction	ΔF	-	-
Pressure	P	-	GPa
Temperature before melting	T	-	°C
Volumetric melt production rate	Γ	-	$m^2\ s^{-1}$
Crustal thickness	t_c	-	m
Concentration of trace element in melt	C_L	-	ppm
Concentration of trace element in source	C_0	-	ppm
Generic bulk partition coefficient	D	-	-
Accumulated concentration in melt	C_L^{acc}	-	ppm
Average concentration in melt	C_L^{av}	-	ppm

Table 6.1: Summary of parameters used in the model, including the value if constant.

Parameter	Symbol	Value	Units
Solidus temperature	T_S	-	°C
Lherzolite liquidus temperature	T_L^{lherz}	-	°C
Liquidus temperature	T_L	-	°C
Solidus constant	A_1	1085.7	°C
Solidus constant	A_2	132.9	°C GPa^{-1}
Solidus constant	A_3	-5.1	°C GPa^{-2}
Lherzolite liquidus constant	B_1	1475.0	°C
Lherzolite liquidus constant	B_2	80.0	°C GPa^{-1}
Lherzolite liquidus constant	B_3	-3.2	°C GPa^{-2}
Liquidus constant	C_1	1780.0	°C
Liquidus constant	C_2	45.0	°C GPa^{-1}
Liquidus constant	C_3	-2.0	°C GPa^{-2}
Reaction coefficient for cpx	R_{cpx}	-	cpx/melt
Cpx constant	r_1	0.5	cpx/melt
Cpx constant	r_2	0.08	cpx/melt/GPa
Melting constant	β_1	1.5	-
Melting constant	β_2	1.5	-
Melt fraction	F, F_{cpx}, F_{opx}	-	-
Initial temperature, before latent heat	T_i	-	°C
Real temperature, after latent heat	T_R	-	°C
Dimensionless temperature (below F_{cpx})	T'	-	-
Dimensionless temperature (above F_{cpx})	T^*	-	-
Hydrous dimensionless temp (below F_{cpx})	T''	-	-
Hydrous dimensionless temp (above F_{cpx})	T^{**}	-	-
Melt fraction of cpx-out	$F_{cpx-out}$	-	-
Temperature of cpx-out	$T_{cpx-out}$	-	-
Modal cpx in the mantle source	M_{cpx}	-	wt fraction
Hydrous solidus temperature decrease	$\Delta T(X_{H_2O})$	-	°C
Water content in the melt	X_{H_2O}	-	wt%
Bulk water content in the mantle	$X_{H_2O}^{bulk}$	-	wt%
Water content in a saturated melt	$X_{H_2O}^{sat}$	-	wt%
Hydrous temperature constant	K	43	°C wt%$^{-\gamma}$
Hydrous temperature constant	γ	0.75	-
Bulk partition coefficient of water	D_{H_2O}	0.01	-
Saturation constant	χ_1	12.00	wt% GPa$^{-\lambda}$
Saturation constant	χ_2	1.00	wt% GPa^{-1}
Saturation constant	λ	0.60	-
Entropy of fusion	ΔS	300	J kg^{-1} °C^{-1}

Table 6.2: Summary of parameters and constants specific to the melting parameterisation (Katz et al., 2003).

6.4 Mantle Flow Field

The geophysical model is based on simple 2D corner flow (figure 6.2) described in detail in Spiegelman and McKenzie (1987) as a summary of several authors: McKenzie (1969), Skilbeck (1975), Lachenbruch (1976) and Batchelor (1967). The ridge is assumed to be symmetrical with simple flow field up through the mantle and away from the centre of the ridge. The solid mantle behaves like a viscous incompressible fluid and in this model melting does not influence the velocity field. Melt is removed instantaneously from the mantle and emplaced as new crust. The crustal thickness is an input to the model and defines a region where no upwelling occurs, i.e. purely horizontal flow. The corner flow solution (Spiegelman and McKenzie, 1987) was converted to Cartesian coordinates by Jull (1997) to provide the following equations for the horizontal (v_x) and vertical velocity (v_z):

$$v_z = A - B\frac{z^2}{x^2 + z^2}\,, \tag{6.1}$$

$$v_x = B\left[\tan^{-1}\left(\frac{x}{z}\right) - \frac{xz}{x^2 + z^2}\right]\,. \tag{6.2}$$

x is the horizontal distance from the rift axis, z is the depth and A and B are constants defined as

$$A = \frac{2u_h \sin^2\theta}{\pi - 2\theta - \sin(2\theta)} \tag{6.3}$$

and

$$B = \frac{2u_h}{\pi - 2\theta - \sin(2\theta)}\,, \tag{6.4}$$

where θ is the wedge angle and u_h is the half-spreading rate. The wedge angle defines the geometry of the upwelling region. Outside the upwelling region half-spreading rate is assumed to prevail over the whole of the lithosphere. The wedge angle is controlled by the upwelling rate of the mantle beneath the ridge. The effect of different wedge angles on the melting regime and composition is presented in section 7.4. The mantle flow model describes upwelling mantle asthenosphere at the centre of the ridge, with increasing horizontal velocity outwards from the rift axis until half spreading rate is achieved. Melting only occurs within the region of upwelling asthenosphere.

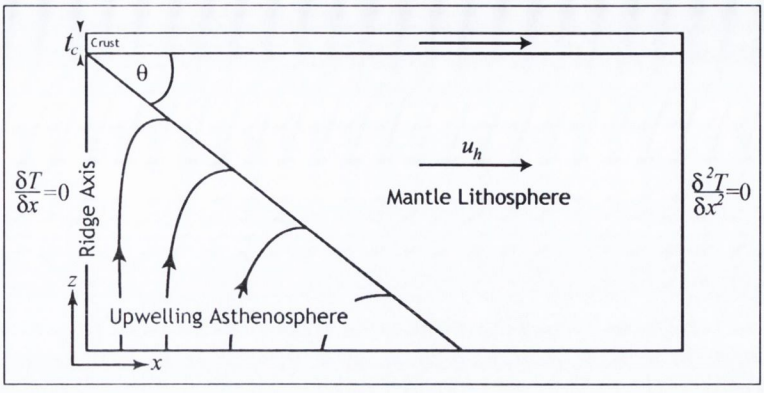

Figure 6.2: Simple 2D corner flow geometry, after Spiegelman and McKenzie (1987); Bown and White (1994). The ridge is assumed to be symmetrical. The flow lines show the velocity field. θ is the wedge angle, defining the boundary between upwelling asthenosphere and mantle lithosphere.

6.5 Thermal Structure

6.5.1 Boundary Conditions

The thermal boundary conditions are constructed according to the steady-state model presented by Bown and White (1994). The thermal boundary condition at the ridge axis assumes no diffusion or advection ($\frac{\partial T}{\partial x} = 0$) and the off-axis boundary allows advection only ($\frac{\partial^2 T}{\partial^2 x} = 0$). The grid should be made sufficiently wide to avoid any interference by the off-axis boundary with the melting region.

The surface temperature, T_0, is set to 0°C and the basal temperature, T_B, is calculated from the input mantle potential temperature, T_p. Mantle potential temperature is the surface temperature that would be reached by a packet of mantle if transported from depth adiabatically to the surface without melting. The basal temperature is defined as

$$T_B = T_p / e^{(-\alpha g z / C_p)} \tag{6.5}$$

where g is the acceleration due to gravity, z is the depth, α is the thermal expansion coefficient and C_p is the specific heat capacity at constant pressure.

6.5.2 Starting Thermal Structure

The starting thermal structure is defined as a conductive geotherm. The temperature field is calculated using a simple linear relationship between the boundary temperatures, assuming that the thermal diffusivity is constant in the mantle, and is given by

$$T_S = \frac{T_B}{z_{max}} z \tag{6.6}$$

where z_{max} is the maximum depth of the grid and T_S is the starting temperature at any point in the grid.

In order to model spreading rate variations for established rifts such as at Iceland, it is first necessary to run the model for several million years to an approximate steady-state.

6.5.3 Thermal Advection and Diffusion

Given the starting thermal structure and the velocity field, the standard thermal advection-diffusion equation is used to calculate the evolution of the temperature field through time:

$$\frac{\partial T}{\partial t} = \kappa \left(\frac{\partial^2 T}{\partial x^2} + \frac{\partial^2 T}{\partial z^2} \right) - v_x \frac{\partial T}{\partial x} - v_z \left(\frac{\partial T}{\partial z} + h \right) \tag{6.7}$$

where t is the time and h is the adiabatic temperature gradient given by

$$h = \frac{g\alpha}{C_p} T \, . \tag{6.8}$$

The advection-diffusion equation gives the temperature, T, before any melting is taken into consideration. The initial temperature is corrected for the latent heat of melting to find the real temperature, T_R (section 6.7.2). The advection-diffusion equation is solved using a fully implicit control volume method (Patankar, 1980), where the flux of heat in and out of each grid square is internally consistent across the whole grid. See appendix D for details of the method and its application to thermal advection and diffusion.

6.6 Mantle Residue

6.6.1 Definition

The mantle residue, R, is defined as the mass fraction of fusible material that remains in the mantle after melting. The residue fraction is reduced after each time step as more melt is removed to form new crust. In reality, the residue composition would change, becoming more depleted in incompatible elements, as more melt is removed. The less fertile mantle would melt at a slower rate. The Katz et al. (2003) parameterisation uses the modal clinopyroxene to estimate the change in melting rate as the mantle is depleted. This simple consideration of the fertility as a mass fraction of the starting material allows modelling of fractional melting and the calculation of trace element concentrations in the melt. The tracking of the melting history of the mantle also allows the boundary of the melting region to be defined. When the calculated melt fraction from the temperature field is smaller than the amount of melt that has already been removed from the mantle, there is no melting.

6.6.2 Boundary Conditions

It is assumed that undepleted mantle is input at the base of the grid. Therefore, the basal boundary condition is set to $R = 1$. This assumption means that melting is not allowed to extend to the base of the grid, otherwise the grid must be extended and the calculation restarted. The surface boundary condition has no influence on the mantle residue as velocities in the crust, and consequently at the surface, are purely horizontal.

The central (ridge-axis) boundary is assumed to be symmetrical and therefore no advection is allowed across this boundary ($\frac{\partial R}{\partial x} = 0$). The off-axis boundary allows continued horizontal advection out of the grid. By this stage, all velocities are horizontal and sufficiently far away from the melting region that this boundary condition will have no impact on the amount of melting.

6.6.3 Initial Conditions

For the starting residue field at the first time step, all nodes are set to 1, assuming no melting has occurred in the mantle previously. This is consistent with a simple

conductive geotherm for the starting temperature field. In reality these starting conditions effectively reflect unstretched continental crust prior to rifting. For calculations involving an established rift, such as at Iceland, the model is run for several million years to reach an appropriate steady-state depletion of the mantle residue.

6.6.4 Residue Evolution

The residue mass fraction at any node is calculated from the total melt fraction by

$$R = 1 - F_t \tag{6.9}$$

where F_t is the total amount that the mantle has melted prior to this time. This residue value is advected for the duration of the next time step using a standard advection equation:

$$\frac{\partial R}{\partial t} + \frac{\partial (v_x R)}{\partial x} + \frac{\partial (v_z R)}{\partial z} = 0 \,. \tag{6.10}$$

This advection equation is solved using the fully implicit control volume method (Patankar, 1980). Details of the method and its application to the mantle residue are given in appendix D.

6.7 Melting

Melt is considered to be extracted from the mantle and instantaneously transported to form the crust, known as fractional melting. At present, the batch melting equations described in Katz et al. (2003) are used to calculate the amount of melting. The effect of employing fractional melting is essentially limited to the calculation of the composition (section 6.9). There is a small adaptation to the calculation of the correction to temperature due to the latent heat of melting, so that only the latent heat for the new melt fraction at any grid square is taken into account and not the total melt fraction that has been removed from the mantle previously. The amount of melting estimated for fractional melting in this new model is essentially the same as it would be for batch melting. To allow for the 5–15% decrease of the total melt fraction pre-

dicted by Iwamori et al. (1995), a parameterisation of a variable solidus and liquidus temperature, following melt extraction, would be required.

This section provides the equations required to calculate the amount of melting according to the temperature and pressure of the mantle for anhydrous and hydrous melting, as developed by Katz et al. (2003). The partial derivatives of melt fraction with respect to pressure and temperature, required to calculate the melting rate (section 6.8), are new equations specific to this time-dependent application of the Katz et al. (2003) parameterisation.

6.7.1 Anhydrous Melting

The solidus temperature, T_S, the temperature of the lherzolite liquidus, T_L^{lherz}, and the liquidus temperature after clinopyroxene exhaustion, T_L, are given by

$$T_S = A_1 + A_2 P + A_3 P^2 \,, \tag{6.11}$$

$$T_L^{lherz} = B_1 + B_2 P + B_3 P^2 \tag{6.12}$$

and

$$T_L = C_1 + C_2 P + C_3 P^2 \,. \tag{6.13}$$

A_{1-3}, B_{1-3} and C_{1-3} are constants and P is the pressure. The two liquidus equations account for the difference in melting when clinopyroxene is available in the residue (T_L^{lherz}) and when clinopyroxene has been exhausted, T_L. Consequently, there are two equations that govern the melt fraction according to whether clinopyroxene is still in the mantle, $F_{cpx}(T')$ (equation 6.14) or clinopyroxene has been exhausted, $F_{opx}(T)$ (equation 6.18). Katz et al. (2003) obtained these equations by parameterising a series of melting experiments. The variation of melt fraction with temperature, for a variety of pressures is shown in figure 6.3. The melt fraction prior to clinopyroxene exhaustion is given by

$$F_{cpx}\left(T'\right) = \left[T'\left(T, P\right)\right]^{\beta_1} \tag{6.14}$$

where $T'(T, P)$ is a dimensionless temperature defined as

$$T'\left(T, P\right) = \frac{T_R - T_S\left(P\right)}{T_L^{lherz}\left(P\right) - T_S\left(P\right)} \tag{6.15}$$

where T is the real temperature, corrected for the latent heat of melting. β_1 is a constant. For a closed (batch) melting system, the melt fraction above which there is no more clinopyroxene remaining in the residue is given by

$$F_{cpx-out} = \frac{M_{cpx}}{R_{cpx}} \tag{6.16}$$

where M_{cpx} is the weight fraction of clinopyroxene in the mantle matrix. R_{cpx} is the reaction coefficient for clinopyroxene during melting reaction given by

$$R_{cpx}(P) = r_1 + r_2 P \tag{6.17}$$

where r_1 and r_2 are constants. Equation 6.17 is not valid for significant melting above 3.5 GPa (Katz et al. 2003). Once clinopyroxene has been exhausted from the residue, the melt productivity is reduced and the melt fraction, $F_{opx}(T)$, is now given by

$$F_{opx}(T) = F_{cpx-out} + (1 - F_{cpx-out}) \left[\frac{T - T_{cpx-out}}{T_L - T_{cpx-out}} \right]^{\beta_2} \tag{6.18}$$

where $T_{cpx-out}$ is the temperature at which clinopyroxene exhaustion occurs, defined as

$$T_{cpx-out} = F_{cpx-out}^{\frac{1}{\beta_1}} \left(T_L^{lherz} - T_S \right) + T_S \tag{6.19}$$

and β_2 is a constant. In order to simplify equation 6.18, a dimensionless temperature, T^*, is defined,

$$T^*(T, P) = \left[\frac{T - T_{cpx-out}}{T_L - T_{cpx-out}} \right] . \tag{6.20}$$

6.7.2 Latent Heat of Melting

The latent heat of melting is the energy required to convert a material from solid to liquid. The melt fraction and the real temperature are implicitly linked by the correction for latent heat. The correct temperature is lower than the initial temperature from advection-diffusion when there is melting, because some of the heat energy has been used to melt the mantle. The relationship between the temperature of the mantle and the entropy of melting is defined as

$$c_p T = (c_p + \Delta F \Delta S) T_R \tag{6.21}$$

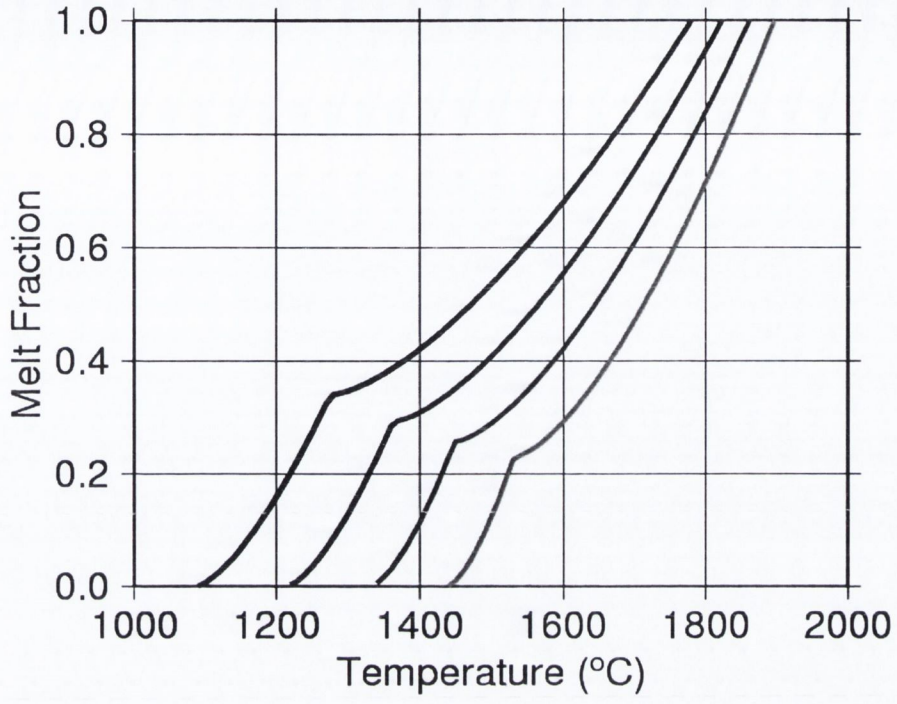

Figure 6.3: Isobaric anhydrous melting curves at a variety of pressures: 0, 1, 2 and 3 GPa (black to light grey) for modal clinopyroxene of 17%. The results were produced from the Katz et al. (2003) parameterisation.

where c_p is the specific heat capacity, T is the temperature before melting, ΔF is the change in melt fraction and ΔS is the entropy of fusion. The final melt fraction is solved for using a root bisection method for the latent heat equation and the appropriate equation for melt fraction (equation 6.14 or 6.18).

6.7.3 Anhydrous Melting Derivatives

The following equations are required to calculate the melting rate for the new total melt fraction. For melting prior to clinopyroxene exhaustion, the partial derivatives of melt fraction with respect to pressure and real temperature are defined as

$$\left(\frac{\partial F_{cpx}}{\partial P}\right)_{T_R} = \frac{\mathrm{d}F_{cpx}}{\mathrm{d}T'}\left(\frac{\partial T'}{\partial P}\right)_{T_R} \tag{6.22}$$

and

$$\left(\frac{\partial F_{cpx}}{\partial T_R}\right)_{P} = \frac{\mathrm{d}F_{cpx}}{\mathrm{d}T'}\left(\frac{\partial T'}{\partial T_R}\right)_{P}. \tag{6.23}$$

The change in melt fraction with respect to dimensionless temperature is obtained by differentiating equation 6.14 to give

$$\frac{\mathrm{d}F_{cpx}}{\mathrm{d}T'} = \beta_1 \left[T'\right]^{\beta_1 - 1} . \tag{6.24}$$

The change in dimensionless temperature with respect to pressure is obtained by differentiating equation 6.15 to give

$$\left(\frac{\partial T'}{\partial P}\right)_{T_R} = \frac{\left(-\frac{\mathrm{d}T_S}{\mathrm{d}P}\right)\left(T_L^{lherz} - T_S\right) - \left(\frac{\mathrm{d}T_L^{lherz}}{\mathrm{d}P} - \frac{\mathrm{d}T_S}{\mathrm{d}P}\right)\left(T_R - T_S\right)}{\left(T_L^{lherz} - T_S\right)^2} . \tag{6.25}$$

The derivatives of the solidus and lherzolite liquidus temperatures with respect to pressure are obtained by differentiating equations 6.11 and 6.12 to give

$$\frac{\mathrm{d}T_S}{\mathrm{d}P} = A_2 + 2A_3 P \tag{6.26}$$

and

$$\frac{\mathrm{d}T_L^{lherz}}{\mathrm{d}P} = B_2 + 2B_3 P . \tag{6.27}$$

The change in dimensionless temperature with respect to real temperature (corrected for latent heat of melting) is obtained by differentiating equation 6.15 to give

$$\left(\frac{\partial T'}{\partial T_R}\right)_P = \frac{1}{\left(T_L^{lherz} - T_S\right)} . \tag{6.28}$$

For melting after clinopyroxene exhaustion, the partial derivatives of melt fraction with respect to pressure and temperature are given by

$$\left(\frac{\partial F_{opx}}{\partial P}\right)_{T_R} = \frac{\mathrm{d}F_{cpx-out}}{\mathrm{d}P}\left(1 - \left[T^*\right]^{\beta_2}\right) + \beta_2 \left[T^*\right]^{\beta_2 - 1}\left(\frac{\partial T^*}{\partial P}\right)_{T_R}\left(1 - F_{cpx-out}\right) \tag{6.29}$$

and

$$\left(\frac{\partial F_{opx}}{\partial T_R}\right)_P = \frac{\mathrm{d}F_{cpx-out}}{\mathrm{d}T_R}\left(1 - \left[T^*\right]^{\beta_2}\right) + \beta_2 \left[T^*\right]^{\beta_2 - 1}\left(\frac{\partial T^*}{\partial T_R}\right)_P\left(1 - F_{cpx-out}\right) . \tag{6.30}$$

The derivatives of $F_{cpx-out}$ are obtained by differentiating equation 6.16 with respect to pressure and real temperature to give,

$$\frac{\mathrm{d}F_{cpx-out}}{\mathrm{d}P} = \frac{-M_{cpx}R_2}{(R_{cpx})^2} \tag{6.31}$$

and

$$\frac{\mathrm{d}F_{cpx-out}}{\mathrm{d}T_R} = 0\,. \tag{6.32}$$

Equation 6.30 for the change in melt fraction with respect to temperature can be simplified by substituting in the derivative of $F_{cpx-out}$ (equation 6.32) to give

$$\left(\frac{\partial F_{opx}}{\partial T_R}\right)_P = \beta_2 \left[T^*\right]^{\beta_2 - 1} \left(\frac{\partial T^*}{\partial T_R}\right)_P (1 - F_{cpx-out})\,. \tag{6.33}$$

The change in dimensionless temperature, T^*, with respect to pressure is obtained by differentiating equation 6.20 to give

$$\left(\frac{\partial T^*}{\partial P}\right)_{T_R} = \frac{-\left(\frac{\mathrm{d}T_{cpx-out}}{\mathrm{d}P}\right)(T_L - T_{cpx-out}) - \left(\frac{\partial T_L}{\partial P} - \frac{\mathrm{d}T_{cpx-out}}{\mathrm{d}P}\right)(T - T_{cpx-out})}{(T_L - T_{cpx-out})^2}\,. \tag{6.34}$$

The derivative of the liquidus temperature with respect to pressure is obtained by differentiating equation 6.13,

$$\frac{\mathrm{d}T_L}{\mathrm{d}P} = C_2 + 2C_3\,. \tag{6.35}$$

The change in $T_{cpx-out}$ with respect to pressure is obtained by differentiating equation 6.19 to give

$$\frac{\mathrm{d}T_{cpx-out}}{\mathrm{d}P} = \frac{1}{\beta_1} F_{cpx-out}^{\left(\frac{1}{\beta_1}-1\right)} \frac{\mathrm{d}F_{cpx-out}}{\mathrm{d}P} \left(T_L^{lherz} - T_S\right) + \left(\frac{\mathrm{d}T_L^{lherz}}{\mathrm{d}P} - \frac{\mathrm{d}T_S}{\mathrm{d}P}\right) F_{cpx-out}^{\frac{1}{\beta_1}} + \frac{\mathrm{d}T_S}{\mathrm{d}P}\,. \tag{6.36}$$

Here $\frac{\mathrm{d}T_L^{lherz}}{\mathrm{d}P}$, $\frac{\mathrm{d}T_S}{\mathrm{d}P}$ and $\frac{\mathrm{d}F_{cpx-out}}{\mathrm{d}P}$ have been defined previously by equations 6.27, 6.26 and 6.31. The change in dimensionless temperature with respect to real temperature

(equation 6.37) is much simpler because $T_{cpx-out}$ and $F_{cpx-out}$ are only dependent on pressure so that

$$\left(\frac{\partial T^*}{\partial T_R}\right)_P = \frac{1}{(T_L - T_{cpx-out})} . \tag{6.37}$$

6.7.4 Hydrous Melting

The introduction of water into the mantle results in a lower solidus temperature, therefore allowing melting to commence at greater depths than for anhydrous melting. A higher melt fraction is achieved, producing thicker crust.

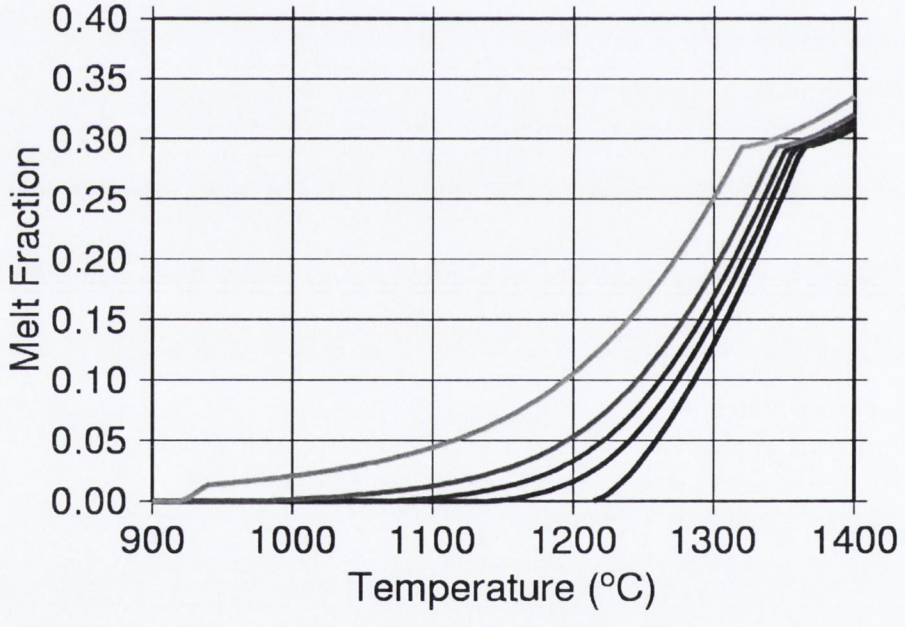

Figure 6.4: Isobaric hydrous melting curves (1 GPa) for a variety of water contents: 0, 0.02, 0.05, 0.1 and 0.3 wt% (black to light grey). Modal clinopyroxene is 17%. The results were produced using the Katz et al. (2003) parameterisation.

Water is treated as an incompatible trace element with a constant bulk partition coefficient, D_{H_2O}, of 0.01. The concentration (dissolved fraction) of water in the melt in weight percent is given by

$$X_{H_2O} = \frac{X_{H_2O}^{bulk}}{D_{H_2O} + F\,(1 - D_{H_2O})} \tag{6.38}$$

where F is the total melt fraction.

The change (decrease) in the solidus and liquidus temperatures, $\Delta T\left(X_{H_2O}\right)$, resulting from the water content of the solid residue is defined by

$$\Delta T\left(X_{H_2O}\right) = K X_{H_2O}^{\gamma}\ ,\ 0 < \gamma < 1 \tag{6.39}$$

where K and γ are constants. The calculation must be consistent with equation 6.40, defining that once the melt is water saturated, the temperature change in the solidus remains constant.

$$\Delta T\left(X_{H_2O} \geq X_{H_2O}^{sat}\right) = \Delta T\left(X_{H_2O}^{sat}\right) \tag{6.40}$$

where $X_{H_2O}^{sat}\left(P\right)$ is the weight percent of water in a completely saturated melt given by

$$X_{H_2O}^{sat} = \chi_1 P^{\lambda} + \chi_2 P\ ,\ 0 < \lambda < 1\ . \tag{6.41}$$

Here χ_1, χ_2 and λ are constants. $\Delta T\left(X_{H_2O}\right)$ is incorporated into the anhydrous parameterisation of the solidus and liquidus temperatures according to equations 6.42 to 6.44.

$$T_S\left(P\right) \rightarrow T_S\left(P\right) - \Delta T\left(X_{H_2O}\right) \tag{6.42}$$

$$T_L^{therz}\left(P\right) \rightarrow T_L^{therz}\left(P\right) - \Delta T\left(X_{H_2O}\right) \tag{6.43}$$

$$T_L\left(P\right) \rightarrow T_L\left(P\right) - \Delta T\left(X_{H_2O}\right) \tag{6.44}$$

These hydrous solidus and liquidus are substituted into the anhydrous equations for melt fraction (equations 6.14 and 6.18) to give new equations for the melt fraction before clinopyroxene exhaustion:

$$F_{cpx}\left(P, T, X_{H_2O}^{bulk}\right) = \left[\frac{T - \left(T_S - \Delta T\left(X_{H_2O}\left(X_{H_2O}^{bulk}, P, F\right)\right)\right)}{T_L^{therz} - T_S}\right]^{\beta_1}\ ; \tag{6.45}$$

and after clinopyroxene exhaustion

$$F_{opx}\left(P,T,X_{H_2O}^{bulk}\right) = F_{cpx-out}+(1-F_{cpx-out})\left[\frac{T-T_{cpx-out}}{T_L-\Delta T\left(X_{H_2O}\left(X_{H_2O}^{bulk},P,F\right)\right)-T_{cpx-out}}\right]^{\beta_2} \tag{6.46}$$

Here $T_{cpx-out}$ is defined as

$$T_{cpx-out} = F_{cpx-out}^{\frac{1}{\beta_1}}\left(T_L^{lherz}-T_S\right)+T_S-\Delta T\left(X_{H_2O}\left(X_{H_2O}^{bulk},P,F\right)\right)\ . \tag{6.47}$$

Calculating the total melt fraction from the hydrous equations is more complex than for anhydrous melting because the equations are implicit for the melt fraction, F. The melt fraction cannot be solved for using analytical methods and therefore, a numerical root-bisection method is employed. The temperature correction for the latent heat of melting must also be consistent with the final melt fraction therefore, a further nested root-bisection is required as described in section 6.7.2. The introduction of a second root-bisection function significantly increases the computation time required to calculate the melt fraction for hydrous compared to anhydrous melting.

6.7.5 Hydrous Melting Derivatives

The following equations are required to calculate the melting rate for the new total melt fraction. Unlike the equations for melt fraction (equations 6.45 and 6.46), the partial derivatives of melt fraction with respect to pressure and real temperature can be solved for analytically. A dimensionless temperature, T'', is defined to simplify the calculation:

$$T'' = \frac{T_R-\left(T_S-\Delta T\left(X_{h_2o}\left(X_{h_2o}^{bulk},P,F_{cpx}\right)\right)\right)}{\left(T_L^{lherz}-T_S\right)}\ . \tag{6.48}$$

For melting prior to clinopyroxene exhaustion, the partial derivative of melt fraction with respect to pressure is obtained by differentiating equation 6.45 to give

$$\left(\frac{\partial F_{cpx}}{\partial P}\right)_{T_R} = \frac{-\frac{\mathrm{d}T_S}{\mathrm{d}P}\left(T_L^{lherz}-T_S\right)-\left(\frac{\mathrm{d}T_L^{lherz}}{\mathrm{d}P}-\frac{\mathrm{d}T_S}{\mathrm{d}P}\right)\left(T-\left(T_S-\Delta T\right)\right)}{\left(\frac{\left(T_L^{lherz}-T_S\right)^2}{\beta_1[T'']^{(\beta_1-1)}}+\frac{K\gamma X_{H_2O}^{(\gamma-1)}\left(1-D_{H_2O}\right)X_{H_2O}^{bulk}\left(T_L^{lherz}-T_S\right)}{\left(D_{H_2O}+F_{cpx}\left(1-D_{H_2O}\right)\right)^2}\right)} \tag{6.49}$$

where $\frac{dT_S}{dP}$ and $\frac{dT_L^{lherz}}{dP}$ are defined by equations 6.26 and 6.27. The partial derivative of melt fraction with respect to real temperature is obtained by differentiating equation 6.45 to give

$$\left(\frac{\partial F_{cpx}}{\partial T_R}\right)_P = \frac{1}{\left(\frac{\left(T_L^{lherz}-T_S\right)}{\beta_1[T'']^{(\beta_1-1)}} + \frac{K\gamma X_{H_2O}^{(\gamma-1)}\left(1-D_{H_2O}\right)X_{H_2O}^{bulk}}{\left(D_{H_2O}+F_{cpx}\left(1-D_{H_2O}\right)\right)^2}\right)} . \tag{6.50}$$

The complexity again increases for melting after the exhaustion of clinopyroxene, therefore in order to simplify the final equations another dimensionless temperature, T^{**}, is defined as

$$T^{**} = \frac{T_R - T_{cpx-out}}{T_L - \Delta T\left(X_{h_2o}\left(X_{h_2o}^{bulk}, P, F_{opx}\right)\right) - T_{cpx-out}} . \tag{6.51}$$

The partial derivative of melt fraction with respect to pressure is obtained by differentiating equation 6.46 to give equation 6.56. The expression for $\left(\frac{\partial F_{opx}}{\partial P}\right)_{T_R}$ is broken down into different parts: W, X, Y, Z given by equations 6.52 to 6.55 which are then incorporated into the final expression (equation 6.56).

Let

$$W = \frac{1}{\beta_1} F_{cpx-out}^{\left(\frac{1}{\beta_1}-1\right)} \left(\frac{dF_{cpx-out}}{dP}\right)\left(T_L^{lherz} - T_S\right) + \left(\frac{dT_L^{lherz}}{dP} - \frac{dT_S}{dP}\right) F_{cpx-out}^{\left(\frac{1}{\beta_1}-1\right)} + \frac{dT_S}{dP} \tag{6.52}$$

where $\frac{dF_{cpx-out}}{dP}$ is defined by equation 6.31. Let

$$X = \frac{\left(1-[T^{**}]^{\beta_2}\right)\left(\frac{dF_{cpx-out}}{dP}\right)\left(T_L - \Delta T - T_{cpx-out}\right)^2}{\left(1-F_{cpx-out}\right)\beta_2\left[T^{**}\right]^{(\beta_2-1)}} . \tag{6.53}$$

Let

$$Y = \frac{\left(T_L - \Delta T - T_{cpx-out}\right)^2}{\left(1-F_{cpx-out}\right)\beta_2\left[T^{**}\right]^{(\beta_2-1)}} . \tag{6.54}$$

Let

$$Z = \frac{K\gamma X_{H_2O}^{(\gamma-1)}\left(1-D_{H_2O}\right)X_{H_2O}^{bulk}}{\left(D_{H_2O}+F_{opx}\left(1-D_{H_2O}\right)\right)^2} \tag{6.55}$$

.

The final expression for the partial derivative of the melt fraction with respect to

pressure is then given by

$$\left(\frac{\partial F_{opx}}{\partial P}\right)_{T_R} = \frac{X + W\left(\Delta T + T_{cpx-out} - T_L\right) - \left(\frac{\mathrm{d}T_L}{\mathrm{d}P} - W\right)\left(T_R - T_{cpx-out}\right)}{\left(Y + Z\left(T_L - \Delta T - T_{cpx-out}\right)\right)} \tag{6.56}$$

where $\frac{\mathrm{d}T_L}{\mathrm{d}P}$ is given by equation 6.35. The partial derivative of melt fraction with respect to real temperature is obtained by differentiating equation 6.46 to give

$$\left(\frac{\partial F_{opx}}{\partial T_R}\right)_P = \frac{\left(T_L - \Delta T - T_{cpx-out}\right)}{\left(\frac{\left(T_L - \Delta T - T_{cpx-out}\right)^2}{\beta_2 [T^{**}]^{(\beta_2 - 1)}(1 - F_{cpx-out})} - Z\left(T_L - \Delta T - T_{cpx-out}\right)\right)} \tag{6.57}$$

where Z is defined by equation 6.55.

6.7.6 Change in Melt Fraction

The change in melt fraction is the amount of melt in the mantle that has been produced at any given place during the previous time step. The change in melt fraction, ΔF is given by

$$\Delta F = F_t - (1 - R) \tag{6.58}$$

where F_t is the new total melt fraction and R is the mass fraction of mantle residue advected round from the previous time step. This value is used for calculating the effect of latent heat of melting on the temperature and the instantaneous melting rate. The melting region is defined as the area where the change in melt fraction is greater than zero.

6.8 Crustal Thickness

The crustal thickness is calculated by integrating all the local instantaneous melting rates to find the total volumetric production rate and dividing this value by the spreading rate (Bown and White, 1994). It is assumed that all the melt produced is transported through the mantle to form the crust. Bown and White (1994) have suc-

cessfully reproduced observed crustal thicknesses from a global data set of mid-ocean ridges and therefore, this assumption is reasonable.

The first task in calculating the crustal thickness is to calculate the local instantaneous melt production rate, given by the Lagrangian derivative of F_t,

$$\frac{\mathrm{D}F_t}{\mathrm{D}t} = \frac{\mathrm{D}P}{\mathrm{D}t}\left(\frac{\partial F_t}{\partial P}\right)_{T_R} + \frac{\mathrm{D}T_R}{\mathrm{D}t}\left(\frac{\partial F_t}{\partial T_R}\right)_P , \tag{6.59}$$

based on Bown and White (1995). In this expression F_t can be substituted for F_{cpx} and F_{opx} for either anhydrous or hydrous calculations. The Lagrangian derivative is defined in appendix D. The various derivatives required to calculate $\left(\frac{\partial F}{\partial P}\right)_{T_R}$ and $\left(\frac{\partial F}{\partial T_R}\right)_P$ are given in section 6.7.3 for anhydrous melting and section 6.7.5 for hydrous melting. The pressure is assumed to be constant in time and constant laterally so that $\frac{\mathrm{D}P}{\mathrm{D}t}$ can be defined as

$$\frac{\mathrm{D}P}{\mathrm{D}t} = -v_z \rho_s g \tag{6.60}$$

where ρ_s is density of the mantle matrix. Density is assumed to be constant throughout the mantle. In reality density may vary with depth and distance from the ridge. However, as shown by several authors including Bown and White (1994), this simplified assumption does not have a significant effect on the model predictions as the results compare well with global observations. Obtaining $\frac{\mathrm{D}T_R}{\mathrm{D}t}$ is more complex. There are two equations for the melt fraction because of the correction for the latent heat of melting and therefore there are also two equations for the Lagrangian derivative of the melt fraction. The Lagrangian derivative of the correction for latent heat of melting (equation 6.21) is given by

$$c_p \frac{\mathrm{D}T}{\mathrm{D}t} = \Delta S \frac{\mathrm{D}\Delta F}{\mathrm{D}t} T_R + \frac{\mathrm{D}T_R}{\mathrm{D}t}\left(c_p + \Delta F \Delta S\right) \tag{6.61}$$

where $\frac{\mathrm{D}T}{\mathrm{D}t}$ is the Lagrangian derivative of the initial (uncorrected) temperature, obtained from the thermal advection-diffusion equation (equation 6.7) and this is calculated using

$$\frac{\mathrm{D}T}{\mathrm{D}t} = \kappa\left(\frac{\partial^2 T}{\partial x^2} + \frac{\partial^2 T}{\partial z^2}\right) - v_z h \tag{6.62}$$

from Bown and White (1995). The local instantaneous melting rate is then calculated using the root-bisection method. Equations 6.59 and 6.61 must be consistent to achieve the appropriate value for the Lagrangian derivative of real temperature and therefore, calculate the final instantaneous melting rate. The rate of change in the new melt fraction, $\frac{\mathrm{D}\Delta F}{\mathrm{D}t}$, and the total melt fraction $\frac{\mathrm{D}F_t}{\mathrm{D}t}$ are the same.

The instantaneous melting rate is integrated over the whole melting region to give, Γ, the total volumetric melt production rate

$$\Gamma = \frac{\rho_s}{\rho_c} \int_A \frac{\frac{\mathrm{D}F}{\mathrm{D}t}}{(R - \Delta F)^2} \mathrm{d}A \tag{6.63}$$

where A is the area of the melting region (adapted from Bown and White, 1994). The volumetric melt production rate actually refers to the area of melt rather than volume because this is a 2D calculation. This expression includes a correction for the density of the mantle compared to the crust and an approximation for the compaction correction (White et al., 1992). The crustal thickness, t_c, is calculated according to the spreading rate using

$$t_c = \frac{2\Gamma}{u_f} \tag{6.64}$$

where u_f is the full spreading rate. The final crustal thickness is saved as the starting crust value for the next time step. The initial value of the crust is set to 0 km.

6.9 Composition

The composition of rift products is required so that comparisons can be made between models of mid-ocean ridge melting and geochemical observations. Constant bulk partition coefficients are used to calculate the concentrations of different trace elements in the mantle melts. This method is over-simplified and will not produce realistic values. However, the relative behaviour of different elements through time can be compared to the relative differences observed in the geochemistry. Fictive elements with standard compatibilities of 5, 2, 1, 0.1, 0.01 and 0.001 provide a quantitative idea of how compatible and incompatible elements behave during melting. Bulk partition coefficients of several trace elements: Nb, Zr, Y, Sm and Yb are used to compare model compositions

with trace element observations from different rift stages at Iceland. The application of the compositional calculation, including chosen bulk partition coefficients and source composition is described in section 7.2. The concentration in the liquid of any element, with a constant bulk partition coefficient, undergoing fractional melting is given by

$$\frac{C_L}{C_0} = \frac{1}{D}(1 - F_t)^{\frac{1}{D}-1} \tag{6.65}$$

where C_L is the concentration in the melt, C_0 is the original concentration in the residue, D is the bulk partition coefficient (Shaw, 1970). The variation in the concentration of fictive elements with melt fraction is shown in figure 6.5.

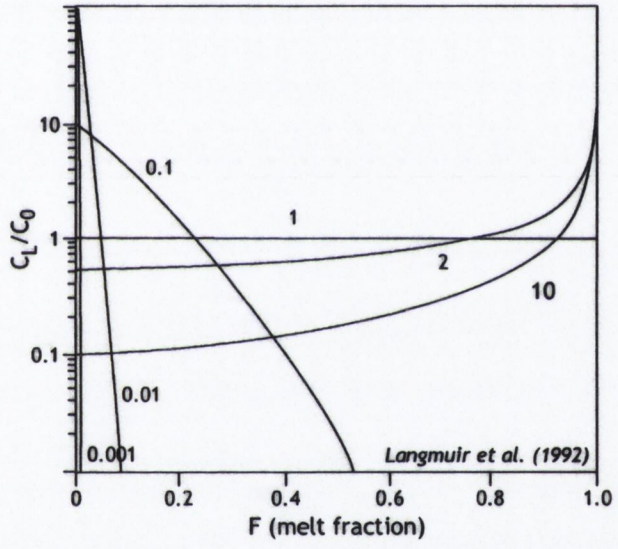

Figure 6.5: The variation in composition (C_L/C_0) with melt fraction for fractional melting, shown for a variety of bulk partition coefficients (D). Adapted from Langmuir et al. (1992).

In order to calculate the average melt composition, which could then be realistically compared to the lava compositions, it is necessary to calculate the accumulated instantaneous composition. Due to computational restrictions the grid size must be kept quite large relative to the changes in melt fraction. The grid size has a significant impact at the edges of the melting region where very small melt fractions result in exceptionally high concentrations of incompatible elements. These high concentrations would be lost if an average of the instantaneous liquid compositions is calculated. Figure 6.5 shows how quickly the concentration of an incompatible element can decrease for increasing melt fraction. Therefore, to include the incompatible element concentration that is excluded by the discretisation, accumulated concentrations in the vertical direction are calculated for each grid square using

$$C_L^{acc} = \int_{F_1}^{F_2} C_L \mathrm{d}F \tag{6.66}$$

where C_L^{acc} is the accumulated instantaneous melt composition, and F_2 and F_1 are the total melt fraction at the grid node of interest and the grid node directly below. Evaluating the definite integral gives

$$C_L^{acc} = \frac{C_0}{D}\left[-\frac{(1-F_t)^{\left(\frac{1}{D}\right)}}{\left(\frac{1}{D}\right)}\right]_{F_1}^{F_2}. \tag{6.67}$$

All the accumulated instantaneous melt compositions are weighted according to the melting rate, $\frac{\mathrm{D}F_t}{\mathrm{D}t}$, and then integrated across the melting region. This compositional value is then averaged over the total volumetric melt production rate (equation 6.63) to give the final average melt composition at the ridge. The average composition in the liquid is given by

$$C_L^{Average} = \frac{\int_A C_L^{acc} \frac{\frac{\mathrm{D}F_t}{\mathrm{D}t}}{(R-\Delta F)^2} \mathrm{d}A}{\int_A \frac{\frac{\mathrm{D}F_t}{\mathrm{D}t}}{(R-\Delta F)^2} \mathrm{d}A}. \tag{6.68}$$

6.10 Summary

The equations presented in this chapter produce a model of mid-ocean ridge melting that can incorporate different temporal changes in the independent variables. In the application to Iceland the spreading rate is varied through time, to reflect changes in spreading rate associated with rift relocations. The results from this application are presented in section 7.5. This method can be applied to any rift situation where the spreading rate may be variable, such as extinct rift segments at the Phoenix-Antarctic Ridge, Drake Passage. Variable spreading rates are also relevant during continental rifting, where the extension will increase through time from initial rifting to full oceanic spreading. Continental rifting may have other variables such as the wedge angle, discussed in section 7.6. At Iceland, temporal variations in the plume may produce pulse of hot material radiating out beneath the rift axes. A variable mantle potential temperature could also be incorporated into the model. The tracking the mass fraction of remaining mantle (residue) facilitates new rift initiation into previously

depleted mantle and therefore, a more realistic model of rift relocations.

A comparison is made between the steady-state results of Bown and White (1994) and Katz et al. (2003) and steady-state crustal thickness and melt fraction-depth profiles produced by the new model (section 7.3). The comparison ensures that the new model is consistent with existing models and that the Katz et al. (2003) parameterisation has been implemented correctly. The effects of varying the spreading rate, wedge angle, mantle potential temperature and water content on the crustal thickness and composition through time are presented in section 7.4.

The program is set up to allow the easy addition of different parameterisations of melting and composition. Further simple additions to the compositional calculation would produce more realistic compositions, discussed in chapter 8.

Chapter 7

Model Application

7.1 Introduction

The next task is to apply the new time-dependent model to a realistic situation relating to rift relocations at Iceland. This application is with a view to understanding whether geochemical differences, outlined in chapters 4 and 5, between different rift stages can be correlated with distinct changes in tectonics or are the result of other influencing factors such as glaciation or plume variations.

The aim of this chapter is to test the model against results presented by previous authors (section 7.3) and experiment by systematically varying several independent variables on an individual basis (section 7.4). The final aim, relating back to the original aim of this project, is to present results from the application of the model to rift relocations at Iceland (section 7.5).

7.2 Background

This section provides necessary background information to allow the useful application of the new time-dependent model to Iceland in section 7.5. Modifications required to model rift jumps are described along with data processing to get a meaningful output.

7.2.1 Wedge Angle Variations

The wedge angle defines a theoretical boundary between the area of the melting region where upwelling takes place and the area where flow is purely horizontal within the limitations of 2D corner flow model (see section 6.4). The wedge angle input has a significant effect on the time taken for a ridge to react to changes in the spreading rate (section 7.4.2). This is shown particularly well when starting a ridge in a mantle with no previous history of rifting, with differences in the time to first melts of more than 7 Ma at slow spreading rates comparable to Iceland. Taking into consideration that the life span of a rift segment at Iceland is less than 15 Ma, setting a realistic wedge angle is clearly very important in order to assess the time-dependent effects of tectonic variations on the composition and crustal thickness.

Neither the melt thickness or the melt chemistry can be used to determine the wedge angle. Previously, the wedge angle has been determined by assuming that the controls on the melting region are known. For example, Spiegelman and McKenzie (1987) assumed that temperature is the main control on rheology, and derived scaling relations for the wedge angle. These expressions were used by Bown and White (1994). However, more a study by Hirth and Kohlstedt (1996) suggests that water is a more important control on rheology.

Recent work by Jones (pers. comm.) has provided new constraints on the wedge angle at Iceland using bathymetric data. This method allows a direct measurement of the upwelling rate which leads to the wedge angle. As described in section 2.2, variations in the melt production rate at Iceland form lineations in the topography of the sea floor, in the North Atlantic, known as V-shaped ridges (Vogt, 1971; Jones et al., 2002). Figure 7.1 shows a cross section of the bathymetry along the North Atlantic Ridge, South of Iceland, identifying a series of peaks and troughs. The peaks represent times of high melt productivity relating to pulses of hot/fertile material spreading out in the asthenosphere from the Iceland plume. The troughs represent times of low melt productivity relating to the cold/less fertile periods between pulses. The time taken to change between the peaks and troughs (high and low productivity) can be used to estimate the upwelling rate of a pulse through the melting region if passive upwelling is assumed above 100 km. Maclennan et al. (2001b) show that to reproduce the crustal thickness and geochemical signature in central Iceland, active upwelling is required to flux material through the melting region below 100 km. Ito et al. (1999) predict a significant viscosity change in plume mantle following dehydration after melting begins. This viscosity increase prevents buoyancy forces from contributing

significantly to plume upwelling above the dry solidus (around 60 km). Therefore, the passive upwelling assumption for the majority of the melting region may be valid. The range of depths that are subject to the effects of plume flow is not yet resolved.

Upwelling rate is controlled by the spreading rate and the wedge angle. Since the spreading rate at Iceland is well constrained at 18 mm yr^{-1} (DeMets et al., 1994) using magnetic variations, it is possible to use the estimated upwelling rates from V-shaped Ridge bathymetry to estimate the wedge angle beneath Iceland. Figure 7.2 shows the estimation of the wedge angle for Iceland based on the range of upwelling rates. The result is a very large wedge angle of between 75° and 82°. These large angles reflect fast upwelling rates relative to the slow spreading rate and indicate a relatively narrow zone of upwelling.

The wedge angle can only be estimated using this method if V-shaped ridges exist. The only other useful example where this method can be applied is at the Mid-Atlantic Ridge, south of the Azores hotspot, which also requires a relatively large wedge angle to explain the V-shaped ridge geometries.

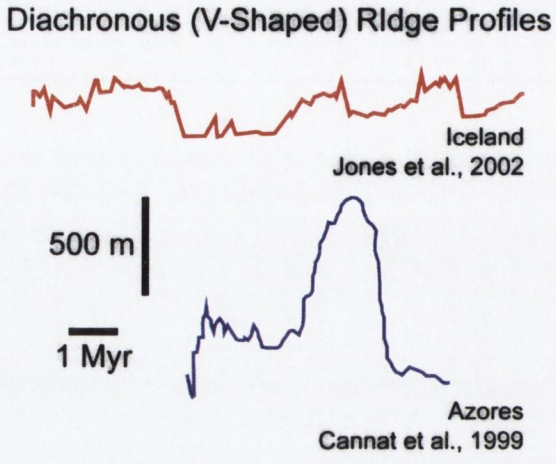

Figure 7.1: Bathymetric cross section, parallel to the plate spreading direction, of V-shaped ridges along the North Atlantic Ridge, South of Iceland and the Mid-Atlantic Ridge south of the Azores hotspot. The vertical scale is distance in m (500m as shown) and the horizontal scale is distance converted into time using the known plate spreading velocity (1Myr as shown). The maximum length of time between peak and trough at Iceland is estimated at 1 Ma (Jones, pers. comm.).

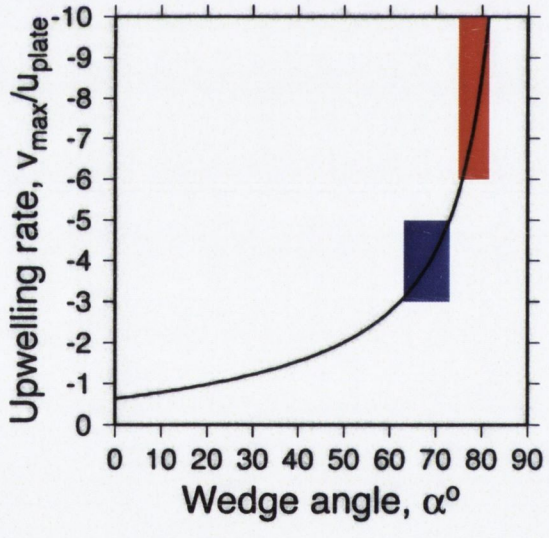

Figure 7.2: The variation in wedge angle with upwelling rate according to the corner flow solution for vertical velocity. The range of upwelling rates are estimated from the peak to trough slopes observed in figure 7.1. Fast upwelling rates at Iceland, relative to the slow spreading rate results in a large wedge angle indicating a narrow zone of upwelling (Jones, pers. comm.).

7.2.2 Modelling Rift Jumps

At Iceland the growth and decline of individual rift segments is part of a system of rift relocations that have occurred at Iceland since its formation at 24 Ma. In order to realistically apply the model to Iceland, the thermal and compositional structure of the mantle must be pre-set to allow for a continuously spreading system where new rifts form within mantle that has already undergone some melting at a pre-existing rift. Rift jumps are included in the new model by running the program for 20 million years until a steady-state is reached that is appropriate for the starting conditions of the new rift. The temperature and residue structure are then transposed laterally by a given distance, representing the rift jump. This models a rift starting to the east of an existing rift, in the crustal and mantle lithosphere conditions created by the existing rift. If the calculation was based solely on temperature, without tracking the mantle residue, the appropriate thermal steady-state starting conditions could be calculated using a half-space cooling model as discussed in section 6.3.

7.2.3 Calculating Mean F

Mean F is the average melt fraction at a particular depth weighted according to the melting rate and provides a good 1D representation of the 2D variation of melt fraction across the melting region. At any particular depth,

$$F(z) = \frac{\int_x F_t \frac{\frac{\mathrm{D}F_t}{\mathrm{D}t}}{(R-\Delta F)} \mathrm{d}x}{\int_x \frac{\frac{\mathrm{D}F_t}{\mathrm{D}t}}{(R-\Delta F)} \mathrm{d}x} \tag{7.1}$$

where x is the horizontal distance across the melting region, F_t is the total melt fraction, $\frac{\mathrm{D}F_t}{\mathrm{D}t}$ is the melting rate and $R - \Delta F$ is a correction for melt extraction based on White et al. (1992).

7.2.4 Composition

The composition is calculated according to accumulated fractional melting for a series of elements with constant bulk partition coefficients (section 6.9). Fictive elements with D values of 5, 2, 1, 0.1, 0.01, 0.001 are used to show the general behaviour of elements with varying compatibility. Composition for fictive elements are plotted as C_L/C_0,

with a constant starting value of C_0 at 1 ppm. The concentrations of real elements Nb, Zr, Y, Sm and Yb in the melt were calculated using bulk partition coefficients and average mantle concentrations presented by Workman and Hart (2005), shown in table 7.1.

The comparison of the model element composition with observations from Iceland is presented in section 7.5.3. It must be noted that this over-simplified approach of using constant bulk partition coefficients to model melt compositions is not expected to reproduce the absolute values observed at Iceland. The comparison concentrates on the relative trends in trace element ratios through time. In reality, the melt composition is influenced by many processes including melting, fractional crystallisation, crustal assimilation, source heterogeneity, alteration and melt transport. The effect of these processes must taken into consideration when analysing the results. The calculation of elements with constant bulk partition coefficients, although very simple, does provide good insight into how the composition may be affected by variations in tectonics and indicates where improvements would be useful in the model.

Element	D	Average DMM (ppm)
Nb	0.0034	0.1485
Zr	0.033	5.082
Y	0.088	3.328
Sm	0.0045	0.239
Yb	0.115	0.365

Table 7.1: Bulk partition coefficients and starting compositions used for the calculation of trace element compositions in the model. Average DMM is the average composition of depleted MORB mantle. Values are from Workman and Hart (2005).

7.3 Model Testing

This section presents a comparison of the new model with the main results presented by Bown and White (1994) and Katz et al. (2003). The new model was based primarily on the Katz et al. (2003) parameterisation, using a similar method to Bown and White (1994). Therefore, it is important to show that the new model produces similar results for the equivalent steady-state results produced by these authors.

The first comparison is made with the predicted anhydrous melt fraction-depth relationship for different spreading rates presented by Bown and White (1994). Figures 7.3 and 7.4 show clearly that the melt fraction-depth profile predicted by the new model compares well with the steady-state results of Bown and White (1994). The overall melt fraction is slightly smaller for any given spreading rate because a different parameterisation is used in the new model compared to the McKenzie and Bickle (1988) parameterisation used by Bown and White (1994). The resultant crustal thickness is similar to that of Bown and White (1994) at 6 km for fast spreading rates and mantle potential temperature of 1300°C (figure 7.7).

The depth of the initiation of melting is around 10 km deeper in the new model. This difference relates to the different parameterisation of the solidus used in the new model. Bown and White (1994) use a length scale argument to obtain the appropriate wedge angle which results in a smaller angle compared to the input of 70° chosen for the new model. The depth of initial melting is the correct result for the Katz et al. (2003) parameterisation as shown in figure 7.5. The depth to the top of the melting region in the new model compares well with Bown and White (1994). The process of conductive cooling at slow spreading rates, identified by Bown and White (1994) as an important constraint on the crustal thickness, is still evident in the results of the new model.

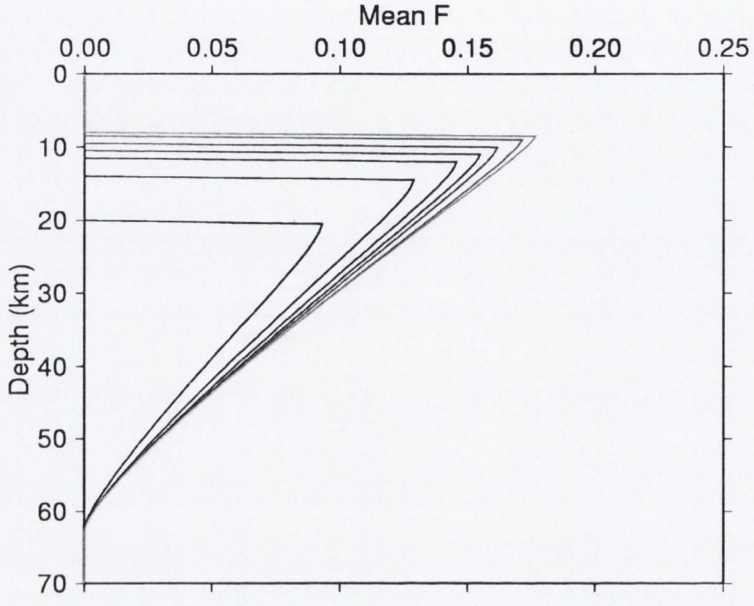

Figure 7.3: Variation in melt fraction with depth from the new model, shown for full spreading rates 10, 20, 30, 40, 50, 75 and 100 mm yr^{-1} (black to light grey) for anhydrous melting. The wedge angle is constant at 70° and mantle potential temperature is constant at 1300°C.

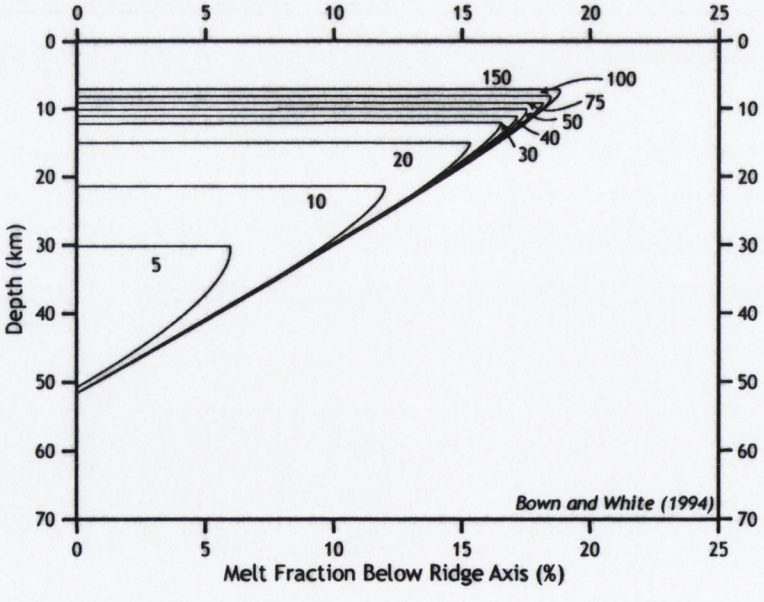

Figure 7.4: Variation in melt fraction with depth, shown for full spreading rates between 5 and 150 mm yr^{-1} for anhydrous melting results from Bown and White (1994). Mantle potential temperature is constant at 1300°C.

The second comparison is made with predicted melt fraction-depth profiles for different water contents for several different mantle potential temperatures presented by Katz et al. (2003). Figure 7.5 shows that the new model melt fraction-depth profiles accurately reproduces the profiles presented by Katz et al. (2003) in figure 7.6. This is important confirmation that the Katz et al. (2003) parameterisation has been implemented correctly. The depth to the top of the melting region is greater for the new model because the velocity model takes into account the presence of the crust and therefore, restricts the zone of upwelling mantle.

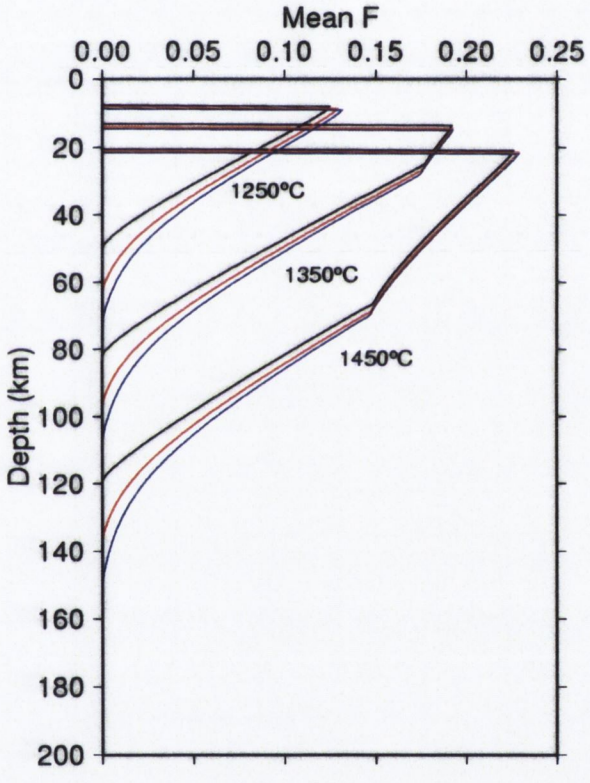

Figure 7.5: Variation in melt fraction with depth from the new model, shown for 1250°C, 1350°C and 1450°C mantle potential temperatures. At each temperature the water content is varied between the following values: 0 (black), 0.01 (red) and 0.02 wt% (blue). Full spreading rate is constant at 50 mm yr^{-1}; wedge angle is constant at 70°.

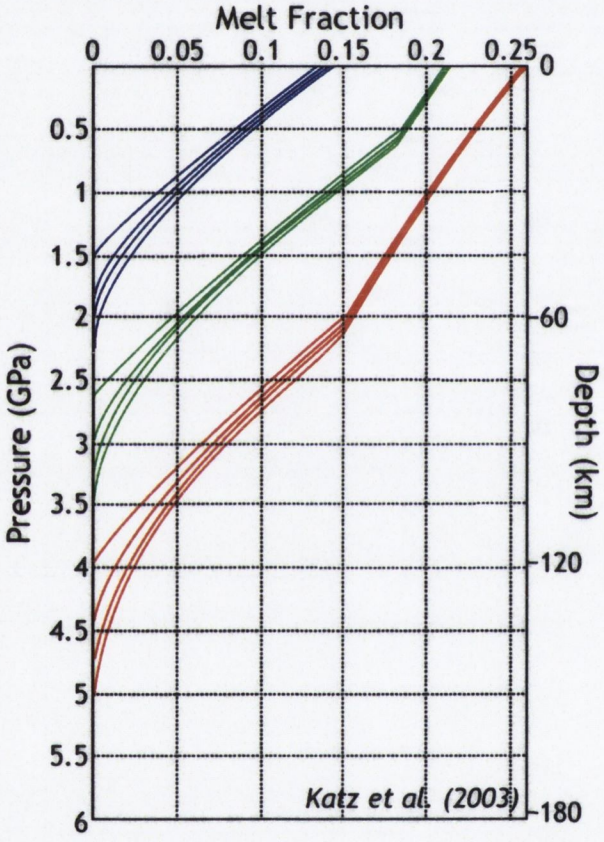

Figure 7.6: Variation in melt fraction with depth, shown for 1250°C (blue), 1350°C (green) and 1450 °C (red) mantle potential temperatures from Katz et al. (2003). At each temperature the water content is varied between 0 and 0.02 wt%.

7.4 Model Experiments

This section presents model data from a series of experiments based on the systematic variation of several independent variables: spreading rate, wedge angle, mantle potential temperature and water content. This is an important part of the testing process, to assess whether the observed effects of varying each of these independently are consistent with existing knowledge of mid-ocean ridge processes. These observations will allow the real application of the model to be made as accurately as possible, with a better understanding of its limitations.

7.4.1 Spreading Rate

The steady-state model of Bown and White (1994) showed that melting and resultant crustal thickness is relatively constant for spreading rates above 15 mm yr^{-1}. Below this value significant changes in the amount and depth of melting occur because conductive cooling has a greater influence over the thermal structure. Slow spreading rates produce significantly less crust with melting occurring over a much smaller depth range. The depth to the top of the melting region is much greater for small spreading rates and this results in a more enriched chemistry for ridge products. Significant decreases start to emerge at 20 mm yr^{-1}.

The variation in crustal thickness for different spreading rates obtained from the new model is shown in figure 7.7. As shown by Bown and White (1994), significant decreases in the steady-state crustal thickness are observed for 20 and 10 mm yr^{-1}. Spreading rates of 30–100 mm yr^{-1} produce steady-state crustal thicknesses within the range of 5.9–6.3 km. At 20 mm yr^{-1} the crustal thickness decreases to 5.6 km, with a further 1.1 km decrease for 10 mm yr^{-1}. The time taken to reach steady-state increases steadily for a decrease in the spreading rate except for very fast rates such as 75 and 100 mm yr^{-1}. For slow spreading rates similar to Iceland the time from initial melting to steady-state is around 4.5 Ma. This is the time taken for a dramatic change in tectonics i.e. from zero spreading instantaneously to 20 mm yr^{-1}. Whether this change is realistic or not, the results have important implications for the application to Iceland. This time is similar to the time between different rift stages at Iceland, therefore the time taken for changes in the spreading rate to be reflected in the ridge products may be too long to produce significant changes before the next rift jump occurs.

The composition varies significantly between fast and slow spreading rates. Figure 7.8 shows the variation in C_L/C_0 for a range of spreading rates for steady-state melting at normal mantle potential temperature. The concentration ratio is essentially constant for fast spreading rates for incompatible elements, with compatible elements ($D > 1$) remaining constant for all spreading rates. Below 40 mm yr^{-1}, the incompatible element concentration starts to increase gradually, and below 20 mm yr^{-1} this increase is more dramatic. These trends compare well with compositional results presented by Bown and White (1994) for major element variations. For example TiO_2 is usually incompatible in basaltic melts, except during fractional crystallisation of magnetite, and is shown to increase in concentration at slow spreading rates (Bown and White, 1994). This incompatible element trend relates back to figures 7.3 and 7.7 where for slow spreading rates of 20 and 10 mm yr^{-1} the amount of melting is reduced to produce thinner crust and the depth to the top of the melting region increases as a result of conductive cooling. These model results are consistent with Bown and White (1994) findings.

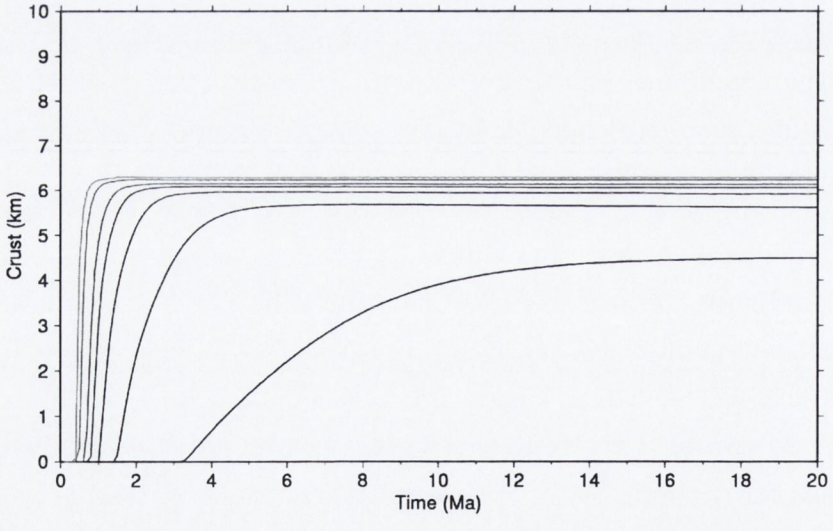

Figure 7.7: The variation in crustal thickness with time, shown for spreading rates 10, 20, 30, 40, 50, 75 and 100 mm yr^{-1} (black to light grey). The wedge angle is constant at 70° with a normal mantle potential temperature of 1300°C and anhydrous melting.

7.4.2 Wedge Angle

As discussed in section 7.2.1, the wedge angle controls the speed of upwelling relative to the spreading rate. A small wedge angle (e.g. 20°) results in a wide melting region with

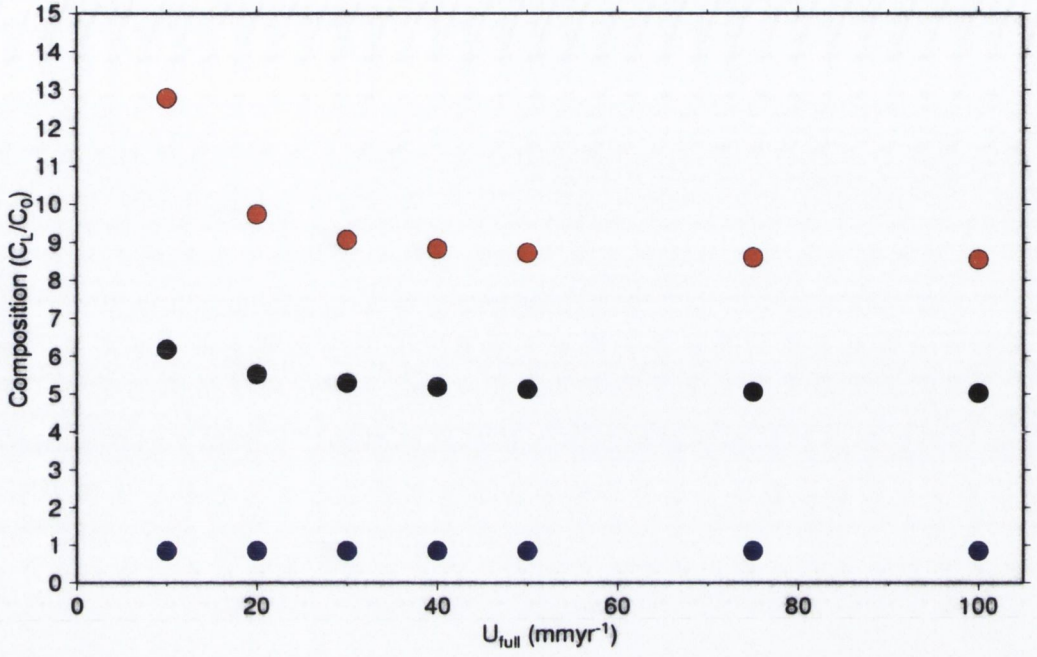

Figure 7.8: The variation in composition (C_L/C_0) with change in spreading rate for anhydrous melting for a range of bulk partition coefficients, D: 1 (blue), 0.1 (black), 0.01 (red). Mantle potential temperature is constant at 1300°C.

low upwelling rates compared to a large wedge angle (e.g. 80°) where the melting region is very narrow with fast upwelling rates. At Iceland, good constraints on the wedge angle are obtained from bathymetric observations (figure 7.2). A well constrained wedge angle may not be available for all applications of the model and therefore, it is important to observe how the wedge angle can impact on the rate and amount of melting at a ridge. There are also interesting implications for the origin of amagmatic continental margins (see section 7.6).

For all spreading rates, the variation in wedge angle has a direct influence on the time taken for melting to start at a new ridge and the time required for the ridge to become fully established i.e. reach steady-state melting. Small wedge angles result in relatively low upwelling rates compared to the spreading rate and the time taken to start melting is longer than for large wedge angles. It follows that for small wedge angles, it takes longer for a ridge to progress from initial melting to steady-state melting compared to large wedge angles. There are also significant effects on the final steady-state crustal thickness.

At fast spreading rates such as 50 mm yr^{-1} (figure 7.9), time to initial melting is

only 0.4 Ma for an 80° wedge angle compared to 2.4 Ma for a 20° wedge angle. The difference in time from initial melting to steady-state melting at fast spreading rates is even more significant, with just over 1 Ma for 80° and nearly 8 Ma for 20°. The final crustal thickness for 20° is 5.3 km where as for 80° it is significantly greater at 6.2 km. The dip in crustal thickness after several million years for smaller wedge angles is the result of the slow upwelling rate. At the beginning all of the mantle is assumed to be without melting history, as the melting starts and increases throughout the mantle to reach the steady-state melting the mantle builds up a melting history. For true steady-state activity the mantle residue across the melting region must also be steady. For very slow upwelling rates it takes much longer for the residue to advect to reach steady-state compared to temperature, which is affected by conduction as well as advection. This dip in crustal thickness is artificial and results from an instantaneous change from zero to full spreading. In reality, the spreading rate across a new rift will increase gradually with time. The results are still important for a good understanding of model behaviour.

These effects of wedge angle variations on the timing of melting are compounded at slow spreading rates such as 20 mm yr^{-1}, similar to Iceland (figure 7.10). The initiation of melting for an 80° wedge angle is after 0.8 Ma compared to 7.5 Ma for a 20° wedge angle. The time between initial melting and steady-state is around 4.5 Ma for 80° and increases to significantly more than 12 Ma for 20°. The difference in crustal thickness between 20° and 80° would be around 2 km if timing continued beyond 20 Ma. The dips in steady-state crustal thickness would be observed at slow spreading rates and small wedge angles if calculations are allowed to continue in time.

The significant time differences clearly have important implications for time-dependent calculations where changes in melting caused by other factors such as spreading rate variations may take longer to be observed in the ridge output. The extreme differences observed in time and crustal thickness at spreading rates similar to Iceland indicate that good constraints on the wedge angle are required to produce a meaningful result.

The effect of different wedge angles on the composition of ridge products is shown in figure 7.11. The concentration of very incompatible elements in the melt at steady-state melting is directly related to the amount of melting and therefore, the variation in composition with the wedge angle is consistent with the crustal thickness variation in figures 7.9 and 7.10. As the wedge angle decreases the concentration of very incompatible elements in the melt increases. The difference in the incompatible element concentration between slow and fast spreading rates reduces for larger wedge angles.

This is consistent with the relatively small difference in crustal thickness between fast and slow spreading rates for large wedge angles.

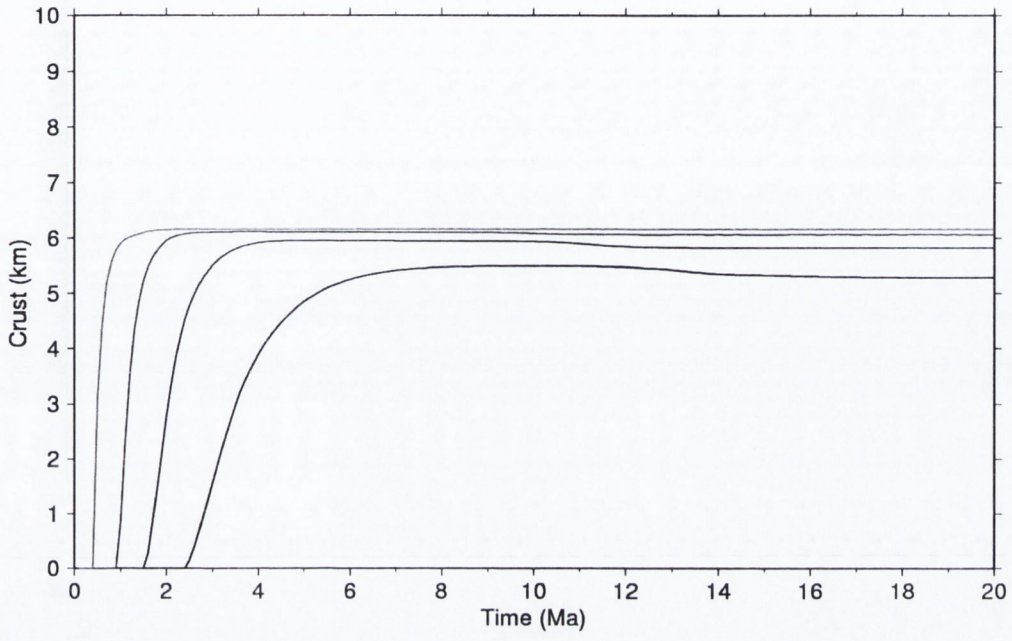

Figure 7.9: The variation in crustal thickness with time, shown for 20, 40, 60 and 80° wedge angles (black to light grey). The full spreading rate is constant at 50 mm yr^{-1} with a normal mantle potential temperature of 1300°C and anhydrous melting.

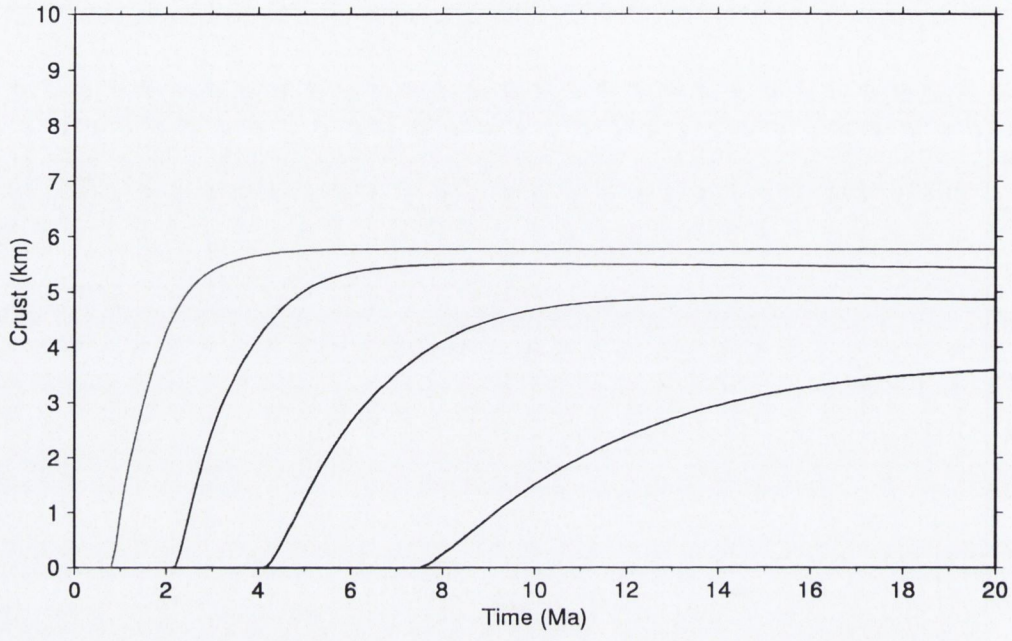

Figure 7.10: The variation in crustal thickness with time, shown for 20, 40, 60 and 80° wedge angles (black to light grey). The full spreading rate is constant at 20 mm yr^{-1} with a normal mantle potential temperature of 1300°C and anhydrous melting.

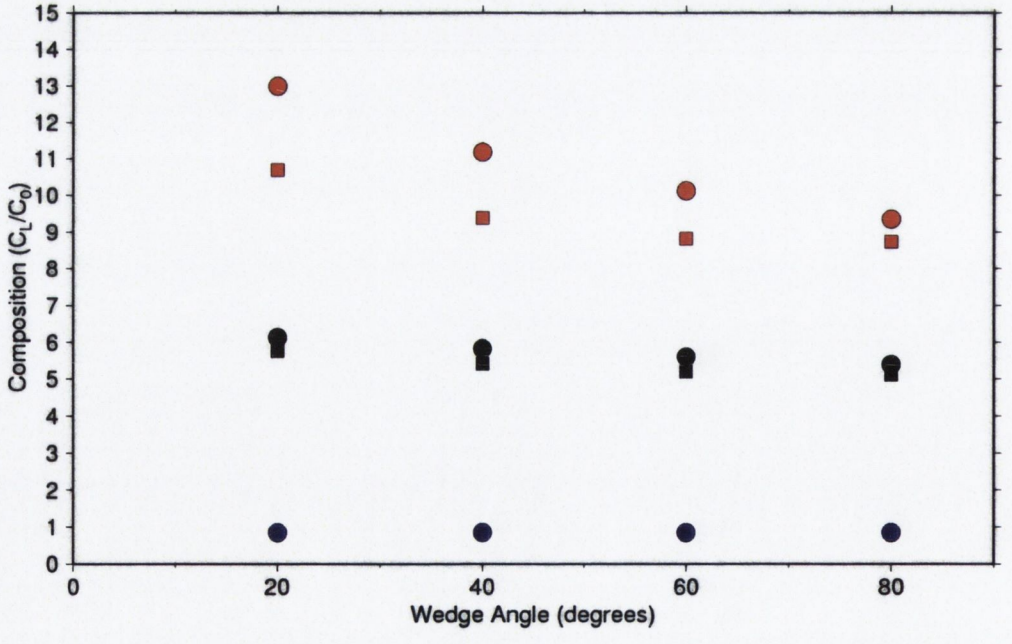

Figure 7.11: The variation in composition (C_L/C_0) with change in the wedge angle for steady-state anhydrous melting for a range of bulk partition coefficients, D: 1 (blue), 0.1 (black), 0.01 (red). Two full spreading rates are shown: 20 mm yr^{-1} (circles) and 50 mm yr^{-1} (squares). Mantle potential temperature is constant at 1300°C.

7.4.3 Mantle Potential Temperature

Mantle potential temperature has a significant influence over the amount of melting at a ridge axis. The extreme mantle potential temperature at Iceland of up to 1500°C (White et al., 1995) results in an average 20 km thick crust. This crustal thickness is compared to a global average at mid-ocean ridges of 6 km for normal mantle potential temperatures of around 1300°C (Bown and White, 1994). Figure 7.12 shows the crustal thickness variation in time for different mantle potential temperatures at a variety of spreading rates. For all spreading rates, increasing potential temperature causes dramatic increases in crustal thickness. An increase from 1250 to 1350°C results in more than double the amount of crust at steady-state melting for a constant wedge angle. At a very high mantle potential temperature (1450°C), the steady-state crustal thickness for slow spreading rates (e.g. 10 mm yr^{-1}) is consistent with the steady-state crustal thickness for faster spreading rates. At lower temperatures, slow spreading rates produce significantly less crust compared to fast spreading rates as shown in figure 7.7.

Significant time differences are also observed for different potential temperatures for the same spreading rate. The time to initial melting is significantly shorter for higher temperatures, for example at 10 mm yr^{-1} initial melting occurs at 5 Ma for 1250°C compared to 1.9 Ma for 1350°C. At a very high mantle potential temperature (1450°C) melting starts immediately, as the starting temperature field crosses the solidus in a mantle with no melting history. Although this is not a realistic situation as discussed in section 7.6, it still provides useful information about how the model behaves. The sharp decreases observed in faster spreading rate curves at 1450°C are artificial, caused by re-equilibration of the mantle residue as the melting history is taken into account. The model is clearly not as stable at very high temperatures, particularly at a slow spreading rates. This could be caused by the relationship between conduction and advection: at high temperatures and slow upwelling rates conduction will have an increased control over melting. The residue is still controlled by advection and this instability maybe caused by a catch up by the residue every few time steps.

The concentration of incompatible elements increases for a decrease in mantle potential temperature non-linearly for constant anhydrous melting (figure 7.13). Slow spreading (10 mm yr^{-1}) results in increasingly higher concentrations compared to fast spreading (50 mm yr^{-1}) as potential temperature decreases. At high mantle potential temperature (1450°) the difference between mild incompatible and very incompatible element concentrations is greatly reduced compared to low temperatures. This is consistent with the variation in C_L/C_0 with melt fraction for fractional melting. Elements with a

D value of 0.1 and 0.01 have the same concentration in the melt relative to the starting composition once the melt fraction is more than 25% (Langmuir et al.,1992). The total melt fraction for 1450°C at 50 mm yr^{-1} (figure 7.5) is 23%, therefore the very similar concentrations of elements with D=0.1 and 0.01 is expected.

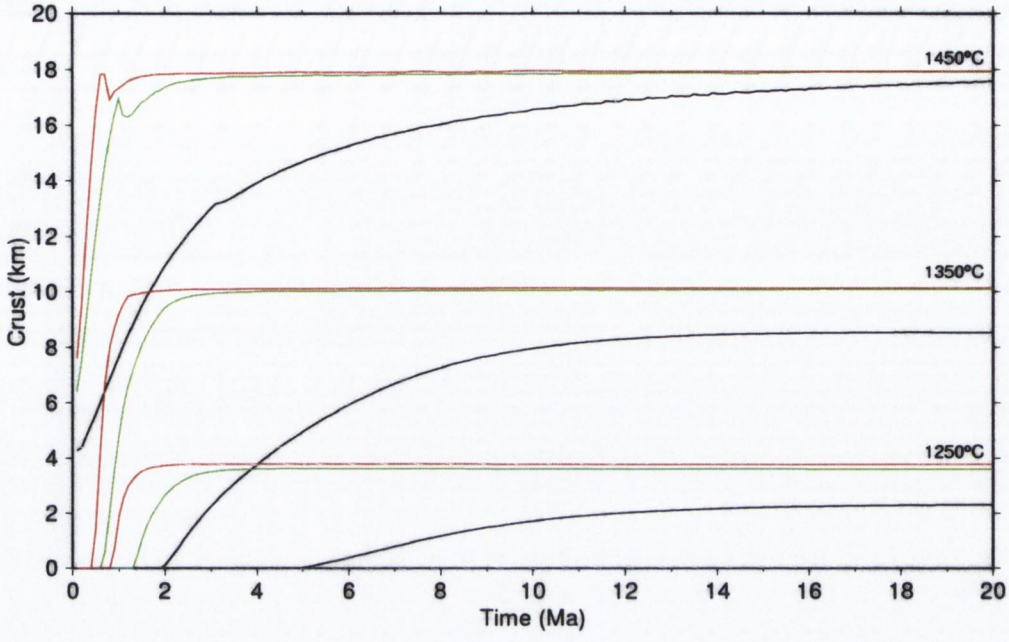

Figure 7.12: The variation in crustal thickness with time for varying mantle potential temperature at different spreading rates. Full spreading rates shown are 10 mm yr^{-1} (black), 30 mm yr^{-1} (green) and 50 mm yr^{-1} (red). The mantle potential temperatures are 1250, 1350 and 1450°C. Wedge angle remains constant at 70° with anhydrous melting.

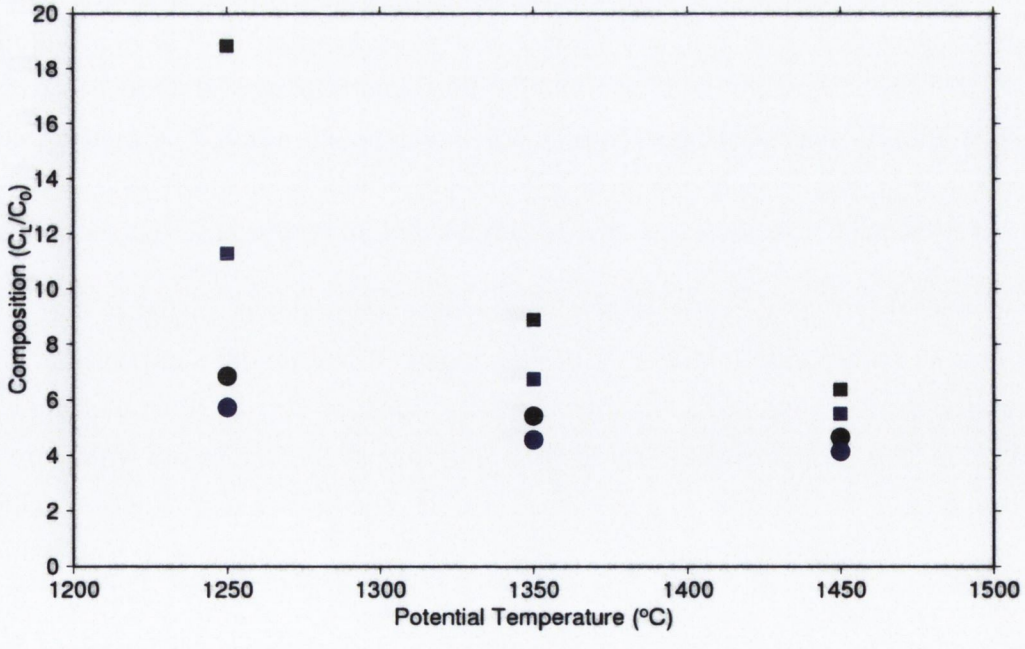

Figure 7.13: The variation in composition (C_L/C_0) with change in the mantle potential temperature for steady-state anhydrous melting for incompatible elements: D= 0.1 (circles), 0.01 (squares). Two full spreading rates are shown: 10 mm yr^{-1} (black) and 50 mm yr^{-1} (blue). Wedge angle is constant at 70°.

7.4.4 Water Content

The main advantage of implementing the Katz et al. (2003) parameterisation is that hydrous melting can be introduced. As discussed in section 2.3.2, it is clear that melting at mid-ocean ridges is influenced by water. Katz et al. (2003) showed that as water content increases the basal depth of the melting region increases to produce low melt fraction tails (figures 7.5 and 7.15). Deep melting at small melt fractions has a significant impact on melt chemistry because of the different bulk partition coefficients associated with garnet during deep mantle melting and the very small melt fractions. As with previous model experiments, it is important to understand how the model behaves in response to different water contents.

The effect of increasing water contents on the crustal thickness is systematic for a range of spreading rates (figure 7.14). For increasing water content, the steady-state crustal thickness increases. The time taken to initial melting is shortened and this effect is particularly significant for a slow spreading rate. Finally the time between initial melting and steady-state melting remains relatively unchanged for different water contents.

The melt fraction-depth profile for steady-state melting (figure 7.15) shows deep low melt fraction tails for increasing water content. The depth of initial melting is constant for different spreading rates with same water content in the mantle. The depth of initial melting increases from around 63 km to 85 km for 0 and 0.02 wt% H_2O respectively for a normal mantle potential temperature. Therefore, a small amount of melting occurs within the garnet-spinel transition zone (80–100 km) when the mantle contains a small amount of water. This result is expected from the evidence presented in section 2.3.2.

The composition (C_L/C_0) for different water contents is shown in figure 7.16. It is clear that the water content has very little impact on the model composition, which is essentially constant for both incompatible D values for steady-state melting. This is because the composition is calculated with bulk partition coefficients which are constant throughout the mantle. The result is that the same total melt fraction achieved for different water contents (figure 7.5) produces similar composition to that achieved by batch melting. In reality, the deep low melt fraction tail would introduce significant differences into incompatible element ratios due to partitioning of elements during melting in the presence of garnet. This constant composition is one significant disadvantage to the simple application of constant bulk partition coefficients in order to estimate the composition of ridge products.

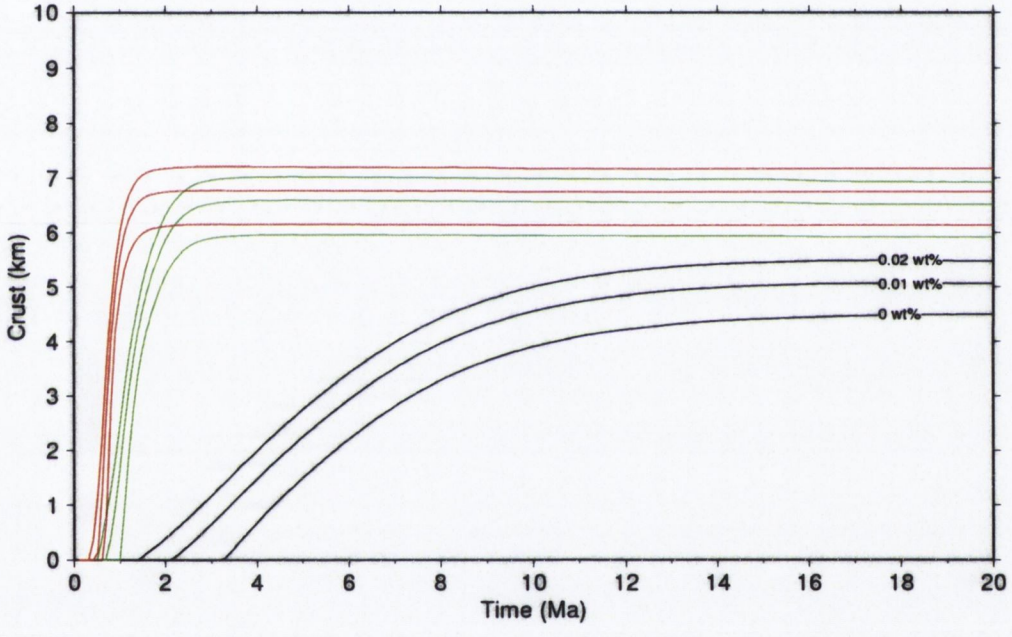

Figure 7.14: The variation in crustal thickness with time for varying water contents at different spreading rates. Hydrous melting is carried out for 0, 0.01 and 0.02 wt% H_2O. Full spreading rates shown are 10 mm yr^{-1} (black), 30 mm yr^{-1} (green) and 50 mm yr^{-1} (red). The mantle potential temperature is constant at 1300°C. Wedge angle remains constant at 70°.

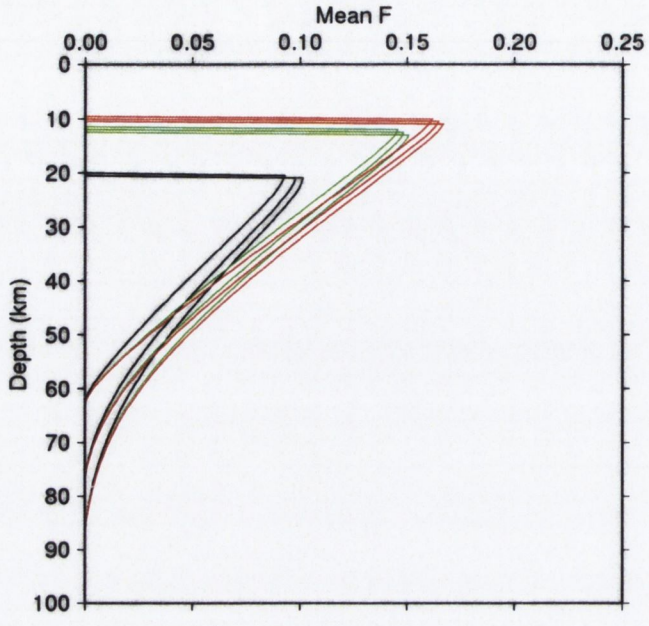

Figure 7.15: Variation in melt fraction with depth at steady-state melting, shown for 0, 0.01 and 0.02 wt% H_2O. Full spreading rate is varied as follows: 10 mm yr^{-1} (black), 30 mm yr^{-1} (green) and 50 mm yr^{-1} (red). The mantle potential temperature is constant at 1300°C. Wedge angle remains constant at 70°.

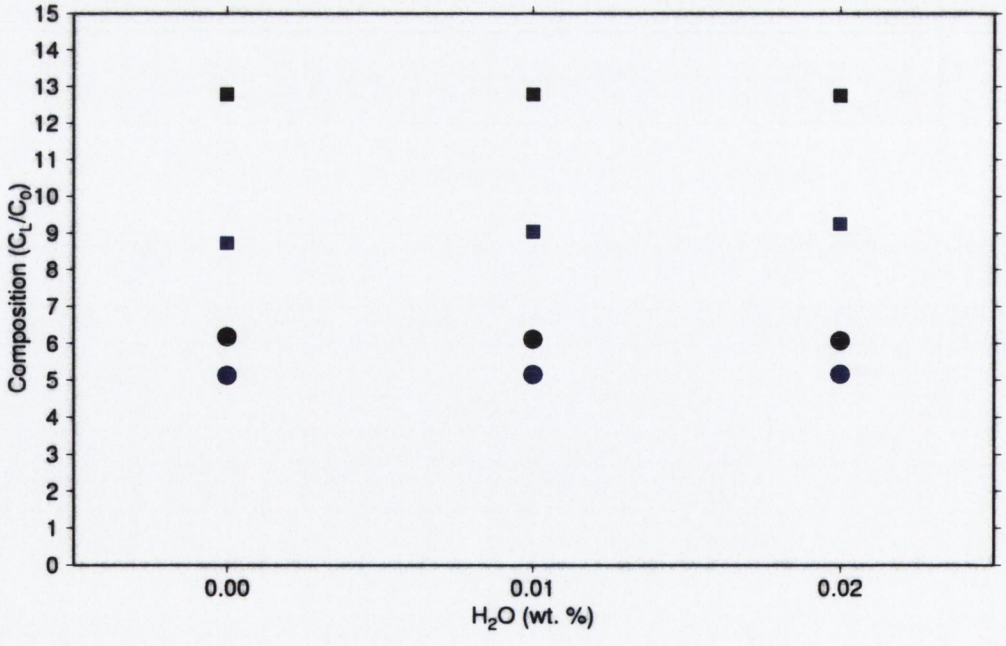

Figure 7.16: The variation in composition (C_L/C_0) with change in water content for steady-state melting for incompatible elements: D= 0.1 (circles), 0.01 (squares). Two full spreading rates are shown: 10 mm yr^{-1} (black) and 50 mm yr^{-1} (blue). Mantle potential temperature is constant at 1300°C and the wedge angle is constant at 70°.

7.5 Application to Iceland

This section presents results from the application of the new model to a rift jump at Iceland. The constraints used for the model, such as spreading rate variation are described below. A brief review of the main conclusions derived from geochemical analysis presented in chapters 4 and 5 is provided for comparison with the model results. The aim of the application is to model the complete rift cycle dictated by rift jumps at Iceland, and correlate any significant changes in melting with geochemical observations from the different rift stages present at Iceland. The rift cycle starts with the initiation of a new rift followed by a period of growth as extension transfers from an adjacent existing rift. The middle stage of the cycle is referred to as steady-state when the new rift takes up full spreading rate at Iceland. The final stage is the decline of the rift segment as extension gradually transfers from the present rift to the next new rift.

7.5.1 Constraints

Constraints on the length of time for each active segment and the associated spreading rate for different rift stages are developed from a combination of DeMets et al. (1994) estimates from geomagnetic reversals; results from dating techniques carried out by Everts et al. (1972) and Garcia et al. (2003); and geodetic GPS data presented by LaFemina et al. (2005). The full spreading rate of the Mid-Atlantic Ridge at Iceland is 18 mm yr^{-1} (DeMets et al., 1994). Garcia et al. (2003) showed that rift relocations are characterised by simultaneous activity across two parallel rifts for several million years prior to the complete extinction of the older rift. Simultaneous activity results in partitioning of plate spreading across the two rifts. LaFemina et al. (2005) presents spreading rate observations from GPS data along the Western and Eastern Volcanic Zones. The slowest rate is observed at the northeast end of the Western Volcanic Zone at 2.6±0.9 mm yr^{-1}. A simple velocity model based on the observations presented by Garcia et al. (2003) and LaFemina et al. (2005) is used to model an Icelandic rift relocation (figure 7.17).

The wedge angle is chosen to be constant at 75° in accordance with results of flow calculations in relation to V-shape ridge geometry, outlined in section 7.2.1. The mantle potential temperature at Iceland is higher than normal 1300°C, estimated at 1500°C over central Iceland (White et al., 1995). The model is applied for potential temper-

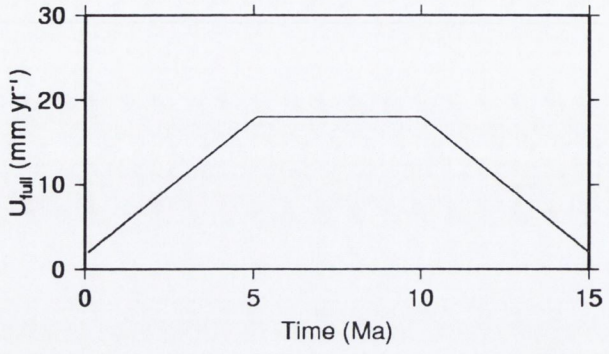

Figure 7.17: Spreading rate variations through time for 15 Ma for one ridge segment on Iceland. Birth of the rift axis starts at 2 mm yr^{-1} and increases linearly with time, over 5 Ma, to reach the full spreading rate at Iceland of 18 mm yr^{-1}. Full spreading rate prevails from 5–10 Ma, known as the steady-state rift stage, when only one rift is active. After 10 Ma the rift declines with spreading rate decreasing linearly over the last 5 Ma to 2 mm yr^{-1}, reflecting the transfer of extension to a new rift. This spreading rate model is based on the results of several authors: DeMets et al. (1994), Garcia et al. (2003) and LaFemina et al. (2005).

atures of 1400–1500°C. The amount of clinopyroxene in the modal mantle mineralogy has a significant influence on the amount of melting. 13% cpx in the mantle is chosen for Iceland as the average % in depleted MORB mantle calculated by Workman and Hart (2005). The initial jump to start the new rift is 50 km as a maximum value, based on a simple measurement of the distance between the Western and Eastern Volcanic Zone minus the amount of spreading during the 2–3 Ma that the Eastern Volcanic Zone has been active.

7.5.2 Comparative Observations

Melting and Crustal Thickness

The total melt fraction evolves from as little as 1–6% for the propagating tip/birth of a rift axis in the Eastern Volcanic Zone (Furman et al., 1991) up to 22% for a fully established steady-state rift such as the Northern Volcanic Zone (Maclennan et al., 2001b). Dramatic differences occur in the crustal thickness in southeast Iceland with over 20 km difference between the thickest crust over the centre (40 km) at the southern end of the established Northern Volcanic Zone and the thinnest crust at the southern tip of the Eastern Volcanic Zone (<20 km). The melting in south-east Iceland

is significantly influenced by the presence of the Iceland plume conduit. However, the change in crustal thickness from central Iceland to the propagating tip of the Eastern Volcanic Zone still suggests that the crustal thickness during the birth of a rift axis should be smaller than for steady state.

Geochemistry

The birth of a rift axis shows significant enrichment in incompatible elements relative to an established rift axis. The Eastern Volcanic Zone exhibits Sm/Yb values up to a factor of 2 greater than the most enriched compositions from Theistareykir and Krafla from the Northern Volcanic Zone. The decline of a rift axis in the Western Volcanic Zone shows no significant changes in the geochemical signature yet (Sinton et al., 2005). The death of the Skagi Rift axis is complicated and as a result it is unclear whether the enriched compositions from the Quaternary lavas are caused by the ridge slow down or by another external factor such as glaciation or plume variations. The evidence for these conclusions is outlined in chapter 4. A summary of the real and model trace element signature for each of the main rift zones is shown in figures 7.27 to 7.29.

7.5.3 Results

The model is run for 15 Ma, with variable spreading rates as described in section 7.5.1. The aim of this application is to identify any significant changes in the melting regime during a complete rift cycle at Iceland and determine whether these changes could result in significant changes in the chemistry of rift products.

Figure 7.18 shows the crustal thickness variation with time for a model rift jump at Iceland, using a range of mantle potential temperatures and anhydrous melting. At all temperatures, the initiation of the new rift produces very thin crust compared to the steady-state crustal thickness. For 1400°C there is no melting immediately after the jump. All temperatures exhibit rapid increases in crust production of up to 10 km over the first 0.5 Ma. The growth of the ridge is more gradual until the ridge reaches full spreading rate at 5 Ma. The higher potential temperatures of 1450°C and 1500°C reach steady-state crustal thickness for 5 Ma, but at 1400°C the crust still increases slightly after full spreading rate is achieved. The crust remains constant throughout the steady-state rift stage, once steady-state crustal thickness has been reached, as would be expected.

After 10 Ma the spreading rate gradually decreases resulting in a gradual decrease in the crustal thickness with a maximum decrease of 3 km over 5 Ma for 1400°C compared to a maximum 13 km increase during the growth stage. The difference in crustal thickness over the 5 Ma of decline is smaller at higher temperatures with only a 2 km difference at 1500°C. The response of the rift during decline is significantly less than the growth stage, despite an equivalent change in spreading rate. This effect is caused by a difference in thermal structure beneath the ridge. The new rift is initiated into old crust which is relatively cold and therefore, the initial amount of melting will be small. The rapid increase occurs as fast upwelling rates advect the changing temperature field through the mantle. The decline of the rift starts with an established steady-state thermal structure and therefore, gradual slowing down does not have such a rapid impact as growth in the new rift.

Seismic observations of the average crustal thickness of the neovolcanic zones away from the plume centre give approximately 20 km. Therefore, the most appropriate mantle potential temperature for the application to Iceland is 1450°C, producing a steady-state crustal thickness of 19.5 km for anhydrous melting. This temperature is used for further modelling. The average crustal thickness away from the plume centre is 25–30 km, but this observation is probably affected by off-axis mass re-distribution of the crust.

The introduction of water at 1450°C (figure 7.19) results in a similar crustal profile to anhydrous melting, with a small increase in the crustal thickness up to 1 km for 0.02 wt% H_2O. Hydrous melting results in a more rapid increase in crustal thickness following the initiation of the new rift. The more significant effect of water is on the melt fraction-depth profile (figures 7.20 and 7.21), resulting in deep low melt fraction tails. Melting starts more than 40 km deeper for 0.02 wt% H_2O compared to anhydrous melting and this has a significant effect on the overall chemistry (figures 7.24 and 7.26).

Figures 7.20 and 7.21 show the difference in the melt fraction-depth profile during the growth and decline stages of rifting compared to steady-state rifting, for anhydrous and hydrous melting. The melt fraction immediately after initiation of the new rift is shown in figure 7.22. Anhydrous melting starts slightly later than hydrous melting. Anhydrous melting produces 7% melting between 70 and 100 km, the difference between the maximum and minimum mean F. Hydrous melting produces two separate areas of melting; it has the same 7% shown for anhydrous melting, but also has an additional 2% of very deep melting below 120 km. The predicted melt fraction for the propagating tip of the Eastern Volcanic Zone vary from as little as 1–6% (Furman

et al., 1991) to 7–8% (Kokfelt et al., 2006). The model values compare well with the published predicted melt fractions. The Vestmannaeyjar system is suggested to have been active for only 0.1 Ma (Jakobsson, 1979) and therefore, the model timescale for the predicted melt fractions also compares well with real observations. The model melt fraction for the steady-state rift stage is 21% for anhydrous melting and 23% for hydrous melting which correlate well with predictions from REE inversion for the Northern Volcanic Zone of 22% (Maclennan et al., 2001b).

As observed in the crustal thickness variations, the change in melt fraction during the decline of a rift axis is not as great as for the growth of a rift axis. The most significant feature of the ridge slow down is an increase in the depth to the top of the melting region from 22 km at 10 Ma to 36 km at 15 Ma for anhydrous melting and a slightly smaller increase of 10 km for hydrous melting. This increase is caused by conductive cooling, as discussed by Bown and White (1994). The melt fraction reduces over the complete decline of the rift by 5% for anhydrous melting and only 3% for hydrous melting.

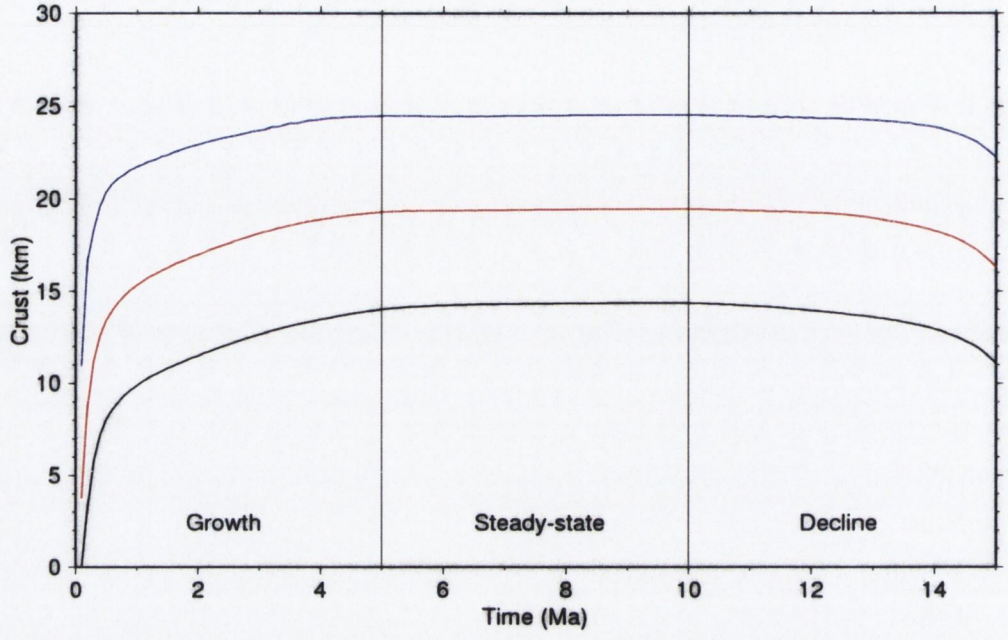

Figure 7.18: The variation in crustal thickness with time for a rift cycle at Iceland, following a 50 km rift jump from steady-state activity. Potential temperature is varied: 1400°C (black), 1450°C (red) and 1500°C (blue). Spreading rate variation is shown in figure 7.17. The wedge angle is constant at 75°, with anhydrous melting.

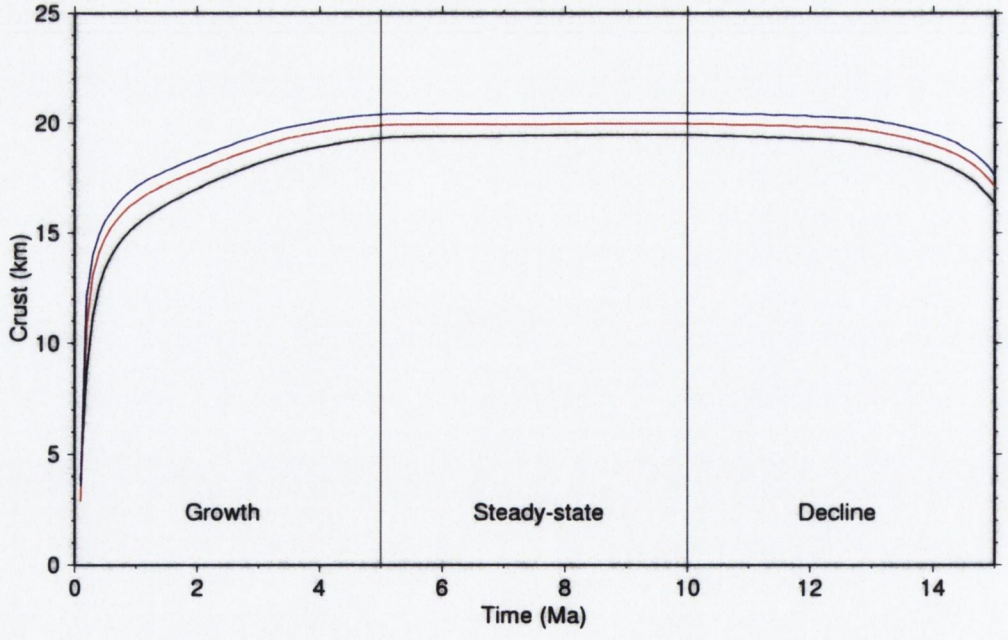

Figure 7.19: The variation in crustal thickness with time for a rift cycle at Iceland, following a rift jump from steady-state activity. Hydrous melting is carried out for 0 (black), 0.01 (red) and 0.02 wt% H_2O (blue). Spreading rate variation is shown in figure 7.17. The wedge angle is constant at 75°, with a constant mantle potential temperature of 1450°C.

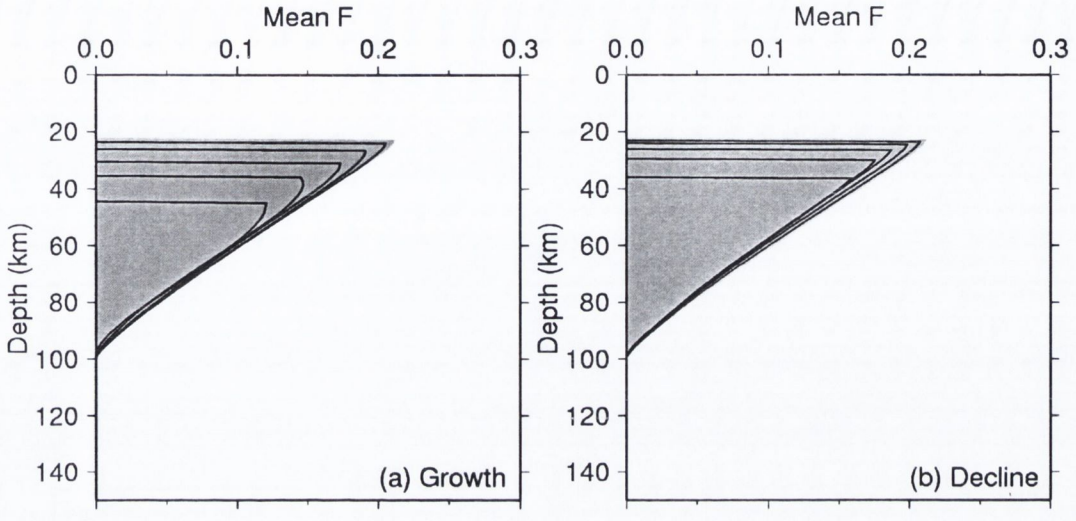

Figure 7.20: Variation in melt fraction with depth for anhydrous melting for (a) growth and (b) decline stages of the rift cycle. Mantle potential temperature is constant at 1450°C, the wedge angle is also constant at 75°. The grey area represents the melt fraction vs depth curve for steady-state rift stage (7.5 Ma). The growth curves start at 1 Ma, increasing in melt fraction until the end of the growth stage at 5 Ma. The decline curves start at 11 Ma, decreasing in melt fraction until the rift becomes extinct at 15 Ma.

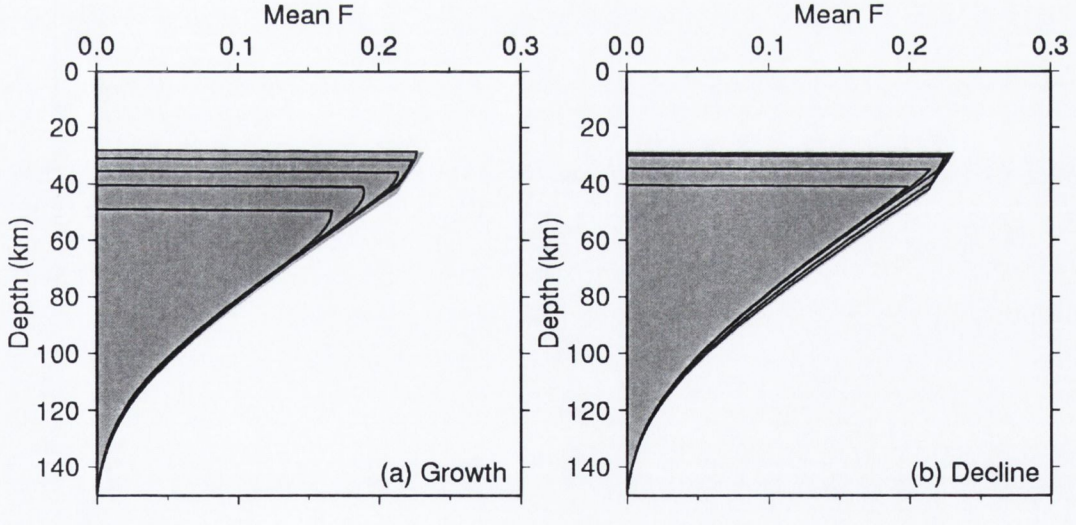

Figure 7.21: Variation in melt fraction with depth for hydrous melting (0.02 wt% H_2O) for (a) growth and (b) decline stages of the rift cycle. Mantle potential temperature is constant at 1450°C, the wedge angle is also constant at 75°. The grey area represents the melt fraction vs depth curve for steady-state rift stage (7.5 Ma). The growth curves start at 1 Ma, increasing in melt fraction until the end of the growth stage at 5 Ma. The decline curves start at 11 Ma, decreasing in melt fraction until the rift becomes extinct at 15 Ma.

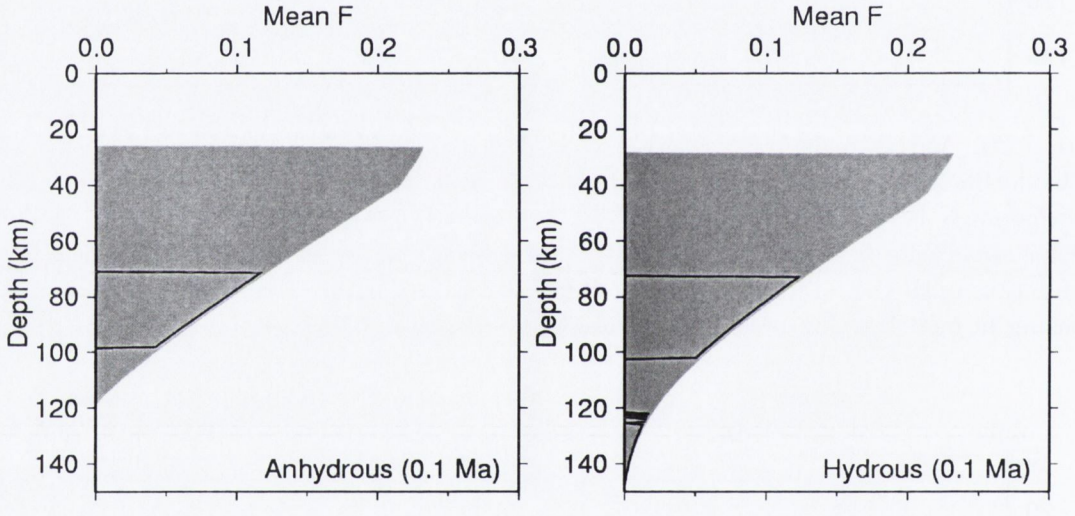

Figure 7.22: Variation in melt fraction with depth for the first melts from the new rift for anhydrous and hydrous melting (black lines). Mantle potential temperature is constant at 1450°C, the wedge angle is also constant at 75°. The grey area represents the melt fraction vs depth curve for steady-state rift stage (7.5 Ma). Ages refer to the first time step after new rift initiation.

The variation in composition of single elements (fictive and real) with time during a rift jump is shown in figures 7.23 to 7.26. It must be noted that the compositional application of the model is very simplistic as described in section 7.2.4. The following results are used to indicate the general behaviour of elements with varying compatibilities during a rift cycle; it is not expected that this method of calculating the composition will reproduce the observed absolute values.

The variation in concentrations for fictive elements is shown in figures 7.23 and 7.24. Compatible elements show very little change throughout the rift jump process. A trace element with a constant D of 1 and a starting composition of 1 ppm should have a constant concentration of exactly 1 throughout changes in melting, however the model produces a constant value of 0.85. This difference is the error involved in the integration of the instantaneous accumulated compositions over the melting region to find the average composition of melt. This error could be improved by using a different method of integration and a smaller grid size in future applications. The error affects all composition calculations equally. Therefore, with the aim of looking at the general behaviour of elements rather than absolute values, the impact on the validity of the results is negligible.

The concentrations of incompatible elements show the most change during the rift cycle, with significant differences in the variation of composition through time between anhydrous and hydrous melting for very incompatible elements. As the incompatibility increases the behaviour of the trace elements becomes more reactive to the change in spreading rate. A mildly incompatible element with a D of 0.1 for anhydrous melting increases in concentration rapidly following new rift initiation to a peak after 0.5 Ma. The concentration then gradually decreases until full spreading rate is achieved after 5 Ma. The composition remains constant through steady-state rifting and increases very gradually through the decline of the rift. This behaviour for a D of 0.1 is very similar for hydrous melting; the peak concentration is slightly higher and reached earlier and the change from increasing to decreasing concentrations is much more abrupt.

A very incompatible element ($D = 0.01$) makes no contribution to the melt composition at the initiation of the new rift for anhydrous melting. This depletion is discussed below. The concentration then increases rapidly to a value higher than the previous steady-state, peaking just after 1 Ma of activity on the new rift. A steady decrease is observed until full spreading is rate is reached. The steady-state rift stage has a slight decrease in concentration at the beginning to a constant value for the rest of the rift stage. As the rift starts to decline at 10 Ma a gradual increase in concentration occurs for 3 Ma,

followed by a very gradual decrease for the last 2 Ma back to the steady-state value. For hydrous melting, the initial concentrations produced by the new rift reach the peak value almost immediately. The peak value is considerably higher for hydrous melting compared to anhydrous melting. Following the peak, the concentration drops steadily towards the start of steady-state rifting at 5 Ma. A further slight decrease is observed at the start of the steady-state rifting stage, followed by constant concentration until 10 Ma. As the ridge slows down, the concentration increases very gradually until death at 15 Ma.

A further increase in incompatibility, to a D value of 0.001, results in more significant changes in composition. For anhydrous melting, this extremely incompatible element does not make a contribution to the melt composition in the new rift until 0.3 Ma after initiation. A rapid increase is then observed towards a peak value after 1 Ma. The concentration is slightly unstable for 1.5 Ma, decreasing steeply. After 2.5 Ma the concentration decreases gradually until the end of the growth stage. The majority of the steady-state rift stage exhibits constant composition, with a slight decrease at the start. The decline of the rift axis produces unusual behaviour in the concentration of the extremely incompatible element, with a gradual decrease for almost 4 Ma before a temporary small increase and a final steep decrease for the last 0.5 Ma. The variation in concentrations for hydrous melting of extremely incompatible elements (D=0.001) is similar to very incompatible elements (D=0.01). The peak concentration is nearly double for $D = 0.001$ compared to $D = 0.01$. This peak is followed by an immediate rapid decrease, followed by a more gradual decrease to steady-state. Again, as for hydrous melting of $D = 0.01$, the hydrous concentration rises very gradually during the decline of the rift.

The variation of single real element concentrations with time is shown in figures 7.25 and 7.26. They show similar behaviours to those described for the fictive elements depending on the bulk partition coefficient, but the absolute values are different because they are weighted according to each elements estimated starting composition in the mantle. It is important to note the significant influence the starting composition has on the absolute values. For example, Nb ($D = 0.0034$) is considerably more incompatible than Zr ($D = 0.033$), but Zr has a much higher concentration in the mantle (5.082 vs 0.1495). The difference in starting compositions results in Zr exhibiting more than 5 ppm difference between peak value after initiation and steady-state concentration. However, Nb changes by less than 1 ppm between peak and steady-state concentrations, despite being more incompatible. The significant influence of starting composition has important implications for understanding the possible impact of a heterogeneous mantle

source on the results.

The difference between hydrous and anhydrous melting for very incompatible elements ($D \leq 0.01$) is related to the difference in the melt fraction-depth profiles (figures 7.20 to 7.22). Water in the mantle reduces the solidus temperature allowing more melting overall and characteristic deep low melt fraction tails. When a new rift initiates into the melting history of old and cold mantle, the first anhydrous melts are not as deep as the previous steady-state melts (figure 7.22). Therefore the new melting cannot access the new mantle material that is replacing the depleted mantle that the rift has propagated into. The zero concentrations for very incompatible elements observed for anhydrous melting for the initiation of a new rift indicate that the old mantle has been leached of its very incompatible elements by previous melting. The depth of hydrous melting starts at the same depth as the previous steady-state melts and can therefore, access the small amount of fresh mantle material upwelling into the melting region as shown in figure 7.22. The immediate exceptional incompatible element enrichment observed for a hydrous melting at a new rift is produced by small degrees of melting of this fresh mantle material (figure 7.26).

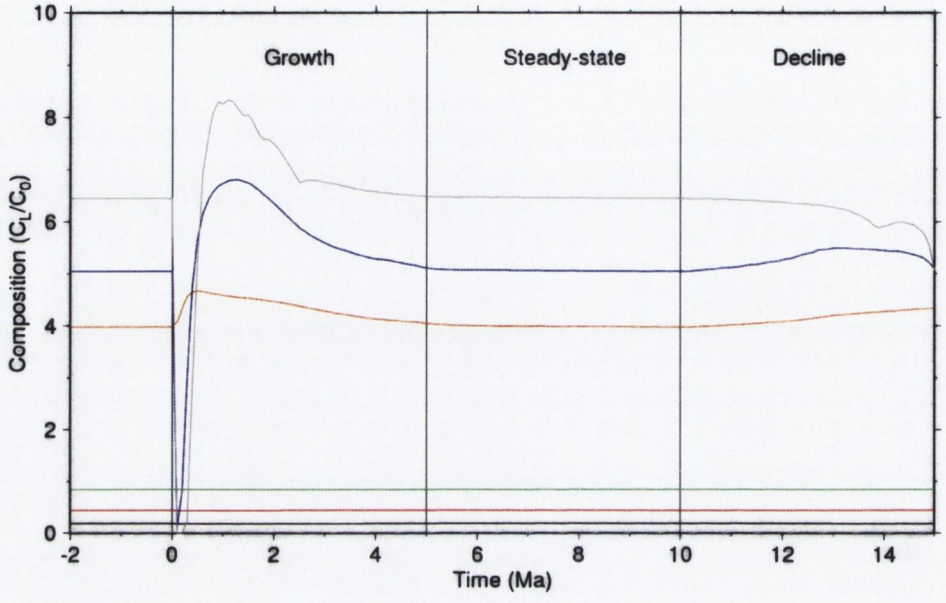

Figure 7.23: The variation in composition (C_L/C_0) with time for anhydrous melting during a complete rift cycle at Iceland, shown for 6 elements with the following D values: 5 (black), 2 (red), 1 (green), 0.1 (orange), 0.01 (blue) and 0.001 (grey). Negative ages refer to the steady-state rifting prior to rift jump. The wedge angle is constant at 75° and a constant mantle potential temperature of 1450°C.

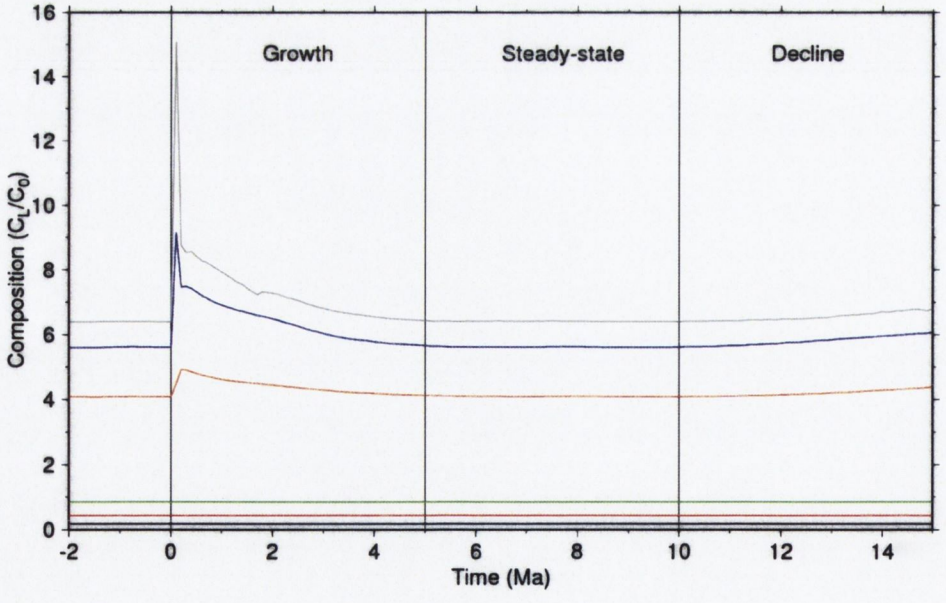

Figure 7.24: The variation in composition (C_L/C_0) with time for hydrous melting (0.02 wt% H_2O) during a complete rift cycle at Iceland, shown for 6 elements with the following D values: 5 (black), 2 (red), 1 (green), 0.1 (orange), 0.01 (blue) and 0.001 (grey). Negative ages refer to the steady-state rifting prior to rift jump. The wedge angle is constant at 75° and a constant mantle potential temperature of 1450°C.

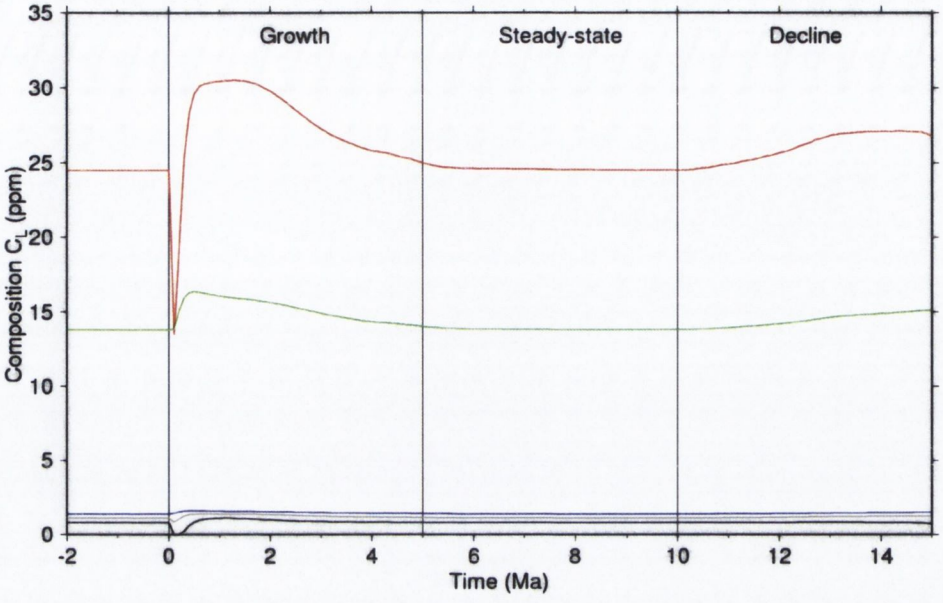

Figure 7.25: The variation in composition with time for anhydrous melting during a complete rift cycle at Iceland, shown for 5 real elements with the following D values: Nb, 0.0034 (black); Zr, 0.033 (red); Y, 0.088 (green); Sm, 0.045 (grey) and Yb, 0.115 (blue). Negative ages refer to the steady-state rifting prior to rift jump. The wedge angle is constant at 75° and a constant mantle potential temperature of 1450°C.

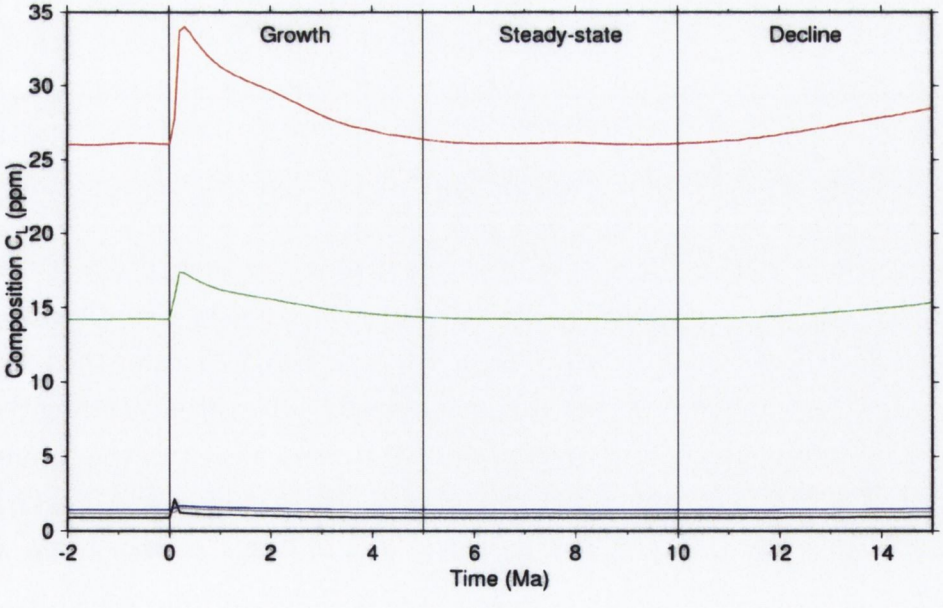

Figure 7.26: The variation in composition with time for hydrous melting (0.02 wt% H_2O) during a complete rift cycle at Iceland, shown for 5 real elements with the following D values: Nb, 0.0034 (black); Zr, 0.033 (red); Y, 0.088 (green); Sm, 0.045 (grey) and Yb, 0.115 (blue). Negative ages refer to the steady-state rifting prior to rift jump. The wedge angle is constant at 75° and a constant mantle potential temperature of 1450°C.

The constant bulk partition coefficients and mantle composition used to calculate model trace element concentrations in the melt are shown in table 7.1. The chosen trace elements ratios (Nb/Y, Zr/Y and Sm/Yb) minimise the effects of fractional crystallisation and alteration. The observations from Iceland integrate large numbers of samples from a wide range of locations for the main rift zones and therefore, the effects of crustal assimilation, melt transport and melt mixing should be averaged between zones. Small scale (<<100 km) heterogeneity in the mantle source will have a significant impact on the composition results presented, accentuating any peaks for incompatible enrichment, discussed further in section 7.6. These trace element ratios are used throughout this dissertation to compare the melting processes and composition of mantle melts from different regions of Iceland. Figures 7.27 to 7.29 compare the range of observed values for the Nb/Y, Zr/Y and Sm/Yb ratios at Iceland, with the predicted values from the model of the different rift stages at Iceland.

The variation in Nb/Y through time for anhydrous and hydrous melting for the rift cycle at Iceland is shown in figure 7.27. For anhydrous melting Nb/Y increases from zero to a peak value 0.5 Ma after initiation of the new rift, decreasing gradually to a steady value at 5 Ma. Nb/Y is constant throughout the steady-state rifting stage and decreases slightly during the decline of the rift. For hydrous melting the Nb/Y value starts at a peak value following the initiation of the new rift, double the peak for anhydrous melting. Nb/Y then decreases immediately to just above the steady-state value, and continues decreasing very gradually to the steady-state value after 5 Ma. The composition remains constant at the steady-state value until the ridge dies at 15 Ma.

Zr/Y produces similar behaviour to Nb/Y through time. For anhydrous melting the rapid increase in Zr/Y following initiation of the rift is followed by a continued gradual increase to reach the peak value after 1.5 Ma of activity. The Zr/Y value then decreases gradually until 5 , remaining constant throughout steady-state rifting. During the ridge slow down, Zr/Y increases slightly over 3 Ma and decreases back to the steady-state value over the last 2 Ma of activity. For hydrous melting the Zr/Y ratio starts at a much higher value compared to anhydrous melting, and increases steeply for a small amount to a peak value after 0.3 Ma, similar to the peak for anhydrous melting. Zr/Y then decreases gradually until 5 Ma to a steady-state value, and then only increases very slightly during the decline of the rift.

The absolute values and differences between peak values and steady-state values are small compared to the real observations from Iceland. Nb/Y varies over a maximum

range of 0.1 in the model values and varies over 0.4 for the mean values and over 1.0 from the main volcanic zones in Iceland. Zr/Y varies over a maximum range of 1.0 for the model values and varies over 3 for the mean values and over 13 for the range of values from the main volcanic zones. Finally, Sm/Yb model values have a maximum range of 0.3 and the observations vary over 0.8 for the mean and 3 for the maximum range. The absolute values for steady-state do overlap with the lower range of values from the Northern Volcanic Zone for all the trace element ratios. Possible methods for improving the reproduction of the absolute values and differences are discussed in section 7.6.

To summarise the general behaviour of the trace element ratios; enriched values are observed following the initiation of the rift, decreasing throughout the growth stage of rifting towards a steady-state value, similar to the observations for the Eastern Volcanic Zone. The composition of melts remains constant throughout steady-state rifting and shows very little or no change during the decline of the rift. Any changes observed during the decline of the rift axis are much smaller than those observed for the growth stage of rifting, particularly for hydrous melting, which is more realistic for Iceland. This constant chemistry correlates well with the similar geochemical signatures produced by the Northern Volcanic Zone and the declining Western Volcanic Zone.

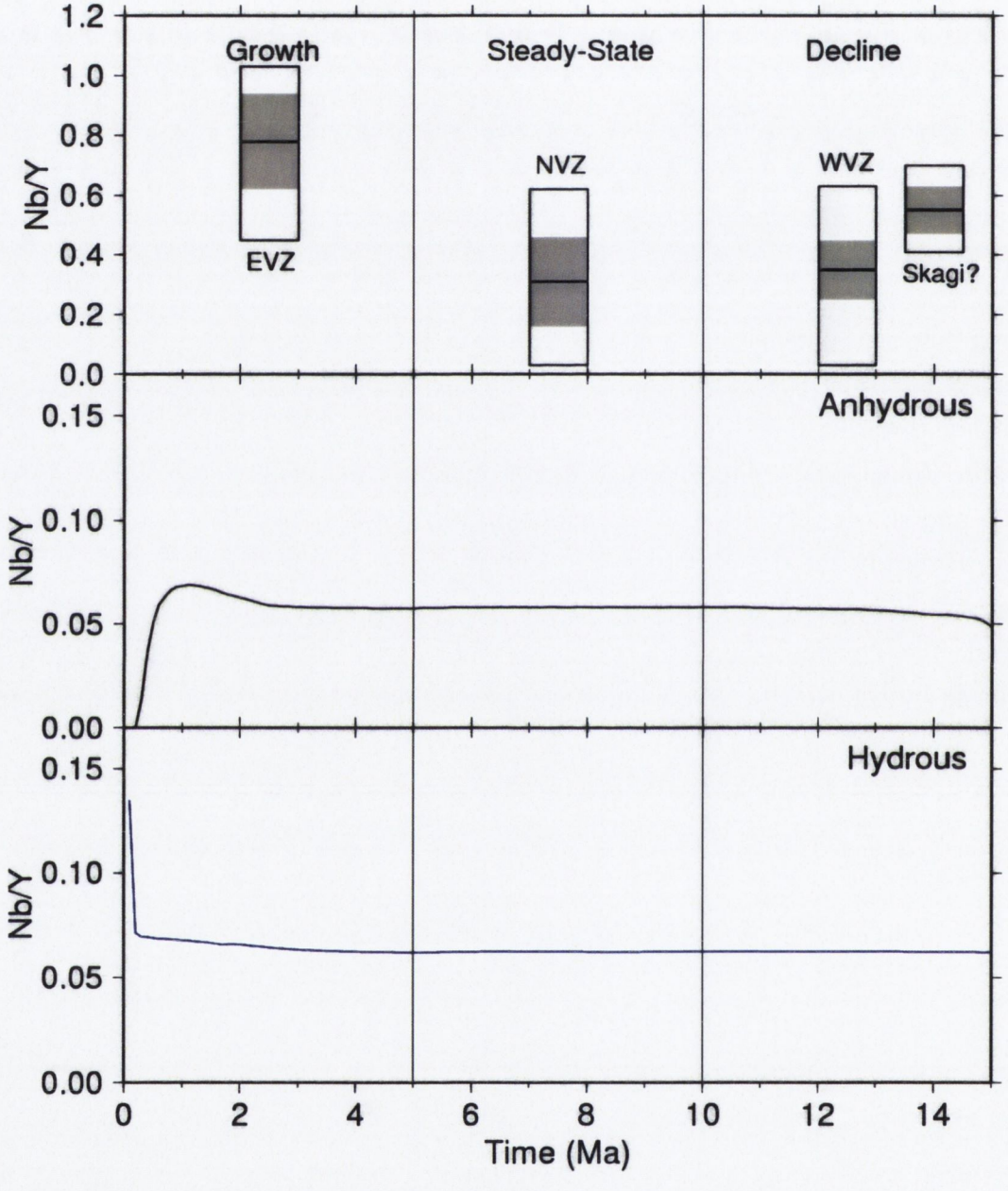

Figure 7.27: The variation in Nb/Y with time during a complete rift cycle. The range of real Nb/Y values is presented in the first diagram with the mean and range shown in black and the grey box denotes ±1 S.D. from the mean. The model results for anhydrous and hydrous melting are shown in the other diagrams. The wedge angle is 75° and a constant mantle potential temperature of 1450°C.

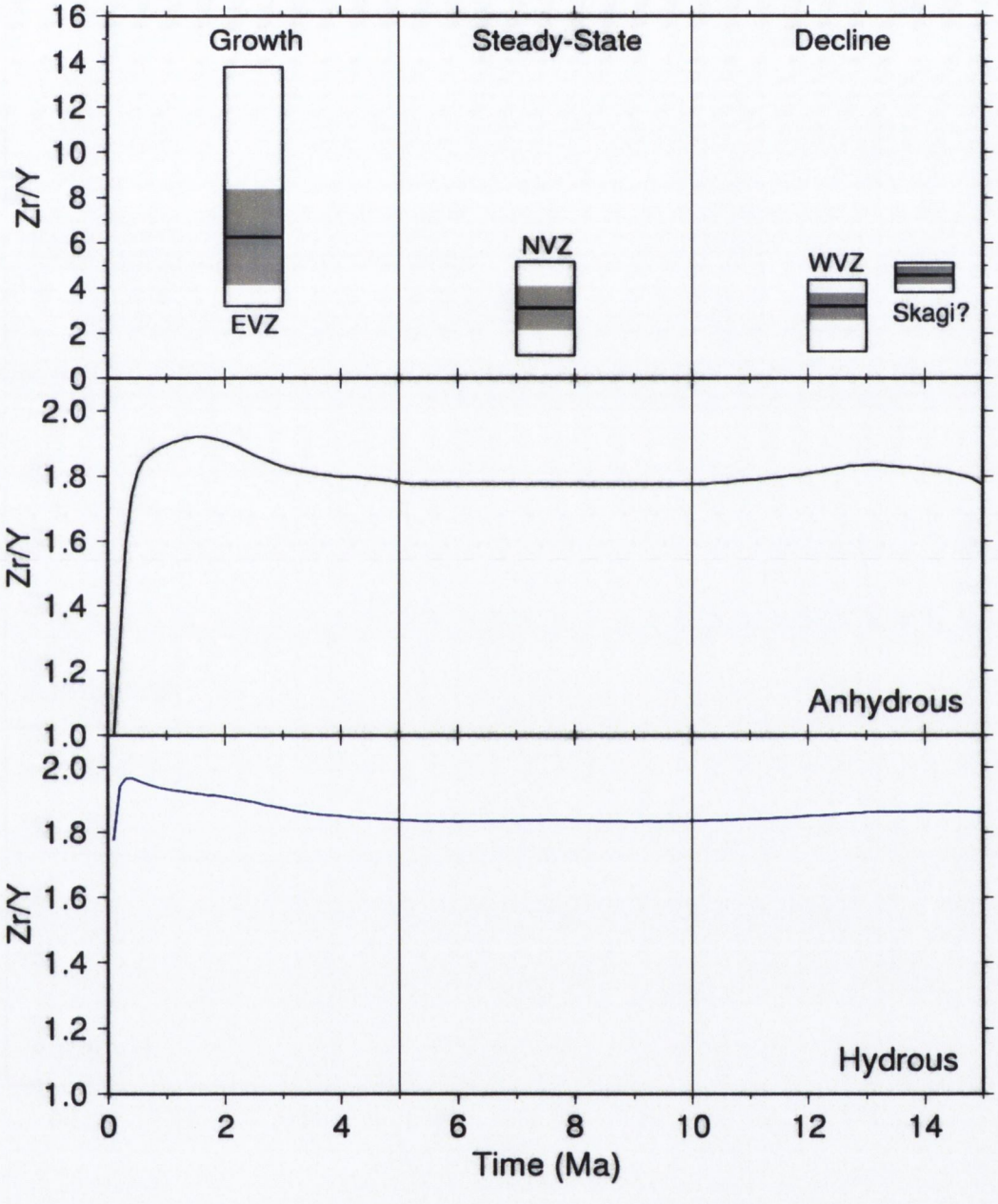

Figure 7.28: The variation in Zr/Y with time during a complete rift cycle. The range of real Zr/Y values is presented in the first diagram with the mean and range shown in black and the grey box denotes ±1 S.D. from the mean. The model results for anhydrous and hydrous melting are shown in the other diagrams. The wedge angle is 75° and a constant mantle potential temperature of 1450°C.

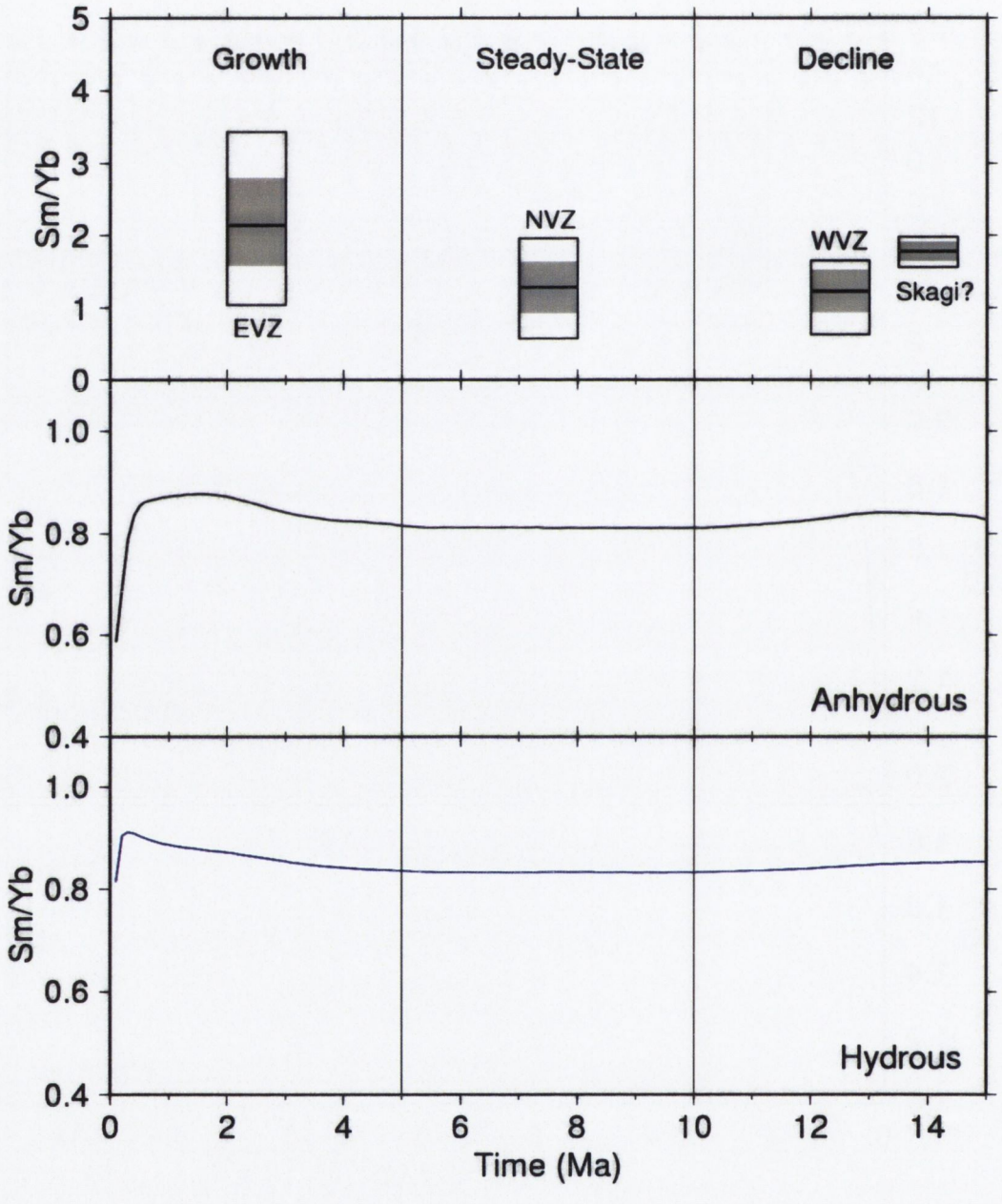

Figure 7.29: The variation in Sm/Yb with time during a complete rift cycle. The range of real Sm/Yb values is presented in the first diagram with the mean and range shown in black and the grey box denotes ±1 S.D. from the mean. The model results for anhydrous and hydrous melting are shown in the other diagrams. The wedge angle is 75° and a constant mantle potential temperature of 1450°C.

7.6 Discussion and Further Application

7.6.1 Iceland

In the application of the model to Iceland, the difference in melting between the steady-state and dying rift stages is not as dramatic as might be expected for a significant reduction in spreading rate. The decline of a rift does not produce the same level of response to the volume and composition of rift products compared to slow spreading rates at the growth of a rift axis. For a mantle potential temperature of 1450°C, which reproduces steady-state crustal thickness (20 km) as observed at Iceland, produces as little as 3 km of crust at the start of a new rift. The same conditions result in only a small decrease from 20 to a minimum of 16 km thick crust at the end of rift activity, following the ridge slow down. This difference in crustal thickness and melting relates to the history of the mantle prior to the growth and decline stages of rifting. The new rift is initiating into lithosphere that has had nearly 5 Ma to cool down and has the equivalent of steady-state melting history from the previous rift. Starting with very slow spreading rates (2 mm yr^{-1} in model), only very small amounts of melt can be produced as the new temperature field starts to transfer through the mantle and fresh mantle material is slowly advected. The dying rift stage has the same steady-state melting history in the mantle as the new rift, but the dying rift already has a steady-state temperature field. Therefore, melting continues and the gradual reduction in crustal thickness results from the gradual decrease in the rate of upwelling and the increase in depth of the top of the melting region, controlled by conductive cooling at slow spreading rates (Bown and White, 1994).

It was not possible due to time constraints to model the effect of two rifts active together, which may result in asymmetrical spreading across each rift. Simultaneous rifting would certainly have an impact on the amount of melting, particularly during the initiation of the new rift. As the rift develops the new melting region will impinge on the edges of the melting region from the existing rift. The base of the melting region for hydrous melting is approximately 150 km and therefore, a wedge angle of 75° results in a 80 km wide base of upwelling for the ridge. The rift jump is modelled as a maximum 50 km and therefore relatively close to the upwelling from the adjacent rift. This observation indicates that the melt fraction may not increase as rapidly as shown by the present model during the growth stage of the rift. Melting in the zone of upwelling that is effectively shared by the two melting regions would be partitioned between the two rifts, reducing the amount of melt contributing to the new rift.

The model geochemical behaviour compares well with the relative differences between the geochemical observations from the main rifts on Iceland. Significant peak in enrichment are observed for incompatible elements and trace element ratio at the start of the growing rift stage, decreasing towards the steady-state value. This decreasing trend is observed in the Eastern Volcanic Zone from the southwest propagating tip towards central Iceland, as described in chapter 4. There is very little enrichment observed for the decline of the rift axis. Zr is the only element which appears to significantly increase above steady-state values, and only a small fraction of the increase observed at the beginning of the rift. The lack of significant changes in the model geochemical signature during the decline of the rift compares well with the similar chemistry observed for the Northern and Western Volcanic Zones.

The results for the model geochemical signature during the decline of the rift imply that it may not be possible to achieve the level of incompatible element enrichment observed in the Quaternary lavas at Skagi by the simple slow down of an existing rift. The model shows that reasonably small degrees of melting of fresh mantle material are required in order to get significant enrichment of very incompatible elements compared to steady-state rifting, similar to the growth of a new rift. Possible causes of melting to produce the young Skagi lavas are discussed in chapter 8.

Further investigation is required to confirm whether or not the slight increases observed for very incompatible elements during the decline of a rift would become significant increases, similar to the enrichment observed at Skagi, if the mantle source was altered to be more realistic. It is certain that the peak values at the beginning of the rift will increase significantly relative to the steady-state values with the introduction of small scale enriched veins in the mantle. The introduction of garnet field melting with appropriate bulk partition coefficients will also impact on the composition. A similar method to Spiegelman (1996) for a two layer mantle would be relatively easy to implement and would significantly improve the calculation of the composition. The introduction of a heterogeneous mantle would be a more complex undertaking and very little research has been done on the modelling of mid-ocean ridge melting of a heterogeneous source.

7.6.2 Phoenix Ridge

Only one application of the new time-dependent model is presented here, but there are other possibilities for further applications. The Phoenix Ridge, Drake Passage,

Antarctica was once an extensive spreading ridge, but became extinct around 3.5–4.5 Ma (Barker, 1982; Larter and Barker, 1991). Unlike Iceland, the Phoenix Ridge is situated away from the influence of mantle plumes and therefore, the mantle has a normal potential temperature. Choe et al. (2007) present geochemical data from different rift segments, with samples from a range of distances away from the rift. They show that during the extinction of the rift a change from predominantly N-MORB to E-MORB compositions is observed. Livermore et al. (2000) provide good constraints on the spreading rate variations based on magnetic variations up to 250 km from the rift. The application of the model to the Phoenix would show whether the lack of change in geochemistry at Iceland during rift decline is the result of higher mantle potential temperatures or if it is not possible to achieve incompatible element enrichment during ridge shut down. Livermore et al. (2000) suggest that the morphology of the extinct rift could be related to localised strong upwelling of the mantle.

7.6.3 Non-volcanic Margins

The model experiments provide very useful insights into how the model responds to different independent variables. The effect of varying the wedge angle on the timing of melting has significant implications for the production of amagmatic margins. As shown in section 7.4 small wedge angles impose significant delays on the initiation of melting at a new rift. This delay is around 2.5 Ma for fast spreading rates (50 mm yr^{-1}) and increases to around 7.5 Ma for slow spreading rates (20 mm yr^{-1}) for normal mantle potential temperatures. This results in around 125–150 km of rifting, depending on the spreading rate, with no melt production and therefore, mantle is emplaced at the surface. The continental margin on the west coast of Iberia is a well studied amagmatic margin and figure 7.30 provides an approximately to scale representation of the crustal components. Continental crust gives way to nearly 200 km of serpentinised mantle emplaced at the surface, before oceanic crust is produced. Reston and Phipps Morgan (2004) propose a cooler mantle to account for the significant period of extension without volcanism. However, the observations of the effect of wedge angles on the timing of melting on a new rift indicates that small wedge angles can result in several million years before any melt is produced. Wedge angle constraints from the North Atlantic V-shaped ridge topography outlined in section 7.2.1 indicate that the upwelling rate for the Mid-Atlantic Ridge requires a steep wedge angle of at least 65°. It is therefore, reasonable to suggest that in the case of the Iberian amagmatic margin, the wedge angle could increase from the start of rifting to full oceanic spreading. This change

could be described as re-focusing of melting towards the ridge axis once melting has been initiated, following continental stretching. This idea of re-focusing of upwelling means that the mantle does not need to be unusually cool to produce a non-volcanic margin.

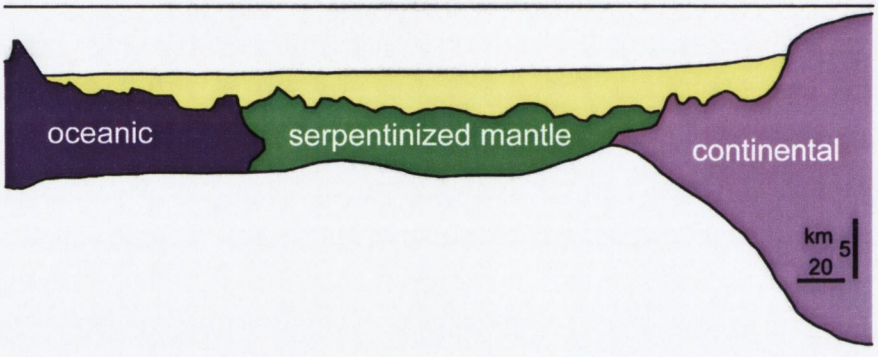

Figure 7.30: An approximately to scale representation of the Iberian continental margin from the west coast of Europe (adapted from Dean et al., 2000).

Further applications to continental margins may provide new insights into the origin of amagmatic margins. This would require a more realistic spreading rate velocity model, with extension increasing gradually rather than instantaneous full spreading as used in the model experiments in section 7.4. It would be an easy addition to the model to vary the mantle potential temperature and this could be used to model the impingement of a mantle plume in a continental rifting situation. A variable basal temperature would also be useful in modelling the changes in mid-ocean ridge melting which produce V-shaped ridges along the Mid-Atlantic Ridge.

7.7 Conclusions

The main conclusions from the model testing and experiments are:

- The new model consistently reproduces the results for melt fraction-depth profiles from Katz et al. (2003) and compares well with the variation in melt fraction for different spreading rate results presented by Bown and White (1994).
- Slow spreading rates below 20 mm yr^{-1} produces significantly less crust and significantly more enriched incompatible element signature compared to fast spreading rates.

- The wedge angle has a significant impact on the time it takes for a rift to respond to major changes in the tectonics, such as spreading rate. Small wedge angles result in a longer time span for tectonic changes to affect melting.

- Potential temperatures have the greatest influence over the degree and depth of melting. An increase of 100°C can result in more than double the crustal thickness.

- Hydrous melting results in small systematic increases in the crustal thickness depending on the water content, but has very little effect on the composition of mantle melts produced by steady-state melting, based on constant bulk partition coefficients. This result would be different with a more comprehensive compositional calculation.

The main conclusions from the application of the model to Iceland are:

- A mantle potential temperature of 1450°C reproduces the observed average crustal thickness, of approximately 20 km, for an established rift at Iceland.

- A model of initial melting at a new rift of 7–9% compares well with predicted melt fractions for the propagating tip of the Eastern Volcanic Zone, estimated from the geochemistry to be 7–8% (Kokfelt et al., 2006).

- Model steady-state melt fractions of 21–23% are very similar to those predicted from REE inversions for the Northern Volcanic Zone, away from plume influence, of 22% (Maclennan et al. 2001b).

- The response of melt fraction and crustal thickness to the decline of a rift axis is not as dramatic as might be expected for a large reduction in spreading rate, and the response is considerably less significant than during the growth stage of rifting.

- Incompatible element enrichment is observed during the development of a new rift, followed by a relatively constant composition throughout the rest of rift activity, including the decline of the rift. Further modelling of the composition is required to confirm this result.

- The relative behaviour of model compositions compare well with the average observed variations from the different rift stages preserved at Iceland.

- The simple slow down of an existing rift appears to be unable to reproduce the enriched geochemical signature observed for young Skagi lavas, indicating that other processes are required to produce these lavas.

Chapter 8

Discussion and Conclusions

The aim of this dissertation was to provide quantitative constraints on the changes in melting and chemistry associated with rift relocations at Iceland, using geochemical observations and a new time-dependent model of melting beneath a mid-ocean ridge. Chapters 3–5 presented new and existing geochemical data and compared the geochemistry of lavas from different volcanic zones at different stages in the rift cycle, with a further comparison to extinct rift chemistry from the Tertiary. Chapters 6 and 7 presented the theory behind a new time-dependent model of melting beneath mid-ocean ridges, and showed results from the application of the model to variable spreading rates associated with rift relocations at Iceland. The aim of this chapter is to discuss how the results of the previous chapters may be linked to the large scale tectonic picture at Iceland, including the influence of plume-ridge interaction.

8.1 Origin of Skagi Quaternary Melts

The new detailed geochemical study of the extinct Skagi Rift showed that no significant geochemical change is observed between the youngest Tertiary lavas and Quaternary lavas outcropping on the Skagi peninsula, despite the presence of a distinct unconformity. This unconformity could signify a hiatus in volcanic eruption and therefore indicate that the Quaternary lavas represent a later period of melting, possibly resulting from a separate transient rifting episode. However, the unconformity could simply reflect the start of glaciation in northern Iceland, with volcanic activity remaining constant through from the Tertiary to the Quaternary. In the former case, the Quaternary

lavas represent renewed eruption activity on an extinct rift and in the latter case they represent the last eruptions on a dying rift.

The accurate timing of the extinction of the rift is very important for determining the likely tectonic origin of these young lavas at Skagi. The kinematic model presented by Garcia et al. (2003), based on dating of dykes, concluded that the Skagi rift became extinct around 3 Ma. This study also suggested that the palaeo-rift axis was located around 60 km east of the widely accepted Húnaflói axis location. Hjartarson (2003) proposed a transient rift axis at this new location that was active 1.6–1.7 Ma. There is no present consensus of locations and timing of rift activity in northern Iceland between the 8–6 Ma initiation of the Northern Volcanic Zone and the extinction of rift activity near Skagi. Well constrained palaeomagnetic dating in northwest Iceland indicates that volcanic activity on the Skagi rift began around 15 Ma (Hardarson et al. 1997). Volcanic activity in the region must have been concentrated at the Húnaflói location for a significant period of time due to the presence of a regional syncline in the Tertiary lava flows.

Pálmason's model of crustal accretion suggests that regional synclines form as a result of continuous emplacement of lava flows at a rift axis, until loading of the crust results in central subsidence. Models by Pálmason (1973) and Bodvarson and Walker (1964) suggest that the rate of subsidence at a rift axis could be up to 1–2 mm yr^{-1}. A simple geometrical calculation shows that regional dip of 5-10° over half the 50 km average width of a volcanic zone would require 2–4 km of subsidence. At 1–2 mm yr^{-1}, it could take up to 4 Ma to form a regional syncline as observed at Iceland. This observation indicates that if any rifting occurred further east of the Húnaflói axis, it must have been short-lived because there is no evidence of a regional syncline in this area. Therefore, there is little field evidence to support the Garcia et al. (2003) kinematic model with an extended period of rifting 60 km east of the current palaeo-rift axis location. This also indicates that the 3 Ma model age for extinction on the Skagi rift presented by Garcia et al. (2003) may not be reliable. Prior to the Garcia et al. (2003) estimate of extinction of the Skagi rift at 3 Ma, Jóhanesson (1980) and Pringle et al. (1997) predicted a 7–5 Ma age of extinction.

Hjartarson (2003) and Hardarson et al. (2008) suggest that Quaternary activity in the Skagafjördur region is related to a transient rift which may have propagated from the fissure swarm extending northwards from Hofsjökull central volcano, in the Mid-Iceland Volcanic Zone. The rift is predicted to have been active for a very short period of time, 1.6–1.7 Ma. This age is consistent with Everts et al. (1972) K-Ar ages of the

Quaternary lavas from Skagi. The K-Ar ages span a longer period of activity, 2.5–0.5 Ma, but it must be noted that large errors of around ±1 Ma are associated with these dates. A short transient rifting episode, such as the one suggested by Hjartarson (2003), is consistent with the lack of evidence for a significant regional syncline.

In theory, there should be little difference between the geochemistry of lava flows from a short-lived Skagafjördur rift and new rift lava flows such as those found in the Eastern Volcanic Zone, particularly at the propagating tip. Both rifts start with slow spreading rates and propagate into depleted mantle which has had several Ma to cool down. The comparison between Skagi Quaternary lavas and Eastern Volcanic Zone lavas shows that for the same MgO composition the Eastern Volcanic Zone lavas are more enriched in incompatible elements. The Eastern Volcanic Zone basalts evolve from transitional to alkaline compositions towards the propagating tip, whereas the Quaternary basalts from the Skagi rift are tholeiitic. Following these observations it is unlikely that Skagi Quaternary lavas represent a transient rifting episode on a newly propagated rift adjacent to the old Skagi rift, as suggested by Hjartarson (2003). The initiation of rifting would also produce extensional faulting in the region, however there is limited evidence for this at Skagi (Everts' map, 1975; appendix A). Further field work focused on the detailed structure of the region would reveal whether extensional faulting and disturbances mapped on Skagi could represent a small scale rifting episode.

It could be argued that the similarly enriched incompatible element signatures of the Tertiary and Quaternary lavas from Skagi indicate that the Quaternary melts are simply a continuation of Tertiary rift activity, i.e. the young lavas represent the last eruptions on a dying rift. This idea is consistent with the lack of change in composition during the decline of a rift as predicted by the new melting model and observed in the Western Volcanic Zone. However, a similar enriched geochemical signature could be created by very different mantle melting processes. For example enriched compositions, such as those found in Skagi lavas, are very similar to the lava compositions observed in central Iceland. In central Iceland the enriched composition is the result of plume influence, with active upwelling fluxing material through the deep melting region. The effect of active upwelling occurs up to 150 km from the plume centre (Maclennan et al., 2001b). Young Skagi lavas are very unlikely to have been influenced by plume-driven upwelling because rift-plume migrations models suggest that the plume conduit has been located more than 150 km away from Skagi in the last 3 Ma (figure 5.40, section 5.5). More importantly, the field observations show that the melt production at Skagi was very small compared to the melt production in central Iceland. Similarly enriched compositions for Tertiary lavas in general are attributed to plume-driven upwelling be-

cause sampling has been biased to locations which are aligned with the 150 km radius of the previous latitudes of the plume centre (section 5.5).

Decompression is required to melt the mantle in a mid-ocean ridge setting so it is necessary to explain how upwelling occurred to produce the Skagi Quaternary melting. The geochemical comparison between Skagi and the Eastern Volcanic Zone shows that it is unlikely that this upwelling is the result of a separate transient rift. Therefore, upwelling associated with the old rift must produce the young melts. A reactivation of the existing rift after several Ma of cooling would probably produce similar enriched alkaline compositions to the Eastern Volcanic Zone, inconsistent with the young Skagi lavas. As noted previously, rifting would also result in extensional faulting and there is little evidence of this at Skagi.

One possibility for renewed upwelling on the Skagi rift, that is not associated with passive upwelling from rifting or active upwelling from the plume, is the propagation of thermal/fertile pulse from the plume beneath a thinned lithosphere from previous rifting. As a pulse of hot/fertile material passed beneath the recently deceased Skagi rift, upwelling occurs as the pulse travelled upwards towards the thinnest lithosphere at the centre of the old rift axis. The most recent pulse of enhanced melt productivity to leave Iceland presently intersects the Reykjanes Ridge at 60.5°N, or c. 750 km from the plume centre. The geometry of the associated V-shaped ridge suggests that the pulse left the plume centre at 3.1 Ma, if radial flow in the plume is assumed (Poore et al., 2009). A even more recent study, which includes geochemical results from dredge samples obtained along the Reykjanes Ridge in 2008, suggests that the pulse left the plume at 2.3 Ma (Jones, pers. comm.). The Skagi lavas lie about 225 km from the plume centre. The radial speed of the pulse beneath Iceland was probably in the range of 300–700 km Myr^{-1} (Poore et al., 2009; Jones, pers. comm.). Therefore, the pulse would have reached Skagi between 2.78 and 1.55 Ma (assuming a starting time of 2.3–3.1 Ma). This age compares well with dating of Quaternary lavas by Everts et al. (1972) and the time range of 1.6–1.7 Ma for other volcanic activity in the region. The upwelling process associated with the passing pulse would probably produce very small degrees of deep melting as predicted by the REE inversion model. In future, the new melting model could be used to confirm whether the chemistry of melts produced by this mechanism would match the observations.

It is conceivable that the rifting and pulse-related upwelling mechanisms could combine. In this case there could be mixing between the small degree, highly enriched melts, from the plume-related upwelling and depleted melt fractions from the small amount

of passive upwelling caused by renewed rifting. This combination of mechanisms may be required to reproduce the observed geochemical signature because the small degree of deep melting from the upwelling pulse may results in too highly enriched, alkaline melts. A more realistic compositional model would allow the composition of a mixture of deep and shallow melts to be modelled. The suggestion of very slow spreading or no extension for Skagi Quaternary melting is consistent with the difference between the predicted crustal thickness of 1.5 km from REE inversion modelling and the observed 25–30 km thick crust (Darbyshire et al., 2000).

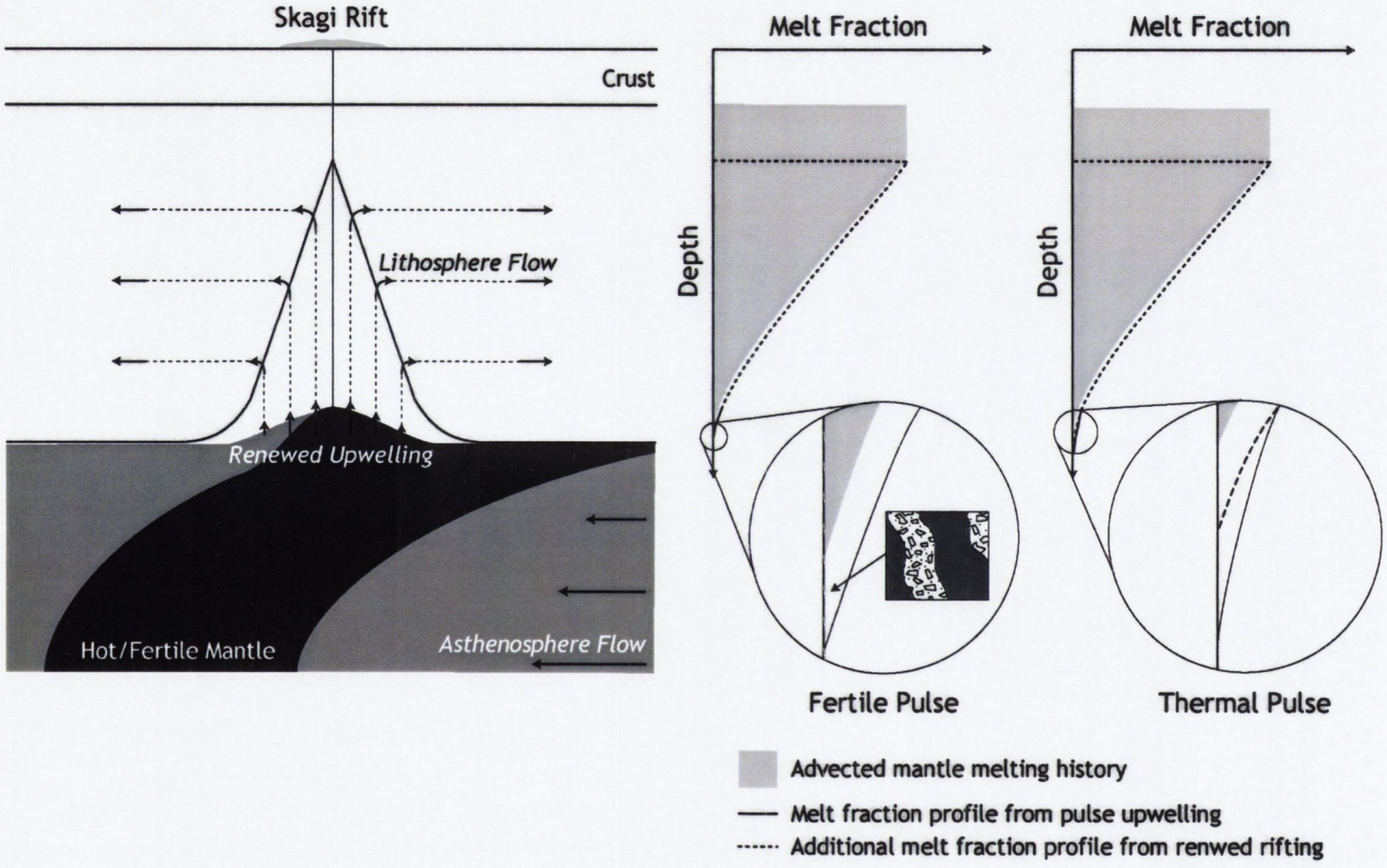

Figure 8.1: Schematic diagram of the interaction between the extinct Skagi Rift and a hot/fertile pulse of mantle material passing beneath the rift. The passing hot/fertile mantle material is drawn into the base of the recently extinct melting region due to the thinned lithosphere. An increase in mantle potential temperature increases the depth of melting so that fresh mantle material is included in the melting. The introduction of more enriched mantle into the deepest parts of the melting region will result in less melt than a thermal pulse, but will increase the concentration of incompatible elements in the deeper melts. The grey area in the estimated melt fraction depth profiles is the previous melting history of the mantle. Lithosphere flow lines represent the case where a small amount of spreading occurs in combination with the pulse.

8.2 Kinematics and Dynamics of Rift Relocations

It is still not clear which processes cause the initiation of a new rift. Rift relocations at Iceland are thought to be driven by the relative eastward migration of the mantle plume relative to Iceland because the rift axes have always been associated with the plume centre. The main evidence for this plume dependence is the current location of the plume centre, estimated to be beneath the axis of the Northern and Eastern Volcanic Zones, under Vatnajökull icecap.

One important constraint on the processes which influence the initiation of a new rift is the horizontal scale. If the distance of rift jumps can be accurately estimated, this would indicate the scale of the lithosphere processes required to cause the jump. For example, Garcia et al. (2003) predicted that the rift jump in northern Iceland could have been as short as 10 km. This value is relatively insignificant when compared to the average width of the volcanic zones at 50 km. Therefore, a 10 km scale rift jump would indicate that rift relocations are not dramatic distinct jumps from one area of the plate to another, but rather a more gradual migration of the rift axis with the relative migration of the plume centre. In this case, the cause of a rift relocation may be linked to the propagation and shut down of the individual fissure systems that make up the axial region. However, the discussion in section 8.1 suggests that conclusions from the Garcia et al. (2003) may not be reliable.

A rough estimation of the distance of the rift relocation between the Western and Eastern Volcanic Zones in southern Iceland gives a maximum of around 50 km. This value is obtained by measuring the distance parallel to the spreading direction between the approximate centre of each rift axis (~80 km) and removing the rough distance that the rifts have separated over the last 2–3 Ma (~35–55 km) based on the full spreading rate of 18 mm yr^{-1}. This estimation is comparable to the average width of the volcanic zones and would require the rift to start around 25 km outside of the existing rift. Off-axis activity, currently or recently active on Iceland, occurs between 15 km (Grímsnes) and 25 km (Snaefell, Öraefajökull Volcanic Belt). Therefore, it is reasonable to suggest that the processes controlling the initiation of a new rift could be linked to the propagation of off-axis activity. Further investigation into how melting occurs to result in an off-axis volcanic centre could be an important step towards understanding rift relocations.

Other important constraints on the processes which underlie rift relocations are accurate dating of each of the rift jumps and the life span of each rift. The evidence in

section 8.1 for the age of extinction of the Skagi rift gives an indication of how poorly the timing of rift relocations is constrained, especially for relocations involving extinct rifts. Questions such as 'are the two rifts always active simultaneously or have past rift jump been more discrete?' cannot be answered without good dating of stratigraphically well defined features. It is relative easy to achieve this through dating of the 'trap' type flows in the Tertiary, where the stratigraphy is regular. However, this kind of sampling is actively biased towards the large volume flows which flow outside the main rift zone (Hardarson and Fitton, 1997) and the more complex structural relationships associated with central volcanic complexes are avoided. The dating and geochemical analysis of these extinct Tertiary calderas may provide new information about the kinematics of the rift activity in northwest Iceland, including the rift jump from the Northwest Rift to the Skagi rift. Garcia et al. (2003) suggest that the Skagi rift and the Northern Volcanic Zone were active simultaneously for a period of up to 5 Ma, similar to the current Western and Eastern Volcanic Zone jump. Simultaneous activity is consistent with the present arrangement of the Western and Eastern Volcanic Zones, and the idea of a less discrete migration of the rift via off-axis activity or individual fissure system propagation.

Finally, it must be remembered that rift relocation is a 3D problem. LaFemina et al. (2005) show, using geodetic GPS data, that the spreading rate varies along-axis in the Western and Eastern Volcanic Zones. The Eastern Volcanic Zone takes almost 100% of the extension at the northern end, and around 60% of the extension at the propagating tip at the southern end. The propagation of a rift adjacent to an existing rift would be easier to explain than the initiation of a complete rift segment. Recent observations by Carbotte et al. (2004) of the difference in axial depth between offset mid-ocean ridge segments show that the shallower rift is usually the leading rift. This difference is modelled by Katz et al. (2004), showing that offset rift axes result in asymmetrical melt production rates between the two rifts, with more melt being produced beneath the propagating rift. A similar process could be occurring at Iceland; this process could be investigated in relation to an initial point source of activity from an off-axis centre as a plausible explanation for rift relocations.

8.3 Conclusions

Similar geochemical signatures are observed for Tertiary and Quaternary lavas from the Skagi peninsula in northern Iceland. The young Skagi lavas have a high Fe-Ti chemistry

and a relatively enriched incompatible element signature compared to the established Western and Northern Volcanic Zones on Iceland. These young lavas also show light REE enrichment relative to the heavy REE, indicating a strong influence of deep mantle melting. The REE inversion predicts very small degrees of melting (1–2%) with around 30–35% of that within the presence of garnet. The similarity between the geochemical signatures from Skagi Quaternary lavas and Tertiary lavas in general is likely to be the result of different mantle processes. The Tertiary geochemistry correlates well with central Iceland geochemistry that has been subject to the geochemical influence of plume-driven upwelling.

The geochemical comparisons of the established volcanic zones provided evidence for a geochemical response to changes in tectonics during a rift relocation. The birth of a new rift axis is associated with very enriched compositions, predicting small degree deep melting up to 7–8% (Kokfelt et al., 2006). The steady-state rifting stage, away from the plume centre, produces relatively depleted incompatible element signatures compared to the new rift segment and predicts around 22% melting (Maclennan et al., 2001b). The decline of a rift shows little evidence of geochemical change (Sinton et al., 2005). All these observations can be reproduced by the new time-dependent model employing a simple variation in spreading rate and a mantle potential temperature of 1450°C. The steady-state model crustal thickness reproduces the 20 km thick average for established rifts at Iceland, away from plume influence.

The origin of the young Skagi lavas is very unlikely to be the last eruptions of a dying rift following a simple ridge slow down. According to the model, other factors are required to produce the enrichment observed in these lavas and it is suggested that variations in plume productivity, radiating out underneath the lithosphere at Iceland could result in renewed activity on the declining Skagi rift after 3 Ma.

The new time-dependent model is an important step towards understanding how mid-ocean ridges evolve through time. Despite its limitations, particularly for calculating compositions, the model manages to reproduce very well the melting regime predicted for different rift stages at Iceland and is consistent with the relative behaviour of the incompatible element signature through time. A few additions to improve the compositional calculation, suggested below, will make this model a very powerful tool for modelling mid-ocean ridge processes globally.

8.4 Further Work

8.4.1 Skagi

The geochemical data implies that the presence of a significant unconformity between the Tertiary and Quaternary lavas on Skagi reflects a hiatus in volcanic eruptions (section 8.1), but it would be good to get more definitive field evidence to confirm that. Dating of youngest Tertiary lavas on Skagi and re-dating of Skagi quaternary lavas would be required to establish whether there is any significant time gap. A subset of around 20 samples from the Skagi Quaternary lavas and dykes was prepared for $^{40}Ar/^{39}Ar$ dating. It is hoped that these will be analysed in the near future. Further sampling of the Tertiary lavas would be required to provide suitable samples for dating purposes.

The new geochemical data in chapter 3 showed that Tertiary lavas from Skagi have a very similar chemistry to Quaternary lavas from Skagi. However, only 5 samples of Tertiary lava flows were collected from the Skagi peninsula and to ensure that this conclusion is correct, further systematic sampling of the Tertiary lavas is required. Whole rock major and trace element data combined with the proposed $^{40}Ar/^{39}Ar$ dating would provide a complete geochemical-time series for activity on the Skagi rift from 15 Ma through the end of activity in the Quaternary, so that any changes in chemistry that would be associated with the decline of a rift axis could be observed. At present, the youngest dated Tertiary lavas from the Skagi rift are 8 Ma, at which time the Northern Volcanic Zone was only just being initiated. Combined isotopic and palaeomagnetic dating of the Tertiary lavas on the Skagi peninsula may be a more efficient way to achieve a well dated stratigraphy. Sr and Nd isotope analysis would also be useful to identify any systematic changes in the source composition through time.

8.4.2 Tertiary crust

The geochemical data presented in chapter 5 shows that strong similarities exist between the geochemical signature of the Tertiary and the central part of the Northern Volcanic Zone, near the plume centre. It is suggested here that previous sampling of the Tertiary has been located in regions which would have been within a 150 km along-axis distance from the plume centre at the time. Two areas of exposed Tertiary

crust exist that may have been located near or outside the 150 km radius of the geochemical influence of the plume (figure 5.40, section 5.5). The first area is in northeast Iceland, east of the Theistareykir volcanic system. The second area in in west Iceland, southwest of Snaefellsnes. Fieldwork and sampling of the area in western Iceland was carried out in June 2009. Whole rock major and trace element data for these new samples and a comparison with existing Tertiary data would indicate if this enriched geochemical signature exists in all exposed Icelandic Tertiary lavas. This result would indicate that the melting regime, source composition and/or the radius of geochemical influence from the plume may have been significantly different in the Tertiary.

The presence of numerous Tertiary central volcanic complexes where there is currently no clear evidence for rifting, has not been explained. Previous sampling of the Tertiary has actively avoided central volcanic complexes. Systematic sampling and geochemical analysis of a series of Tertiary central volcanoes would be useful to determine their tectonic origin and may provide new insights into how the exposed Tertiary crust is preserved. A comparison of their geochemical signature to the 'trap' type lava flow data from the Tertiary may indicate whether the central volcanoes are on-axis or off-axis features.

8.4.3 Numerical Modelling

The present model has further applications in addition to the decline of the Phoenix Ridge described in section 7.6. Firstly, the model can be applied to explain the temporal variations in melting that produce the V-shaped ridge geometry on the Mid-Atlantic Ridge. This application is currently in progress in connection with a new combined geophysical and geochemical dataset from the Reykjanes Ridge obtained during summer 2008 by *Celtic Explorer* cruise CE0806. The thermal pulse is implemented in the model as a spatial and time dependent bottom boundary condition. A second application would be to model the evolution of non-volcanic continental margins. Reston and Phipps Morgan (2004) suggest that the mantle potential temperature is up to 100°C cooler under the continents in order to produce amagmatic rifted margins. However, the preliminary experiments from the model indicate that the time to initiation of melting and the time to steady-state melting is strongly dependent on the geometry of the melting region. Small wedges angles that reflect wide zones of upwelling beneath a new rift can cause delays of several Ma before melting begins, as shown in chapter 7. It might therefore prove possible to explain the evolution of non-volcanic margins in

terms of a transition from small to large wedge angles (that is re-focusing of upwelling) without the need for an unusually cool mantle.

The model would be greatly improved by a more comprehensive calculation of the composition. The introduction of a two-layer mantle with different bulk partition coefficients for spinel and garnet field melting, similar to the method employed by Spiegelman (1996), would be a relatively straight-forward addition to make. This method would enable an improved estimation of the incompatible element enrichment resulting from small degrees of melting, strongly influenced by deep mantle melting. Compositions produced by garnet field melting are particularly important for modelling mantle melt compositions resulting from hydrous melting, which is characterised by deep low melt fraction tails at the base of the melting region. The parameterisation of major elements compositions presented by Watson and McKenzie (1991) would allow the prediction of phase proportions in the mantle and a more comprehensive calculation of trace element abundances. The application of this parameterisation would require a considerable amount of coding work. A simpler approach would be to transplant INVMEL forward modelling routines into the model.

There has been very little work on the development of a melting model that includes a heterogeneous source. The presence of fertile veins within a depleted mantle matrix would have a significant impact on the incompatible element signature, producing exceptionally enriched values for small degree, deep melts such as those observed in the Eastern Volcanic Zone at Iceland. The inclusion of fertile veins in the source in the new time-dependent model, combined with garnet field melting, would produce more realistic values for trace element concentrations. A simple model that includes a fertile mantle component as a mass fraction in the mantle, with separate partition coefficients, would be relatively easy to implement. This mass fraction method would be a first step towards a more realistic model of trace element composition. The introduction of a realistic model of heterogeneous mantle melting, including the thermodynamic properties of the different mantle components, would be a complex undertaking (e.g. Phipps Morgan, 2001).

Observations of the geochemical signature of off-axis volcanic activity in chapters 4 and 5 show a relative enriched chemistry compared to the main rift zones at Iceland. This activity could be initially modelled by integrating the instantaneous melts produced in the outer corners of the melting region. The cause of this anomalous melt migration is an interesting problem. An investigation of the conditions which may lead to off-axis melt migration and eruption would provide significant insights into the trigger for rift

relocations at Iceland.

Further improvements to the model could be made by using a new velocity model of mantle flow beneath mid-ocean ridges that can incorporate simultaneous rift activity and asymmetric spreading. The impact of simultaneous rift activity on the composition of melts produced at each rift could be very significant. The corner flow solution of velocity used in the model is limited to simple flow of the lithosphere. However, hydrous melting predicts melting at depths of up to 150 km beneath Iceland. The flow of asthenospheric mantle at greater depths may be significantly different to the simple 2D corner flow. A flow difference could influence the amount of melting and composition of melts by changing the speed of upwelling beneath the ridge. A 3D velocity model for Iceland would be more appropriate for modelling propagating rifts.

References

Allen, R. M., Nolet, G., Morgan, W. J., Vogfjörd, K., Nettles, M., Ekström, G., Bergsson, B. H., Erlendsson, P., Foulger, G. R., Jakobsdóttir, S., Julian, B. R., Pritchard, M., Ragnarsson, S. and Stefánsson, R. 2002. Plume-driven plumbing and crustal formation in Iceland. *J. Geophys. Res.,* 107(B8), 2163, doi:10.1029/2001JB000584.

Ahern, J. L. and Turcotte, D. L., 1979. Magma migration beneath an ocean ridge. *Earth Planet. Sci. Lett.,* 45, 115–122.

Aigner-Torres, M., Blundy, J., Ulmer, P. and Pettke, T., 2007. Laser Ablation ICPMS study of trace element partitioning between plagioclase and basaltic melts: an experimental approach. *Contrib. Mineral. Petrol.,* 153, 647–667.

Asimow, P. D., Hirschmann, M. M. and Stolper, E. M., 1997. An analysis of variations in isentropic melt productivity. *Phil. Trans. R. Soc. Lond. A,* 355, 255–281.

Barker, P. F., 1982. The Cenozoic subduction history of the Pacific margin of the Antarctic Peninsula—Ridge crest trench interactions. *Geol. Soc. Lond. J.,* 139, 787–801.

Batchelor, G. K., 1967. An Introduction to Fluid Dynamics. *Cambridge Univ. Press, New York.*

Becker, J. J. and Sandwell, D. T., 2005. SRTM30 Plus: SRTM30, Coastal & Ridge Multibeam, Estimated Topography. *Website,* http://topex.ucsd.edu/WWW_html/srtm30_plus.html.

Bindeman, I. N., Davis, A. M. and Drake, M. J., 1998. Ion microprobe study of plagioclase-basalt partition experiments at natural concentration levels of trace elements. *Geochim. Cosmochim. Acta,* 62, 1175–1193.

Blundy, J. and Wood, B., 2003. Partitioning of trace elements between crystals and melts. *Earth Planet. Sci. Lett.,* 210, 383–397.

Bown, J. W. and White, R. S., 1994. Variation with spreading rate of oceanic crustal thickness and geochemistry. *Earth Planet. Sci. Lett.,* 121, 435–449.

Bown, J. W. and White, R. S., 1995. Effect of finite extension rate on melt generation at rifted continental margins. *J. Geophys. Res.,* 100(B9), 18011–18029.

Cannat, M., Briais, A., Deplus, C., Escartin, J., Georgen, J., Lin, J., Mercouriev, S., Meyzen, C., Muller, M., Pouliquen, G., Rabain, A. and da Silva, P., 1999. Mid-Atlantic Ridge-Azores hotspot interactions: along-axis migration of a hotspot-derived event of enhanced magmatism 10 to 3 Ma ago. *Earth Planet. Sci. Lett.,* 173 257–269.

Carbotte, S., Small, C. and Donnelly, K., 2004. The influence of ridge migration on the magmatic segmentation of mid-ocean ridges. *Nature,* 429, 743–746.

Chauvel, C. and Hémond, C., 2000. Melting of a complete section of recycled oceanic crust: Trace element and Pb isotopic evidence from Iceland. *Geochem. Geophys. Geosyst.,* 1, 1999GC000002.

Choe, W. H., Lee, J. I., Lee, M. J., Hur, S. D. and Jin, Y. K., 2007. Origin of E-MORB in a fossil spreading center: the Antarctic-Phoenix Ridge, Drake Passage, Antarctica. *Geos. J.,* 11(3), 185–199.

Darbyshire, F. A., Bjarnason, I. Th., White, R. S. and Flovenz, O. G., 1998. Crustal structure above the Iceland mantle plume imaged by the ICEMELT refraction profile. *Geophys. J. Int.,* 135, 1131–1149.

Darbyshire, F. A., White, R. S. and Priestley, K. F. 2000. Structure of the crust and uppermost mantle of Iceland from a combined seismic and gravity study. *Earth Planet. Sci. Lett.,* 181, 409–428.

Davies, J. and Bickle, M., 1991. A physical model for the volume and composition of melt produced by hydrous fluxing above subduction zones. *Philos. Trans. R. Soc. London Ser. A,* 335 355–364.

Dean, S. M., Minshull, T. A., Whitmarsh, R. B. and Louden, K. E. 2000. Deep structure of the ocean-continent transition in the southern Iberia Abyssal Plain from seismic refraction: The IAM-9 transect at 40°20'N. *J. Geophys. Res.,* 105(B3), 5859–5885.

DeMets, C., Gordon, R. G., Argus, D. F. and Stein, S. 1990. Current plate motions. *Geophys. J. Int.,* 101, 425–478.

DeMets, C., Gordon, R. G., Argus, D. F. and Stein, S. 1994. Effect of recent revisions to the geomagnetic time scale on estimates of current plate motions. *Geophys. Res. Lett.,* 21, 2191–2194.

Einarsson, P. and Saemundsson, K. 1987. Map accompanying the festschrift *Í HLUTARINS EDLI,* Menningarsjódur, Reykjavik.

Elliot, T. R., Hawkesworth, C. J. and Grönvold, K. 1991. Dynamic melting of the Iceland plume. *Nature.* 351, 201–206.

Everts, P., Koerfer, L. E. and Schwarzbach, M. 1972. Neue K/Ar-Datierungen isländisher Basalte. *Neues Jahrb. Geol. Paläontol. Monatsh.,* 5, 280–284.

Everts, P. 1975. Die Geologie von Skagi und der Ost-Küste des Skagafjords (Nord-Island). *PhD Thesis,* Geologischen Instituts der Universität Köln.

Fitton, J. G., Saunders, A. D., Larsen, L. M., Hardarson, B. S. and Norry, M. J. 1998. Volcanic rocks from the southeast Greenland margin at 63°N: Composition, petrogenesis and mantle sources, In *Proc. Ocean Drilling Program, Scientific results,* 152, 331–350.

Fitton, J. G., Saunders, A. D., Norry, M. J., Hardarson, B. S. and Taylor, R. N. 1997. Thermal and chemical structure of the Iceland plume. *Earth Planet. Sci. Lett.,* 153, 197–208.

Foulger, G. R., Du, Z. and Julian, B. R. 2003. Icelandic-type crust. *Geophys. J. Int.,* 155, 567–590.

Fujikami, H., Tatsumoto, M. and Aoki, K. -I. 1984. Partition coefficients of Hf, Zr and REE between phenocrysts and groundmasses. In Proceedings of the fourteenth Lunar and Planetary Science Conference, Part 2. *J. Geophys. Res.,* 89 (supplement), B662–B672.

Furman, T., Frey, F. and Park, K. -H. 1991. Chemical constraints on the petrogenesis of mildly alkaline lavas from Vestmannaeyjar, Iceland: the Eldfell (1973) and Surtsey (1963–1967) eruptions. *Contrib. Mineral. Petrol.,* 109, 19–37.

Garcia, S., Arnaud, N. O., Angelier, J., Bergerat, F. and Homberg, C. 2003. Rift jump process in Northern Iceland since 10 Ma from $^{40}Ar/^{39}Ar$ geochronology. *Earth Planet. Sci. Lett.,* 214, 529–544.

Gast, P. W., 1968. Trace element fractionation and the origin of tholeiitic and alkaline magma types. *Geochim. Cosmochim. Acta,* 32, 1057–1086.

Gee, M. A. M., Taylor, R. N., Thirwall, M. F. and Murton, B. J. 1998. Glacioisostacy controls chemical and isotopic characteristics of tholeiites from the Reykjanes Peninsular, SW Iceland. *Earth Planet. Sci. Lett.,* 164, 1–5.

Ghiorso, M. S. and Sack, R. O. 1995. Chemical mass transfer in magmatic processes IV. A revised and internally consistent thermodynamic model for the interpolation and extrapolation of liquid-solid equilibria in magmatic systems at elevated temperatures and pressures. *Contrib. Mineral. Petrol.,* 119, 197–212.

Govindaraju, K., 1994. 1994 compilation of working values and sample description for 383 geostandards. *Geostandards Newsletter,* 18, 1–158.

Grove, T., 2001. Vapor-saturated melting of fertile peridotite revisited: A new experimental approach and re-evaluation of the hydrous peridotite solidus. *EOS Trans. AGU, 82(47), Fall Meet. Suppl.,* Abstract T31F-05.

Grove, T. L., Kinzler, R. J. and Bryan, W. B. 1992. Fractionation of mid-ocean ridge basalt (MORB), In Mantle flow and melt generation at mid-ocean ridges. *A.G.U. Geophys. Monograph,* Eds Phipps Morgan, J., Blackman, D. K., and Sinton, J. M., 71, 67–102.

Gudmundsson, A. T. 2007. Living Earth: outline of the geology of Iceland. *Reykjavik: Mál og Mennig.*

Hardarson, B. S. 1993. Alkalic rocks in Iceland with special reference to the Snaefellsjökull volcanic system. *PhD Thesis,* University of Edinburgh.

Hardarson, B. S., Fitton, J. G., Ellam, R. M. and Pringle, M. S. 1997. Rift relocation—a geochemical and geochronological investigation of a paleo-rift in NW Iceland. *Earth Planet. Sci. Lett.,* 153, 181–196.

Hardarson, B. S. and Fitton, J. G. 1997. Mechanisms of crustal accretion in Iceland. *Geology,* 25, 1043–1046.

Hardarson, B. S., Fitton, J. G. and Hjartarson, Á., 2008 Tertiary volcanism in Iceland. *Jökull,* 58, 161–178.

Hards, V. L. 1995. The evolution of the Snaefell volcanic centre, Eastern Iceland. *PhD Thesis* University of Durham.

Hards, V. L., Kempton, P. D., Thompson, R. N. and Greenwood, P. B. 2000. The magmatic evolution of the Snaefell volcanic centre; an example of volcanism during incipient rifting in Iceland. *J. Volcanol. Goetherm. Res.* 99, 97–121.

Harlou, R., Pearson, D. G., Nowell, G. M., Ottley, C. J. and Davidson, J. P. 2009. Combined Sr isotope and trace element analysis of melt inclusions at sub-ng levels using micro-milling, TIMS and ICPMS. *Chem. Geol.* 260, 254–268.

Hart, S. R., Schilling, J. -G. and Powell J. L. 1973. Basalts from Iceland and along the Reykjanes Ridge: Sr isotope geochemistry. *Nature* 246, 104–107.

Hémond, C., Arndt, N. T., Lichenstein, U. and Hofmann, A. W. 1993. The Heterogeneous Iceland Plume: Nd-Sr-O Isotopes and Trace Element Constraints. *J. Geophys. Res.,* 98(B9), 15833–15850.

Hirschmann, M. M., Ghiorso, M. S., Wasylenki, L. E., Asimow, P. D. and Stolper, E. M., 1998. Calculation of peridotite partial melting from thermodynamic models of minerals and melts. I. Review of methods and comparison with experiments. *J. Petrol.,* 39, 1091–1115.

Hirth, G. and Kohlstedt, D. L. 1996. Water in the oceanic mantle: implications for rheology, melt extraction, and the evolution of the lithosphere. *Earth Planet. Sci. Lett.,* 144, 93–108.

Hjartarson, A. 2003. The Skagafjördur Unconformity. *PhD Thesis,* University of Copenhagen.

Irvine, T. N. and Baragar, W. R. A. 1971. Guide to chemical classification of common volcanic rocks. *Can. J. Earth Sci.,* 8,523–546.

Ito, G., Lin, J. and Gable, C. W. 1996. Dynamics of mantle flow and melting at a ridge-centered hotspot: Iceland and the Mid-Atlantic Ridge. *Earth Planet. Sci. Lett.,* 144,53–74.

Ito, G., Shen, Y., Hirth, G and Wolfe, C. G. 1999. Mantle flow, melting, and dehydration of the Iceland mantle plume. *Earth Planet. Sci. Lett.,* 165, 81–96.

Iwamori, H., McKenzie, D. and Takahashi, E., 1995. Melt generation by isentropic mantle upwelling. *Earth Planet. Sci. Lett.,* 134, 253–266.

Iwamori, H., 1997. Compression melting in subduction zones. *Terr. Nova,* 9, 9–13.

Iwamori, H. 1994. $^{238}U/^{230}Th/^{226}Ra$ and $^{235}U/^{231}Pa$ disequilibria produced by mantle melting with porous and channel flows. *Earth Planet. Sci. Lett.,* 125, 1–16.

Jakobsson, S. P. 1972. Chemistry and distribution pattern of Recent basaltic rocks in Iceland. *Lithos,* 5, 365–386.

Jakobsson, S. P. 1979. Petrology of recent basalts of the eastern volcanic zone, Iceland. *Acta Nat. Isl.,* 26, 1–103.

Jakobsson, S. P., Jonasson, K. and Sigurdsson, I. A. 2008. The three igneous rock series of Iceland. *Jökull,* 58, 117–138.

Jarvis, K. E., Gray, A. L. and Houk, R. S., 1992. Handbook of inductively coupled mass spectrometry. *Blackie,* pp380, 1992.

Jha, K., Parmentier, E. and Phipps Morgan, J., 1994. The role of mantle-depletion and melt-retention buoyancy in spreading center segmentation. *Earth Planet. Sci. Lett.,* 125, 221–234.

Jochum, K. P., Seufert, H. M. and Thirwall, M. F., 1990. High sensitivity Nb analysis by spark-source mass spectrometry (SSMS) and calibration of XRF Nb and Zr. *Chem. Geol.,* 81, 1–16.

Jóhannesson, H. 1975 Structure and petrochemistry of the Reykjadalur central volcano and the surrounding areas, Midwest Iceland. *PhD Thesis,* University of Durham.

Jóhannesson, H. 1980 Evolution of rift zones in western Iceland. *Natturufraedingurinn,* 50, 13–31.

Jóhannesson, H. and Saemundsson, K. 1998. Geological Map of Iceland. 1:500 000. Bedrock Geology. *Icelandic Institute of Natural History, Reykjavik,* 2nd edition.

Johnson, K. T. M. 1994. Experimental cpx/ and garnet/melt partitioning of REE and other trace elements at high pressures; petrogenetic implications. *Mineralogical Magazine,* 58, 454–455.

Johnson, K. T. M., 1998. Experimental determination of partition coefficients for rare earth and high-field-strength elements between clinopyroxene, garnet, and basaltic melt at high pressure. Contrib. Mineral. Petrol., 133, 60–68.

Jones, S. M., White, N. and Maclennan, J. 2002. V-shaped ridges around Iceland: Implications for spatial and temporal patterns of mantle convection. *Geochem. Geophys. Geosyst.,* 3(10), 1059,doi:10.1029/2002GC000361.

Jones, S. M. 2003. Test of a ridge-plume interaction model using oceanic crustal thickness structure around Iceland. *Earth Planet. Sci. Lett.,* 208,205–218.

Jones, S. M. and Maclennan, J. 2005. Crustal flow beneath Iceland. *J. Geophys. Res.,* 110(B09410), doi:10.1029/2004JB003592.

Jull, M. G., 1997. The effect of glaciation on mantle melting beneath Iceland. PhD Thesis, University of Cambridge.

Jull, M. and McKenzie, D. 1996. The effect of deglaciation on mantle melting beneath Iceland. *J. Geophys. Res.,* 101(B10), 21815–21828.

Katz, R. F., Spiegelman, M. and Langmuir, C. H. 2003. A new parameterisation of hydrous mantle melting. *Geochem. Geophys. Geosyst.,* 4(9), 1073, doi:10.1029/2002GC000433.

Katz, R. F., Spiegelman, M. and Carbotte, S., 2004. Ridge migration, asthenospheric flow and the origin of magmatic segmentation in the global mid-ocean ridge system. *Geophys. Res. Lett.,* 31, L15605, doi:10.1029/2004GL020388.

Kawamoto, T. and Holloway, J., 1997. Melting temperature and partial melt chemistry of H_2O saturated mantle peridotite to 11 gigapascals. *Science,* 276, 240–243.

Kelemen, P. B., Hirth, G., Shimizu, N., Spiegelman, M. and Dick, H. J. B. 1997. A review of melt migration processes in the adiabatically upwelling mantle beneath oceanic spreading ridges. *Phil. Trans. R. Soc. Lond. A,* 355, 283–318.

Kinzler, R., 1997. Melting of mantle peridotite at pressures approaching the spinel-garnet transition: Application to mid-ocean ridge basalt petrogenesis. *J. Geophys. Res.,* 102, 853–874.

Kinzler, R. and Grove, T., 1992. Primary magmas of mid-ocean ridge basalts: 1. Experiments and methods. *J. Geophys. Res.,* 97, 6885–6906.

Kitagawa,H., Kobatashi, K., Makishima, A. and Nakamura, E. 2008. Multiple Pulses of the Mantle Plume: Evidence from Tertiary Icelandic Lavas. *J. Petrol.,* 49, 1365–1396.

Klein, E. M. and Langmuir, C. H. 1987. Global correlations of ocean ridge basalt chemistry with axial depth and crustal thickness. *J. Geophys. Res.,* 92(B8), 8089–8115.

Kogiso, T., Hirschmann, M. M. and Reiners, P. W., 2004. Length scales of mantle heterogeneities and their relationship to ocean island basalt chemistry. *Geochim. Cosmochim. Acta,* 68, 345–360.

Kokfelt, T. F., Hoernle, K., Hauff, F., Fiebig, J., Werner, R. and Garbe-Schönberg, D. 2006. Combined Trace Element and Pb-Nd-Sr-O Isotope Evidence for Recycled Oceanic Crust (Upper and Lower) in the Iceland Mantle Plume. *J. Petrol.,* 47(9), 1705–1749.

Kumar, P., Kind, R., Priestley, K. and Dahl-Jensen, T. 2007. Crustal structure of Iceland and Greenland from receiver functions. *J. Geophys. Res.,* 112(B3), B03301, doi:10.1029/2005JB003991.

Lachenbruch, A. H., 1976. Dynamics of a passive spreading center. *J. Geophys. Res.,* 81, 1883–1902.

LaFemina, P. C., Dixon, T. H., Malservisi, R., Árnadóttir, T., Sturkell, E., Sigmundsson, F. and Einarsson, P. 2005. Geodetic GPS measurements in south Iceland: Strain accumulation and partitioning in a propagating ridge system. *J. Geophys. Res.,* 110(B11405), doi:10.1029/2005JB003675.

Langmuir, C. H., Bender, J. F., Bence, A. E., Hanson, G. N. and Taylor, S. R. 1977. Petrogenesis of basalts from the Famous area, Mid-Atlantic Ridge. *Earth Planet. Sci. Lett.,* 36, 133–156.

Langmuir, C. H. 1989. Geochemical consequences of in situ crystallisation. *Nature,* 340, 199–205.

Langmuir, C. H., Klein, E. M. and Plank, T. 1992. Petrological systematics of mid-ocean ridge basalts: constraints on melt generation beneath ocean ridges, In Mantle flow and melt generation at mid-ocean ridges. *A.G.U. Geophys. Monograph,* Eds. Phipps Morgan, J., Blackman, D. K. and Sinton, J. M., 71, 183–280.

Larter, R. D. and Barker, P. F., 1991. Effects of ridge crest trench interaction on Antarctic Phoenix spreading—Forces on a young subducting plate. *J. Geophys. Res.,* 96, 19583–19607.

Le Maitre, R. W., Bateman, P., Dudek, A., Keller, J., Lameyre, J., Le Bas, M. J., Sabine, P. A.. Schmid, R., Sorensen, H., Streckeisen, A., Woolley, A. R. and Zanettin, B. 1989. A classification of Igneous Rocks and Glossary of Terms: Recommendations of the International Union of Geological Sciences Subcommision on the Systematics of Igneous Rocks. *Oxford: Blackwell Scientific.*

Livermore, R., Balanyá, J. C., Malando, A., Martínez, J. M., Rodríguez-Fernández, J., de Galdeano, C. S., Zaldívar, J. G., Jabaloy, A., Barnolas, A, Somoza, L., Hernándew-Molina, J., Suriñach, E. and Viseras, C. 2000. Autopsy on a dead spreading center: The Phoenix Ridge, Drake Passage, Antarctica. *Geology,* 28, 607–610.

McKenzie, D. 1967. The viscosity of the mantle. *Geophys. J. Roy. Astr. Soc.,* 15, 297–305.

McKenzie, D. 1969. Speculations on the consequences and causes of plate motions. *Geophys. J. Roy. Astr. Soc.,* 18, 1–32.

McKenzie, D. 1984. The generation and compaction of molten rock. *J. Petrol.,* 25, 713–765.

McKenzie, D. and O'Nions, R. K. 1991. Partial melt distributions from inversion of Rare Earth Element concentrations. *J. Petrol.,* 32, 1021–1091.

McKenzie, D. and O'Nions, R. K. 1992. Correction to Partial melt distributions from inversion of Rare Earth Element concentrations. *J. Petrol.,* 33, 1453.

McKenzie, D. and Bickle, M. J. 1988. The volume and composition of melt generated by extension of the lithosphere. *J. Petrol.,* 29, 625–679.

McKenzie, D. and Blundy, J. 1999. Partial melt distributions from inversions with $D = D(P, T, X)$ (abstract). *EOS Tans. 80, Fall Meet. Suppl.,* F1112.

Maclennan, J. 2000. Melt generation and movement under Northern Iceland. *PhD Thesis,* University of Cambridge.

Maclennan, J., McKenzie, D., Gronvöld, K. and Slater, L. 2001a. Crustal accretion under northern Iceland. *Earth Planet. Sci. Lett.,* 191, 295–310.

Maclennan, J., McKenzie, D. and Gronvöld, K. 2001b. Plume-driven upwelling under central Iceland. *Earth Planet. Sci. Lett.* 194, 67–82.

Maclennan, J., Jull, M., McKenzie, D., Slater, L. and Gronvöld, K. 2002. The link between volcanism and deglaciation in Iceland. *Geochem. Geophys. Geosyst.,* 3(11),1062, doi:10.1029/2001GC000282.

Maclennan, J., McKenzie, D., Gronvöld, K., Shimizu, N., Eiler, J. M. and Kitchen, N. 2003. Melt mixing and crystallisation under Theistareykir, northeast Iceland. *Geochem. Geophys. Geosyst.,* 4(11),824, doi:10.1029/2003GC000558.

Maclennan, J. 2008a. Lead isotope variability in olivine-hosted melt inclusions from Iceland. *Geochim. Cosmochim. Acta,* 72, 4159–4176.

Maclennan, J. 2008b. Concurrent Mixing and Cooling of Melts under Iceland. *J. Petrol.,* 49(11), 1931-1953.

Macdougall, L., Saemundsson, K., Jó hannesson, H., Watkins, N. D. and Kristjansson, L. 1977. Extension of the geomagnetic polarity time scale to 6.4 m.y. K-Ar dating, geological and palaeomagnetic study of a 3500 m lava succession in western Iceland. *Geol. Soc. Am. Bull.,* 88, 1–15.

Mattsson, H. and Höskuldsson, Á. 2003. Geology of the Heimaey volcanic centre, south Iceland: early evolution of a central volcano in a propagating rift? *J. Volcanol. Goetherm. Res.,* 127, 55–71.

Mattsson, H. B. and Oskarsson, N. 2005. Petrogenesis of alkaline basalts at the tip of a propagating rift: Evidence from the Heimaey volcanic centre, south Iceland. *Earth Planet. Sci. Lett.,* 147, 245–267.

Meyer, P. S., Sigurdsson, H. and Schilling, J. -G. 1985. Petrological and geochemical variations along Iceland Neovolcanic Zones. *J. Geophys. Res.,* 90(NB12), 43–72.

Mittelstaedt, E., Ito, G. and Behn, M. D. 2008. Mid-ocean ridge jumps associated with hotspot magmatism. *Earth Planet. Sci. Lett.,* 266, 256–270.

Nicholson, H. 1990. The magmatic evolution of Krafla, NE Iceland. *PhD Thesis,* University of Edinburgh.

Pálmason, G. and Saemundsson, K. 1974. Iceland in relation to the Mid-Atlantic Ridge. *Annual Review of Earth Sciences,* 2, 25–50.

Patankhar, S. V., 1980. Numerical heat transfer and fluid flow. *Series in computational methods in mechanics and thermal sciences,* McGraw-Hill, New York.

Pearce, J. A. 1982. Trace element characteristics of magmas erupted along destructive plate margins; In Andesites, Ed. Thorpe, R. S., *John Wiley and Sons,* 549–571.

Phipps Morgan, J., 2001. Thermodynamics of pressure release melting of a veined plum pudding mantle. *Geochem. Geophys. Geosyst.,* 2, doi:10.1029/2000GC000049.

Poore, H. R., White, N. and Jones, S., 2009. A Neogene chronology of Iceland plume activity from V-shaped ridges. *Earth Planet. Sci. Lett.,* 283, 1–13.

Pringle, M. S., Hardarson, B. S., Kristjansson, L. and Johanesson, H., 1997. Decrease in crustal production rate from established and dying rifts: examples from western Iceland. *EOS, Transactions, American Geophysical Union,* 78, 656.

Prytulak, J. and Elliott, T. 2007 TiO_2 enrichment in ocean island basalts. *Earth Planet. Sci. Lett.,* 263, 388–403.

Reston, T. J. and Phipps Morgan, J., 2004. Continental geotherm and the evolution of rifted margins. *Geology,* 32, 133–136.

Robinson, J. A. C. and Wood, B. J. 1998. The depth to the spinel to garnet transition at the peridotite solidus. *Earth Planet. Sci. Lett.,* 164, 277–284.

Saemundsson, K. 1974. Evolution of the axial rifting zone in northern Iceland and the Tjörnes fracture zone. *Bull. Geol. Soc. Am.,* 85, 495–504.

Saemundsson, K. 1978. Fissure swarms and central volcanoes of the neovolcanic zones of Iceland, In; Crustal evolution in northwest Britain and adjacent regions. *Geol. Jl. Spec. Issue,*Eds Bowes, D. R. and Leake, B. E., 10, 415–432.

Saemundsson, K. 1979. Outline of the geology of Iceland. *Jökull,* 29, 7–28.

Schilling, J. -G., 1966. Rare earth fractionation in Hawaii volcanic rocks. *PhD Thesis,* Mass. Inst. Technology.

Schilling, J. -G. 1972. Iceland mantle plume; geochemical study of Reykjanes Ridge. *Nature,* 242, 565–571.

Schilling, J. -G., Sigurdsson, H. and Kingsley, R. H. 1978. Skagi and Western Neovolcanic Zones in Iceland: 2. Geochemical Variations. *J. Geophys. Res.,* 83(B8), 3983–4002.

Shaw, D. M. 1970. Trace element fractionation during anatexis. *Geochim. Cosmochim. Acta,* 34, 237–243.

Shen, Y. and Forsyth, D. W. 1995. Geochemical constraints on initial and final depths of melting beneath mid-ocean ridges. *J. Geophys. Res.,* 100(B2), 2211–2237.

Sigmarsson, O., Hémond, C., Condomines, M., Fourcade, S. and Oskarsson, N. 1991. Origin of silicic magmas in Iceland revealed by Th isotopes. *Geology,* 19, 621–624.

Sigmarsson, O., Condomines, M. and Fourcade, S. 1992. Mantle and crustal contribution in the genesis of Recent basalts from off-rift zones in Iceland. *Earth Planet. Sci. Lett.,* 110, 149–162.

Sigmarsson, O., Maclennan, J. and Carpentier, M. 2008. Geochemistry of igneous rocks in Iceland: a review. *Jökull,* 58, 139–160.

Sigurdsson, H., Schilling, J. -G. and Meyer, P. S. 1978. Skagi and Langjökull Volcanic Zones in Iceland: 1. Petrology and Structure. *J. Geophys. Res.,* 83(B8), 3971–3982.

Sinha, M. C., Navin, D. A., MacGregor, L. M., Constable, S., Peirce, C., White, A., Heinson, G. and Inglis, M. A. 1997. Evidence for accumulated melt beneath the slow-spreading Mid-Atlantic Ridge. *Phil. Trans. R. Soc. Lond.,* A355, 233–253.

Sinton, J., Grönvold, K. and Saemundsson, K. 2005. Postglacial eruptive history of the Western Volcanic Zone, Iceland. *Geochem. Geophys. Geosyst.,* 6(Q12009), doi:10.1029/2005GC001021.

Skilbeck, J. N., 1975. Stability of 2-dimensional convection rolls and its relevance to mantle convection. *EOS Trans. AGU, 56(3), Fall Meet. Suppl.,* Abstract, 168–168.

Slater, L., Jull, M., McKenzie, D. and Grönvold, K. 1998. Deglaciation effects on mantle melting under Iceland: results from the northern volcanic zone. *Earth Planet. Sci. Lett.,* 164, 151–164.

Slater, L.,, McKenzie, D., Grönvold, K. and Shimizu, N. 2001. Melt generation and Movement beneath Theistareykir, NE Iceland. *J. Petrol.,* 42, 321–354.

Small, C. 1995. Observations of ridge-hotspot interactions in the Southern Ocean. *J. Geophys. Res.,* 100(B9), 17931–17946.

Sparks, R. S. J., Huppert, H. E., Koyaguchi, T. and Hallworth, M. A. 1993. Origin of modal and rhythmic igneous layering by sedimentation in a convecting magma chamber. *Nature,* 361, 246–249.

Sparks, R. S. J., Huppert, H. E. and Turner, J. S. 1984. Fluid dynamics of evolving magma chambers. *Phil. Trans. R. Soc. Lond.,* A310, 511–534.

Spiegelman, M. 1996. Geochemical consequences of melt-transport in 2-D: the sensitivity of trace elements to mantle dynamics. *Earth Planet. Sci. Lett.,* 139, 115–132.

Spiegelman, M. and Kelemen, P. B. 2003. Extreme geochemical variability as a consequence of channelized melt transport. *Geochem. Geophys. Geosyst.,* 4(7), 1055, doi:10.1029/2002GC000336.

Spiegelman, M. and Elliot, T. 1993. Consequences of melt transport for uranium series disequilibrium. *Earth Planet. Sci. Lett.,* 118, 1–20.

Spiegelman, M. and McKenzie, D., 1987. Simple 2-D models for melt extraction at mid-ocean ridges and island arcs. *Earth Planet. Sci. Lett.,* 83, 137–152.

Srivastava, S. P., Voppel, D. and Tucholke, B. 1988. Geophysical Atlas of the North Atlantic between 50° to 60°N and 0° to 65°W. *Dtsch. Hydrogr. Inst.,* Hamburg.

Staples, R. K., White, R. S., Brandsdóttir, B., Menke, W., Maguire, P. K. H. and McBride, J. H. 1997. Färoe-Iceland Ridge Experiment 1. Crustal structure of northeastern Iceland. *J. Geophys. Res.,* 102, 7849–7866.

Steinthorsson, S., Oskarsson, N. and Sigvaldason, G. E. 1985. Origin of alkali basalts in Iceland—a plate tectonic model. *J. Geophys. Res.,* 90(NB12), 27–42.

Stracke, A., Bizmis, M. and Salters, V. J. M. 2003. Recycling oceanic crust: Quantitative constraints. *Geochem. Geophys. Geosyst.,* 4(3), 8003, doi:10.1029/2001GC000223.

Thirwall, M. F., Gee, M. A. M., Taylor, R. N. and Murton, B. J., 2004. Mantle components in Iceland and adjacent ridges investigated using double-spike Pb isotope ratios. *Geochim. Cosmochim. Acta,* 68, 361–386.

Vogt, P. R. 1971. Asthenosphere motion recorded by the ocean floor south of Iceland. *Earth Planet. Sci. Lett.,* 13, 153–160.

Walker, G. P. L. 1960. Zeolite zones and dike distribution in relation to the structure of the basalts of eastern Iceland. *J. Geol.,* 68, 515–528.

Watkins, N. D. and Walker, G. P. L. 1977. Magnetostratigraphy of eastern Iceland. *Am. J. Sci.,* 277, 513–584.

Watson, S. and McKenzie, D., 1960. Melt generation by plumes - a study of Hawaiian volcanism. *J. Petrol.,* 32, 501–537.

White, R. S., McKenzie, D. and O'Nions, R. K. 1992. Oceanic Crustal Thickness From Seismic Measurements and Rare Earth Element Inversions. *J. Geophys. Res.,* 97(B13), 19683–19715.

White, R. S. and McKenzie, D. 1995. Mantle plumes and flood basalts. *J. Geophys. Res.,* 100(B9), 17543–17585.

White, R. S., Bown, J. W. and Smallwood, J. G. 1995. The temperature of the Iceland plume and origin of outward-propagating V-shaped ridges. *J. Geol. Soc., London,* 152, 1039–1045.

Wood, D. A., Joron, J. L., Treuil, M., Norry, M. and Tarney, J. 1979. Elemental and Sr isotope variations in basic lavas from Iceland and the surrounding ocean floor. *Contrib. Mineral. Petrol.,* 70,319–339.

Workman, R. K. and Hart, S. R. 2005. Major and trace element composition of the depleted MORB mantle (DMM). *Earth Planet. Sci. Lett.,* 231 53–72.

Zindler, A., Hart, S. R., Frey, F. A. and Jakobsson, S. P. 1979. Nd and Sr isotope ratios and Rare Earth Element abundances in Reykjanes Peninsular basalts: Evidence for mantle heterogeneity beneath Iceland. *Earth Planet. Sci. Lett.,* 45, 249–262.

Appendix A

Geological Map of Skagi

A digitised version of the geological map of Skagi and the coasts of Skagafjördur, produced by Everts (1975), is provided as an insert inside the back cover of this dissertation.

Appendix B

Analytical Methods

B.1 Whole-rock Powder Preparation

A diamond-tipped saw was used to cut small slices from each sample for crushing and to remove any weathered surfaces. Thin sections were taken from each sample and, together with the hand specimens, were checked for signs of hydrothermal alteration. Samples were observed to be fresh, except for one sample from Austurdalur (A17164) that contained hydrothermal mineral deposits. This sample is noted in chapter 3. The sliced samples were rinsed under clean tap water and place in an oven at 50°C for a minimum of 24 hours. The dry samples were put through a jaw crusher to produce cm-scale rock chips. The rock chips were placed in a tungsten-carbide Tema barrel and ground for 2 minutes. The whole-rock powders were used for major element, trace element, REE element and Sr and Nd isotope analysis.

B.2 X-ray Fluorescence Analysis

The powdered samples were prepared for X-ray fluorescence (XRF) analysis at the University of Edinburgh using the method described by Fitton et al. (1998). Major element concentrations were determined from fusion discs. A small amount of rock powder was transferred to a clean glass vial and dried in an oven at 110° for at least 2 hours. Approximately 1 g of powder was weighed precisely into a platinum alloy crucible and ignited in a muffle furnace at 1100°C for 20 minutes. The crucible was then

re-weighed precisely to determine the mass loss on ignition (LOI). Lithium tetraborate flux was added to the sample residue in a sample to flux ratio of 1:5. The sample was then returned to the furnace for a further 20 minutes to allow initial fusion of the sample and flux. After the initial fusion the sample was re-weighed and any loss of flux mass was replaced until the precise sample:flux ratio (± 0.0003 g) was reached. The final mixture of sample and flux was fused over a Meker burner for at least 5 minutes, during which the molten mixture was swirled vigorously to guarantee homogeneity. The final stage was to cast the melt onto a graphite mould to produce a disc.

Trace element concentrations were determined from pressed powder pellets. Approximately 8 g of rock powder was weighed into a Pyrex beaker and mixed with 8 drops of a 2% aqueous solution of polyvinyl alcohol, which acts as a binder. The mixture was transferred to a thin-walled aluminium cap, placed between two tungsten-carbide discs and compressed at 8 tons for 2 minutes.

The fused and pressed discs were run on a Philips PW 2404 automatic X-ray fluorescence spectrometer with a Rh-anode X-ray tube. The analytical conditions are described by Fitton et al. (1998). The spectrometer was calibrated with USGS and CRPG standards using the values given by Jochum et al. (1990) and Govindaraju (1994). The LOI was negative for the majority of samples with most values ranging between 0 and -1%. The totals for the major element data presented in appendix B were all $100 \pm 0.5\%$; any samples outside this limit were repeated. Precision and accuracy estimates for major and trace element XRF are provided in tables B.1 and B.2. The precision and for all elements is generally very good, with poor accuracy for Rb and Ba and extremely poor accuracy for low concentrations of Ca and P.

Sample		SiO_2	Al_2O_3	Fe_2O_{3T}	MgO	CaO	Na_2O	K_2O	TiO_2	MnO	P_2O_5
SK40	$\bar{x}$	48.35	12.69	16.89	5.46	9.66	2.49	0.5	3.56	0.25	0.37
	σ	0.04	0.03	0.01	0.02	0.02	0.04	0	0.01	0	0
	V	0.09	0.22	0.06	0.3	0.19	1.61	0.47	0.15	0.71	0.45
BHVO-1	$\bar{x}$	50.28	13.78	12.31	7.07	11.39	2.33	0.53	2.72	0.17	0.3
	x_r	49.94	13.8	12.35	7.23	11.4	2.26	0.52	2.71	0.17	0.27
	S	0.67	−0.14	−0.32	−2.28	−0.09	2.88	1.15	0.33	1.79	9.34
FKN	$\bar{x}$	65.27	18.87	0.09	0.02	0.17	2.37	12.73	0.01	0.01	0.02
	x_r	65.02	18.61	0.09	0.01	0.11	2.58	12.81	0.02	0.01	0.02
	S	0.38	1.37	3.85	50	54.55	−8.33	−0.59	−55	20	−35.42

Table B.1: Precision and accuracy estimates for major element XRF analysis. The precision estimate was obtained from 10 repeat runs of SK40 from Hafnahudir on the north coast of Skagi. $\bar{x}$ is the mean and σ is the standard deviation. The coefficient of variation is given by $V = 100\sigma/\bar{x}$. USGS standards BHVO-1 and FKN are used to estimate the accuracy of the analyses with reference values, x_r, from Govindaraju (1994). The mean observed values for the standards are based on two runs. The accuracy is given by $S = 100(O - E)/E$, where O is the observed value and E is the reference value.

Sample		Nb	Zr	Y	Sr	Rb	Zn	Cu	Ni	Cr	V	Ba	Sc
SK40	$\bar{x}$	26.1	230.9	50.3	229.7	9.7	131.0	79.6	36.6	32.7	500.2	128.6	39.2
	σ	0.11	0.68	0.1	0.24	0.13	0.83	0.74	0.85	1.17	4.45	4.28	0.57
	V	0.44	0.29	0.2	0.1	1.34	0.63	0.93	2.33	3.58	0.89	3.32	1.46
BIR-1	$\bar{x}$	0.6	16.21	16.21	106.55	0.25	70.6	127.68	163.28	374.82	319	8.24	41.75
	σ	0.18	0.14	0.15	0.19	0.17	0.88	2.8	0.7	6.76	3.84	1.88	1.44
	V	30.04	0.89	0.9	0.18	67.82	1.25	2.19	0.43	1.8	1.2	22.85	3.46
	x_r	0.60	15.50	16.00	108.00	0.25	71.00	126.00	166.00	382.00	313.00	7.00	44.00
	S	0.28	4.6	1.28	−1.34	0.66	−0.56	1.33	−1.64	−1.88	1.92	17.66	−5.11
BHVO-1	$\bar{x}$	19.8	174.9	27.19	397.41	9.09	106.06	134.3	124.65	289.68	311.83	137.51	33.53
	σ	0.07	0.73	0.13	0.98	0.14	0.32	2.74	0.83	1.19	4	3.56	0.85
	V	0.37	0.42	0.48	0.25	1.5	0.3	2.04	0.67	0.41	1.28	2.59	2.54
	x_r	19.0	179.0	27.6	403.0	11.0	105.0	136.0	121.0	289.0	317.0	139.0	31.8
	S	4.2	−2.29	−1.47	−1.39	−17.34	1	−1.25	3.01	0.24	−1.63	−1.07	5.45

Table B.2: Precision and accuracy estimates for trace element XRF analysis. The precision estimate was obtained from 5 repeat runs of SK40 from Hafnahudir on the north coast of Skagi. $\bar{x}$ is the mean and σ is the standard deviation. The coefficient of variation is given by $V = 100\sigma/\bar{x}$. USGS standards BIR-1 and BHVO-1 are used to estimate the accuracy of the analyses with reference values, x_r, from Govindaraju (1994). The mean observed values for the standards are based on 6 runs. The accuracy is given by $S = 100(O - E)/E$, where O is the observed value and E is the reference value.

B.3 Inductively Coupled Plasma Mass Spectrometry

Two sessions of inductively coupled plasma mass spectrometry (ICP-MS) were carried out in 2006 and 2007. A subset of samples were sent to the Scottish Universities Environmental Research Centre (SUERC) for analysis. The samples were prepared using a standard acid digestion, similar to the one described below. Another subset of samples were prepared and analysed at the University of Cambridge. The precision and accuracy estimates for the two sessions of ICP-MS are shown in table B.3. The precision and accuracy is generally very good for all elements from both data sets. The data from SUERC is slightly more consistent than the data from the University of Cambridge. A review of the ICP-MS technique is presented by Jarvis et al. (1990).

The method of acid digestion used at the University of Cambridge is described here. A small amount of powder was transferred into a clean glass vial, covered and placed into an oven at 110°C for at least 4 hours. 0.1±0.01 g of dried powder was weighed into a clean Teflon vial and 1 ml of HF and 4 ml of HNO_3 were added to the rock powder. The Teflon vials were placed in a hot block at 110°C overnight to allow the rock powder to be digested. Once all the rock had been dissolved the vials were removed from the hot block and placed in an elbow evaporator. Ca-Mg fluorides were present as a white precipitate at this stage; they were dissolved through later stages in the digestion process. The elbow was placed in a hot block to allow evaporation of the solution down to a crystal slurry at approximately 1 ml. 1 ml of HNO_3 was then added to the crystal slurry and the elbows returned to the hot block to allow evaporation down to 1 ml again. This step was repeated once. After the final evaporation, 2.5 ml of HNO_3 and a small volume of ultra-pure distilled water was added to the sample solution and replaced to the hot block over night to allow dissolution of any Ca-Mg fluoride precipitates. Finally, the samples were transferred to clean plastic bottles and diluted to approximately 50±1 ml with ultra-pure distilled water. One standard and one blank solution were prepared with each sample set of 10. The standards used were AVG-2 and BCR-2.

Sample		La	Ce	Pr	Nd	Sm	Eu	Gd	Tb	Dy	Ho	Er	Tm	Yb	Lu
BCR-2	$\bar{x}$	24.84	53.41	6.78	28.74	6.59	1.97	6.71	1.05	6.39	1.27	3.68	0.56	3.41	0.51
SUERC	σ	0.12	0.2	0.03	0.14	0.04	0.01	0.03	0.01	0.02	0.01	0.03	0	0.02	0
(12)	V	0.49	0.37	0.39	0.48	0.67	0.7	0.41	0.88	0.39	0.65	0.88	0.68	0.59	0.68
	x_r	24.9	52.9	6.57	28.7	6.58	1.96	6.75	1.07	6.41	1.3	3.66	0.54	3.38	0.5
	S	−0.22	0.96	3.21	0.13	0.09	0.32	−0.61	−1.68	−0.24	−2.38	0.44	4.56	1.01	2.31
BCR-2	$\bar{x}$	25.74	53.31	6.76	29.08	6.83	1.99	6.9	1.1	6.66	1.36	3.8	0.56	3.5	0.52
Cambridge	σ	0.16	1.05	0.18	0.52	0.14	0.04	0.12	0.02	0.09	0.03	0.06	0.01	0.05	0.01
(3)	V	0.63	1.97	2.65	1.79	2.03	1.86	1.7	1.38	1.29	2.14	1.69	1.96	1.56	2.03
	x_r	24.9	52.9	6.57	28.7	6.58	1.96	6.75	1.07	6.41	1.3	3.66	0.54	3.38	0.5
	S	3.36	0.78	2.92	1.32	3.77	1.77	2.17	3.21	3.95	4.92	3.88	4.14	3.69	3.18
AVG-2	$\bar{x}$	38.28	70.36	8.04	30.91	5.72	1.56	4.73	0.68	3.57	0.69	1.89	0.27	1.67	0.25
Cambridge	σ	0.39	2.89	0.17	0.72	0.1	0.03	0.05	0.01	0.08	0.01	0.03	0	0.02	0
(3)	V	1.01	4.1	2.09	2.34	1.83	1.8	1.13	1.72	2.38	2.12	1.55	1.5	1.49	1.4
	x_r	38.28	70.36	8.04	30.91	5.72	1.56	4.73	0.68	3.57	0.69	1.89	0.27	1.67	0.25
	S	1	2.57	2.58	1.34	4.14	1.87	4.59	5.41	2.8	5.41	4.48	3.33	3.19	1.75

Table B.3: Precision and accuracy estimates for REE ICP-MS analysis. The numbers in brackets indicate the number of runs of each standard. $\bar{x}$ is the mean and σ is the standard deviation. The coefficient of variation is given by $V = 100\sigma/\bar{x}$. Reference values, x_r, are given by Govindaraju (1994). The accuracy is given by $S = 100(O - E)/E$, where O is the observed value and E is the reference value.

B.4 Solid Source Mass Spectrometry: Sr and Nd Isotope Analysis

A small subset of 12 samples were prepared for Sr and Nd isotope analysis at the University of Cambridge. The samples were prepared using a standard acid dissolution method described below. The precision of results for each sample is shown in table D.9, showing a negligible % error and, therefore, indicating that the results are very precise. Standard runs during 2006–2007 produce a precision of $0.710258 \pm 1.8e^{-5}$ for $^{87}Sr/^{86}Sr$ for NBS87 standard and $0.511120 \pm 1.4e^{-5}$ for $^{143}Nd/^{144}Nd$ for Johnson Mathey standard. Again the errors are negligible.

150 mg of dry rock powder was weighed into clean Teflon FEP vials with hex nuts. Approximately 0.5 ml of HNO_3 and 5 of HF were added to each sample. The Teflon vials were then placed into stainless steel pressure vessels (bombs) and placed in an oven at 180°C for 8 hours to allow digestion of the rock powder. Once cool, the vials were uncovered and placed under evaporators until the sample was completely dry. The bomb digestion was repeated twice with the addition of 5 ml of 6M HNO_3 for the first repeat and 5 ml of 6M HCl for the second repeat. A precisely weighed Sm-Nd spike was added to the solution before the final evaporation. The sample was evaporated to incipient dryness before 2 ml of 1M HCl was added. The solution was then transferred to the cation I column, where Sr was collected in 5 ml of 3M HCl. REE were also collected from the cation I column in 18 ml of 6M HCl. The REE solution was then transferred to the cation II column, where Sm and Nd were collected in 9.5 ml of 6M HCl. Sm and Nd were separated by the cation III column, where Nd is collected first in 4 ml of 0.3M HCl, followed by Sm in 4 ml of 0.66M HCl. The final solutions containing each of the cations were then evaporated until dry.

For loading Sr samples into the solid source mass spectrometer, single Ta filaments were used. The sample was taken up in 1M HCl, and 1μl loaded on to the filament. The sample was dried using a gradually increasing current, up to 2 A, before finally loading into the mass spectrometer for analysis. For loading Sm and Nd samples, a triple filament arrangement was used, with a central Re filament to provide the heat source and a Ta filament on either side for the sample. Nd and Sm samples were loaded in quartz-distilled water with 0.5μl aliquots on each Ta filament. These filaments were dried at 1 A before finally loading into the mass spectrometer.

Appendix C

Data Tables

Table C.1: Sample locations and descriptions for Skagi and Tröllaskagi samples. Letters in brackets in the description refer to Everts' (1975) stratigraphy, except for ep5 which is from Hjartarson's (2003) stratigraphy. Ages are from Garcia et al. (2003).

Sample	Longitude (°W)	Latitude (°N)	Location	Description	Age (Ma)
TSK01	19.41	66.06	Hrolleifshofdi	Quaternary lava	-
TSK02	19.37	66.07	Hrolleifshofdi	Tertiary/Quaternary lava	-
TSK03	19.43	65.9	Hofsos	Quaternary lava	-
TSK04	19.49	65.95	Thordarhofdi	Quaternary lava	-
TSK05	19.49	65.95	Thordarhofdi	Quaternary lava	-
SK01	20.27	65.66	Blonduos	Dyke, cuts Tertiary	-
SK02	20.27	65.66	Blonduos	Dyke, cuts Tertiary	-
SK03	19.86	65.83	Tindastoll	Composite cone sheet, cuts Tertiary	6.4?
SK04	19.86	65.83	Tindastoll	Composite cone sheet, cuts Tertiary	6.4?
SK05	19.93	65.96	Selnes	Dyke, cuts Tertiary	-
SK06	19.93	65.97	Selnes	Quaternary dyke	-
SK07	19.94	65.96	Selnes	Quaternary lava	-
SK08	19.93	65.98	Selnes	Tertiary lava	-
SK09	19.93	65.98	Selnes	Tertiary lava	-
SK10	19.93	65.98	Bergskali	Quaternary dyke	2.4
SK11	20.05	65.08	Husnes	Quaternary lava	-
SK12	20.12	65.96	Olvesvatn	Quaternary lava	-
SK13A	20.29	66.1	Selvik	Quaternary dyke	-
SK13B	20.29	66.1	Selvik	Quaternary dyke	-
SK14	20.28	66.1	Selvik	Quaternary lava	-
SK15	20.28	66.1	Selvik	Quaternary lava	-
SK16	20.32	65.83	Skagastrond	Basalt plug	-
SK17	20.29	65.83	Skagastrond	Gabbro sill	-
SK18	20.26	65.78	Hafursstadaa	Tertiary dyke	7.65?
SK19	20.25	65.78	Hafursstadaa	Tertiary dyke	7.65?
SK20	20.01	65.58	Solheimar	Tertiary dyke	3.5
SK21	19.57	65.57	Saemundarhlid	Tertiary dyke	-
SK22	19.69	65.81	Reykjastrond	Quaternary dyke	2.2
SK23	20.01	65.78	Nordurardalur	Tertiary lava	-
SK24	19.91	65.81	Laxardalur	Cone sheet/Dyke, cuts Tertiary	-
SK25	19.91	65.81	Laxardalur	Tertiary lava, cut by SK24	-
SK26	19.91	65.81	Laxardalur	Dyke/cone sheet, cuts Tertiary	-
SK27	19.91	65.81	Laxardalur	Dyke/cone sheet, cuts Tertiary	-
SK28	19.91	65.81	Laxardalur	Dyke/cone sheet, cuts Tertiary	-
SK29	19.91	65.81	Laxardalur	Dyke/cone sheet, cuts Tertiary	-
SK30	19.91	65.81	Laxardalur	Cone sheet, cuts Tertiary	-
SK31	19.78	65.78	Tindastoll	Hyaloclastite	-
SK32	19.81	65.78	Tindastoll	Dyke/cone sheet, cuts Tertiary	-
SK33	20.66	65.43	Vatnsnes	Quaternary lava	-
SK34	18.8	65.29	Austurdalur	Quaternary lava flow (ep5?)	-
SK35	18.79	65.29	Austurdalur	Quaternary lava flow (ep5?)	-
SK36	20.01	66.03	Ketubjorg	Quaternary volcanic vent (B2R)	-
SK37	20.27	66.1	Gotunuipur	Quaternary lava flow (B3R)	-
SK38	20.3	66.11	Dingrimuli	Quaternary lava flow (B3R)	-
SK39	20.4	66.09	Hafnahudir	Alk-Ol-Basalt Intrusion (Everts, 1975)	-
SK40	20.39	66.09	Hafnahudir	Alk-Ol-Basalt Intrusion (Everts, 1975)	-
SK41	19.94	65.96	Selnes	Tertiary lava	-
SK42	20.01	66.03	Ketubjorg	Quaternary lava flow (B0R)	-
SK43	20	66.03	Ketubjorg	Quaternary lava flow (B-1R)	-
SK44	19.99	66.02	Ketubjorg	Compositie dyke, cuts Tertiary	-
SK45	19.99	66.02	Ketubjorg	Compositie dyke, cuts Tertiary	-

Table C.2: Sample locations and descriptions for samples donated by A. Hjartarson and S. Garcia. Letters in brackets in the description refer to Hjartarson's (2003) stratigraphy. Ages are from Garcia et al. (2003) and Hjartarson (2003) in italics.

Sample	Longitude (°W)	Latitude (°N)	Location	Description	Age (Ma)
A17160	19.11	65.33	Vesturdalur	Quaternary lava (dd)	*1.48*
A17161	19.09	65.3	Vesturdalur	Quaternary dyke	-
A17162	19.09	65.3	Vesturdalur	Quaternary lava (dd)	*1.48*
A17164	19.09	65.3	Vesturdalur	Tertiary lava (me2)	-
A17168	19.06	65.32	Vesturdalur	Quaternary lava (dd)	*1.48*
A17176	18.46	65.12	Austurdalur	Quaternary lava (ep2)	*1.66*
A17178	18.43	65.1	Austurdalur	Quaternary lava (ep2)	*1.66*
00A1	17.61	65.79	-	Quaternary dyke	2.3
00A3	-	-	-	Dyke	-
00C1	-	-	-	Dyke	-
00C2	18.07	66	-	Tertiary dyke	8.9
00C10	18.06	66.09	Flateyjarskagi	Tertiary dyke	7.2
00C11	18.08	66.15	Flateyjarskagi	Tertiary dyke	8.1
00C12	18.08	66.15	Flateyjarskagi	Tertiary dyke	8.2
00D1	17.88	65.94	Flateyjarskagi	Tertiary dyke	5.5
00D3	17.87	66.03	Flateyjarskagi	Tertiary dyke	6.3
00D4	-	-	-	Dyke	-
00D5	17.93	66.15	Flateyjarskagi	Tertiary dyke	7.4
00D6	-	-	-	Dyke	-
00E4	18.56	65.98	Trollaskagi	Tertiary dyke	7.3
00E6	18.86	65.46	Trollaskagi	Tertiary dyke	6.6
00E9	19.04	65.37	Trollaskagi	Tertiary dyke	6.2
00F4	-	-	-	Dyke	-
00G3	20.57	65.43	-	Tertiary dyke	8.2
00G5	20.34	65.55	-	Tertiary dyke	7.6
00G7	20.85	65.61	Vatnsnes	Tertiary dyke	8.3
00J2	15.94	65.46	Kverkfjoll	Quaternary dyke	0.4
00J3	15.75	65.46	Kverkfjoll	Quaternary dyke	6?
00K4	14.84	65.35	-	Tertiary dyke	12.6
00K7	14.69	65.17	-	Tertiary dyke	8.1
00K9	-	-	-	Dyke	-

Table C.3: Major element data for Skagi and Tröllaskagi samples. All values are wt% oxides obtained by XRF analysis.

Sample	SiO_2	Al_2O_3	Fe_2O_{3T}	MgO	CaO	Na_2O	K_2O	TiO_2	MnO	P_2O_5
TSK01	48.66	12.61	16.8	5.12	9.27	2.69	0.52	3.64	0.25	0.44
TSK02	48.85	13.86	14.27	6.16	10.59	2.6	0.44	2.75	0.2	0.28
TSK03	49.06	13.53	14.48	6.31	10.83	2.36	0.37	2.55	0.23	0.28
TSK04	48.79	12.54	16.73	5.1	9.3	2.73	0.51	3.6	0.25	0.43
TSK05	48.2	12.74	16.31	5.62	9.83	2.64	0.55	3.48	0.24	0.39
SK01	46.49	13.42	17.23	5.35	10.15	2.48	0.3	3.76	0.33	0.49
SK02	47.66	11.76	17.9	4.9	9.93	2.21	0.48	4.31	0.3	0.56
SK03	49.99	12.52	16.81	5.11	8.97	2.47	0.63	2.93	0.24	0.32
SK04	49.78	12.57	17.02	4.98	9.32	2.29	0.5	2.96	0.26	0.33
SK05	47.49	13.2	15.41	6.98	10.96	2.54	0.2	2.74	0.21	0.27
SK06	48.63	12.6	16.67	4.85	9.08	2.91	0.71	3.77	0.25	0.53
SK07	48.42	13.48	14.51	6.76	11.4	2.38	0.25	2.35	0.23	0.22
SK08	51.19	13.13	15.21	4.95	8.98	2.91	0.62	2.49	0.22	0.3
SK09	49.53	13.89	13.41	6.17	11.23	2.59	0.23	2.42	0.28	0.26
SK10	47.27	13.31	15.74	7.62	10.51	2.22	0.13	2.73	0.25	0.23
SK11	47.83	12.85	15.89	6.26	10.63	2.55	0.36	3.07	0.24	0.32
SK12	48.82	13.08	15.64	5.82	10.21	2.56	0.45	2.85	0.24	0.33
SK13A	48.92	12.74	15.98	5.52	10.08	2.49	0.46	3.1	0.25	0.46
SK13B	48.65	13.41	14.76	6.4	10.69	2.38	0.39	2.74	0.23	0.35
SK14	48.19	13.01	15.61	6.17	10.58	2.41	0.4	3.06	0.24	0.33
SK15	48.1	13.72	14.23	6.99	11.56	2.38	0.25	2.32	0.22	0.22
SK16	45.93	11.68	20	5.24	9.58	2.41	0.27	4.09	0.32	0.48
SK17	47.83	10.95	19.39	4.26	9.04	2.5	0.57	4.52	0.3	0.65
SK18	48.46	12.38	17.41	4.73	9.73	2.19	0.63	3.67	0.32	0.47
SK19	44.36	12.02	19.58	5.4	11.5	1.8	0.08	4.36	0.33	0.56
SK20	76.42	12.66	2.3	0.15	0.71	4.32	3.24	0.16	0.03	0.02
SK21	48.55	13.67	14.55	6.86	11.27	2.27	0.08	2.26	0.22	0.27
SK22	48.29	13.01	16.37	5.5	10.65	2.36	0.28	2.93	0.28	0.33
SK23	52.37	12.7	15.55	3.89	7.97	2.68	1.07	2.88	0.26	0.63
SK24	48.12	16.41	11.11	6.91	13.64	1.68	0.31	1.54	0.17	0.1
SK25	53.96	14.16	12.99	4.25	7.16	3.65	1.16	2.27	0.19	0.23
SK26	49.1	12.98	15.83	5.67	10.72	2.07	0.34	2.76	0.26	0.26
SK27	49.17	12.93	15.61	5.78	10.8	2.08	0.46	2.67	0.25	0.26
SK28	48.71	18.96	9.87	5.07	12.43	2.26	0.94	1.52	0.15	0.1
SK29	48.95	13.1	15.61	5.89	10.86	2.18	0.37	2.55	0.24	0.25
SK30	48.23	15.95	11.15	7.3	13.8	1.5	0.21	1.6	0.18	0.09
SK32	48.47	12.32	17.88	4.86	9.27	2.29	0.31	3.77	0.29	0.53
SK33	48.28	12.04	17.84	4.96	9.09	2.67	0.55	3.89	0.26	0.42
SK34	48.57	14.43	13.41	7.04	11.63	2.17	0.24	2.15	0.2	0.16
SK35	48.48	13.86	14.08	7.01	11.41	2.15	0.28	2.35	0.21	0.18
SK36	47.96	12.71	16.01	6.15	10.72	2.3	0.41	3.19	0.24	0.32
SK37	48.73	12.95	15.55	6.18	10.42	2.41	0.37	2.85	0.23	0.31
SK38	48.82	12.97	15.64	6.1	10.33	2.33	0.39	2.87	0.23	0.32
SK39	48.21	12.42	17.19	5.28	9.48	2.63	0.47	3.65	0.26	0.41
SK40	48.29	12.7	16.77	5.46	9.66	2.46	0.5	3.56	0.25	0.36
SK41	51.85	12.66	16.14	4.14	7.88	2.98	0.62	3.02	0.28	0.43
SK42	49.95	12.83	15.39	5.35	9.33	2.61	0.61	3.3	0.24	0.39
SK43	48.91	13.09	15.3	5.93	10.11	2.48	0.49	3.11	0.23	0.35
SK44	47.83	14.75	12.74	8.56	11.75	2.11	0.11	1.82	0.18	0.16
SK45	47.54	13.47	15.59	7.39	10.52	2.36	0.2	2.5	0.23	0.2

Table C.4: Major element data for samples donated by A. Hjartarson and S. Garcia. All values are wt% oxides obtained by XRF analysis.

Sample	SiO_2	Al_2O_3	Fe_2O_{3T}	MgO	CaO	Na_2O	K_2O	TiO_2	MnO	P_2O_5
A17160	49.24	12.46	16.61	4.72	8.82	2.68	0.75	3.82	0.27	0.61
A17161	51.7	14.4	12.51	5.72	10.18	2.49	0.6	1.93	0.2	0.27
A17162	48.29	15.93	12.67	7.34	11.71	1.86	0.09	1.8	0.19	0.13
A17164	49.19	13.22	16.06	4.94	9.01	3	0.47	3.5	0.21	0.41
A17168	48.11	18.24	12.15	5.23	11.21	2.54	0.25	1.94	0.17	0.15
A17176	48.25	13	16.96	5.29	9.08	2.69	0.65	3.49	0.24	0.34
A17178	48.19	13.07	16.98	5.32	9.13	2.59	0.63	3.52	0.24	0.34
00A1	47.51	13.34	15.56	6.75	10.94	2.25	0.33	2.78	0.23	0.31
00A3	49.4	13.6	13.96	6.49	11.55	2.29	0.09	2.2	0.22	0.2
00C1	50.21	13.11	15.34	4.89	9.21	2.51	0.56	3.52	0.21	0.45
00C2	74.72	12.34	4.25	0.3	1.27	4.65	2	0.32	0.09	0.05
00C10	49.4	13.43	13.89	6.36	10.64	2.47	0.25	3	0.21	0.34
00C11	48.86	12.39	16.2	4.93	9.18	2.71	0.86	4.08	0.23	0.56
00C12	48.3	13.64	15.68	5.15	9.93	3.08	0.55	3.12	0.21	0.33
00D1	47.8	14.06	13.9	7.31	11.67	2.2	0.33	2.34	0.18	0.23
00D3	48.85	14.52	13.45	6.12	11.32	2.38	0.36	2.5	0.2	0.29
00D4	48.96	13.52	14.6	6.53	10.85	2.27	0.19	2.56	0.22	0.29
00D5	48.84	13.8	13.54	6.66	10.88	2.59	0.5	2.65	0.2	0.33
00D6	48.92	13.87	13.61	6.9	10.51	2.6	0.6	2.5	0.2	0.29
00E4	49.3	13.12	15.09	5.81	10.16	2.56	0.52	2.92	0.22	0.32
00E6	48.73	13.21	16.35	4.87	9.29	2.97	0.49	3.39	0.26	0.44
00E9	51.43	13.48	14.43	4.38	8.48	3.2	0.83	3.06	0.23	0.5
00F4	51.15	12.91	15.48	4.23	8.34	2.99	0.84	3.25	0.25	0.57
00G3	48.42	12.6	16.42	4.92	9.25	2.86	0.91	3.9	0.25	0.46
00G5	52.42	11.87	18.05	2.62	7.7	2.99	0.43	2.4	0.32	1.2
00G7	48.54	12.63	16.68	5.18	9.47	2.76	0.56	3.45	0.26	0.47
00J2	49.35	13.2	15.65	5.17	9.42	2.72	0.66	3.25	0.23	0.36
00J3	49.82	13.35	15.08	5.39	9.78	2.75	0.59	2.71	0.22	0.32
00K4	48.57	12.75	16.21	5.12	9.59	2.95	0.45	3.58	0.26	0.51
00K7	49	13.06	15.83	5.36	9.85	2.8	0.43	3.06	0.23	0.39
00K9	49.33	13.08	16.27	5.1	9.49	2.71	0.61	2.73	0.25	0.42

Table C.5: Trace element data for Skagi and Tröllaskagi samples. All values are in ppm, obtained by XRF analysis.

Sample	Nb	Zr	Y	Sr	Rb	Zn	Cu	Ni	Cr	V	Ba	Sc
TSK01	33.0	249.8	49.8	261.8	9.5	142.9	91.0	34.0	26.9	430.7	147.6	39.4
TSK02	18.6	165.1	35.4	272.9	5.3	122.3	134.2	68.9	53.6	400.8	95.5	41.8
TSK03	20.6	168.2	38.4	191.4	6.7	125.5	145.0	65.7	118.5	419.4	95.0	45.2
TSK04	33.3	249.8	50.2	256.3	10.4	154.1	110.4	39.3	35.4	451.2	135.2	43.5
TSK05	31.8	231.2	45.4	238.8	10.9	139.9	132.3	55.1	69.0	469.8	145.3	43.4
SK01	33.0	240.2	55.4	234.9	3.5	173.0	218.3	53.9	35.3	531.9	78.9	48.9
SK02	32.2	298.6	73.4	187.2	10.4	193.9	349.6	77.1	95.2	516.7	105.2	52.3
SK03	23.9	198.3	45.3	258.2	13.3	136.6	124.8	32.1	25.8	472.7	134.3	42.4
SK04	24.9	205.3	47.4	210.0	6.8	140.0	137.1	33.1	24.8	478.1	95.5	42.0
SK05	15.0	146.5	40.9	180.0	3.0	128.9	208.3	82.2	238.8	458.8	58.8	50.2
SK06	41.6	290.8	53.2	270.5	13.4	160.1	81.1	23.5	0.5	422.2	160.4	39.7
SK07	14.7	137.0	35.9	202.1	3.4	114.3	137.9	66.6	194.9	417.5	64.7	50.7
SK08	23.8	198.3	42.1	225.0	13.9	134.8	111.5	33.6	1.4	399.3	118.4	42.3
SK09	18.8	146.2	35.5	246.7	2.6	122.4	102.8	49.3	25.4	425.2	122.0	47.5
SK10	12.4	123.3	34.5	162.7	1.2	127.0	210.2	96.2	228.9	458.8	45.9	48.9
SK11	23.4	199.5	44.8	229.9	6.6	127.9	210.1	62.4	118.8	472.2	96.2	49.1
SK12	25.8	194.0	44.7	220.4	8.6	123.3	103.5	52.1	72.0	440.9	131.8	47.2
SK13A	30.1	258.0	59.2	212.7	9.0	152.9	210.9	65.4	108.5	425.2	119.3	46.6
SK13B	22.8	197.6	46.5	206.9	7.2	132.1	146.0	83.8	179.9	422.4	92.8	47.8
SK14	23.6	200.9	44.7	229.7	6.7	131.3	201.0	65.7	118.8	468.8	99.3	46.8
SK15	15.0	138.9	35.5	211.5	3.8	103.7	118.6	68.3	168.9	366.2	72.1	48.0
SK16	28.2	266.4	66.3	207.2	4.4	187.5	345.0	56.5	18.1	545.3	91.1	52.9
SK17	45.1	433.3	103.9	205.4	10.3	209.6	365.1	39.5	0.0	353.6	157.8	50.4
SK18	32.5	250.2	58.0	215.1	10.7	169.6	157.3	35.3	4.0	492.4	138.7	46.2
SK19	32.7	298.9	72.4	175.2	0.5	183.2	347.8	73.1	101.5	536.3	54.0	51.8
SK20	70.5	490.5	102.3	52.9	71.8	122.2	11.8	0.0	0.0	0.0	434.5	2.8
SK21	13.4	143.6	38.6	192.2	0.6	116.5	224.9	76.2	101.4	414.7	45.9	43.3
SK22	18.7	172.5	47.3	203.7	4.9	143.0	244.6	57.0	46.5	501.9	59.6	50.0
SK23	39.5	318.7	70.9	215.6	21.6	153.2	47.5	12.4	4.6	238.1	199.3	34.5
SK24	9.2	75.5	20.6	232.3	6.5	84.3	128.9	71.4	153.0	293.2	49.2	40.3
SK25	17.5	193.4	37.3	312.5	22.5	116.8	172.9	31.6	8.5	364.0	165.2	30.7
SK26	22.7	177.0	40.9	206.3	5.4	131.5	161.6	44.7	18.1	458.9	78.7	42.1
SK27	21.9	174.0	40.9	207.3	7.5	124.9	154.9	46.4	31.4	438.6	80.1	42.2
SK28	9.5	74.4	19.0	379.3	24.1	80.1	119.3	47.3	70.2	268.4	141.6	30.9
SK29	20.9	166.8	39.4	204.7	5.4	116.9	153.9	47.8	26.3	420.7	73.8	44.3
SK30	8.5	69.5	18.8	200.5	4.7	83.2	148.3	72.4	150.9	304.0	44.0	39.2
SK32	27.8	267.0	68.5	218.2	3.8	176.0	50.1	14.8	3.7	373.6	112.9	43.7
SK33	32.6	277.2	54.3	278.4	10.1	149.9	95.0	21.1	0.1	454.2	145.4	41.0
SK34	14.8	121.7	27.7	236.0	4.1	105.6	156.5	76.0	119.5	378.0	67.0	42.1
SK35	16.1	134.1	30.3	234.0	4.5	109.8	140.7	72.7	109.5	398.3	75.2	42.9
SK36	24.6	215.8	48.1	230.0	7.3	126.8	215.3	58.2	106.5	460.5	103.1	45.9
SK37	22.1	207.5	49.2	198.9	7.2	122.0	87.6	57.9	116.3	424.4	102.5	45.0
SK38	22.6	210.5	49.9	198.3	7.8	122.2	63.8	57.5	112.1	415.3	103.0	45.6
SK39	28.5	248.9	52.7	227.3	8.8	141.2	94.1	39.1	41.0	500.7	143.0	44.8
SK40	26.2	230.3	50.4	229.5	9.7	131.3	80.2	36.6	31.0	501.9	125.8	39.2
SK41	39.2	382.6	69.3	223.8	7.3	154.4	69.8	13.7	2.5	298.6	180.2	38.2
SK42	34.4	291.7	57.8	231.4	11.9	139.7	111.4	44.5	71.8	378.7	167.5	40.8
SK43	28.6	236.9	48.6	236.5	8.6	136.0	130.5	53.8	103.4	405.6	126.1	43.7
SK44	11.9	105.8	29.2	203.1	0.9	103.4	162.1	151.6	361.6	313.1	48.7	38.7
SK45	12.6	132.9	39.3	177.4	2.0	124.6	193.2	98.5	184.6	416.6	58.4	45.6

Table C.6: Trace element data for samples donated by A. Hjartarson and S. Garcia. All values are in ppm, obtained by XRF analysis.

Sample	Nb	Zr	Y	Sr	Rb	Zn	Cu	Ni	Cr	V	Ba	Sc
A17160	36.9	335.0	65.6	254.1	16.4	144.2	73.5	15.8	13.2	297.4	184.4	39.5
A17161	21.9	204.2	48.9	189.1	12.3	116.1	146.8	59.5	104.7	331.8	125.9	35.1
A17162	9.8	99.3	21.4	235.2	0.7	98.7	114.5	148.1	76.2	293.1	35.4	36.7
A17164	26.7	232.3	47.2	292.9	4.5	139.7	147.7	25.3	3.7	441.6	144.7	39.0
A17168	11.6	117.4	24.2	315.3	3.2	90.3	190.2	49.3	10.5	254.2	60.6	28.7
A17176	27.1	249.6	49.4	263.5	14.0	135.3	185.8	39.1	23.8	406.0	154.5	38.2
A17178	26.9	247.1	49.0	264.1	13.2	133.6	185.3	42.4	25.6	401.3	151.7	38.0
00A1	19.9	180.2	40.7	238.1	5.9	114.3	163.7	69.0	185.5	397.0	110.7	44.8
00A3	11.1	118.2	35.5	174.8	1.0	110.5	183.7	61.7	42.3	381.8	43.9	42.6
00C1	27.4	260.1	50.9	267.5	9.2	117.4	182.6	25.8	7.0	349.4	136.7	30.1
00C2	44.2	536.6	86.5	126.8	44.7	126.3	17.2	0.0	0.0	0.0	333.0	12.1
00C10	23.2	212.4	41.2	278.5	4.3	127.0	173.0	74.3	150.7	358.8	108.6	33.0
00C11	39.0	332.5	59.6	272.5	19.1	152.2	257.5	54.2	80.8	406.6	181.7	34.8
00C12	24.3	210.7	41.6	285.2	9.7	127.3	140.5	38.8	27.3	395.1	142.4	31.4
00D1	13.3	126.8	29.4	256.6	4.7	94.1	142.2	85.9	142.9	330.9	74.4	34.5
00D3	16.7	168.1	35.5	285.9	6.5	99.5	147.2	66.0	71.3	319.2	95.8	32.9
00D4	17.9	165.8	42.8	188.8	8.6	111.2	165.8	73.0	102.4	370.4	70.8	36.9
00D5	20.1	184.1	36.4	285.3	7.3	101.5	148.2	71.9	107.3	331.0	104.0	37.1
00D6	19.6	161.9	34.2	279.4	11.4	91.5	148.0	103.5	183.2	302.0	114.8	33.9
00E4	21.7	202.6	41.3	262.3	9.5	119.1	133.7	49.9	56.7	389.3	114.4	34.5
00E6	26.8	234.5	47.0	301.5	8.6	134.7	127.6	25.9	4.3	410.5	144.7	34.6
00E9	35.9	310.8	60.3	277.5	23.4	122.1	83.8	25.0	14.5	338.3	196.0	32.0
00F4	42.2	327.7	67.0	240.7	23.4	151.7	77.8	14.7	0.0	335.5	193.9	32.3
00G3	36.8	228.0	45.9	325.3	15.6	151.7	51.8	11.7	0.0	385.2	196.9	37.1
00G5	54.3	546.2	134.6	215.5	15.6	222.8	36.5	5.5	0.4	24.6	241.1	33.0
00G7	30.7	242.2	51.6	275.2	10.5	137.9	99.9	31.1	29.6	394.2	133.4	37.3
00J2	24.4	213.6	39.7	246.5	13.1	126.6	100.1	28.6	30.2	444.2	133.8	41.3
00J3	24.4	204.2	38.9	244.0	12.0	128.1	141.0	33.3	20.1	394.4	130.0	41.4
00K4	30.4	258.4	56.6	292.8	10.5	156.0	97.8	31.0	28.7	426.5	176.8	40.7
00K7	21.3	217.9	49.2	268.6	6.2	127.0	147.5	38.3	36.4	373.8	126.6	35.9
00K9	21.7	198.8	54.0	233.0	11.2	134.6	105.9	40.1	39.8	430.3	157.9	38.3

Table C.7: Rare Earth Element data for Skagi and Tröllaskagi samples. All values are in ppm, obtained by ICP-MS at the Scottish Universities Research Centre.

Sample	La	Ce	Pr	Nd	Sm	Eu	Gd	Tb	Dy	Ho	Er	Tm	Yb	Lu
TSK01	21.009	51.310	7.013	32.294	8.144	2.620	8.904	1.426	8.571	1.674	4.701	0.701	4.212	0.626
TSK02	14.256	34.613	4.756	22.024	5.853	1.946	6.503	1.052	6.353	1.233	3.406	0.509	3.001	0.446
TSK03	14.409	35.008	4.757	21.852	5.639	1.780	6.302	1.035	6.419	1.271	3.679	0.561	3.336	0.497
TSK04	22.391	54.074	7.351	33.751	8.384	2.681	9.129	1.442	8.784	1.705	4.771	0.727	4.236	0.628
TSK05	21.226	50.410	6.774	30.613	7.501	2.394	8.100	1.282	7.783	1.506	4.226	0.660	3.822	0.565
SK01	24.144	55.448	7.370	33.600	8.322	2.646	9.271	1.492	9.174	1.808	5.221	0.796	4.739	0.709
SK02	22.555	56.417	8.025	38.187	10.233	3.167	11.717	1.937	12.209	2.424	6.976	1.077	6.446	0.954
SK03	18.013	42.592	5.749	26.187	6.771	2.090	7.535	1.239	7.699	1.537	4.426	0.676	4.040	0.604
SK04	17.939	42.620	5.788	26.197	6.806	2.025	7.577	1.250	7.691	1.540	4.439	0.677	4.055	0.604
SK05	10.080	25.930	3.821	18.635	5.326	1.791	6.262	1.049	6.633	1.351	3.911	0.599	3.652	0.548
SK06	26.752	64.009	8.588	38.101	9.314	2.831	9.716	1.520	9.121	1.757	5.007	0.756	4.446	0.656
SK07	10.082	25.712	3.685	17.707	4.920	1.673	5.718	0.939	5.930	1.186	3.401	0.523	3.080	0.460
SK08	17.832	41.121	5.499	24.359	6.203	1.946	6.866	1.110	6.851	1.373	3.931	0.598	3.615	0.538
SK09	13.443	31.965	4.395	20.035	5.218	1.750	5.940	0.972	5.985	1.196	3.426	0.523	3.157	0.469
SK10	8.145	21.094	3.108	15.203	4.366	1.524	5.247	0.885	5.584	1.130	3.284	0.502	3.042	0.447
SK11	16.723	41.138	5.759	26.643	7.015	2.247	7.822	1.267	7.749	1.525	4.413	0.667	3.974	0.580
SK12	17.300	41.376	5.594	25.227	6.486	2.050	7.235	1.184	7.356	1.464	4.269	0.645	3.878	0.585
SK13A	20.231	49.830	6.874	31.723	8.325	2.521	9.404	1.509	9.388	1.864	5.420	0.818	4.922	0.731
SK13B	15.550	38.674	5.376	24.926	6.646	2.078	7.549	1.233	7.689	1.541	4.442	0.673	4.076	0.606
SK14	16.392	40.539	5.688	26.058	6.816	2.193	7.683	1.243	7.684	1.511	4.312	0.652	3.835	0.570
SK15	10.947	27.182	3.816	18.064	4.963	1.661	5.637	0.941	5.896	1.167	3.358	0.508	3.027	0.453
SK16	19.597	49.567	7.108	33.882	9.343	2.951	10.755	1.739	11.126	2.227	6.440	0.980	5.935	0.880
SK17	33.598	81.452	11.274	52.654	13.856	4.063	15.962	2.624	16.366	3.315	9.572	1.476	9.008	1.357
SK18	22.534	53.651	7.295	33.534	8.617	2.702	10.064	1.586	9.762	1.942	5.561	0.866	5.161	0.764
SK19	21.283	53.593	7.674	36.535	9.885	3.096	11.519	1.887	11.772	2.357	6.801	1.048	6.260	0.952
SK20	75.106	157.777	18.773	75.248	16.929	2.747	17.281	2.815	16.914	3.278	9.457	1.507	9.262	1.368
SK21	10.110	25.631	3.672	17.735	5.006	1.633	5.901	0.981	6.257	1.246	3.661	0.562	3.358	0.507
SK22	12.970	31.998	4.596	22.129	6.131	2.048	7.398	1.221	7.736	1.541	4.509	0.703	4.168	0.620

Table C.8: Rare Earth Element data continued for Skagi and Tröllaskagi and donated samples from Austurdalur and Vesturdalur (A. Hjartarson). All values are in ppm, obtained by ICP-MS at the University of Cambridge.

Sample	La	Ce	Pr	Nd	Sm	Eu	Gd	Tb	Dy	Ho	Er	Tm	Yb	Lu
SK23	31.828	71.835	9.664	44.481	11.201	3.233	12.312	1.999	12.307	2.506	6.893	1.013	6.251	0.912
SK25	20.951	43.973	5.440	24.297	6.034	1.902	6.450	1.059	6.579	1.342	3.739	0.553	3.448	0.504
SK32	20.114	48.243	6.961	33.881	9.399	3.175	10.830	1.829	11.835	2.414	6.646	0.994	6.145	0.904
SK33	23.404	54.232	7.473	35.562	9.031	2.922	9.788	1.579	9.459	1.901	5.141	0.746	4.579	0.659
SK34	10.491	24.349	3.417	16.495	4.381	1.509	4.844	0.794	4.902	0.981	2.679	0.390	2.397	0.344
SK35	11.052	26.162	3.655	17.306	4.673	1.593	5.075	0.843	5.163	1.052	2.855	0.416	2.572	0.366
SK36	17.326	40.585	5.723	27.497	7.418	2.355	8.169	1.348	8.109	1.660	4.559	0.664	4.066	0.586
SK37	15.702	37.699	5.234	25.129	6.892	2.202	7.748	1.298	8.113	1.670	4.615	0.692	4.254	0.621
SK38	15.732	37.505	5.259	25.383	6.778	2.221	7.837	1.315	8.224	1.695	4.684	0.698	4.348	0.633
SK39	19.183	47.326	6.397	30.709	8.158	2.703	9.051	1.500	9.213	1.874	5.116	0.757	4.647	0.673
SK40	19.097	44.307	6.172	29.009	7.737	2.540	8.450	1.396	8.806	1.764	4.798	0.705	4.310	0.627
SK41	30.066	67.481	9.063	40.951	10.590	3.123	11.326	1.896	11.825	2.442	6.835	1.015	6.239	0.924
SK42	25.177	58.050	7.713	36.106	9.272	2.804	9.795	1.625	10.039	2.007	5.534	0.823	5.020	0.728
SK43	20.359	47.334	6.458	30.301	7.798	2.485	8.443	1.383	8.508	1.705	4.652	0.683	4.184	0.606
SK44	8.693	20.786	3.054	14.833	4.195	1.474	4.677	0.807	5.199	1.059	2.924	0.435	2.692	0.390
A17160	29.966	69.107	9.550	44.056	11.509	3.513	12.035	1.935	11.550	2.330	6.252	0.901	5.464	0.792
A17161	17.643	42.443	5.645	26.555	7.008	2.131	7.727	1.317	8.270	1.683	4.692	0.694	4.277	0.623
A17162	7.999	20.214	2.889	13.871	3.814	1.359	4.062	0.671	4.041	0.809	2.154	0.309	1.855	0.265
A17176	22.087	52.598	7.162	33.454	8.615	2.739	9.022	1.491	8.965	1.780	4.813	0.690	4.165	0.602

Table C.9: $^{87}Sr/^{86}$ and $^{143}Nd/^{144}Nd$ values for Skagi and Tröllaskagi samples, obtained by mass spectrometry.

Sample	$^{87}Sr/^{86}Sr$	$2\sigma x10^{-6}$	% Error	$^{143}Nd/^{144}Nd$	$2\sigma x10^{-6}$	% Error	ϵ_{Nd}
TSK04	0.703187	15	0.0011	0.513034	4	0.0004	7.72
SK06	0.703613	10	0.0007	0.513010	6	0.0006	7.26
SK09	0.703565	11	0.0008	0.513024	6	0.0006	7.53
SK12	0.703152	10	0.0007	0.513054	10	0.0010	8.11
SK13B	0.703289	10	0.0007	0.513038	6	0.0006	7.80
SK33	0.703185	15	0.0011	0.513032	7	0.0007	7.69
SK34	0.703187	11	0.0008	0.513017	7	0.0007	7.39
SK36	0.703241	10	0.0007	0.513028	12	0.0012	7.61
SK37	0.703232	11	0.0008	0.513034	4	0.0004	7.72
SK38	0.703254	14	0.0010	0.513039	5	0.0005	7.82
SK41	0.703281	10	0.0007	0.513034	4	0.0004	7.72
SK42	0.703317	10	0.0007	0.513015	6	0.0006	7.35

Table C.10: Compilation of published data from across Iceland containing major element, trace element, REE element and isotope data. This is an electronic appendix and can be viewed using the CD inside the back cover of this dissertation.

Appendix D

Additional Model Theory

This appendix provides additional information for chapter 6. The half-space cooling model and control volume formulation method are described in sections D1 and D2. The final section presents the definition of the Lagrangian derivative.

D.1 Half-Space Cooling Model

The half-space cooling model is an alternative method for calculating appropriate starting temperature conditions for modelling spreading rate changes to an established (steady-state) rift. The temperature is calculated using

$$T_S = T_B \text{erf}\left(\frac{z}{2\sqrt{\kappa t}}\right) . \tag{D.1}$$

This starting temperature would provide a faster approach for complex rift jump calculations where steady-state starting conditions are required. However, at present an equivalent method for estimating the depletion of the mantle residue has not been developed so the half-space is not employed in the new model.

D.2 Control Volume Formulation Method

A control volume method is used to calculate the value of dependent variables which are subject to advection and/or conduction. In the new model presented in chapter

6, the method used is based directly on work by Patankhar (1980) and applied to temperature and mantle residue depletion as a mass fraction. The method is based on solving a series of discretization equations which describe the flux of a variable in and out of each grid square so that the flux across each grid square boundary throughout the whole grid is consistent to a specified tolerance level.

The new model employs a node-centred grid and figure D.1 shows how the node and control volume geometry is set up. Each node is centered on a grid square or control volume, with a special conditions for boundary nodes. The calculation is then based on the flux of the dependent variables in and out of the control volume; the behaviour of the dependent variable is defined by a partial differential equation. The value of a dependent variable at any grid node depends on the advection and diffusion in and out of the relevant grid square and the amount created or destroyed within the grid square, during a specified time step. The value at the central node in a control volume is assumed to prevail over the whole volume, otherwise known as stepwise profile. A series of discretization equations are obtained from the partial differential equation according to the methods prescribed in Patankhar (1980). The discretization equations are then solved iteratively until the fluxes are internally consistent across the whole grid.

This method is more complex and more computationally intensive than the standard finite differencing schemes used to calculate advection and diffusion. However, it is useful because the method is implicit and therefore gives more accurate results for larger time steps compared to finite differencing. The control volume method is also more versatile, allowing variations in the geometry of the calculation domain, including the introduction of a finer grid size only where it is needed to improve the calculation.

One disadvantage for all discrete methods is that they automatically introduces diffusion on the scale of the grid size because the value of the central node in each grid square is assumed to prevail over the whole square; the step-wise profile. The grid size and the time step control the amount of error introduced by artificial diffusion. The grid size of 0.5 km and time step of 0.1 Ma used in the model application produce a very small error of 3%.

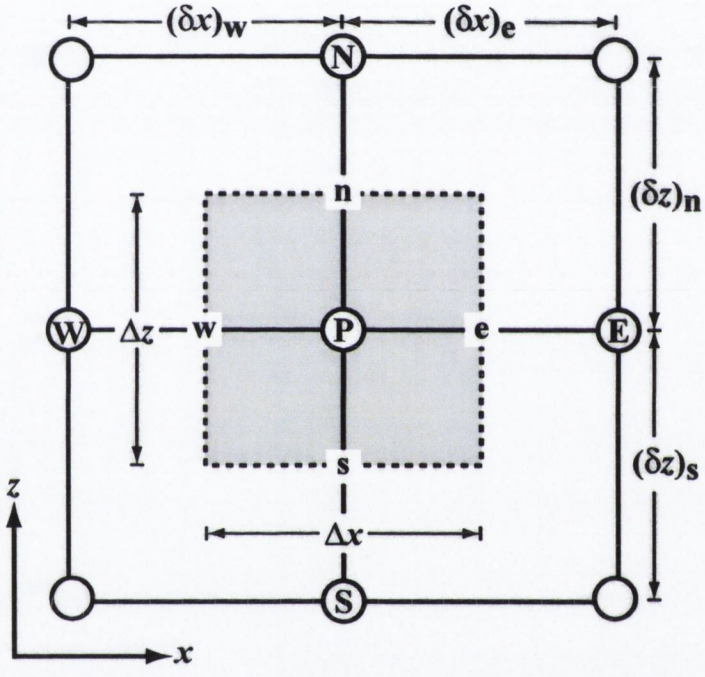

Figure D.1: The control volume grid set up, based on Patankhar (1980). The shaded region defines the control volume for a central node P. Adjacent nodes are labelled according to their location with respect to the central node i.e. N(North), S(South), E(East) and W(West). The control volume interfaces are labelled accordingly with small n, s ,e and w. The value of the dependent variable at node P is related to the adjacent node values by a series of discretization equations.

D.2.1 General Features of the Control Volume Method

The general form of a partial differential equation is defined as

$$\frac{\partial}{\partial t}(\rho\phi) + \frac{\partial J_x}{\partial x} + \frac{\partial J_z}{\partial z} = S \tag{D.2}$$

where ϕ is the dependent variable, S is the source term and J_x and J_y are fluxes defined by

$$J_x \equiv \rho v_x \phi - \Gamma \frac{\partial \phi}{\partial x} \tag{D.3}$$

and

$$J_z \equiv \rho v_z \phi - \Gamma \frac{\partial \phi}{\partial z} \,. \tag{D.4}$$

Γ is the diffusion coefficient and ρ is the density. The source term is related to the generation (or destruction) of the dependent variable. The source term is often dependent on the dependent variable, as is the case for temperature, and therefore must be expressed as a linear function

$$S = S_C + S_P \phi_P \tag{D.5}$$

where S_C is the constant part of the source term and S_P is the variable source coefficient at the central node P in the control volume. The discretization equations are obtained by integrating over the control volume and time and simplified using various substitutions to give

$$a_P \phi_P = a_E \phi_E + a_W \phi_W + a_N \phi_N + a_S \phi_S + b \tag{D.6}$$

where a_E, a_W, a_N, a_S and a_P are the coefficients for the neighbouring and central nodes. a_S is the coefficient of the source term and b is a constant term. The coefficients and constant terms are given as

$$a_E = D_e A\left(|P_e|\right) + [\![-F_e, 0]\!] \,, \tag{D.7}$$

$$a_W = D_w A\left(|P_w|\right) + [\![F_w, 0]\!] \,, \tag{D.8}$$

$$a_N = D_n A\left(|P_n|\right) + [\![-F_n, 0]\!] \,, \tag{D.9}$$

$$a_S = D_s A\left(|P_s|\right) + [\![F_s, 0]\!] \,, \tag{D.10}$$

$$a_P^0 = \frac{\rho_P^0 \Delta x \Delta z}{\Delta t} \,, \tag{D.11}$$

$$b = S_C \Delta x \Delta z + a_P^0 \phi_P^0 \,, \tag{D.12}$$

and

$$a_P = a_E + a_W + a_N + a_S + a_P^0 - S_P \Delta x \Delta z \,. \tag{D.13}$$

F_e, F_w, F_n and F_s are the mass flow rates through the faces of the control volume. The flow rate, ρv, is assumed to prevail over the whole face so that the mass flow rate through the whole face can be defined for each face as

$$F_e = (\rho v_x)_e \, \Delta z \,, \tag{D.14}$$

$$F_w = (\rho v_x)_w \, \Delta z \,, \tag{D.15}$$

$$F_n = (\rho v_z)_n \, \Delta x \,, \tag{D.16}$$

and

$$F_s = (\rho v_z)_s \, \Delta x \,. \tag{D.17}$$

D_e, D_w, D_n and D_s are diffusion conductances defined by

$$D_e = \frac{\Gamma_e \Delta y}{(\delta x)_e} \,, \tag{D.18}$$

$$D_w = \frac{\Gamma_w \Delta y}{(\delta x)_w} \,, \tag{D.19}$$

$$D_n = \frac{\Gamma_n \Delta x}{(\delta z)_n} \,, \tag{D.20}$$

and

$$D_s = \frac{\Gamma_s \Delta x}{(\delta z)_s} \,. \tag{D.21}$$

The power-law scheme is chosen to define the function $A|P|$ because of its closeness to the exact solution for different Peclet numbers and it is the recommended choice by Patankhar (1980). The function $A|P|$ is therefore given by

$$A(|P|) = [\![0, (1 - 0.1|P|)^5]\!] \tag{D.22}$$

where P is the Peclet number. The Peclet number represents the ratio of the strengths of convection and diffusion and can be defined for each node as

$$P_e = \frac{F_e}{D_e}\,, \tag{D.23}$$

$$P_w = \frac{F_w}{D_w}\,, \tag{D.24}$$

$$P_n = \frac{F_n}{D_n}\,, \tag{D.25}$$

and

$$P_s = \frac{F_s}{D_s}\,, \tag{D.26}$$

where $D_{e,w,n,s}$ and $F_{e,w,n,s}$ are defined by equations D.18 to D.21 and D.23 to D.26. Complete details of derivation of the general discretization equations are given in Patankhar (1980) in chapters 3, 4 and 5. The discretization equations are solved using a tridiagonal matrix algorithm on alternate horizontal and vertical passes across the grid with a specified tolerance level for convergence. Note: the code for the control volume method was written by Dr. Stephen Jones.

D.2.2 Application to Temperature

The general form of the differential equation with temperature, T, as the dependent variable is

$$\frac{\partial}{\partial t}(\rho T) + \frac{\partial}{\partial x}\left(\rho v_x T - \frac{\partial T}{\partial x}\right) + \frac{\partial}{\partial z}\left(\rho v_z T - \frac{\partial T}{\partial z}\right) = -v_z \rho h\,. \tag{D.27}$$

The diffusion coefficient, Γ, required for the discretization equations, is defined as

$$\Gamma = \kappa\rho \equiv \frac{k}{C_p} \tag{D.28}$$

where k is the thermal conductivity. The source term, related to the generation/destruction

of temperature (heat energy) at any node is governed by the adiabatic temperature gradient. There is no constant term in the source ($S_C = 0$) and S_P is defined as

$$S_P = \frac{-v_z \rho h}{T_P} \tag{D.29}$$

where T_P is the temperature at node P. The diffusion coefficient and the source terms are substituted into the discretization equations. The equations are solved to find the temperature with a tolerance of 0.1°C for the maximum and mean changes in temperature between solutions. Higher tolerance levels make negligible differences to the final results and require a significantly longer time to solve.

D.2.3 Application to Residue

The general form of the differential equation with the mass fraction of mantle residue, R, as the dependent variable is

$$\frac{\partial(\rho R)}{\partial t} + \frac{\partial(\rho v_x R)}{\partial x} + \frac{\partial(\rho v_z R)}{\partial z} = 0\,. \tag{D.30}$$

The diffusion coefficient, Γ, is assumed to be zero because the transfer of material by diffusion of a solid mass is negligible compared to the advective transfer. The source terms, S_C and S_P, are also zero. In the future it may be possible to include the destruction of the residue by melting in the source term, but at present the residue field is altered according to the amount of melting at the end of each time step.

The diffusion and source terms are substituted into the discretization equations and the equations are solved to find the mass fraction of the mantle residue with a tolerance of 0.000001 for the maximum and mean changes in the mass fraction between solutions. Higher tolerance levels make negligible differences to the final results.

This method automatically introduces diffusion on the scale of the grid size. Therefore, it is important to consider the error introduced by this artificial diffusion.

D.3 Lagrangian Derivative

The Lagrangian derivative of a function is the derivative taken with respect to a moving coordinate system e.g. an advecting fluid. It is defined as

$$\frac{\mathrm{D}f}{\mathrm{D}t} = \frac{\partial f}{\partial t} + v_x \frac{\partial f}{\partial x} + v_z \frac{\partial f}{\partial z} \tag{D.31}$$

for two dimensions.

For reference, partial derivatives are defined as the derivative of functions which are dependent on multiple variables when all variables are kept constant during the differentiation, except for the variable of interest. Standard differentiation is the derivative of a function which is dependent on only one variable and the value is the change in the function for an infinitesimal change in the variable.

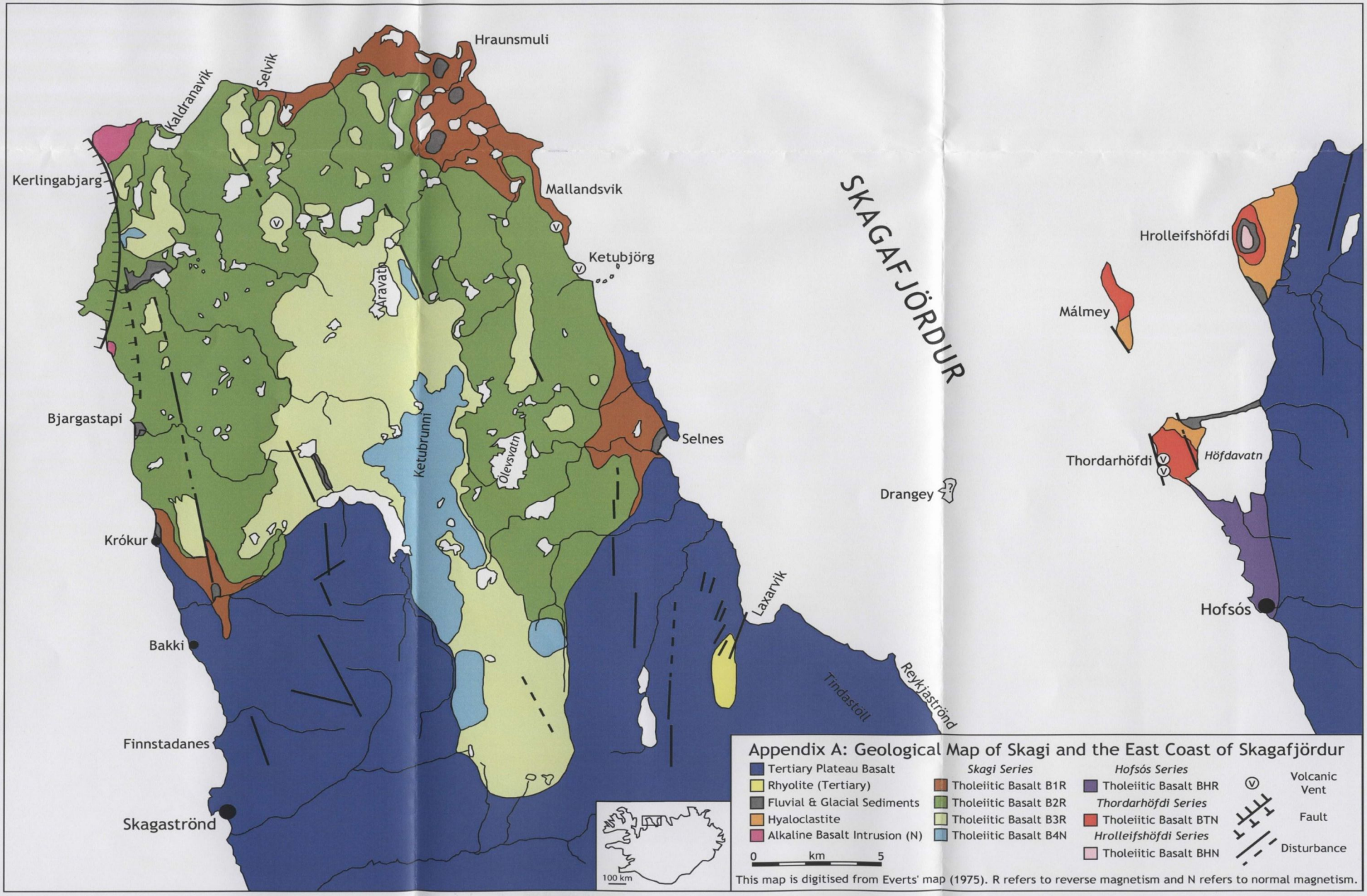
Hraunsmuli
Kaldranavik
Selvik
Kerlingabjarg
Mallandsvik
Ketubjörg
Afravatn
SKAGAFJÖRDUR
Hrolleifshöfdi
Málmey
Bjargastapi
Ketubrunni
Olevsvatn
Selnes
Thordarhöfdi
Höfdavatn
Drangey
Krókur
Laxarvik
Hofsós
Bakki
Tindastöll
Reykjaströnd
Finnstadanes
Skagaströnd
100 km
Appendix A: Geological Map of Skagi and the East Coast of Skagafjördur
Tertiary Plateau Basalt
Rhyolite (Tertiary)
Fluvial & Glacial Sediments
Hyaloclastite
Alkaline Basalt Intrusion (N)
Skagi Series
Tholeiitic Basalt B1R
Tholeiitic Basalt B2R
Tholeiitic Basalt B3R
Tholeiitic Basalt B4N
Hofsós Series
Tholeiitic Basalt BHR
Thordarhöfdi Series
Tholeiitic Basalt BTN
Hrolleifshöfdi Series
Tholeiitic Basalt BHN
Volcanic Vent
Fault
Disturbance
0 km 5
This map is digitised from Everts' map (1975). R refers to reverse magnetism and N refers to normal magnetism.